

# **PROGRESS IN RESEARCH**

**April 1, 2006 - March 31, 2007**

## **CYCLOTRON INSTITUTE**

**Texas A&M University**

**College Station, Texas**

**PROGRESS IN RESEARCH**

**APRIL 1, 2006 - MARCH 31, 2007**

**Prepared By**

**The Cyclotron Institute Staff**

**Texas A&M University**

**College Station, TX 77843-3366**

**Phone: (979) 845-1411**

**Fax: (979) 845-1899**

**Web: <http://cyclotron.tamu.edu>**

**July 2007**

## TABLE OF CONTENTS

<b>Introduction .....</b>	<b>ix</b>
R.E. Tribble, Director	
<b>SECTION I: NUCLEAR STRUCTURE, FUNDAMENTAL INTERACTIONS AND ASTROPHYSICS</b>	
<b>Giant resonances strength in <math>^{28}\text{Si}</math> .....</b>	<b>I-1</b>
D. H. Youngblood, Y. -W. Lui, and H. L. Clark	
<b>Folding model analysis for 240 MeV <math>^6\text{Li}</math> elastic scattering on <math>^{28}\text{Si}</math> and <math>^{24}\text{Mg}</math> .....</b>	<b>I-5</b>
X. Chen, Y. -W. Lui, H. L. Clark, Y. Tokimoto, and D. H. Youngblood	
<b>Study of the <math>^{12}\text{N}(p,\gamma)^{13}\text{O}</math> reaction from a (<math>^{12}\text{N}</math>, <math>^{13}\text{O}</math>) proton transfer reaction .....</b>	<b>I-11</b>
A. Banu, T. Al-Abdullah, V. Burjan, F. Carstoiu, C. Fu, C. A. Gagliardi, M. McCleskey, G. Tabacaru, L. Trache, R. E. Tribble, and Y. Zhai	
<b>Single and double proton emission from the <math>^{14}\text{O}+^4\text{He}</math> interaction .....</b>	<b>I-15</b>
Changbo Fu, V. Z. Goldberg, A. M. Mukhamedzhanov, G. G. Chubarian, G. V. Rogachev, B. Skorodumov, M. McCleskey, Y. Zhai, T. Al-Abdullah, G. Tabacaru, A. Banu, L. Trache, and R. E. Tribble	
<b>Decay of <math>^{10}\text{C}</math> excited states above the <math>2p+2\alpha</math> threshold .....</b>	<b>I-17</b>
R. J. Charity, K. Mercurio, L. G. Sobotka, J. M. Elson, M. Famiano, A. Banu, C. Fu, L. Trache, and R. E. Tribble	
<b>Characterization of novel square-bordered position-sensitive silicon detectors with a four-corner readout .....</b>	<b>I-20</b>
A. Banu, Y. Li, M. McCleskey, M. Bullough, S. Walsh, C. A. Gagliardi, L. Trache, R. E. Tribble, and C. Wilburn	
<b>Elastic scattering of <math>^{12}\text{N}</math> at 12 A MeV on <math>^{12}\text{C}</math>.....</b>	<b>I-24</b>
A. Banu, T. Al-Abdullah, C. Fu, C. A. Gagliardi, Y. Li, M. McCleskey, L. Trache, R. E. Tribble, and Y. Zhai	
<b>Further studies of <math>\beta</math>-decay of proton-rich nucleus <math>^{23}\text{Al}</math>.....</b>	<b>I-27</b>
Y. Zhai, T. Al-Abdullah, A. Banu, C. Fu, V. Golovko, J. C. Hardy, V. E. Iacob, N. Nica, H. I. Park, L. Trache, and R. E. Tribble	

<b>Technique to study <math>\beta</math>-delayed p-decay of proton-rich nuclei .....</b>	<b>I-29</b>
L. Trache, T. Al-Abdullah, A. Banu, C. Fu, V. Golovko, J.C. Hardy, V.E. Iacob, H.I. Park, G. Tabacaru, R.E. Tribble, Y. Zhai, J. Aysto, A. Saastamoinen, M. A. Bentley, D. Jenkins, T. Davinson, and P. J. Woods	
<b>Breakup of <math>sd</math>-shell proton-rich nuclei for nuclear astrophysics.....</b>	<b>I-32</b>
A. Banu, L. Trache, R. E. Tribble, Y. Zhai, N. Orr, L. Achouri, B. Laurent, B. Roeder, M. Charrier, B. Fernandez-Dominguez, S. Paschalis, B. Pietras, W. Catford, N. Patterson, J. Thomas, M. Freer, P. Roussel-Chomaz, L. Gaudefroy, F. Carstoiu, F. Negoita, F. Rotaru, and A. Bonaccorso	
<b>Determination of the <math>^{17}\text{F}(p,\gamma)^{18}\text{Ne}</math> reaction rate using the neutron transfer reaction <math>^{13}\text{C}(^{17}\text{O},^{18}\text{O})^{12}\text{C}</math> .....</b>	<b>I-34</b>
T. Al-Abdullah, F. Carstoiu, X. Chen, C. A. Gagliardi, Y.-W. Lui, G. Tabacaru, Y. Tokimoto, L. Trache, R. E. Tribble, and Y. Zhai	
<b>Study of low-lying resonant states in <math>^{16}\text{F}</math> using an <math>^{15}\text{O}</math> radioactive ion beam.....</b>	<b>I-37</b>
V. Z. Goldberg, D. W. Lee, K. Peräjärvi, J. Powell, J. P. O'Neil, D. M. Moltz, and Joseph Cerny	
<b>Study of the <math>^{20}\text{O}+p</math> interaction .....</b>	<b>I-38</b>
Changbo Fu, V. Z. Goldberg, G. G. Chubarian, M. McCleskey, Y. Zhai, T. Al-Abdullah, G. Tabacaru, and R. E. Tribble	
<b>Search for violation of the spin-parity and isospin conservation law in the decay of the 3.56 MeV <math>0^+</math> level in <math>^6\text{Li}</math>.....</b>	<b>I-39</b>
V. Z. Goldberg, J. C. Hardy, A. Mukhamedzhanov, G. Tabacaru, G. Chubarian, R. E. Tribble, G. V. Rogachev, E. Johnson, C. Spitaleri, S. Cherubini, S. Romano, M. Gulino, A. Tumino, R. G. Pizzone, M. La Cognata, L. Lamia, N. Shulgina, and W.H. Trzaska	
<b><math>T = 3/2</math> states in <math>^{13}\text{C}</math>.....</b>	<b>I-40</b>
V. Z. Goldberg, R. E. Tribble, B. B. Skorodumov, G. V. Rogachev, A. Aprahamian, J. J. Kolata, S. Almaraz, H. Amro, L. O. Lamm, M. Quinn, A. Teymurazyan, and A. Woehr	
<b>Superaligned beta decay.....</b>	<b>I-42</b>
J. C. Hardy, I. S. Towner, V. E. Iacob, N. Nica, V. Golovko, H. I. Park, J. Goodwin, C. A. Gagliardi, L. Trache, and R. E. Tribble	
<b>The status of <math>V_{ud}</math> .....</b>	<b>I-46</b>
J. C. Hardy	
<b>Precise half-life measurements for the superallowed <math>\beta^+</math> emitter <math>^{34}\text{Ar}</math> and <math>^{34}\text{Cl}</math>.....</b>	<b>I-48</b>
V. E. Iacob, J. C. Hardy, J. F. Brinkley, C. A. Gagliardi, V.E. Mayes, N. Nica,	

M. Sanchez-Vega, G. Tabacaru, L. Trache, and R. E. Tribble

<b>Precise <math>\beta</math> branching ratios in <math>^{34}\text{Ar}</math> from <math>\beta</math>-<math>\gamma</math> coincidences .....</b>	<b>I-51</b>
V. E. Iacob, J. C. Hardy, and V. Golovko	
<b>The Half Life of <math>^{10}\text{C}</math> .....</b>	<b>I-55</b>
V. E. Iacob, J. C. Hardy, and V. Golovko, J. Goodwin, N. Nica, H. I. Park, L. Trache and R. E. Tribble	
<b>High precision half-life measurement in <math>^{38}\text{Ca}</math> .....</b>	<b>I-58</b>
H. I. Park, J. C. Hardy, V. V. Golovko, V. E. Iacob, N. Nica, A. Banu, L. Trache, R. E. Tribble, and Y. Zhai	
<b>TRIUMF E-823: Measurements of the <math>^{37,38\text{m}}\text{K}</math> half-lives .....</b>	<b>I-59</b>
V. E. Iacob and J. C. Hardy	
<b>JYFLTRAP : <math>Q_{\text{EC}}</math>-values of the superallowed decays of <math>^{50}\text{Mn}</math> and <math>^{54}\text{Co}</math> .....</b>	<b>I-61</b>
J. C. Hardy	
<b>Branching ratios for the beta decay of <math>^{21}\text{Na}</math> .....</b>	<b>I-62</b>
V. E. Iacob, J. C. Hardy, C. A. Gagliardi, J. Goodwin, N. Nica, H. I. Park, G. Tabacaru, L. Trache, R. E. Tribble, Y. Zhai and I. S. Towner	
<b>Tests of internal-conversion theory and efficiency calibration with precise <math>\gamma</math>- and x-ray spectroscopy: <math>^{134}\text{Cs}^{\text{m}}</math>, <math>^{137}\text{Ba}</math>, <math>^{139}\text{La}</math>.....</b>	<b>I-66</b>
N. Nica, C. Balonek, J. C. Hardy, V. E. Iacob, J. Goodwin, H. I. Park, W. E. Rockwell and M. B. Trzhaskovskaya	
<b>Evaluated nuclear structure data file (ENSDF) at Texas A&amp;M: <math>A=140</math>.....</b>	<b>I-70</b>
N. Nica, and J. C. Hardy	
<b>TWIST: measuring the space-time structure of muon decay .....</b>	<b>I-72</b>
C. A. Gagliardi, R. E. Tribble, K. Williams and the TWIST Collaboration	
<b>Spin and low-x physics with STAR at RHIC.....</b>	<b>I-74</b>
J. L. Drachenberg, C. A. Gagliardi, T. W. Henry, M. Sarsour, R. E. Tribble, and the STAR Collaboration	
<b>Toward understanding relativistic heavy-ion collisions with the STAR detector at RHIC.....</b>	<b>I-76</b>
M. Cervantes, R. Clarke, M. Codrington, L. Dunkelberger, A. Hamed, S. Mioduszewski, and the STAR Collaboration	

## SECTION II: HEAVY ION REACTIONS

<b>Alternative mechanisms for heavy element production .....</b>	<b>II-1</b>
P. K.Sahu, J. B. Natowitz, R. Wada, K. Hagel, T. Materna, Z. Chen, L. Qin, M. Barbui, S. Moretto, D. Fabris, M. Lunardon, M. Morando, G. Nebbia, S. Pesente, V. Rizzi, G. Viesti, V. Bocci, A. Andrighetto, M. Cinausero, G. Prete, Z. Majka, A. Wieloch, and S. Kowalski	
<b>Z-dependence of isoscaling parameter in central heavy ion collisions at intermediate energy.....</b>	<b>II-3</b>
Z. Chen, R. Wada, T. Keutgen, K. Hagel, J. Wang, L. May, L. Qin, J. B. Natowitz, T. Materna, S. Kowalski, and P.K. Sahu	
<b>Dynamical and statistical nature of heavy ion reactions at 47A MeV .....</b>	<b>II-5</b>
L. J. Qin, R. Wada, K. Hagel, J. B. Natowitz, J. S. Wang, Y. Ma, T. Materna, T. Keutgen, Z. Chen, and P. K Sahu	
<b>Progress in BRAHMS.....</b>	<b>II-9</b>
K. Hagel, R. Wada, J. B. Natowitz, and the BRAHMS Collaboration	
<b>N/Z equilibration in deep inelastic collisions.....</b>	<b>II-11</b>
A. L. Keksis, M. Veselsky, G. A. Souliotis, D. V. Shetty, M. Jandel, E. Bell, A. Ruangma, E. M. Winchester, J. Garey, S. Parketon, C. Richers, and S. J. Yennello	
<b>The fragmentation of quasiprojectiles . .....</b>	<b>II-14</b>
A. L. Keksis, M. Veselsky, G. A. Souliotis, D. V. Shetty, M. Jandel, E. Bell, A. Ruangma, E. M. Winchester, J. Garey, S. Parketon, C. Richers, and S. J. Yennello	
<b>Nucleon transfer calculations using HIPSE model . .....</b>	<b>II-18</b>
Z. Kohley, D. Lacroix, G. A. Souliotis, A. L. Keksis, B. Stein, D. V. Shetty, S. Soisson, and S. J. Yennello	
<b>Using light cluster production to determine the density dependence of the nuclear symmetry energy.....</b>	<b>II-21</b>
S. N. Soisson, L. W. Chen, E. Bell, B. A. Li, D. V. Shetty, G. A. Souliotis, A. L. Keksis, S. J. Yennello and the NIMROD Collaboration	
<b>An update to the dual-axis dual-lateral upgrade to the FAUST detector array . .....</b>	<b>II-23</b>
S. N. Soisson, B. C. Stein, and S. J. Yennello	
<b>Comparisons of microscopic calculations with experimental heavy residue distributions and the sensitivity to the density dependence of the nuclear symmetry energy .....</b>	<b>II-25</b>
G. A. Souliotis, D. V. Shetty, and S. J. Yennello	

**Production and separation of rare isotope beams at K150 energies ( $E/A=10-15$  MeV/nucleon)...II-29**  
 G. A. Souliotis, B. C. Stein, Z. Kohley, S. Galanopoulos, A. L. Keksis, D. V. Shetty,  
 S. N. Soisson, S. Wuenschel, and S. J. Yennello.

**Study of projectile multifragmentation in the reactions  $^{24}\text{Mg} + ^{112,124}\text{Sn}$  and  
 the effect of system N/Z at 32 MeV/u. ....II-32**  
 S. Galanopoulos, G. A. Souliotis, A. L. Keksis, M. Veselsky, M. Jandel, D. V. Shetty,  
 S. Soisson, B. Stein, S. Wuenschel, and S. J. Yennello

**Status of the NIMROD upgrade .....II-34**  
 S. Wuenschel, K. Hagel, Z. Kohley, L. May, J. B. Natowitz, R. Wada, and S. J. Yennello

**Density dependence of the symmetry energy and the nuclear equation of state :  
 A dynamical and statistical model perspective .....II-36**  
 D. V. Shetty, S. J. Yennello, and G. A. Souliotis

**Symmetry energy, temperature, density and isoscaling parameter as a function of  
 excitation energy in  $A \sim 100$  mass region .....II-41**  
 D. V. Shetty, S. J. Yennello, G. A. Souliotis, A. L. Keksis, S. N. Soisson,  
 B. C. Stein, and S. Wuenschel

**Thermal expansion, effective mass and nuclear caloric curve .....II-46**  
 D. V. Shetty, S. J. Yennello, G. A. Souliotis, S. Galanopoulos, A. L. Keksis,  
 S. N. Soisson, B. C. Stein, S. Wuenschel, and Z. Kohley

**Investigating the symmetry and surface energy co-efficient from fragment isotope and  
 charge yield distribution using statistical multifragmentation model .....II-49**  
 D. V. Shetty, A. E. Echeverria, S. J. Yennello, G. A. Souliotis, S. Galanopoulos,  
 A. L. Keksis, S. N. Soisson, B. C. Stein, S. Wuenschel, and Z. Kohley

**Effect of symmetry energy evolution during sequential de-excitation on isoscaling  
 parameter of the fragments produced in multifragmentation reaction .....II-52**  
 D. V. Shetty, J. Igljo, A. E. Echeverria, S. J. Yennello, G. A. Souliotis, S. Galanopoulos,  
 A. L. Keksis, S. N. Soisson, B. C. Stein, S. Wuenschel, and Z. Kohley

### SECTION III: NUCLEAR THEORY

**Heavy quark three-body collisional energy loss in quark-gluon plasma ..... III-1**  
 C. M. Ko and Wei Liu

**Elliptic flow of deuterons in relativistic heavy ion collisions..... III-2**  
 Y. Oh and C.M. Ko

<b>Equation of state of the hot dense matter in a multiphase transport model.....</b>	<b>III-3</b>
B. Zhang, L.W. Chen, and C.M. Ko	
<b>Jet flavor conversions in a quark-gluon plasma .....</b>	<b>III-4</b>
W. Liu, C. M. Ko, and B. W. Zhang	
<b>Charmonium absorption by nucleons in the meson-exchange model .....</b>	<b>III-5</b>
Y. Oh, C. M. Ko, and W. Liu	
<b>Heavy ion collisions at LHC in a multiphase transport model .....</b>	<b>III-6</b>
C. M. Ko, L. W. Chen, and B. W. Zhang	
<b><math>D_{sJ}(2317)</math> meson production at RHIC .....</b>	<b>III-7</b>
L. W. Chen, C. M. Ko, W. Liu, and M. Nielsen	
<b>T-matrix approach to quarkonium correlation functions in the quark-gluon plasma .....</b>	<b>III-8</b>
Daniel Cabrera and Ralf Rapp	
<b>Transverse-momentum spectra of dilepton radiation at the CERN-SPS .....</b>	<b>III-11</b>
Hendrik van Hees, Trenton Strong, and Ralf Rapp	
<b>Quark coalescence based on a transport equation .....</b>	<b>III-13</b>
Lorenzo Ravagli and Ralf Rapp	
<b>The initial state of high energy nuclear collisions.....</b>	<b>III-15</b>
R. J. Fries, J. Kapusta, and Y. Li	
<b>Perturbative QCD and multiple scattering in nuclear matter .....</b>	<b>III-16</b>
R. J. Fries and A. Majumder	
<b>The recombination model.....</b>	<b>III-17</b>
R. J. Fries and collaborators	
<b>Suppression of the Coulomb interaction in the off-energy-shell <math>p - p</math> scattering from the <math>p + d \rightarrow p + p + n</math> reaction .....</b>	<b>III-18</b>
A. M. Mukhamedzhanov, A. Tumino, C. Spitaleri, G. G. Rapisarda, S. Cherubini, V. Crucillá, M. Gulino, M. La Cognata, L. Lamia, F. Mudó, R.G. Pizzone, S. Romano, M. L. Sergi, Z. Elekes, Z. Fülöp, G. Gyürky, G. Kiss, and E. Somorjai	
<b>Are spectroscopic factors from transfer reactions consistent with asymptotic normalization coefficients? .....</b>	<b>III-20</b>
D. Y. Pang, F. M. Nunes, and A. M. Mukhamedzhanov	
<b>Deuteron elastic scattering and stripping processes off <math>^{12}\text{C}</math> as a three-body problem .....</b>	<b>III-22</b>
E. O. Alt, L. D. Blokhintsev, A. M. Mukhamedzhanov, and A. I. Sattarov	

<b>Troajn horse for resonance reactions .....</b>	<b>III-24</b>
A. M. Mukhamedzhanov, C. Spitaleri, and R. E. Tribble	
<b>Asymptotic normalization coefficient and spectroscopic factor from <math>^{48}\text{Ca}(\text{d,p})^{49}\text{Ca}</math> and <math>^{48}\text{Ca}(\text{n},\gamma)^{49}\text{Ca}</math> .....</b>	<b>III-26</b>
A. M. Mukhamedzhanov, P. Mohr, and F. M. Nunes	
<b>Troajn horse for direct reactions .....</b>	<b>III-27</b>
A. M. Mukhamedzhanov, C. Spitaleri, and R. E. Tribble	
<b>Superaligned Fermi beta decay: the isospin-symmetry-breaking correction .....</b>	<b>III-29</b>
I. S. Towner and J. C. Hardy	
<b>Superaligned Fermi beta decay: the radiative correction .....</b>	<b>III-31</b>
I. S. Towner and J. C. Hardy	
<b>Renormalized self consistent continuum random phase approximation .....</b>	<b>III-34</b>
Voung Kim Au, Nguyen Dinh Dang, and Shalom Shlomo	
<b>Constraining the symmetry energy from nuclear giant resonances.....</b>	<b>III-36</b>
Tapas Sil, and Shalom Shlomo	
<b>Effects of long range correlations on nuclear charge radii in fully self-consistent Hartree-Fock RPA method .....</b>	<b>III-38</b>
Tapas Sil, and Shalom Shlomo	

#### SECTION IV: ATOMIC, MOLECULAR AND MATERIALS SCIENCE

<b>A semiempirical scaling law for target K x-ray production in heavy ion collisions.....</b>	<b>IV-1</b>
R. L. Watson, Y. Peng, V. Horvat, and A. N. Perumal	
<b>Systematics of L x-ray satellite spectra .....</b>	<b>IV-4</b>
V. Horvat, R.L. Watson, Y. Peng and J. M. Blackadar	
<b>Single and multiple L-shell ionization by fast heavy ions.....</b>	<b>IV-7</b>
V. Horvat , R.L. Watson, Y. Peng, and J. M. Blackadar	

#### SECTION V: SUPERCONDUCTING CYCLOTRON, INSTRUMENTATION AND RIB UPGRADE

<b>K500 operations and development .....</b>	<b>V-1</b>
D. P. May, G. J. Kim, H. L. Clark, and F. P. Abegglen	

<b>Progress on ECR2 .....</b>	<b>V-3</b>
D. P. May	
<b>Radiation effects facility .....</b>	<b>V-5</b>
H. L. Clark, J. Brinkley, G. Chubarian, V. Horvat, B. Hyman, G. Souliotis and G. Tabacaru	
<b>Cyclotron computing .....</b>	<b>V-7</b>
R. Burch, and K. Hagel	
<b>Cyclotron institute upgrade project .....</b>	<b>V-8</b>
H. L. Clark	
<b>Compact injection line for K150 cyclotron.....</b>	<b>V-15</b>
G. J. Kim	
<b>Progress on the light ion guide facility .....</b>	<b>V-20</b>
G. Tabacaru, J. Arje, and H. L. Clark	
<b>Progress on the shielding evaluation for the beam dump .....</b>	<b>V-21</b>
G. Tabacaru and H. L. Clark	
<b>The use of Geant4 simulate the response function of a plastic <math>\beta</math>-detector to standard <math>\beta</math>-sources of <math>^{133}\text{Ba}</math> and <math>^{137}\text{Cs}</math>.....</b>	<b>V-23</b>
V. V. Golovko, J. C. Hardy, and V. E. Iacob	

## SECTION VI: PUBLICATIONS

<b>Papers Published.....</b>	<b>VI-1</b>
------------------------------	-------------

## SECTION VII: APPENDIX

<b>Talks Presented .....</b>	<b>VII-1</b>
<b>Research Personnel and Engineering Staff .....</b>	<b>VII-10</b>
<b>Students.....</b>	<b>VII-11</b>
<b>Organizational Chart.....</b>	<b>VII-12</b>
<b>Graduate Degree Students .....</b>	<b>VII-13</b>
<b>Institute Colloquia and Seminars .....</b>	<b>VII-14</b>

**Introduction**  
**April 1, 2006 – March 31, 2007**

Progress in research and operations at the Texas A&M Cyclotron Institute is summarized in this report for the period April, 1, 2006 through March 31, 2007. Sections I through IV contain reports from individual research projects. Operation and technical developments are given in Section V. Section VI lists the publications with Cyclotron Institute authors and the Appendix gives additional information including talks presented by members of the Institute during the past year. Once again, the full volume of this year's Progress in Research is available only on our web site (<http://cyclotron.tamu.edu>). *Since most of the contributions presented here are truly reports on progress in research, results and conclusions should not be quoted from the report without the consent of the authors.*

We have now completed 2 1/2 years of the Upgrade Project which ultimately will give us accelerated radioactive beams at intermediate energies. The progress on the project continues to be very good—we remain close to schedule as of the second quarter of FY07. During the past year the K500 cyclotron has continued to perform well. We have had increasing pressure on beam time for testing electronics components which has made juggling the schedule quite difficult.

Institute programs continue to thrive. In the fall of 2006, Dr. Rainer Fries was appointed as an Assistant Professor of Physics and became a member of the Cyclotron Institute. Dr. John Hardy was named Distinguished Professor in the spring of 2007. Also in the spring, an offer was made to Dr. Dan Melconian to join the Institute and the Physics Department as an Assistant Professor. He accepted the offer and will come in late fall of 2007.

Some highlights of work over the past year are given below.

Research highlights:

- (1) The half-life and branching ratio of the superallowed beta-decay of  $^{34}\text{Ar}$  have been measured for the first time with high precision ( $<0.1\%$ ). Combined with the previously well measured Q value, this yields a corrected  $f$  value with 0.1% precision, which is also in good agreement with the world average of other superallowed decays. This result is particularly significant because  $^{34}\text{Ar}$  has the largest calculated isospin-symmetry-breaking correction of any of the measured cases between  $A=10$  and  $A=54$ , the region where the nuclear models used in the calculation are most trustworthy. The fact that the calculated correction leads to good agreement with the  $f$ -value average in this case, where the correction is large, provides strong independent validation of the calculational approach, particularly for the other cases where the corrections themselves are much smaller.
- (2) The ANCs for  $^{18}\text{Ne} \leftrightarrow ^{17}\text{F} + p$  have been determined from a study of  $^{13}\text{C}(^{17}\text{O}, ^{18}\text{O})^{12}\text{C}$ , and used to infer the  $^{17}\text{F}(p,\gamma)^{18}\text{Ne}$  astrophysical reaction rate. The results support enhanced production of  $^{17}\text{F}$  and  $^{18}\text{F}$  in ONe novae.

- (3) Temperature and density dependent symmetry energies have been determined experimentally at nuclear densities near  $0.05 \rho(0)$  where  $\rho(0)$  is the ground state density of symmetric nuclear matter. Ranging from 9.03 to 13.6 MeV, they are much larger than those derived from effective interactions in mean field models. This reflects cluster formation, primarily of alpha particles, not included in such calculations. Such clusterization plays a significant role in astrophysical environments.
- (4) The beta branching ratio for the transition from  $^{21}\text{Na}$  to the first excited state of  $^{21}\text{Ne}$  has been measured with sub-percent precision. Previously measured values had differed from one another by more than a factor of two, and had severely limited the effectiveness of a test of the Standard Model based on a measurement of the beta-neutrino correlation in the decay of  $^{21}\text{Na}$ .
- (5) The longitudinal spin correlation,  $A_{LL}$ , has been determined via inclusive jet production, based on data recorded by STAR in 2005. The results provide significant new constraints on the gluon contribution to the proton spin.
- (6) The giant monopole resonance strengths found in  $^{116}\text{Sn}$  and  $^{28}\text{Si}$  using inelastic  $^6\text{Li}$  scattering are consistent with those extracted from inelastic  $\alpha$  scattering, showing that GMR strengths could be extracted for unstable nuclei using a  $^6\text{Li}$  target.
- (7) Measurements of the  $\beta$  decay of  $^{23}\text{Al}$  have confirmed that its ground state spin-parity is  $5/2^+$ , thus contradicting the assertion, based on results from  $^{23}\text{Al}$  breakup, that it is  $1/2^+$ . The assignment of  $5/2^+$  significantly lowers the rate of the  $^{22}\text{Mg}(p,\gamma)^{23}\text{Al}$  reaction relative to a  $1/2^+$  assignment.
- (8) A reformulation of quark coalescence models has been developed at the hadron-QGP phase boundary based on a Boltzmann equation with resonant  $2 \rightarrow 1$  interactions. It overcomes the problem of energy violation and the lack of a thermal equilibrium limit in earlier approaches.
- (9) Heavy quarkonium correlation functions in the QGP have been calculated using a T-matrix approach with heavy-quark potentials extracted from lattice QCD. The consistent treatment of bound and scattering states is essential for a reliable interpretation of Euclidean correlation functions as directly computed in lattice QCD.
- (10) New results have been obtained that give strong evidence for correlated two proton decay from a state in  $^{18}\text{Ne}$  at 8.5 MeV. The state was populated by the  $^{14}\text{O} + \alpha$  resonance reaction.
- (11) A new determination of the astrophysical S factor for the  $^{13}\text{C}(\alpha,n)^{16}\text{O}$  neutron generator reaction in the AGB stars has been done by measuring the ANC in the sub-Coulomb transfer reaction  $^{13}\text{C}(^6\text{Li},d)^{17}\text{O}$  reaction. The reaction rates determined for  $^{13}\text{C}(\alpha,n)^{16}\text{O}$  are 3 times lower than in previous compilations.

(12) A stripping reaction has been calculated in the genuine three-body approach using the modified Faddeev equations for the first time.

As in the past, Institute scientists remain active in a number of collaborative research efforts around the world. Major programs include: a measurement of Michel parameters in normal  $\mu^+$  decay at TRIUMF in Vancouver, B.C.; mass measurements using the Canadian Penning Trap (CPT) at Argonne National Laboratory; and continued work with both the BRAHMS and STAR collaborations at RHIC.

Once again, I am indebted to Dr. Y.-W. Lui who has managed to assemble this report in a very prompt and efficient manner.

R.E. Tribble  
June 26, 2007

## **SECTION I**

# **NUCLEAR STRUCTURE, FUNDAMENTAL INTERACTIONS, AND ASTROPHYSICS**

## Giant resonance strength in $^{28}\text{Si}$ .

D. H. Youngblood, Y. -W. Lui, and H. L. Clark

We report here a reanalysis of the 240 MeV  $^{28}\text{Si}$  inelastic  $\alpha$  scattering data reported in Ref. [1] up to an excitation energy of 42 MeV where the assumption is made that ALL of the cross section is due to multipole processes having  $L \leq 4$  (i.e. there has been no continuum or background subtraction). Alpha particles from the decay of the mass 5 ejectile created in the  $(\alpha, ^5\text{He})$  and  $(\alpha, ^5\text{Li})$  reactions will be a competing process above  $E_x=42$  MeV ( $^5\text{Li}$ ) and 50 MeV ( $^5\text{He}$ ), so this “zero continuum” analysis would not be appropriate above  $E_x=42$  MeV.

The multipole components were obtained [1] by dividing the data into multiple regions (bins) by excitation energy and then comparing the angular distributions obtained for each of these bins to distorted wave Born approximation (DWBA) calculations to obtain the multipole components. The uncertainty from the multipole fits was determined for each multipole by incrementing (or decrementing) that strength, then adjusting the strengths of the other multipoles to minimize total  $\chi^2$ . This continued until the new  $\chi^2$  was 1 unit larger than the total  $\chi^2$  obtained for the best fit.

The DWBA calculations were described in Ref. [1] and the same density dependent Woods-Saxon folding potentials were used for the calculations in this work. A sample of the angular distributions obtained are shown in Fig. 1. Fits to the angular distributions were carried out with a sum of isoscalar  $0^+$ ,  $1^-$ ,  $2^+$ ,  $3^-$ , and  $4^+$  strengths. The limited angular range of the data prevents distinguishing  $L=4$  and higher contributions. The isovector giant dipole resonance (IVGDR) contributions are small, but were calculated from the known distribution [2] and held fixed in the fits. Sample fits obtained, along with the individual components of the fits, are shown superimposed on the data in Fig. 1.

The strength distributions obtained for

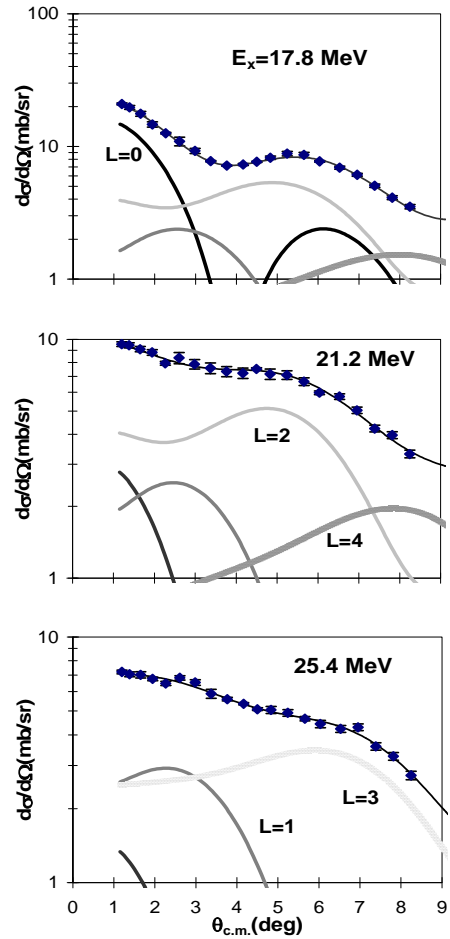


**Figure 1.** Angular distributions obtained for inelastic  $\alpha$  scattering for three excitation ranges in  $^{28}\text{Si}$ . The energy bins are approximately 450 keV wide. The medium black line shows the fits. Contributions of each multipole are shown. When not shown, errors are smaller than the data points.

isoscalar  $L = 0,1,2,3$ , and 4 are shown in Fig. 2. The E0 multipole distribution is superimposed on the distribution from Ref. [1]. They are in reasonable agreement over the entire energy region. The EWSR strength obtained,  $74 \pm 7\%$  of the E0 EWSR, the centroid energy ( $m1/m0$ )  $20.89 \pm 0.38$  MeV and RMS width  $5.9 \pm 0.6$  MeV all agree within the errors with those from Ref. [1] ( $81 \pm 10\%$ ,  $21.25 \pm 0.38$  MeV and  $6.4 \pm 0.6$  MeV respectively). This work and Ref. [1] used the same data, DWBA calculations, and fitting routines so that the small differences can be attributed entirely to the choice of continuum. This suggests that the extracted monopole strength is only weakly dependent on the assumptions made about the continuum, which we have seen in analyses of data for other nuclei. This is not true for other multipolarities.

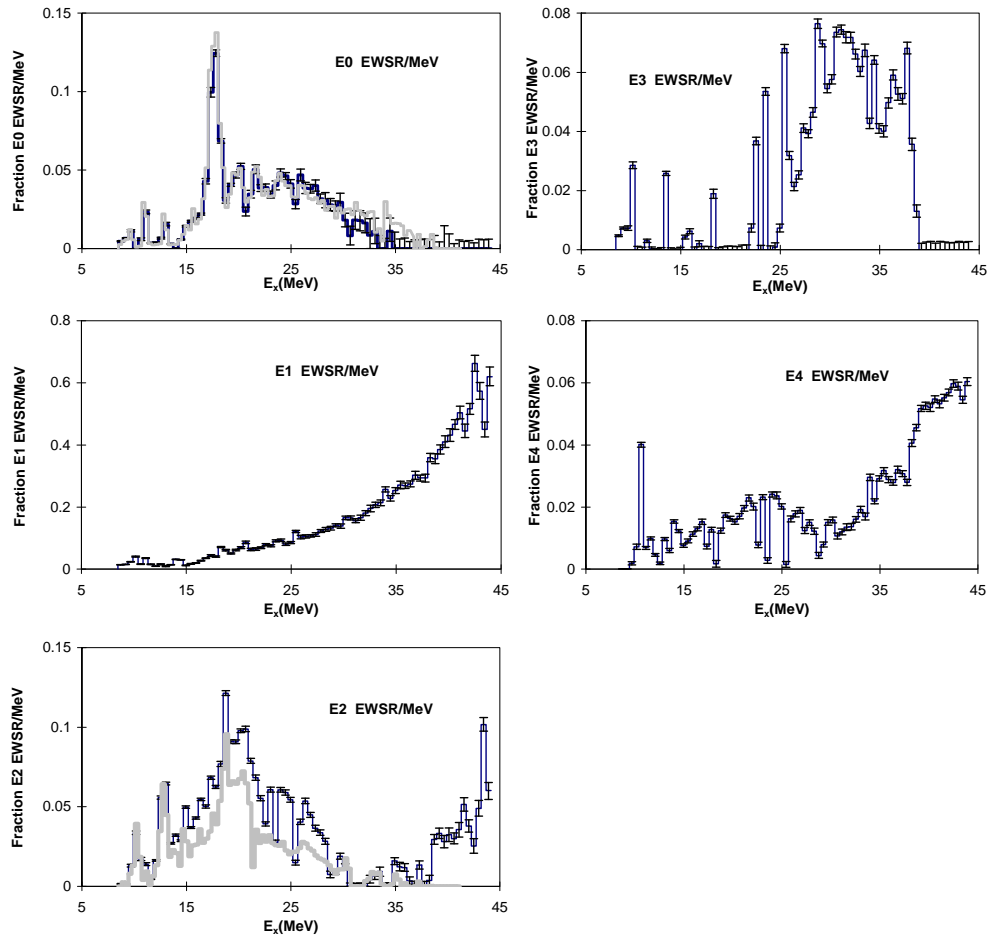


**Figure 2.** The E0, E1, E2, E3 and “E4” strength distributions obtained are shown by the gray histogram. Error bars represent the uncertainty due to the fitting of the angular distributions as described in the text. The grey lines shows the E0 and E2 distributions reported in Ref. [1].

In the region  $E_x=9\text{--}35$  MeV E2 strength corresponding to  $102\pm 11\%$  of the E2 EWSR was identified in a broad peak with a centroid of  $18.77\pm 0.35$  MeV and RMS width of  $5.45\pm 0.20$  MeV. This contrasts sharply with the results of Ref. [1] (shown for comparison in Fig. 3) where after a continuum was subtracted, E2 strength was identified corresponding to  $68\pm 9\%$  of the E2 EWSR. The centroid and RMS width of the E2 strength reported in Ref. [1] were  $18.54\pm 0.25$  MeV and  $4.7\pm 0.6$  MeV suggesting that the additional strength identified in this analysis lies predominantly in the higher energy region as might be expected since the continuum assumed in Ref. [1] was lower at lower excitation. The known  $2^+$  strength in states below  $E_x\sim 9.5$  MeV corresponds to  $\sim 11.4\%$  of the E2 EWSR [3], so that all of the expected isoscalar E2 strength in  $^{28}\text{Si}$  is accounted for below 35 MeV. Above  $E_x=35\text{--}38$  MeV the E2 strength appears to increase up to the highest energy analyzed apparently containing another 27% of the E2 EWSR. This is likely due to unidentified continuum processes that have distributions similar to an  $L=2$  multipole.

As can be seen in Fig. 2, our analysis shows a small amount of E3 strength between 10 and 18 MeV (3% of the E3 EWSR) and a much larger amount ( $81\pm 8\%$  of the E3 EWSR) between 23 and 39 MeV centered at 32 MeV with an RMS width of  $5.3\pm 0.4$  MeV. Only small amounts of E3 strength have been seen in other nuclei with  $A < 56$ . In heavier nuclei ( $A=90\text{--}208$ ), approximately 75% of the E3 EWSR was identified at higher excitation [4] and  $E_{\text{HEOR}}*A^{1/3}$  lies between 92 and 116 MeV. The observed HEOR strength in  $^{28}\text{Si}$  corresponds to  $E_{\text{HEOR}}*A^{1/3}=95$  MeV, consistent with what is expected for

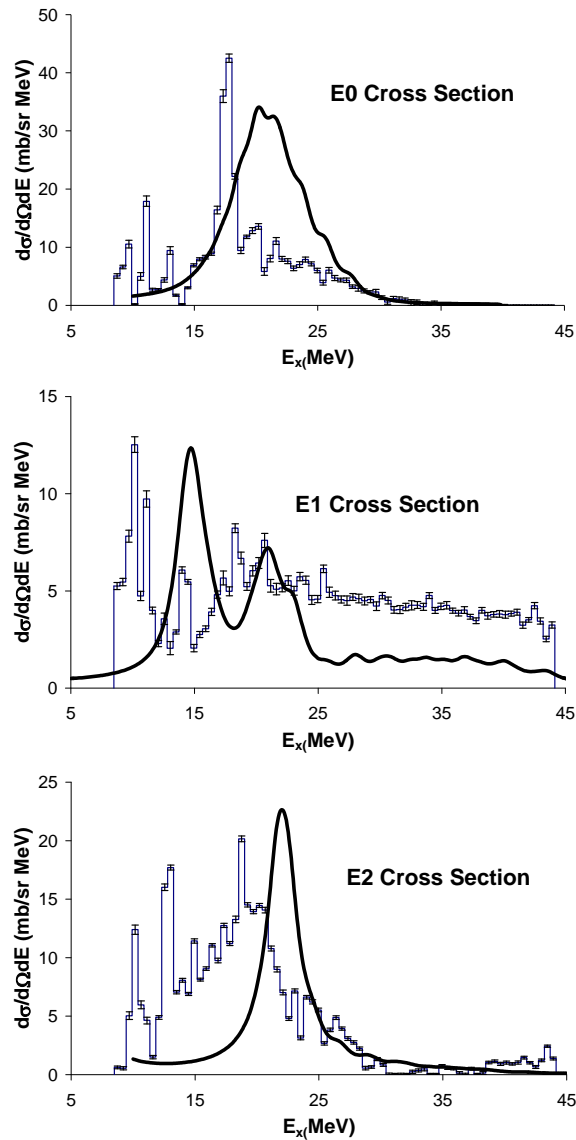


**Figure 3.** Cross sections (at the peak of the angular distributions) for E0, E1, and E2 excitation (obtained from the strength distributions shown in Fig. 3) are shown by the histograms. The solid lines are calculations from Ref. [5].

the  $3\hbar\omega$  component of the E3 strength.

The “E4” ( $L\geq 4$ ) strength has a broad peak between 9 and 30 MeV followed by a dramatic increase above  $E_x=30$  MeV. The total strength observed corresponds to  $\sim 80\%$  of the E4 EWSR, but the relatively fast increase above 30 MeV is likely due to continuum processes having relatively flat angular distributions.

The “isoscalar E1 strength” obtained rises sort of smoothly from 9 MeV to 40 MeV and corresponds to 140% of the isoscalar E1 EWSR. In the analysis reported in Ref. [1] as well as analyses of the data for other nuclei [4], the isoscalar E1 strength extracted from a multipole analysis of the continuum rises almost monotonically up to the highest excitation energy studied and corresponds to significantly more than the sum rule strength. There are likely continuum processes which are responsible for much of this (apparent) E1 strength as discussed below.

In Fig. 3 the E0, E1, and E2 strength functions from Fig. 2 have been converted into cross section at the peak of the angular distribution. Also plotted are Hartree-Fock Random Phase Approximation calculations [5] for strength distributions converted to cross sections (at the peak of the angular distribution for each multipole) using double folding calculations where the transition densities for each multipole were obtained from the HF-RPA calculations. These calculations did not include specific nuclear structure effects and show no structure whereas in this light nucleus considerable structure is present in the data as expected. Of particular interest are the calculations for the E1 strength. Above  $E_x \sim 25$  MeV the E1 double differential cross section is about 50% of the observed cross section for all processes and is  $\sim 2.5$  times the predicted cross section, suggesting that some (significant?) part of the data is not due to E1 excitation but other (unidentified) processes that somewhat mimic an E1 angular distribution.

[1] D. H. Youngblood, Y. -W. Lui, and H. L. Clark, Phys. Rev. C **65**, 034302 (2002).

[2] S. S. Dietrich and B. L. Berman, At. Data Nucl. Data Tables **38**, 199 (1988).

[3] P. M. Endt, Nucl. Phys. **A633**, 1 (1998), and interim evaluation, B. Singh (2001). Data extracted from the ENSDF database, revision of July 24, 2003, NNDC.

[4] D. H. Youngblood, Y. -W. Lui and H. L. Clark, B. John, Y. Tokimoto, and X. Chen, Phys. Rev. C **69**, 034315 (2004), *ibid* Phys. Rev. C **69**, 054312 (2004).

[5] S. Shlomo, B. Debresch, A. I. Sanzhur, and A. Moalem (private communication).

## Folding model analysis for 240MeV ${}^6\text{Li}$ elastic scattering on ${}^{28}\text{Si}$ and ${}^{24}\text{Mg}$

X. Chen, Y. -W. Lui, H. L. Clark, Y. Tokimoto, and D. H. Youngblood

In order to study giant resonance induced by  ${}^6\text{Li}$  scattering, optical model (OM) analysis of  ${}^6\text{Li}$  elastic scattering is necessary to get the optical parameters. OM has been widely used to analyze the heavy ion scattering data in term of empirical Woods-Saxon (W-S) parameterizations of the nuclear potential. However, it was found that a satisfactory microscopic understanding of heavy ion scattering can be obtained if one relates the optical potential to a fundamental nucleon-nucleon (NN) interaction through the double folding (DF) approach by folding this interaction with the nuclear matter distributions of both the target and projectile nuclei [1]. Since  ${}^6\text{Li}$  is a loosely bound nucleus, breakup has a large contribution to the real part of the nuclear potential and is responsible for the substantial renormalization factor  $N_R$  for the real folded potential [2].  ${}^6\text{Li}$  elastic scattering itself is very interesting.  ${}^6\text{Li}$  is in the mass number range  $A=4-12$ , where the elastic scattering show a transition between characteristics of light ions ( $A\leq 4$ ) and characteristics of heavy ion ( $A\geq 12$ ). Such data could provide a stronger test of the validity of any model for heavy ion potentials [3,4].

A beam of 240MeV  ${}^6\text{Li}$  ions from the Texas A&M University K500 superconducting cyclotron bombarded self-supporting  ${}^{28}\text{Si}$  and  ${}^{24}\text{Mg}$  target foil in the target chamber of the multipole-dipole-multipole spectrometer. Elastic scattering and inelastic scattering to the low-lying states were measured from  $5^\circ$ - $35^\circ$ . The calibration procedures were described in details in Refs. [5,6]. The experimental cross sections were obtained from the charge collected, target thickness, dead time and known solid angle. The cumulative uncertainties in target thickness, solid angle, etc., result in about a  $\pm 10\%$  uncertainty in absolute cross section.

Two different NN effective interactions (M3Y[7] and JLM[8]) were used to get the folded potential. Folding calculation **I** (FCI) used density dependent M3Y NN interaction and was described in detail by D.T. Khoa [9], while folding calculation **II** (FCII) with JLM effective interaction was described and discussed by F. Carstoiu *et al.* [10], L. Trache [11] and the references in these two papers. Two different density forms, Fermi distribution and Hartree Fork (HF) density [12], were used for target ground density during the folding procedures and are listed in Table I. The cluster-orbital shell-model approximation [13] form was used for  ${}^6\text{Li}$  ground density with FCI. FCI was carried out with code DFPD4 [14] and elastic scattering data were fitted with code ECIS[15]. The optical parameters obtained are listed in Table II. FCII and the elastic scattering fit were carried out with code OPTJLM1[16]. HF densities were used for both target and projectile. The optical parameters are listed in Table III. The angular distributions of the calculated cross-section are plotted along with data in Fig.1 for  ${}^{24}\text{Mg}$  and Fig.2 for  ${}^{28}\text{Si}$ . Both FCI and FCII give almost the same quality fits for each nucleus. The FCII fit has large oscillations at large angles than the FCI fit.

A scaling factor on radius of the real optical potential is necessary to fit the elastic scattering for both  ${}^{24}\text{Mg}$  and  ${}^{28}\text{Si}$  when FCI is used. Different densities choices (as shown in Table I) will slightly change the value of the scaling factor (as shown in Table II.), but it can not

eliminate the factor. Different types of density dependent M3Y interactions such as CDM3Y4, CDM3Y5, CDM3Y6 [17] give almost the same scaling factors for  $^{24}\text{Mg}$  elastic scattering. One possible reason for this factor could be the density used in the density dependent function. The density is defined as the sum of the densities of target and projectile, which may over-estimate the nuclear matter density at certain point.

DWBA calculations for  $^6\text{Li}$  inelastic scattering to the low-lying  $2^+$  state of  $^{24}\text{Mg}$  and to low-lying  $2^+$  and  $3^-$  states of  $^{28}\text{Si}$  were carried out with the optical parameter sets obtained by folding model I. CDM3Y5 density dependent NN interaction was used here and the Den1 form (as shown in Table I) was chosen as target density for both  $^{24}\text{Mg}$  and  $^{28}\text{Si}$ . The transition potentials were calculated with DFPD4 and the cross sections were calculated with ECIS. Deformation parameters for  $2^+$  and  $3^-$  states were obtained from electromagnetic B(EL) values by assuming the mass deformation length and coulomb deformation length are the same. The calculated angular distribution for the  $2^+$  state in  $^{24}\text{Mg}$  is plotted in Figure 3 along with the data. The calculated angular distributions for  $2^+$  and  $3^-$  states of  $^{28}\text{Si}$  are plotted in Figure 4 and Figure 5 along with data. All the calculations of  $2^+$  states agree well with the data. However, the DWBA calculation for the  $3^-$  state of  $^{28}\text{Si}$  does not agree well with the data as the calculated cross sections are slightly higher than the data.

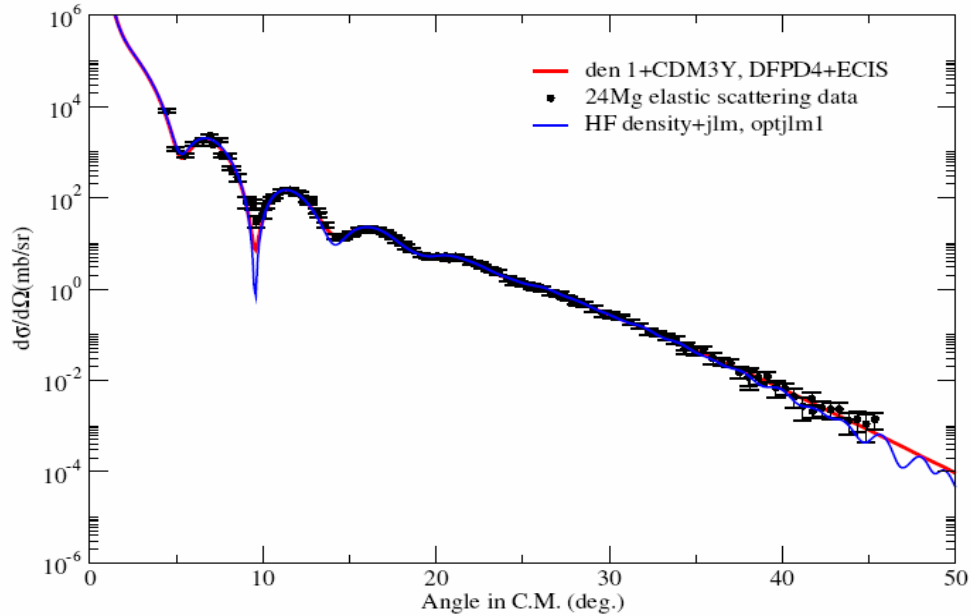


**Figure 1.** Angular distribution for  $^6\text{Li}+^{24}\text{Mg}$  elastic scattering cross section. The red line shows the calculation using real folded potential with CDM3Y5 NN interaction and a W-S imaginary term. The blue line shows the calculation using both real and imaginary potential folded with JLM interaction.

**Table I.** Density parameters for different density choices. Den1 and Den2 are Fermi distributions.  $R_p$ ,  $R_n$ ,  $R_m$ ,  $R_{ch}$  means the root mean square radii of the calculated proton, neutron, mass and charge distributions respectively.

target	Density choice	$\rho_0$	c	a	$R_p$	$R_n$	$R_m$	$R_{ch}$
$^{24}\text{Mg}$	Den1 <sup>[18]</sup>	0.17	2.995	0.478	2.922	2.922	2.922	3.040
	Den2 <sup>[19]</sup>	0.166	2.979	0.523	3.017	3.017	3.017	3.040
	HF	-----	-----	-----	2.928	2.906	2.917	3.000
$^{28}\text{Si}$	Den1 <sup>[18]</sup>	0.175	3.15	0.475	3.010	3.010	3.010	3.875
	Den2 <sup>[19]</sup>	0.167	3.155	0.523	3.123	3.123	3.123	3.154
	HF	-----	-----	-----	3.059	3.031	3.045	3.132

**Table II.** Optical model parameters obtained from fits of elastic scatterings with folding calculation I.  $N_r$  is renormalization factor for real potential.  $S_r$  is scaling factor for real potential radius.  $W, r_{i0}, a_i$  are W-S parameters for imaginary potentials.  $J_v$  and  $J_w$  are the volume integral per nucleon pair for real and imaginary potentials respectively.  $\sigma_r$  is total reaction cross section.

Target	N-N int	Target density	$N_r$	$S_r$	W	$r_{i0}$	$a_i$	$J_v$	$J_w$	$\sigma_r$	$\chi^2$
$^{24}\text{Mg}$	CDM3Y6	Den1	0.824	1.062	58.7	0.731	1.204	242	154	1799	1.038
	CDM3Y5	Den1	0.823	1.062	58.67	0.731	1.204	242	154	1799	1.039
	CDM3Y4	Den1	0.822	1.062	58.73	0.7311	1.204	242	154	1799	1.039
	CDM3Y5	HF	0.766	1.055	59.14	0.728	1.208	240	155	1803	1.042
	CDM3Y5	Den2	0.846	1.079	57.92	0.737	1.198	242	154	1793	1.032
$^{28}\text{Si}$	CDM3Y5	Den1	0.887	1.0624	41.33	0.9049	1.048	256	136	1757	1.461
	CDM3Y5	Den2	0.924	1.083	41.38	0.9049	1.046	258	136	1755	1.439
	CDM3Y5	HF	0.933	1.059	41.85	0.9011	1.051	257	137	1761	1.485

**Table III.** Optical potential parameters obtained from the fit of elastic scatterings with folding calculation II.  $N_r$  and  $N_w$  are the normalization factor for real and imaginary potential respectively.  $t_r$  and  $t_w$  are range parameters for real and imaginary potential respectively.

Target	N-N int.	target density	$N_r$	$t_r$	$N_w$	$t_w$	$J_v$	$J_w$	$\sigma_r$	$\chi^2$
$^{24}\text{Mg}$	JLM	HF	0.519	0.9559	0.862	2.586	237	144	1803	1.6
$^{28}\text{Si}$	JLM	HF	0.546	0.9165	0.825	2.4275	248	137	1734	1.94

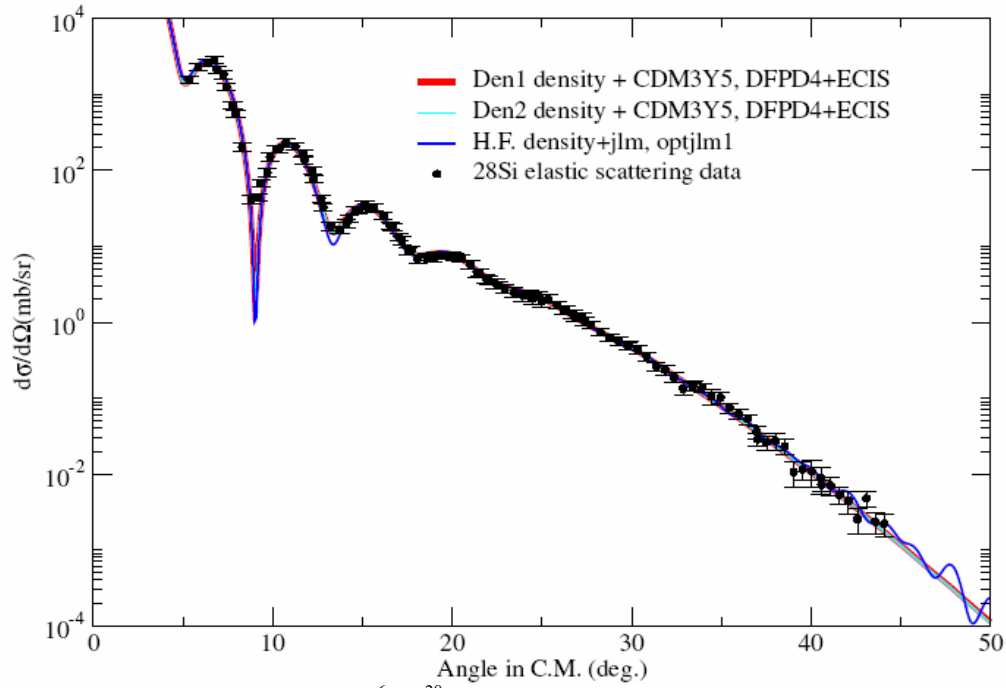


**Figure 2.** Angular distribution for  ${}^6\text{Li}+{}^{28}\text{Si}$  elastic scattering cross section. Both red and cyan lines show the calculation using real folded potential with CDM3Y5 N-N interaction and a W-S imaginary term. Den1 density is used for red line and Den2 density is used for cyan line. The blue line shows the calculation using both real and imaginary potential folded with JLM interaction.

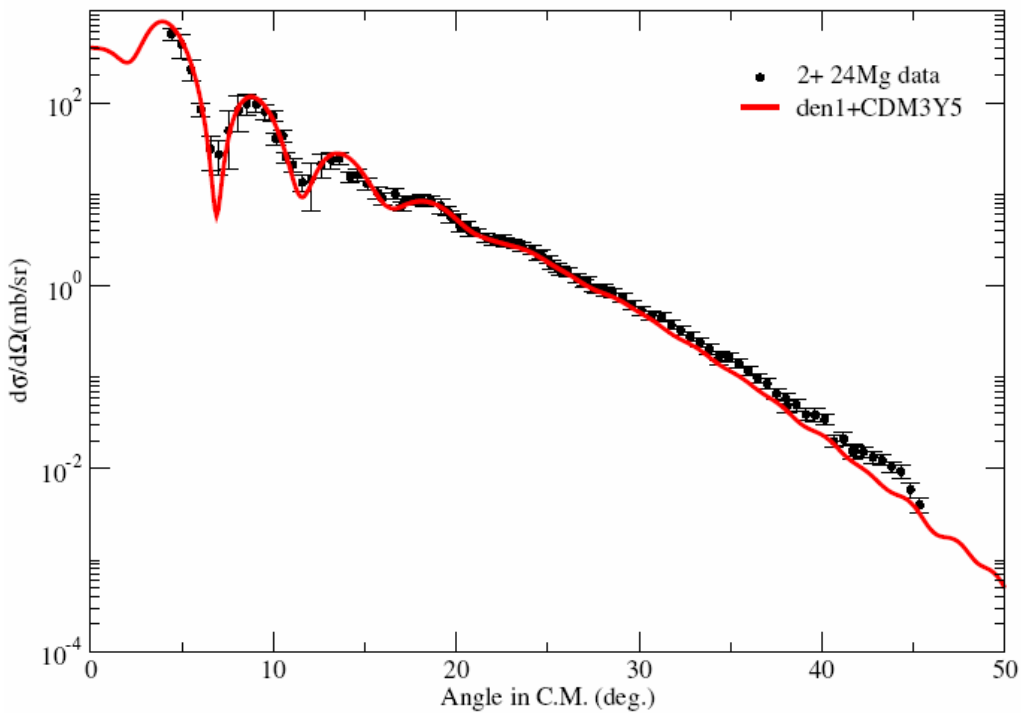


**Figure 3.** The line shows the calculated differential cross section using CDM3Y5 NN interaction for inelastic scattering to the 1.369MeV  $2^+$  state in  ${}^{24}\text{Mg}$  plotted versus average center-of-mass angle along

with the data points. The electromagnetic  $B(E2)$  value [20] was used and the corresponding deformation length  $\delta=1.978\text{fm}$ .

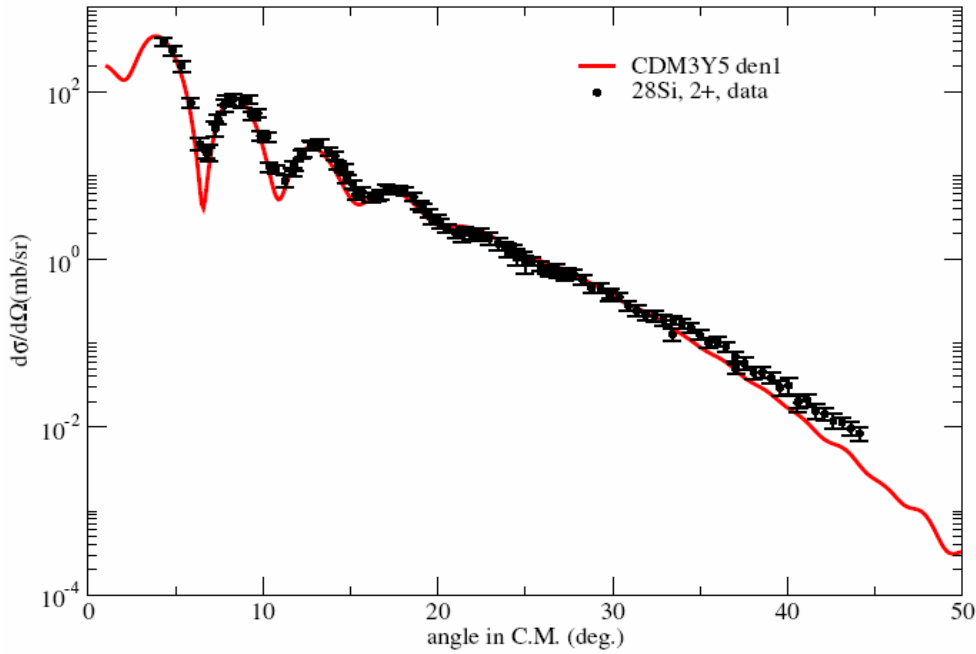


**Figure 4.** The line shows the calculated differential cross section using CDM3Y5 NN interaction for inelastic scattering to the  $1.779\text{MeV } 2^+$  state in  $^{28}\text{Si}$  plotted versus average center-of-mass angle along with the data points. The electromagnetic  $B(E2)$  value [20] was used here and the corresponding deformation length  $\delta=1.426\text{fm}$ .

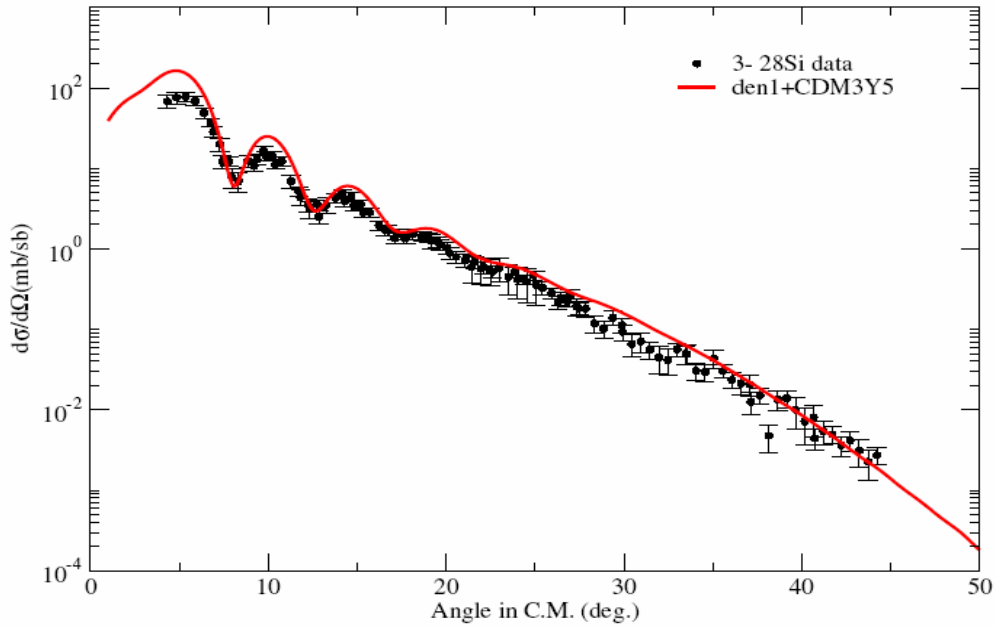


**Figure 5.** The line shows the calculated differential cross section using CDM3Y5 NN interaction for inelastic scattering to the  $6.879\text{MeV } 3^-$  state in  $^{28}\text{Si}$  plotted versus average center-of-mass angle along with the data points. The electromagnetic  $B(E3)$  value [21] was used here and the corresponding deformation length  $\delta=1.336\text{fm}$ .

We thank Dr. Livius Trache and Dr. Florin Carstoiu for their help in JLM folding calculation. We thank Dr. D.T.Khoa and Mr. Hoang Sy Than for their help and offer of the computer codes to do the CDM3Yn folding calculation and cross-section calculation.

- [1] G. R. Satchler and W. G. Love, *Phys. Rep.* **55**, 183(1979).
- [2] Y. Sakuragi, *Phys. Rev. C* **35** 2161 (1987); Y. Sakuragi, M. Yahiro, M. Kmimura, *Prog. Theor. Phys. Suppl.* **89** (1986) 136; Y. Sakuragi, M. I. Hirabayashi, M. Kamimura, *Prog. Theor. Phys.* **98** 521(1997).
- [3] R.M. DeVries, *et al.*, *Phys. Rev. Lett.* **39** 450 (1977).
- [4] M. El-Azab Farid, M.A. Hassanain, *Nucl. Phys.* **A678**, 39 (2000).
- [5] D. H. Youngblood, Y. -W.Lui, H. L. Clark, P. Oliver, and G. Simler, *Nucl. Instrum. Methods Phys. Res.* **A361**, 539 (1995).
- [6] H. L. Clark, Y. -W.Lui, and D. H. Youngblood, *Nucl. Phys.* **A589**, 416 (1995).
- [7] G. Bertsch, J. Borysowicz, H. McManus and W. G. Love, *Nucl. Phys.* **A284**, 399 (1977).
- [8] J. P. Jeukenne, A. Lejeune, and C. Mahaux, *Phys. Rev. C* **16**, 80(1977).
- [9] Dao T. Khoa and G. R. Satchler, *Nucl. Phys.* **A668**, 3 (2000).
- [10] F. Carstoiu, L. Trache, R. E. Tribble and C. A. Gagliardi, *Phys. Rev. C* **70**, 054610 (2004).
- [11] L. Trache, *et al.*, *Phys. Rev. C* **61**, 024612 (2000).
- [12] M. Beiner and R. J. Lombard, *Ann. Phys.* **86**, 262 (1974); F. Carstoiu and R. J. Lombard, *ibid.* **217**, 279 (1992).
- [13] A. Korshenninnikov, *et al.*, *Nucl. Phys.* **A617**, 45 (1997).
- [14] D.T. Khoa, unpublished.
- [15] Jacques Raynal, *Computing as a Language of Physics*, ICTP International Seminar Course, Trieste, Italy, Aug. 2-10, 1971 (IAEA,1972), p281; M.A. Melkanoff, T. Sawada and J. Raynal, *Methods in Computational Physics.6: Nuclear Physics* (Academy Press, New York, 1966) p1.
- [16] F. Carstoiu, unpublished.
- [17] D. T. Khoa, G. R. Satchler and W. von Oertzen, *Phys. Rev. C* **56**,954 (1997).
- [18] M. Pignanelli *et al.*, *Phys. Rev. C* **33** 40(1986).
- [19] G. Fricke *et al.*, *Atomic Data and Nuclear Data Tables* **60**, 177 (1995).
- [20] S. RAMAN, C. W. NESTOR, JR., and P. TIKKANEN, *At. Data Nucl. Data Tables* **78**, 1 (2001).
- [21] T. KIBEDI and R. H. SPEAR, *At. Data Nucl. Data Tables* **80**, 35 (2002).

## Study of the $^{12}\text{N}(p,\gamma)^{13}\text{O}$ reaction from a ( $^{12}\text{N},^{13}\text{O}$ ) proton transfer reaction

A. Banu, T. Al.-Abdullah, V. Burjan,<sup>1</sup> F. Carstoiu,<sup>2</sup> C. Fu, C. A. Gagliardi, M. McCleskey,  
G. Tabacaru, L. Trache, R. E. Tribble, and Y. Zhai

<sup>1</sup>*Institute of Nuclear Physics, Czech Academy of Sciences, Prague, Czech Republic*

<sup>2</sup>*IFIN-HH, Bucharest, Romania*

The reaction rate for the radiative proton capture on the drip line nucleus  $^{12}\text{N}$  is studied at the Cyclotron Institute using an indirect method. The reaction is important in the hot pp chain nuclear burning in H-rich massive objects [1]. In 1986, Fuller *et al.* [2] addressed the classic problem of supermassive star evolution — *given that a nonrotating supermassive star has formed and contracted to its instability point, does the rapid nuclear burning in the subsequent collapse generate enough thermal energy to stabilize the collapse and trigger an explosion?*

They found that Population III stars with  $M > 5 \times 10^5$  solar masses and  $Z \ll 0.005$  will collapse to black holes, while stars of higher metallicity will explode. For those failing to explode, it is reasoned that in the short time before the collapse insufficient amounts of  $^{12}\text{C}$  and other heavier nuclei are produced by the  $3\alpha$ -process. However, alternative paths to the slow  $3\alpha$ -process to produce CNO seed nuclei could change their fate. In 1989, M. Wiescher *et al.* [1] reinvestigated the reaction rates for nuclei up to oxygen and suggested several reaction sequences (hot pp chains) that would permit very massive stars with low metallicity to bypass the  $3\alpha$ -process.  $^{12}\text{N}(p,\gamma)^{13}\text{O}$  is an important branching point in such alternative paths.

The reaction is studied here by an indirect method using the peripheral proton-transfer reaction  $^{14}\text{N}(^{12}\text{N},^{13}\text{O})^{13}\text{C}$ . The radioactive beam  $^{12}\text{N}$  was produced and separated in MARS from a primary beam of  $^{12}\text{C}$  at 23 AMeV with an intensity of 150 pA impinging on a LN<sub>2</sub> cooled H<sub>2</sub> gas cell. The gas cell was operated at a pressure of 2.2 atm and its entrance and exit windows were made of havar foils 13  $\mu\text{m}$  and 4  $\mu\text{m}$  thick, respectively. Due to the large negative Q-value of the reaction used to produce the  $^{12}\text{N}$  secondary beam (-18.12 MeV), the energy of the primary beam had to be large, resulting in an energy of the recoiling  $^{12}\text{N}$  products larger than the typical energy regime of our secondary proton transfer reactions (10-12 AMeV). To bring it down to 12 AMeV where the reaction is peripheral and where we have a proven recipe for the optical potentials needed for the DWBA analysis, the energy of the beam was degraded by a 250- $\mu\text{m}$ -thick Al foil right behind the gas cell.

The resulting secondary beam at a rate of  $\sim 2 \times 10^5$  pps, and a purity of  $\sim 99.8\%$  [3] impinged on a 1.6 mg/cm<sup>2</sup>-thick composite melamine target (C<sub>3</sub>H<sub>6</sub>N<sub>6</sub>) at the focal plane on MARS. MARS was operated with D3 at an inclination angle of 5°. The experimental setup used is shown in Figure 1. It was also used before to study the  $^{14}\text{N}(^7\text{Be},^8\text{B})^{13}\text{C}$  reaction [4].

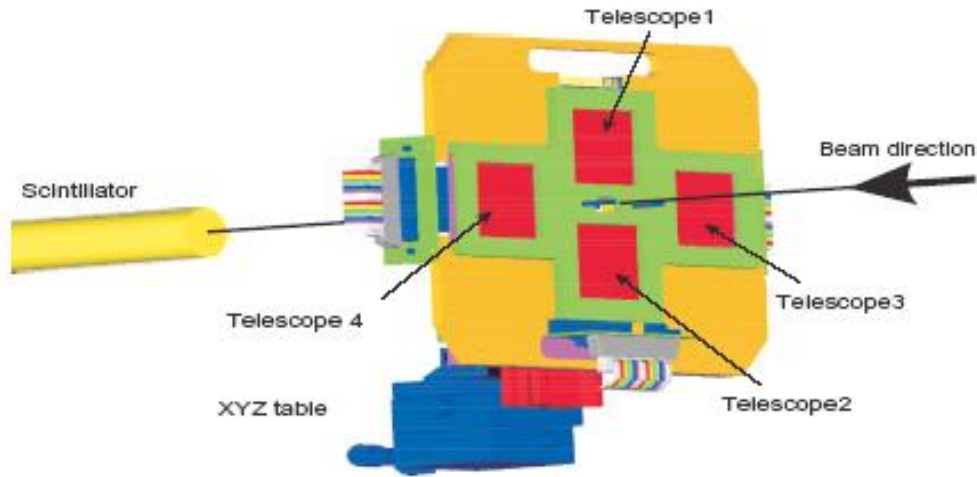


**Figure 1.** A 3D-view of the detector assembly. Four  $5 \times 5 \text{ cm}^2$  Si  $\Delta E$ -E telescopes are used for particle identification and for angular distribution measurement. The 16 strip  $\Delta E$ -detectors are position sensitive (PSD). A plastic scintillator positioned at  $0^\circ$  behind the target is employed for beam counting.

The identification of the reaction channels is shown in Figure 2 along with the elastic scattering position distributions in the four  $\Delta E$ -E telescopes employed as detection system. The identification of the reaction products is marked on left side panel, including the  $^{13}\text{O}$  well separated spots identifying the transfer on the  $^{12}\text{C}$  and  $^{14}\text{N}$  components in the target. Another observation worth noticing is the presence of a proton breakup channel of the  $^{12}\text{N}$  projectile leading to a large production of  $^{11}\text{C}$ . This is due to the small binding energy of the last proton in  $^{12}\text{N}$   $S_p=601 \text{ keV}$ .

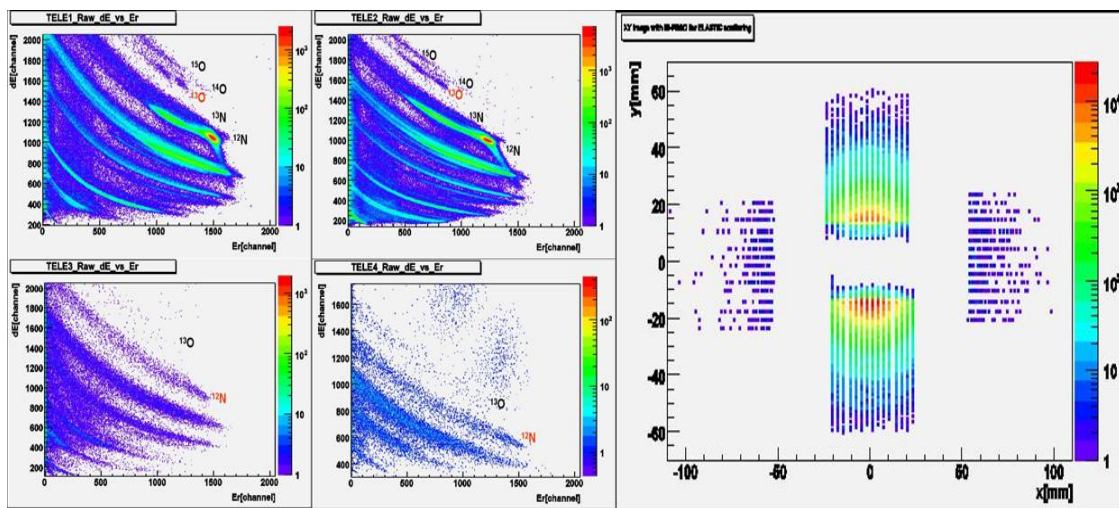


**Figure 2.**  $\Delta E$ -E reaction channel identification (right) and the elastic scattering position distributions (left).

The data analysis procedure starts with the analysis of the elastic channel —  $^{12}\text{N}(^{14}\text{N}, ^{12}\text{N})^{14}\text{N}$  — in order to determine the optical-model potential (OPM) needed for DWBA calculations performed in the transfer channel —  $^{12}\text{N}(^{14}\text{N}, ^{13}\text{O})^{13}\text{C}$  — to determine the ANC (asymptotic normalization coefficient). During most of the experiment, which lasted two weeks in May 2006, in order to have good statistics for the transfer reaction, we worked at MARS settings that allowed maximum intensity of the secondary  $^{12}\text{N}$  beam, but degraded some of its angular resolution. In the last three days of the run we closed the slits situated behind the last pair of dipoles of MARS in order to improve the angular definition of the secondary beam on target. This reduced the intensity, but allowed us to get much better elastic scattering angular distributions, with clearly visible Fraunhofer oscillations, even for such a composite target like melamine. These data allow a more confident extraction of the optical potentials to be used in the DWBA analysis. Following we report preliminary results (shown in Figure 3) for the ANC of the system  $^{13}\text{O} \rightarrow ^{12}\text{N} + \text{p}$ . In order to disentangle the elastic scattering on  $^{14}\text{N}$  only, in March 2007 we carried out an elastic scattering measurement on a pure C-target [6]. Data analysis of this experiment is still in progress, but once completed it will enable us to extract from data a less uncertain ANC value, from which the rate of the  $^{12}\text{N}(p, \gamma)^{13}\text{O}$  reaction will be evaluated.

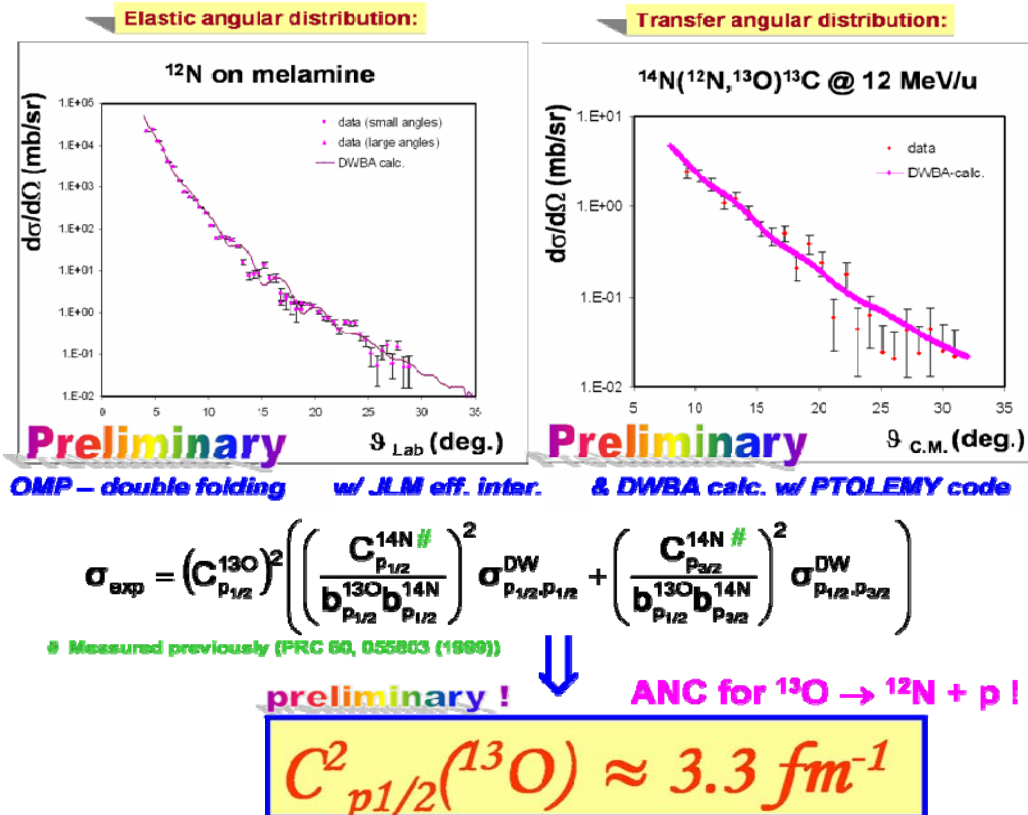


**Figure 3.** The angular distribution for elastic scattering on melamine (data points, left) compared with the prediction (curve) using the double folding potential procedure of Ref. [5], no parameters fitted. DWBA calculations are fitted to data to extract the ANC (right).

- [1] M. Wiescher *et al.*, *Astrophys. J.* **343**, 352 (1989).
- [2] G. M. Fuller *et al.*, *Astrophys. J.* **307**, 675 (1986).
- [3] A. Banu *et al.*, *Progress in Research*, Cyclotron Institute, Texas A&M University (2005 – 2006), p. I-15
- [4] G. Tabacaru *et al.*, *Phys. Rev. C* **73**, 025808 (2006).
- [5] L. Trache *et al.*, *Phys. Rev. C* **61**, 024612 (2000).
- [6] A. Banu *et al.*, *Progress in Research*, Cyclotron Institute, Texas A&M University (2006 – 2007), p. I-24.

## Single and double proton emission from the $^{14}\text{O} + ^4\text{He}$ interaction

Changbo Fu, V. Z. Goldberg, A. M. Mukhamedzhanov, G. G. Chubarian,  
G. V. Rogachev,<sup>1</sup> B. Skorodumov,<sup>2</sup> M. McCleskey, Y. Zhai,  
T. Al-Abdullah, G. Tabacaru, A. Banu, L. Trache, and R. E. Tribble

<sup>1</sup>*Department of Physics, Florida State University, Tallahassee, Florida 32306*

<sup>2</sup>*Department of Physics, University of Notre Dame, South Bend, Indiana 46556*

Reactions between unstable nuclei and helium influence a variety of astrophysical processes [1]. The present measurements were made with the aim to understand the origin of the protons emerging in interactions of  $^{14}\text{O}$  with helium.

By using a 32.7 MeV  $^{14}\text{O}$  beam provided by the MARS at TAMU [2] and a modified Thick Target Inverse Kinematics (TTIK) technique, we have measured the excitation function for  $(\alpha, 2p)$  reaction. The conditions of the experiment were tuned to obtain a unique kinematics interpretation of the double proton events for the broad excitation energy region of the TTIK technique. The measured excitation function is shown in Fig.1. It clearly shows that the process is dominated by resonances in  $^{18}\text{Ne}$  in the region between 7.5–12.0 MeV, which should be very unusual for the  $(\alpha, 2p)$  reactions on stable nuclei. The large, resonance yield of protons, mainly from the successive decays, makes suspicious former astrophysically important interpretations of the proton spectra from the  $^{14}\text{O}(\alpha, p)$  reaction [3]. We showed how the single proton measurements can be improved by using a time-of-flight method.

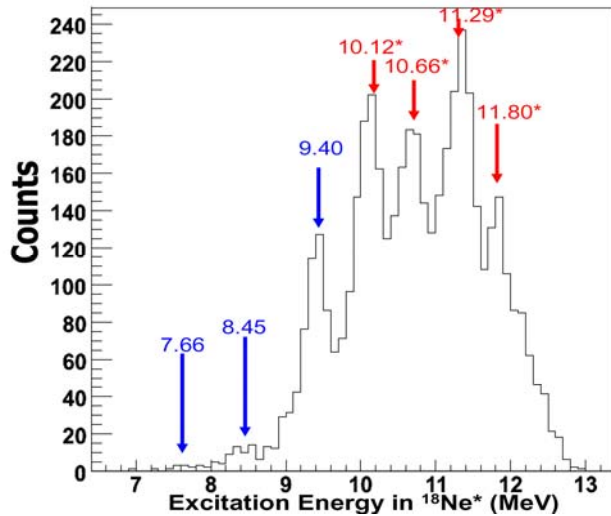


**Figure 1.** The excitation function for the  $^{14}\text{O}(\alpha, 2p)$  reaction.

Most of the resonances (levels in  $^{18}\text{Ne}$ ) were not observed before, and spin assignments of these levels are not known. The proton decay of the  $^{18}\text{Ne}$  level at 8.45 MeV differs from the clearly sequential decay of other  $^{18}\text{Ne}$  states. To describe it, we calculated the two proton relative energy distributions for this decay using the Faddeev approach. Fig. 2 shows these energy distributions for different angular orbital moment for the decay of  $^{18}\text{Ne}$  and with/without the virtual level in the  $pp$  interaction. The shape and the probability of the decay in question could be considered as an evidence for the decay by the correlated proton pair.

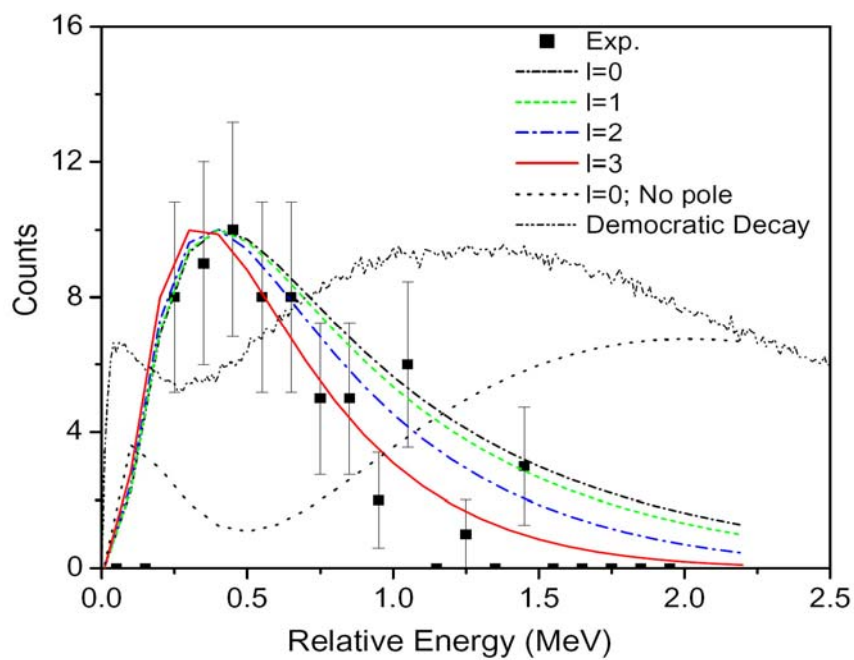


**Figure 2.** The relative energy between two protons emitted from the 8.45 MeV level in  $^{18}\text{Ne}$ .

- [1] A. E. Champagne and M. Wiescher, *Ann. Rev. Nucl. Part. Sci.* **42**, 39 (1992).  
 [2] R. E. Tribble *et al.*, *Nucl. Instrum. Methods Phys. Res.* . **A285**, 441 (1989).  
 [3] M. Notani *et al.*, *Nucl. Phys.* **A746**, 113c (2004); *Eur. Phys. J.* **A27**, Supplement 1, 327(2006).

## Decay of $^{10}\text{C}$ excited states above the $2p+2\alpha$ threshold

R. J. Charity,<sup>1</sup> K. Mercurio,<sup>1</sup> L. G. Sobotka,<sup>1</sup> J. M. Elson,<sup>1</sup> M. Famiano,<sup>1</sup>

A. Banu, C. Fu, L. Trache, and R. E. Tribble

<sup>1</sup>Washington University, St. Louis, Missouri 63130

The level structure of  $^{10}\text{C}$  is not well known. Only the first excited state, which gamma decays, is fully characterized. All other excited states are particle unstable and above the threshold for decay into the  $2p+2\alpha$  channel. There are a variety of ways one can envision creating this decay channel, either through three sequential binary-decay steps or through a direct three or four-body breakup. In order to investigate these possible decay modes, an experimental study of the correlations between the 4 decay products was initiated.

Using a  $^{10}\text{B}$  beam,  $^{10}\text{C}$  fragments were created using the  $^{10}\text{B}(p,n)^{10}\text{C}$  reaction. The fragments at  $E/A = 10.7$  MeV were selected with MARS and were impinged on a  $^9\text{Be}$  target. Following inelastic excitations, the decay products were detected and identified in four position-sensitive  $E-\Delta E$  telescopes. The telescopes, part of the HiRA array, each consist of a  $65\ \mu\text{m}$  single-sided Si strip detector followed by a 1.5 mm double-sided Si strip detector.

For each detected  $2p+2\alpha$  event, the  $^{10}\text{C}$  excitation energy was reconstructed from the summed kinetic energy of the detected fragments in their center-of-mass frame minus the breakup Q-value ( $-3.726$  MeV). The distribution of this reconstructed excitation energy, shown in Fig. 1a, contains two peaks at 5.2 and 6.5 MeV. Levels at these energies are known from a number of previous studies, but their decay modes were not determined.

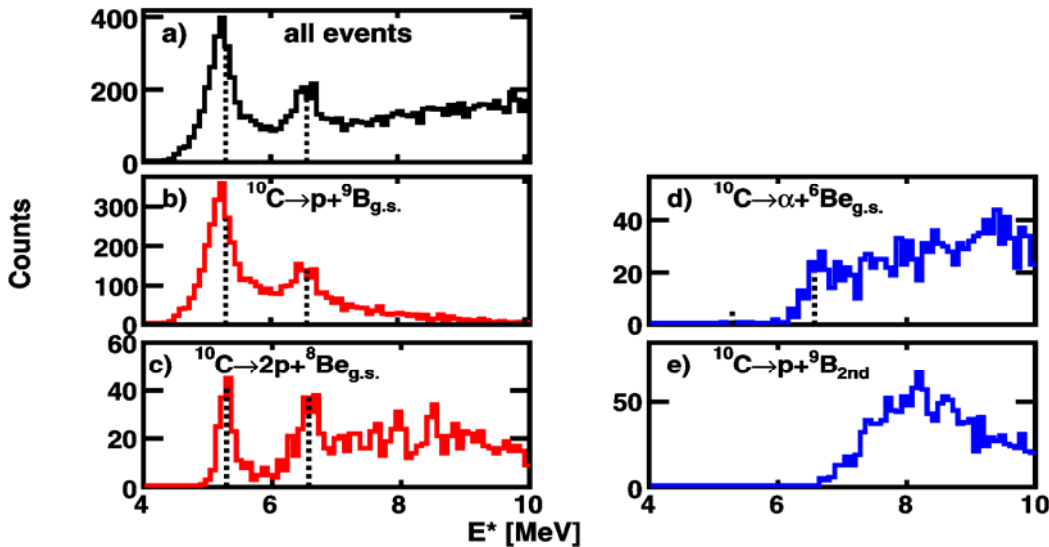


**Figure 1.** Distribution of reconstructed  $^{10}\text{C}$  excitation energy for a) all  $2p+2\alpha$  events and with a b)  $^9\text{B}_{\text{gs}}$ , d)  $^6\text{Be}_{\text{gs}}$ , and e)  $^9\text{B}(E^*=2.35\ \text{MeV})$  intermediate. c) events with a  $^8\text{Be}_{\text{gs}}$ , but no  $^9\text{B}_{\text{gs}}$  intermediate. To aid in comparing peak energies, the dash lines indicate the centroids of the peaks in c)

To search for the presence of long-lived intermediates associated with possible sequential decay processes, the correlations between the decay fragments were investigated. From the  ${}^8\text{Be}$  excitation energy reconstructed from all  $\alpha$ - $\alpha$  pairs, most of the events associated with the two peaks were found to involve  ${}^8\text{Be}$  ground-state fragment. From the excitation energy reconstructed from  $p$ - $\alpha$ - $\alpha$  triplets, the  ${}^9\text{B}$  ground-state intermediate was also identified. The  ${}^{10}\text{C}$  excitation-energy distribution for events with a  ${}^9\text{B}$  ground-state fragment is shown in Fig. 1b. The two peaks are still present and it is clear that these states have a proton decay branch that produces a  ${}^9\text{B}$  (ground state) fragment which sequentially proton decays to  ${}^8\text{Be}$  (ground state) and which further decays to two alpha particles.

Correlations between the fragments also indicate the presence of  ${}^6\text{Be}$  (ground state) and  ${}^9\text{B}$  ( $E^*=2.35$  MeV) intermediates. However, the  ${}^{10}\text{C}$  excitation-energy distributions, for events containing these fragments, Figs. 1d and 1e, do not show any statistically significant peaks. One further group of events was identified, those containing  ${}^8\text{Be}$  (ground state) intermediate, but not a  ${}^9\text{B}$  (ground state) fragment. For these events, the  ${}^{10}\text{C}$  excitation-energy distribution, shown in Fig. 1c, also contains two peaks. The lower-energy peak is shifted relative to the low-energy peak in Fig. 1b associated with sequential two-proton decay. Also the width is narrower suggesting that there are two levels in this region ( $E^*=5.18$  and  $5.3$  MeV) The higher-energy peaks in Figs. 1b and 1c have consistent centroids and thus these may represent two branches of a single level.

For the latter group of events, containing an  ${}^8\text{Be}$  (ground state) but no  ${}^9\text{B}$  (ground state) intermediate, we investigated the possibility of sequential proton decay through the wide first-excited state of  ${}^9\text{B}$  rather than the ground state. A Monte Carlo simulation indicated, that for the 6.5 MeV state, the two protons should have similar energies in  $2p+2\alpha$  center-of-mass frame. This was not observed experimentally and furthermore the relative emission angles of the two protons (again in the  $2p+2\alpha$  center-of-mass frame) shown in Fig. 2 is asymmetric about 90 degrees. This also is inconsistent with sequential emission of the two protons and thus implies the emissions of these protons are more direct and correlated, i.e., both protons are emitted from the same side of the  ${}^{10}\text{C}$  fragment.

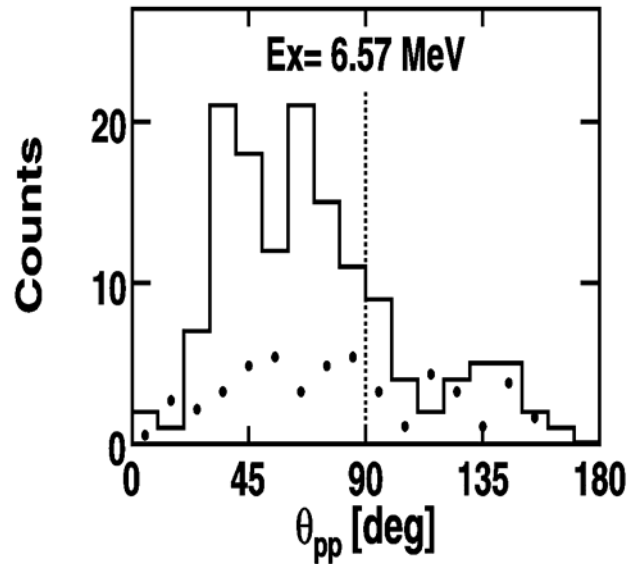


**Figure 2.** Distribution of relative angle between the two protons in the  $2p+2\alpha$  center-of-mass frame for events in the 6.57 MeV level which do not decay through the  ${}^9\text{B}$  ground state. The data points are an estimate of the background.

In summary, we have studied  $^{10}\text{C}$  levels at 5.18, 5.3, and 6.5 MeV which decay to the  $2p+2n$  exit channel. The 6.5 MeV level can decay by two branches. These include a sequential two-proton emission passing through the  $^9\text{B}$  (ground state) and then the  $^8\text{Be}$  (ground state) intermediates. In addition we identified a branch where the two protons are promptly emitted from the same side of the  $^{10}\text{C}$  fragment, leaving an  $^8\text{Be}$  (ground state) residue. The 5.18 MeV level also decays via sequential two-proton emission, while the decay of the 5.3 MeV state is still not clear.

## Characterization of novel square-bordered position-sensitive silicon detectors with a four-corner readout

A. Banu, Y. Li, M. McCleskey, M. Bullough,<sup>1</sup> S. Walsh,<sup>1</sup> C. A. Gagliardi,  
L. Trache, R. E. Tribble, and C. Wilburn<sup>1</sup>

<sup>1</sup>*Micron Semiconductor Ltd., 1 Royal Buildings, Marlborough Road, Lancing Business Park,  
Lancing, Sussex, BN15 8SJ, England*

We report here about systematic investigation studies performed on silicon position sensitive detectors recently developed in collaboration with Micron Semiconductor Ltd. [1]. The interest in the fabrication of the kind of detectors described in the following was initiated by Micron Semiconductor under contract with the Japan Aerospace Exploration Agency (JAXA) interested to invest in its ongoing GEOTAIL mission observing the magnetosphere of Earth [2]. Measurement of elemental and isotopic composition in the solar energetic particles (SEP) and galactic cosmic rays (GCR) provides important information for understanding the stellar nucleosynthesis, the chemical evolution of the galaxy and the history of the solar system material. In addition, it offers new possibilities for the study of particle acceleration and transport mechanism in the solar/stellar atmosphere and interplanetary/interstellar space. The High Energy Particle Experiment in the GEOTAIL satellite program was constructed to measure the composition of heavy ions in space. A particle telescope not only with a large geometric factor but also with a high mass resolution is required for an isotopic observation of elements from He up to the Fe group nuclei in SEP and GCR. The particle telescope aboard the satellite consists of a stack of Si detectors and uses the well-known  $\Delta E$ -E algorithm for mass identification. An increase of the geometric factor of the telescope is realized by the use of Si detectors with a large sensitive area combining position-sensitive detectors (PSDs) to the telescope for the determination of particle trajectories. The energy loss in a  $\Delta E$ -detector varies accordingly with the incident angle of a particle to the plane of the detector. To determine the mass of a particle with high resolution, information concerning the incident angle at which the particle passes through the  $\Delta E$ -detector is needed to minimize the uncertainty of the path length, hence good position resolutions for the PSDs are demanded.

Using <sup>241</sup>Am and <sup>228</sup>Th alpha sources as well as various possible beams like — <sup>63</sup>Cu<sup>21+</sup> at 40 AMeV, 30 AMeV, 15 AMeV, <sup>16</sup>O<sup>8+</sup> at 60 AMeV, 45 AMeV, 30 AMeV, 16 AMeV, 7 AMeV, and <sup>4</sup>He<sup>1+</sup> at 25 AMeV, 20 AMeV, 15 AMeV, 7 AMeV — delivered by the K500 cyclotron of Texas A&M University at the SEE LINE of the Radiation Effects Testing Facility, we have examined basic characteristics of the large position-sensitive detectors in terms of their most important operation parameters: position resolution along with position non-linearity determination (the strength of the so-called “pin-cushion” pattern), as well as energy resolution.

The detectors investigated, at least 27 in total, are continuous PSDs of four-corners type with an active area of 62 mm × 62 mm, and of three thicknesses namely 200 μm, 250 μm and 400 μm. The boron-implanted resistive layer on the n-type Si surface serves as the resistive anode for the charge division and forms the p-n junction. There is a phosphorus implantation for the n side. The front (position sensitive) electrode of the PSDs is a square-shaped resistive anode of surface resistance  $R_{\square}$ , bordered by additional

resistive strip lines with a low resistance per unit length,  $R_L$ . The width of the strip lines,  $w$ , is 0.5 mm. Four electrodes, one at each corner of the anode are formed from aluminum contacts. The four signals generated at these contacts are used to determine the position of the incident ion. A fifth signal is taken from the rear face of the detector via an aluminum-evaporated contact (the ohmic contact). This signal provides an independent energy measurement. A collimation plate with a  $11 \times 11$  matrix of pinholes with diameter of 1 mm and spacing of the pinholes of 5 mm (from center to center) was placed in front of the detectors for non-linearity and position/energy resolution determination.

Exactly 20 years ago, T. Doke *et al.* [3] developed a type of position sensitive silicon detector (PSSD) which provided an excellent two-dimensional position linearity using resistive charge division. They found that, if  $R_{\square}$  is larger than  $R_L \times L$  (where  $L$  is the length of the squared-shaped anode) by a factor of 10 to 15, the resultant deformation of the position pattern was greatly reduced and the non-linearity was found to be less than 2%. Since then, this kind of design rule was used as a standard in large area continuous PSDs fabrication technology.

In our work, we have found a new design rule: with a factor of 2 between the sheet surface resistance and the low resistance strip, we could obtain non-linearity in the position deformation pattern less than 1%. The results of our work are discussed at length in a forthcoming NIM publication [4]. Here we just summarize them in an illustrative manner as per following figures.

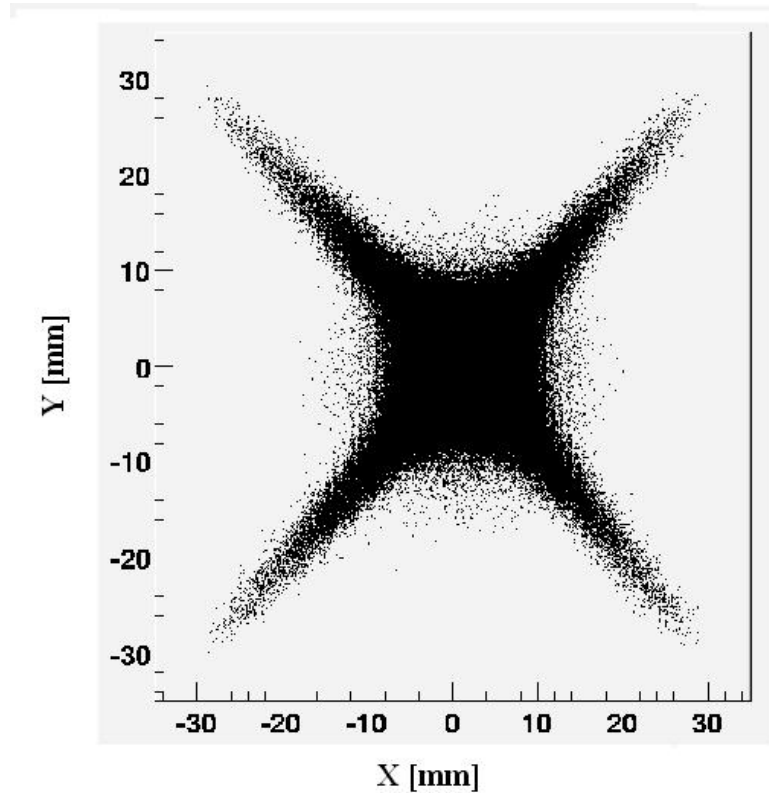


**Figure 1.** Two-dimensional pattern for PSD without a resistive strip connecting two adjacent corners of the resistive squared-shaped anode: the design rule we started with.

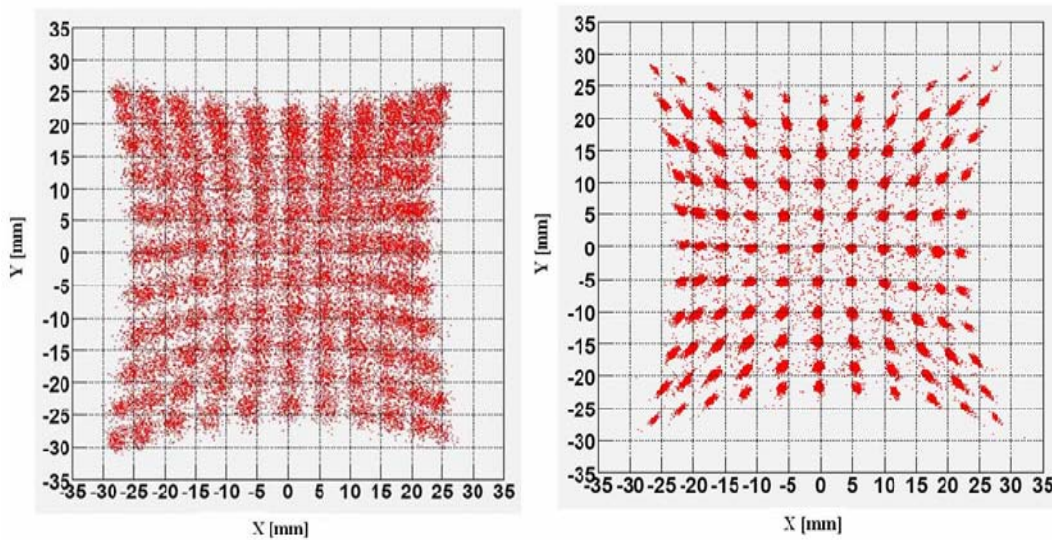


**Figure 2.** Two-dimensional patterns for PSD with resistive strip connecting two adjacent corners, tested with alpha source (left) and tested with beam (right). In-beam data shows better position resolution due to larger energy loss deposited in the detector.

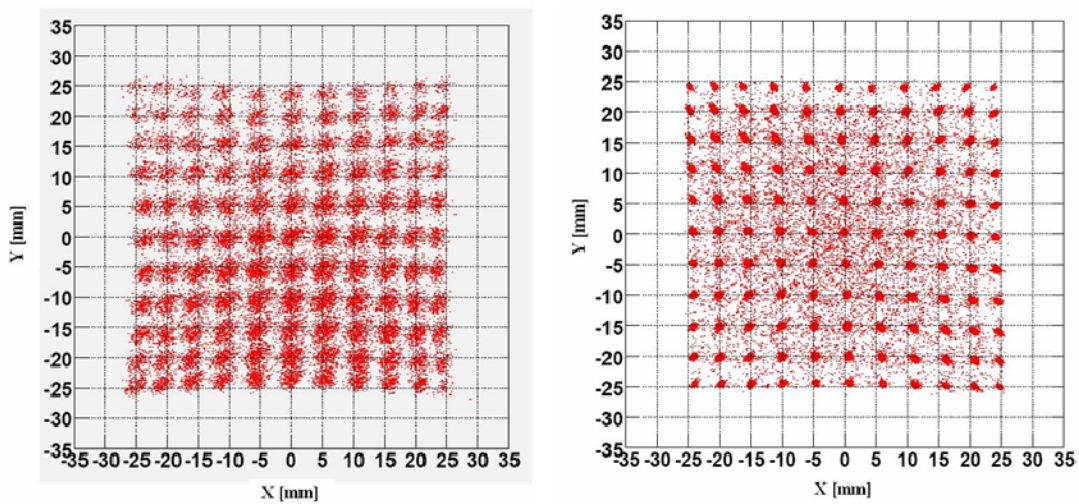


**Figure 3.** Two-dimensional patterns for PSD with resistive strip connecting adjacent corners, tested with alpha source (left) and tested with beam (right). Here we applied the design rule with a ratio of 2 between anode sheet resistance and the resistance of the resistive strip, unlike Figure 2 for which a ratio of 0.23 was used in the design.

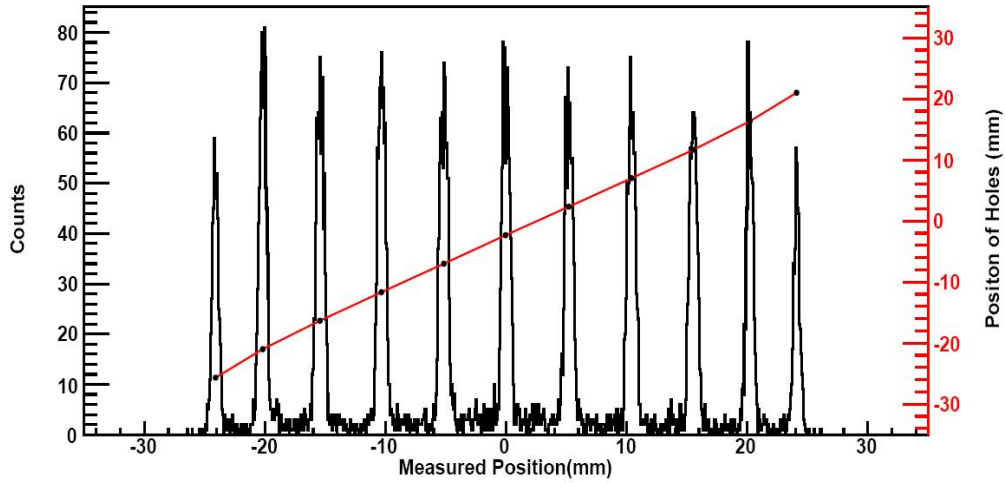


**Figure 5.** Non-linearity of less than 1% determined along the X position of PSD manufactured with the new design rule and tested with beam using the collimating plate with a matrix of  $11 \times 11$  pinholes. The red line is to guide the eyes with respect to variation of the non-linearity along the central row on the collimating plate on the detector X position. In this case a position resolution of 0.69 (7) mm (FWHM) was measured.

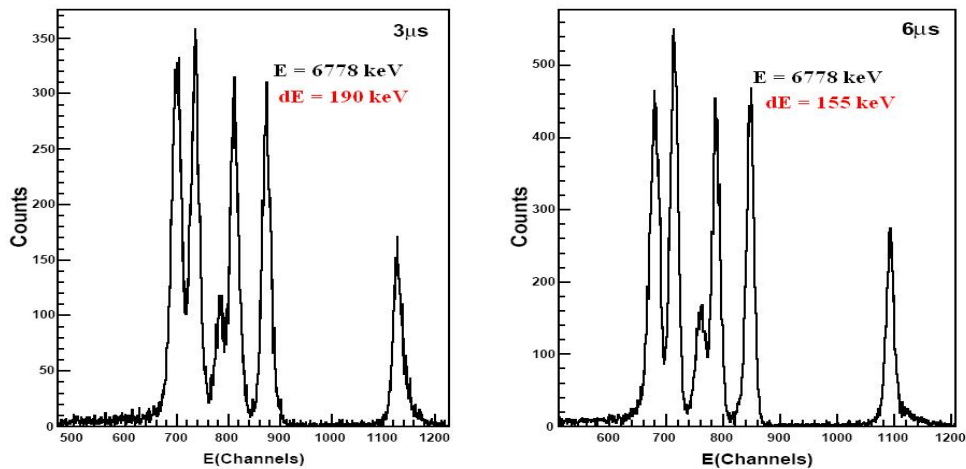


**Figure 4.** Energy resolution ( $dE/E$ ) measured with  $^{228}\text{Th}$  source measured for 3  $\mu\text{s}$  (left) shaping time as being of 3% (FWHM) and for 6  $\mu\text{s}$  (right) shaping time as being of 2% (FWHM).

- [1] [www.micronsemiconductor.co.uk](http://www.micronsemiconductor.co.uk)
- [2] H. Matsumoto *et al.*, Jpn. J. App. Phys. **44**, 6870 (2005).
- [3] T. Doke *et al.*, Nucl. Instrum. Methods Phys. Res. **A261**, 605 (1987).
- [4] A. Banu *et al.* (to be published).

## Elastic scattering of $^{12}\text{N}$ at 12 AMeV on $^{12}\text{C}$

A. Banu, T. Al-Abdullah, C. Fu, C. A. Gagliardi, Y. Li, M. McCleskey, L. Trache,  
R. E. Tribble, and Y. Zhai

An elastic scattering measurement of 12 AMeV  $^{12}\text{N}$  beam off a  $^{12}\text{C}$  target was carried out in March this year at MARS. The experiment is directly related to the peripheral proton-transfer measurement performed last year on a composite melamine target ( $\text{C}_3\text{H}_6\text{N}_6$ ) employing the reaction ( $^{12}\text{N},^{13}\text{O}$ ) at 12 AMeV [1]. The aim of that experiment was to use an indirect method to determine the ANC for the system  $^{13}\text{O} \rightarrow ^{12}\text{N} + \text{p}$ . The ANC is extracted from the DWBA analysis of measured angular distributions. For that we need to know the optical potential for both entrance/exit channels of the transfer reaction. When possible, this kind of information can be obtained from elastic scattering measurements. In the case of the ( $^{12}\text{N},^{13}\text{O}$ ) experiment using the melamine target, the elastic channel of interest  $^{12}\text{N}+^{14}\text{N}$  needs to be disentangled against the  $^{12}\text{N}+^{12}\text{C}$  and  $^{12}\text{N}+\text{H}$  elastic channels, due to the presence of C and H atoms in the melamine target. This is important in order to extract from the data a more certain value for the ANC.

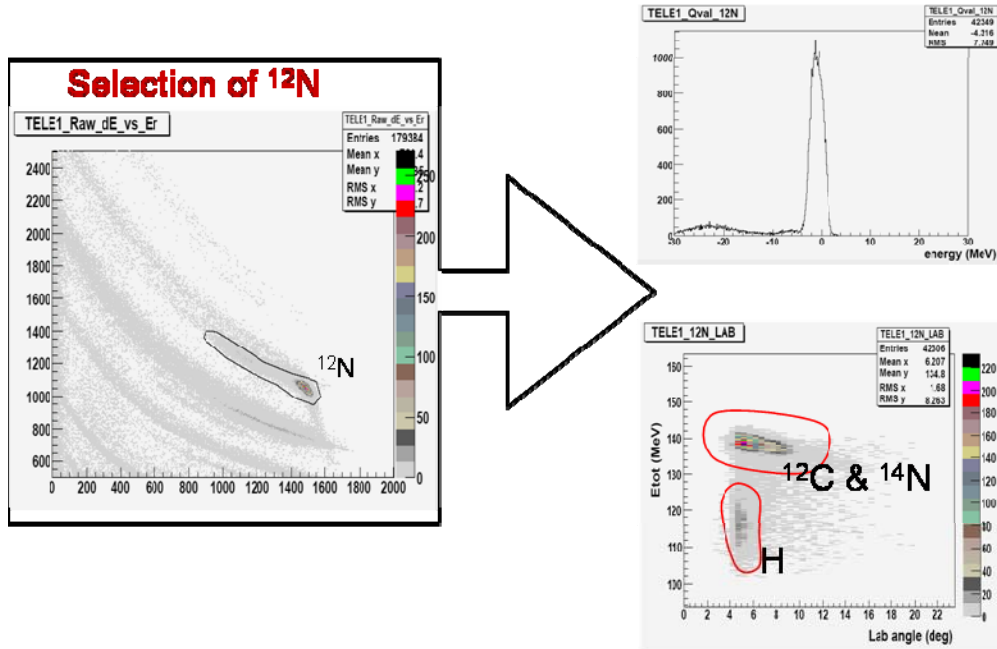


**Figure 1.** Data analysis of  $^{12}\text{N}$  elastic scattering off the melamine target.  $\Delta E$ -E selection of  $^{12}\text{N}$  reaction channels (left). Elastic channel selection by the Q-value = 0 condition (right, top). The three elastic channels separated by their individual kinematics in the E vs. lab angle matrix (right, bottom).

If the elastic scattering of  $^{12}\text{N}$  off H in the melamine target can be eliminated by applying proper kinematics cuts in the data analysis, this is not possible for the  $^{12}\text{N}$  elastic scattering off  $^{12}\text{C}$  nuclei, which can not be separated from the  $^{12}\text{N}+^{14}\text{N}$  elastic channel, as clearly illustrated in Figure 1.

Calculations for the angular distributions of the elastic channels  $^{12}\text{N}+^{12}\text{C}$  and  $^{12}\text{N}+^{14}\text{N}$ , were done with double folded potentials using JLM interaction with the procedure and the average parameters of Refs. [2, 3]:  $N_v=0.37$ ,  $N_w=1.0$ ,  $t_v=1.20$  fm,  $t_w=1.75$  fm. They are shown in Figure 2, after being transformed to the laboratory system. From them one can understand to which extent it is important to disentangle the two contributions for a more accurate optical model determination.

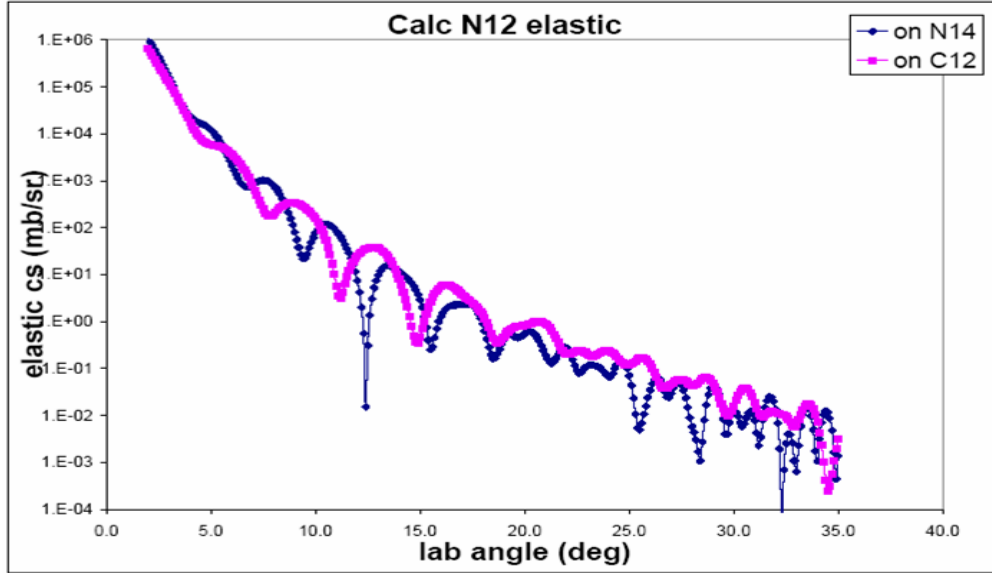


**Figure 2.** Calculated angular cross section distributions for the two elastic scattering channels  $^{12}\text{N}$  off  $^{12}\text{C}$  (magenta) and  $^{12}\text{N}$  off  $^{14}\text{N}$  (dark blue).

Because at the end we are interested in subtracting the differential cross section of  $^{12}\text{N}+^{12}\text{C}$  elastic data from the melamine elastic data, the measurement of  $^{12}\text{N}$  elastic scattering off  $^{12}\text{C}$  target had to be performed under similar conditions. Hence, a  $^{12}\text{C}$  primary beam at 23 AMeV impinging on a  $\text{LN}_2$ -cooled  $\text{H}_2$  gas cell was used to produce the radioactive  $^{12}\text{N}$  beam. This time the gas cell havar entrance/exit windows were both made with a thickness of  $13\ \mu\text{m}$ .

Therefore, the gas cell was operated at a pressure of  $\sim 1.6$  atm and the secondary beam was degraded by the same  $250\text{-}\mu\text{m}$ -thick Al foil positioned behind the gas cell. The reaction  $^{12}\text{C}$ -target employed had a thickness of  $2\ \text{mg}/\text{cm}^2$ . The  $^{12}\text{N}$  was produced at a rate of  $0.6 \div 1 \times 10^5$  pps. Since this time the aim of the experiment was to get good quality elastic scattering data, to improve the angular definition of the secondary  $^{12}\text{N}$  beam on target the slits situated behind the last pair of dipoles of MARS were closed to  $L/R=\pm 1.0$  cm from the beginning of the measurement. MARS D3 dipole had an inclination angle of  $5^\circ$ .

The identification of the reaction channels are shown in Figure 3 with emphasis on  $^{12}\text{N}$  reaction channels along with the position distribution in the four  $\Delta E$ -E telescopes used as detection system.

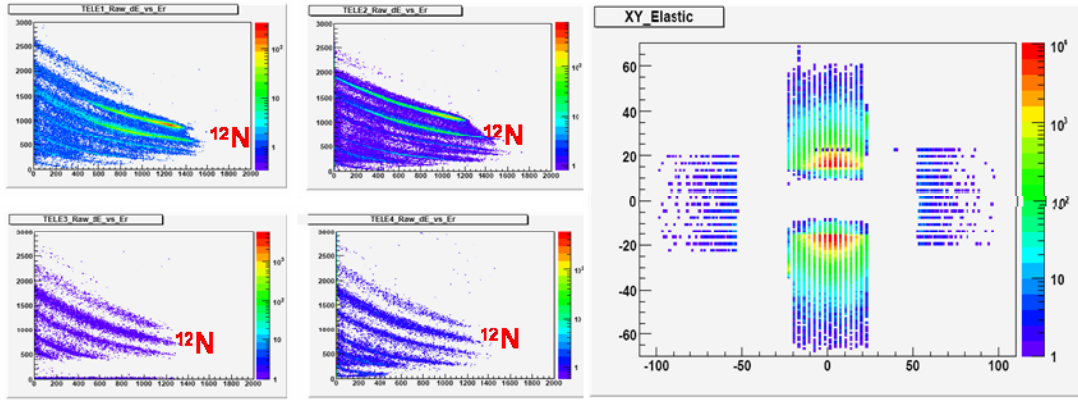


**Figure 3.**  $\Delta E$ -E reaction channel identification (right) and the elastic scattering position distribution (left).

Data analysis for this measurement is currently in progress. Once completed, it will enable us to use its results as an input for data analysis on ( $^{12}\text{N}$ ,  $^{13}\text{O}$ ) to extract more accurately the ANC for the system  $^{13}\text{O} \rightarrow ^{12}\text{N} + \text{p}$ , and from it to be able to evaluate the reaction cross section of radiative proton capture  $^{12}\text{N}(p,\gamma)^{13}\text{O}$ . The reaction is relevant to the evolution of the Pop III supermassive stars with low metallicity [1].

- [1] A. Banu *et al.*, *Progress in Research*, cyclotron Institute, Texas A&M University (2006-2007), p. I-XX
- [2] L. Trache *et al.*, *Phys. Rev. C* **61**, 024612 (2000).
- [3] F. Carstoiu *et al.*, *Phys. Rev. C* **70**, 054610 (2004).

## Further studies of $\beta$ -decay of proton-rich nucleus $^{23}\text{Al}$

Y. Zhai, T. Al-Abdullah, A. Banu, C. Fu, V. Golovko, J. C. Hardy, V. E. Jacob,  
N. Nica, H. I. Park, L. Trache, and R. E. Tribble

In 2005, we had experiments to produce, separate and study the  $\beta$ -decay of  $^{23}\text{Al}$ . In September 2005 we separated  $^{23}\text{Al}$  and studied its  $\beta$ -decay using MARS and the fast tape transport system. The interest was spurred by a nuclear astrophysics problem: the need to unambiguously determine the spin and parity of  $^{23}\text{Al}$  ground state, and remove an ambiguity of factors 30-50 in the  $^{22}\text{Mg}(p,\gamma)^{23}\text{Al}$  cross section at astrophysically relevant energies. We successfully and easily determined the spin and parity  $J^\pi=5/2^+$  from the beta-decay pattern. Parts of the results were already published [1]. It was for the first time that pure samples of  $^{23}\text{Al}$  could be separated and their decay studied. In addition to the g.s.  $J^\pi$  determination, a number of other states in the daughter nucleus  $^{23}\text{Mg}$  were populated and the absolute *logft* values for the transitions were determined. In particular we could identify the Isobaric Analog State (IAS) of  $^{23}\text{Al}$  gs at  $E^*=7803(2)$  keV through the measurement of its *logft*=3.31. Other states in  $^{23}\text{Mg}$  above the proton threshold at  $Sp=7580$  keV constitute resonances in the proton capture reaction  $^{22}\text{Na}(p,\gamma)^{23}\text{Mg}$  and are crucially important for the depletion of  $^{22}\text{Na}$  in ONe novae [2, 3]. We also determined the half-life of  $^{23}\text{Al}$  with much better precision.

To further improve the data, two more experiments were planned and carried out in September and November 2006. The first one was meant to simply improve the statistics we had earlier (and we got about a factor of 2 higher statistics for gamma-ray energies above 4 MeV). We also re-measured the  $\beta$ -decay of  $^{24}\text{Al}$  to improve the precision of our energy and efficiency calibration of the Ge detector at energies  $E_\gamma=3.5$  to 8 MeV. In the second experiment we added a BGO Compton shield around our Ge detector to clean the gamma-ray spectrum at large energies ( $E_\gamma=6-8$  MeV), in particular in the highly interesting region of the IAS.

In both experiments we used a 48 MeV/nucleon  $^{24}\text{Mg}$  beam from the K500 cyclotron and the fusion-evaporation reaction  $^{24}\text{Mg}(p, 2n)^{23}\text{Al}$  on a hydrogen gas cryogenic target cell cooled by  $\text{LN}_2$ . The  $^{23}\text{Al}$  beam was obtained as described before [1, 4] and we could get the same parameters as in September 2005: about 4000 pps at the extraction slits in the MARS focal plane. Its  $\beta$ -decay was further studied using the fast tape transport system and the  $\beta$ - $\gamma$  detectors.  $^{23}\text{Al}$  was taken out in air through a 50  $\mu\text{m}$  thick Kapton window, a stack of degraders and collected on the aluminized Mylar tape of the fast tape-transport system. Because the ranges of impurities in the beam are different from that of  $^{23}\text{Al}$ , a virtually pure  $^{23}\text{Al}$  sample was collected on the tape. In both measurements, we collected  $^{23}\text{Al}$  on the tape for 1 second. Then we shifted the RF phase to stop the  $^{24}\text{Mg}$  beam, moved the  $^{23}\text{Al}$  sample in 177 ms with the tape transport system to the counting station which consists of a HPGe  $\gamma$  detector and a  $\beta$  detector.  $\beta$  and  $\beta$ - $\gamma$  coincidence data were recorded for a predetermined counting period of 2 seconds. This cycle was precisely clock controlled and was repeated continuously. The sample was positioned between the HPGe  $\gamma$ -ray detector and a 1-mm-thick BC404 plastic scintillator used to detect  $\beta$  particles. This experimental setup is a typical one for measuring  $\beta$ - $\gamma$  coincidences. In September 2006 the HPGe detector was closer

than usual ( $d=4.9$  cm) and in the November 2006 experiment the BGO shield was added around the Ge detector.

We measured  $\gamma$ -rays in the energy range  $E_\gamma=0-9$  MeV. A spectacular cleaning of the background of gamma-ray spectrum at large energies was obtained with the BGO shield, as shown in Fig. 1. This spectrum and the better statistics data from the September run allowed us to identify weaker lines and improve the  $\beta$ -decay level scheme. We also separated pure samples of  $^{24}\text{Al}$ , by tuning MARS for this product, and did a similar  $\beta$ - $\gamma$  measurement. We use its known gamma-rays up to  $E_\gamma=7.8$  MeV for energy and efficiency calibration in the range  $E_\gamma=4-9$  MeV. The new data confirm the previous  $\beta$  &  $\gamma$ -branching ratios, strengthen and justify the previous level scheme.

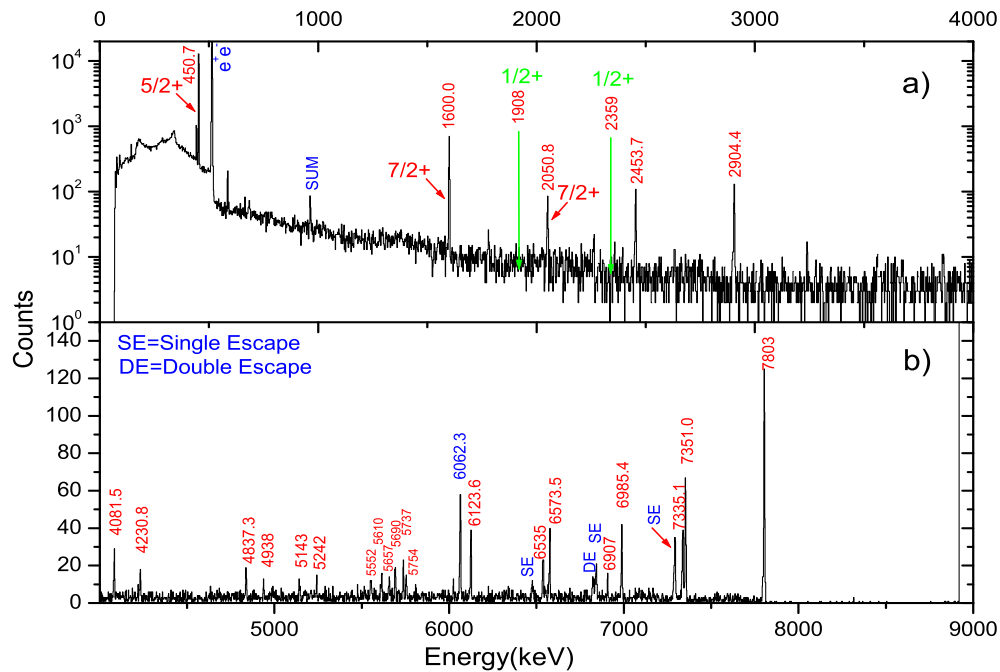


**Figure 1.**  $^{23}\text{Al}$   $\beta$ - $\gamma$  coincidence spectrum taken with a BGO Compton shield around the HpGe detector.

- [1] V. E. Jacob *et al.*, Phys. Rev. C **74**, 045810 (2006).
- [2] J. Jose, A. Coc, M. Hernanz, Astroph. J. **520**, 347 (1999).
- [3] C. Rolfs and W.S. Rodney, *Cauldrons in the Cosmos*, (University of Chicago Press, 1988).
- [4] Y. Zhai *et al.*, *Progress in Research*, Cyclotron Institute, Texas A&M University (2005-2006), p. I-5.

## Technique to study $\beta$ -delayed p-decay of proton-rich nuclei

L. Trache, T. Al-Abdullah, A. Banu, C. Fu, V. Golovko, J. C. Hardy, V. E. Iacob,  
H. I. Park, G. Tabacaru, R. E. Tribble, Y. Zhai, J. Aysto,<sup>1</sup> A. Saastamoinen,<sup>1</sup>  
M. A. Bentley,<sup>2</sup> D. Jenkins,<sup>2</sup> T. Davinson,<sup>3</sup> and P. J. Woods<sup>3</sup>

<sup>1</sup>*Department of Physics, University of Jyväskylä, Jyväskylä, Finland,*

<sup>2</sup>*Department of Physics, University of York, Heslington, York, United Kingdom,*

<sup>3</sup>*School of Physics, University of Edinburgh, Edinburgh, EH9 3JZ, United Kingdom.*

In the last two years we had at TAMU cyclotron experiments to produce, separate and study the  $\beta$ -decay of  $^{23}\text{Al}$ . The interest was initially spurred by a nuclear astrophysics problem: the need to unambiguously determine the spin and parity of  $^{23}\text{Al}$  ground state, and remove an ambiguity of factors 30-50 in the  $^{22}\text{Mg}(p,\gamma)^{23}\text{Al}$  cross section at astrophysically relevant energies. Parts of the results were already published [1], proving that this reaction is not a leading competitor to explain the non-observation of the 1.275 MeV gamma-ray from the decay of long-lived  $^{22}\text{Na}$  from space telescopes. It was for the first time that pure samples of  $^{23}\text{Al}$  could be separated and their decay studied. Before,  $\beta$ -decay of  $^{23}\text{Al}$  could only be studied using the small p-decay branches following the  $\beta$ -decay to levels in  $^{23}\text{Mg}$  above the proton threshold at  $S_p=7580$  keV. These states constitute resonances in the proton capture reaction  $^{22}\text{Na}(p,\gamma)^{23}\text{Mg}$ , crucially important for the depletion of  $^{22}\text{Na}$  in ONe novae [2, 3]. Two different experiments [4, 5] concur in their results at proton energies above  $E_p=500$  keV, but differ at lower energies, in particular in the region  $E_p=200$  keV where the important resonances lay, and in particular in the decay of the Isobar Analog State. Also the protons to gamma branching ratios were only poorly determined in this nucleus. All of the above led us to seek the study of  $\beta$ -delayed proton decay of this nucleus using our well separated, high energy  $^{23}\text{Al}$  beam.

To measure protons at such low energies, the windows of the detectors are always a problem. We decided to avoid it by implanting the source in the detector. This can be done given the large kinetic energy of our sources produced in inverse kinematics. A setup consisting of a thin Si strip detector (p-detector) and a thick Si detector ( $\beta$ -detector) was designed and realized (Figure 1). The two detectors were mounted on an Al frame which was cooled to minimize the noise. This telescope is at  $45^\circ$  to the beam axis to allow for good gamma-ray detection with the HpGe detector situated at  $90^\circ$  outside the small chamber. A variable energy degrader consisting of an Al foil (0.8 mm thick in our case) on a computer controlled rotating feed-through was used to stop the source nuclei in the middle of the thin p-detector. We pulse the beam from the cyclotron, implanting the source nuclei (for 1 sec. in the case of  $^{23}\text{Al}$ ), then switch the beam off and, after a very short delay (10 msec), measure for  $\beta$ -p and  $\beta$ - $\gamma$  coincidences simultaneously (1 sec. again). Si detectors are sensitive to positrons, and the total signal in the implantation detector is the sum of the proton and beta contributions. The latter is a continuum, which shifts the proton peak and produces an asymmetry on the high energy side of it. It also produces a large background at lower energies. To minimize these effects, the p-detector must be as thin as possible, and the size of the pixel must be small.

The setup was used in a very recent experiment. The  $^{23}\text{Al}$  beam was obtained as described before [1]: using a 48 MeV/nucleon  $^{24}\text{Mg}$  beam from the K500 cyclotron and MARS to separate  $^{23}\text{Al}$  (at 40 MeV/nucleon). The measurements used the telescope in two different modes:

- a) – the implantation control mode, in which the two detectors worked as a  $\Delta E$ -E HI telescope. It was used to determine the correct angle of the energy degrader for which the desired source was implanted in the first detector and to make sure the implantation is restricted to a central region of the detector. The signals in each detector were up to 300 MeV.
- b) – the decay mode, in which the gain was adjusted to accommodate the detection of low energy protons and betas (up to 2.5 MeV in the p-detector and 5-6 MeV in the  $\beta$ -detector).

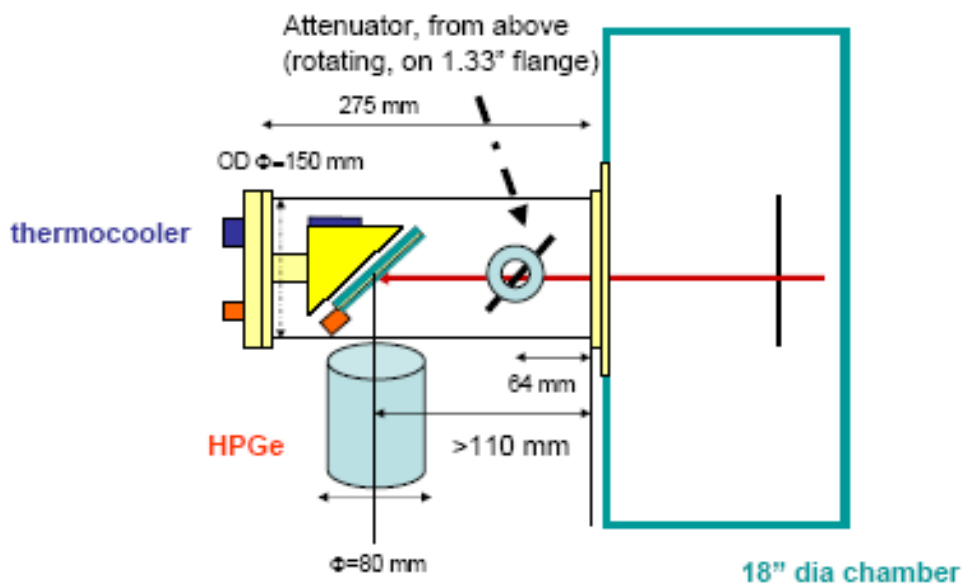


**Figure 1.** The experimental setup used to measure  $\beta$ -delayed p-decay from implanted sources.

After checking various configurations, in the end we opted for a W1(DS)-70 detector and the RAL108 preamp with CAEN N568B shapers. W1 are  $50 \times 50 \text{ mm}^2$  double sided Si  $16 \times 16$  strip detectors produced by Micron Semiconductor Ltd. The high gain, low noise RAL108 preamplifiers were developed at the University of Edinburgh. The thinner detector was good for resolution, but implied a more careful implantation control. Mesytec electronics promised similar resolution.

We have measured in the setup above, the following:

- implantation control in the "HI telescope mode" for  $^{24}\text{Al}$  (and later for  $^{23}\text{Al}$ ,  $^{22}\text{Mg}$ ,  $^{20}\text{Na}$ , and  $^{21}\text{Mg}$ )
- gamma-ray detector calibration with  $^{24}\text{Al}$  implanted at the p-det position (either in p-det, or in an Al thin foil)
- $^{23}\text{Al}$   $\beta$ -delayed p-decay with  $^{23}\text{Al}$  implanted in the p-detector.  $\beta$ -proton and  $\beta$ - $\gamma$  coincident spectra were measured here to identify the proton peaks and get the proton branchings.

- $\beta$ -background with  $^{22}\text{Mg}$  implanted in the p-detector.
- $\beta$ -detector calibration with  $^{20}\text{Na}$  implanted in  $\beta$ -detector.
- p-detector calibration with:
  - $^{20}\text{Na}$  (known  $\beta\alpha$  emitter) implanted in p-detector
  - $^{21}\text{Mg}$  (known  $\beta\text{p}$  emitter) implanted in p-detector
- off-line Ge detector efficiency calibration with sources ( $^{152}\text{Eu}$ ,  $^{60}\text{Co}$ ,  $^{137}\text{Cs}$ ).

## Figures from TAMU Run0507

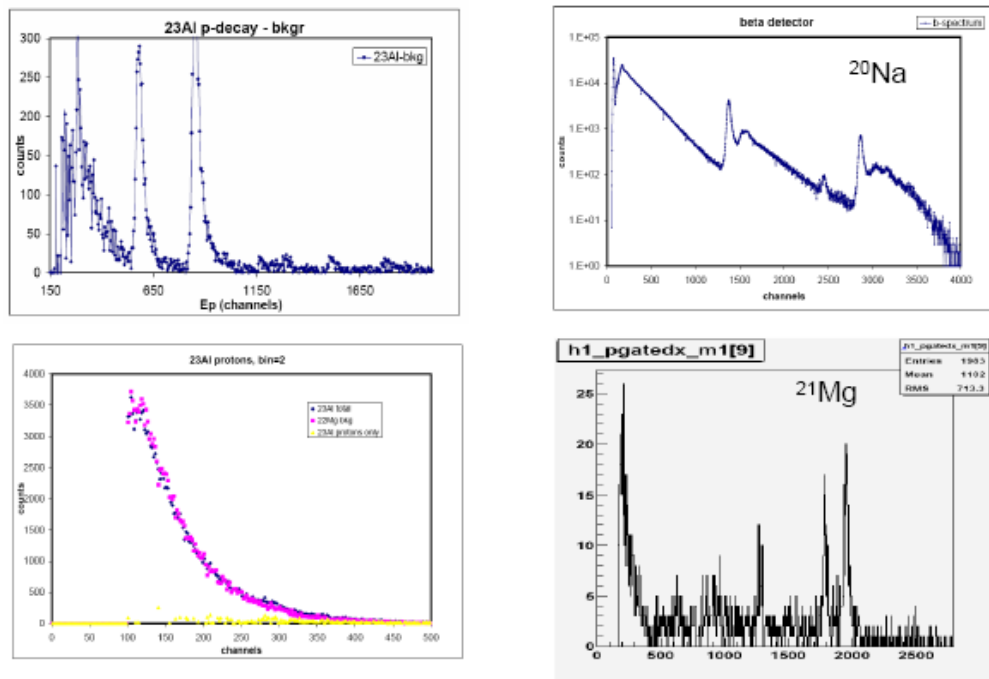


**Figure 2.** Spectra from the study of  $\beta$ -delayed p-decay of  $^{23}\text{Al}$ . Preliminary data only! Top left: a proton spectrum with  $\beta$  background subtracted. The proton peaks at 550 and 824 keV are very well separated. Bottom left: comparison of lower energy part of the spectra in p-detector from the decay of  $^{23}\text{Al}$  ( $\beta$  and p-decay) and of  $^{22}\text{Mg}$  ( $\beta$  only). Right: calibration spectra. Top: of the thick  $\beta$ -detector using implanted  $^{20}\text{Na}$  ( $\beta$  and  $\alpha$ ), bottom: of the thin p-detector using implanted  $^{21}\text{Mg}$ .

We intend to continue our studies to nuclei with similar properties and similar importance in explosive H-burning in stars:  $^{27}\text{P}$  and  $^{31}\text{Cl}$ .

- [1] V. E. Jacob *et al.*, Phys. Rev. C **74**, 045810 (2006).
- [2] J. Jose, A. Coc, and M. Hernanz, Astroph. J. **520**, 347 (1999).
- [3] C. Rolfs and W.S. Rodney, *Cauldrons in the Cosmos*, (University of Chicago Press, 1988).
- [4] R. J. Tighe *et al.*, Phys. Rev. C **52**, R2298, (1995).
- [5] K. Peräjäärvi *et al.*, Phys. Lett. B **492**, 1 (2000).

## Breakup of *sd*-shell proton-rich nuclei for nuclear astrophysics

A. Banu, L. Trache, R. E. Tribble, Y. Zhai, N. Orr,<sup>1</sup> L. Achouri,<sup>1</sup> B. Laurent,<sup>1</sup> B. Roeder,<sup>1</sup> M. Chartrier,<sup>2</sup> B. Fernandez-Dominguez,<sup>2</sup> S. Paschalis,<sup>2</sup> B. Pietras,<sup>2</sup> W. Catford,<sup>3</sup> N. Patterson,<sup>3</sup> J. Thomas,<sup>3</sup> M. Freer,<sup>4</sup> P. Roussel-Chomaz,<sup>5</sup> L. Gaudefroy,<sup>5</sup> F. Carstoiu,<sup>6</sup> F. Negoita,<sup>6</sup> F. Rotaru,<sup>6</sup> and A. Bonaccorso<sup>7</sup>  
<sup>1</sup>LPC Caen, France, <sup>2</sup>University of Liverpool, UK, <sup>3</sup>University of Surrey, UK, <sup>4</sup>University of Birmingham, UK, <sup>5</sup>GANIL, Caen, France, <sup>6</sup>IFIN-HH Bucharest, Romania, <sup>7</sup>INFN, Sezione di Pisa, Italy

At the end of 2004 the experiment E491 entitled “**<sup>23</sup>Al proton breakup at intermediate energies and astrophysical consequences**” proposed by a group of scientists from our laboratory, IFIN-HH Bucharest, LPC Caen, France and a number of British universities was accepted by the PAC at GANIL Caen, France, and given maximum priority. In September-October 2006 we could run the experiment at GANIL. The initial motivation and the focus of the experiment was the determination of the spin and parity, of the ANC and of the configuration mixing in the ground state of <sup>23</sup>Al from the measurement of the momentum distribution of the core after the proton breakup on a light target. The method to use breakup reaction for nuclear astrophysics was proposed earlier by our group [1]. In order to do that, a special experimental setup was put together mostly by our collaborators at LPC. The Ge clover detectors of EXOGAM were arranged in a new configuration at the target position of the magnetic spectrograph SPEG. Also 12 NaI detectors were included in the system. The setup was meant for two experiments measuring coincidences between gamma-rays detected at the target position and the core remnants after breakup measured at the focal plane of SPEG. The two experiments were aimed at two different classes of nuclei: our experiment E491 was doing it for a number of radioactive proton-rich nuclei around <sup>23</sup>Al, the companion experiment E452 concentrated on neutron-rich nuclei around <sup>23</sup>O. They were the first experiments of this class to use high resolution Ge detectors for the detection of gamma-rays from the core excitations.

The primary beam from the GANIL cyclotrons was 95 MeV/u <sup>32</sup>S. A relatively stable current of 2 eμA was delivered on a 450 mg/cm<sup>2</sup> carbon target in SISSI. SISSI was tuned for a <sup>23</sup>Al secondary beam at magnetic rigidity Bρ=1.95 Tm. That gave about 15 kHz of secondary beam on the second target (C at 180 mg/cm<sup>2</sup>), made mostly of <sup>24</sup>Si, <sup>23</sup>Al, <sup>22</sup>Mg and <sup>21</sup>Na, with <sup>23</sup>Al @ 50 MeV/u being about 1.4% of total. With it on the C secondary target, we run at about 200 Hz of SPEG events and with each Ge and NaI detectors loaded at about 50, and 400 Hz, respectively.

With SPEG tuned at 1.75 Tm (later 1.76 Tm) we could see that we measure the momentum distributions for the cores of the beam nuclei after the removal of one proton: <sup>23</sup>Al, <sup>22</sup>Mg, <sup>21</sup>Na and <sup>20</sup>Ne. We have inclusive momentum distributions and in coincidence with gammas. We have good data collected in the 7 days of runtime.

One puzzle we had during the run, which appeared in the end to be good physics, rather than a problem. It turned out that in addition to <sup>23</sup>Al, <sup>22</sup>Mg, <sup>21</sup>Na, ... products, in the ΔE-bands we have their isobars <sup>23</sup>Mg, <sup>22</sup>Na, <sup>21</sup>Ne, ... (in pairs), and gamma-rays from each pair show in the gated Ge spectra. We found ways to clearly separate the two masses in each band and showed that they come from different mechanisms. In the conditions we ran, in the spectrometer, ΔE separates on mass (not Z). The <sup>22</sup>Mg

component in the A=22 band, for example, comes from one-roton-removal from  $^{23}\text{Al}$ , but the  $^{22}\text{Na}$  component (and accompanying gammas) present at similar strength must appear from a charge-exchange reaction  $^{12}\text{C}(^{22}\text{Mg},^{22}\text{Na})^{12}\text{N}$ . Several states appear to be populated in each case. Below we see this separation, and we'll see what we can learn from here about the reaction mechanism and the structure of the states involved, it certainly looks interesting.

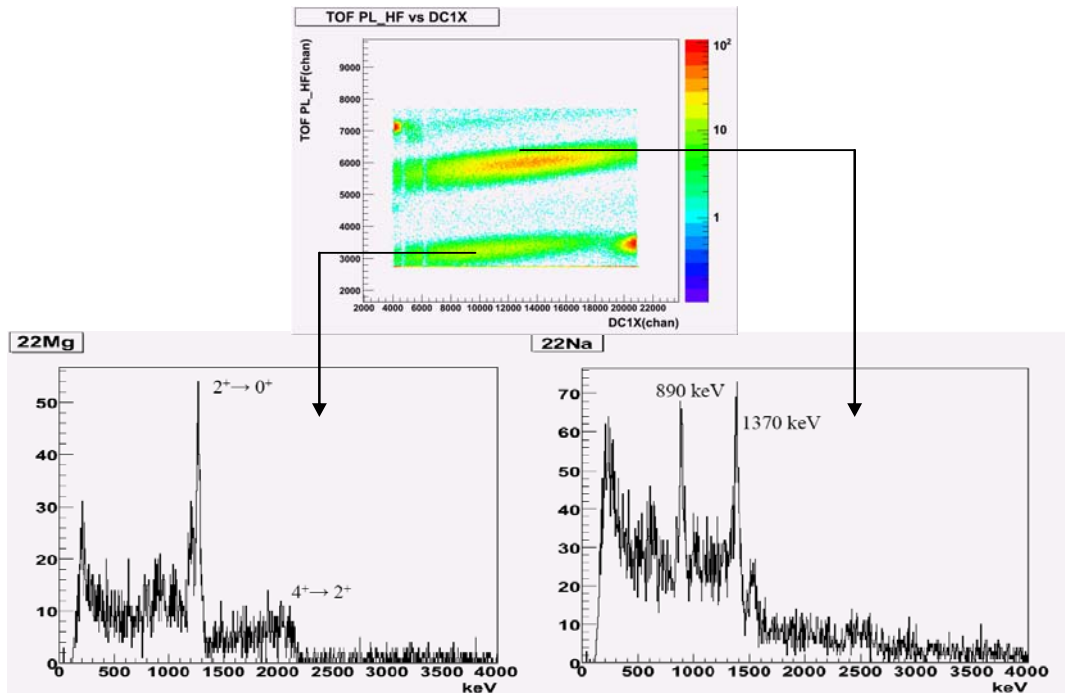


**Figure 1.** Illustration of the superposition of the two reaction mechanisms discussed in text. Top part shows for the same mass A=22 separated in the focal plane of SPEG split into  $^{22}\text{Mg}$  and  $^{22}\text{Na}$ . Bottom parts show the gamma-rays in coincidence with each one, separately.

The data analysis is still in progress. So far we have the data transposed from the GANIL format to a format that we can handle at TAMU, and we have the code for the analysis written from scratch, compiled and checked partially. In the same time we cooperate with colleagues from other teams to check the algorithms we use and the parameters we obtain, but also to minimize duplication of work.

[1] L. Trache, F. Carstoiu, C. A. Gagliardi, and R. E. Tribble, Phys. Rev. Lett. **87**, 271102 (2001).

## Determination of the $^{17}\text{F}(p,\gamma)^{18}\text{Ne}$ reaction rate using the neutron transfer reaction $^{13}\text{C}(^{17}\text{O}, ^{18}\text{O})^{12}\text{C}$

T. Al-Abdullah, F. Carstoiu, X. Chen, C. A. Gagliardi, Y.-W. Lui, G. Tabacaru,  
Y. Tokimoto, L. Trache, R. E. Tribble, and Y. Zhai

It is believed that the abundance of  $^{18}\text{F}$  can be influenced by the  $^{17}\text{F}(p,\gamma)^{18}\text{Ne}$  reaction. Its reaction rate at astrophysical energies has been determined for the first time through measurements of the ANC's in the mirror nuclear system. The peripheral  $^{13}\text{C}(^{17}\text{O}, ^{18}\text{O})^{12}\text{C}$  reaction was performed using the MDM spectrometer. The elastic scattering for  $^{17}\text{O}+^{13}\text{C}$  and  $^{18}\text{O}+^{12}\text{C}$  were also measured to obtain the OMPs that give the best description of the input and exit channels of the  $^{13}\text{C}(^{17}\text{O}, ^{18}\text{O})^{12}\text{C}$  reaction [1]. The radiative capture reaction  $^{17}\text{F}(p,\gamma)^{18}\text{Ne}$  is dominated by the direct capture to the first and second  $2^+$  states in  $^{18}\text{Ne}$  due to the  $s_{1/2}$  component in their wave functions. The angular distributions for the transfer to the states  $J^\pi = 0_1^+, 2_1^+, 4_1^+$ , and  $2_2^+$  in  $^{18}\text{O}$  are shown in Fig. 1. In our transfer calculations, the  $2^+$  states result

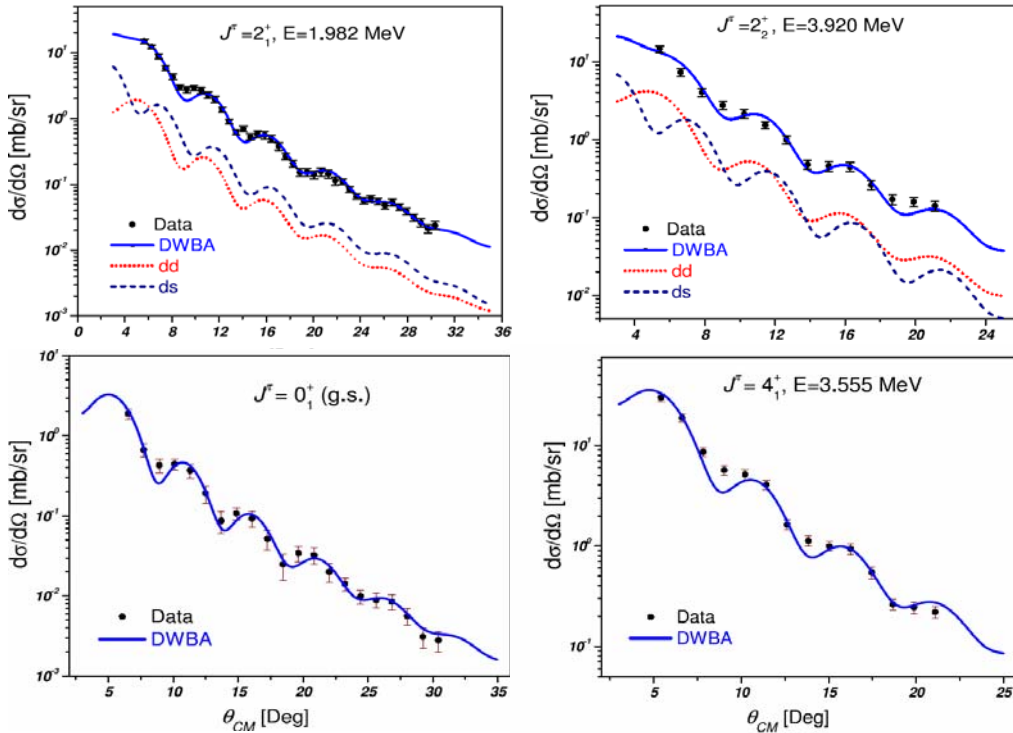


**Figure 1.** The angular distribution for the neutron transfer to the low-lying states in  $^{18}\text{O}$ ,  $J^\pi = 0_1^+, 2_1^+, 4_1^+$ , and  $2_2^+$ , populated in the  $^{13}\text{C}(^{17}\text{O}, ^{18}\text{O})^{12}\text{C}$  reaction. The solid lines represent the DWBA fit taking into account the shell model configurations for each state.

from the coupling of  $1d_{5/2}$  or  $2s_{1/2}$  neutron to the  $d_{5/2}$  ground state of  $^{17}\text{O}$ , while the  $0_1^+$  and  $4_1^+$  states can be obtained from adding a  $1d_{5/2}$  neutron to the  $1d_{5/2}$  core configuration. Therefore, the asymptotic normalization coefficients for each  $2^+$  state are obtained by

$$\frac{d\sigma}{d\Omega} = \frac{C_{p_{1/2}}^2({}^{13}\text{C})}{b_{p_{1/2}}^2({}^{13}\text{C})} \left\{ C_{\frac{5}{2},\frac{5}{2}}^2({}^{18}\text{O}) \frac{\sigma_{\frac{5}{2},\frac{5}{2}}^{\text{DWBA}}}{b_{\frac{5}{2},\frac{5}{2}}^2({}^{18}\text{O})} + C_{\frac{5}{2},\frac{1}{2}}^2({}^{18}\text{O}) \frac{\sigma_{\frac{5}{2},\frac{1}{2}}^{\text{DWBA}}}{b_{\frac{5}{2},\frac{1}{2}}^2({}^{18}\text{O})} \right\}.$$

The ANCs for  $0_1^+$  and  $4_1^+$  are extracted using a similar relation, but without the second term on the right hand side. The ANCs are listed in Table I. The astrophysical  $S$ -factor calculations for each

**Table I.** The binding energies (B.E.) and the ANCs of the low-lying levels in  ${}^{18}\text{O}$  and its mirror  ${}^{18}\text{Ne}$ .

$J^\pi$	Proton Orbital	${}^{18}\text{O}$		${}^{18}\text{Ne}$	
		B.E. [MeV]	$C_{\ell j}^2$ [ $\text{fm}^{-1}$ ]	B.E. [MeV]	$C_{\ell j}^2$ [ $\text{fm}^{-1}$ ]
$0_1^+$	$d_{5/2}$	8.04	$7.33 \pm 0.73$	3.92	$10.76 \pm 0.97$
$2_1^+$	$d_{5/2}$	6.06	$2.06 \pm 0.21$	2.04	$2.17 \pm 0.24$
	$s_{1/2}$		$6.55 \pm 0.69$		$14.29 \pm 1.71$
$4_1^+$	$d_{5/2}$	4.48	$1.05 \pm 0.11$	0.54	$2.17 \pm 0.22$
$2_2^+$	$d_{5/2}$	4.12	$0.49 \pm 0.06$	0.31	$2.69 \pm 0.32$
	$s_{1/2}$		$4.47 \pm 0.54$		$127 \pm 17$

$(\ell, j)$  configuration of the table were done depending on their related ANCs, as shown in Fig. 2, where the  $S$  factors for the  $2_1^+$  and  $2_2^+$  states are the sum of their  $(dd)$  and  $(ds)$  components. The figure shows

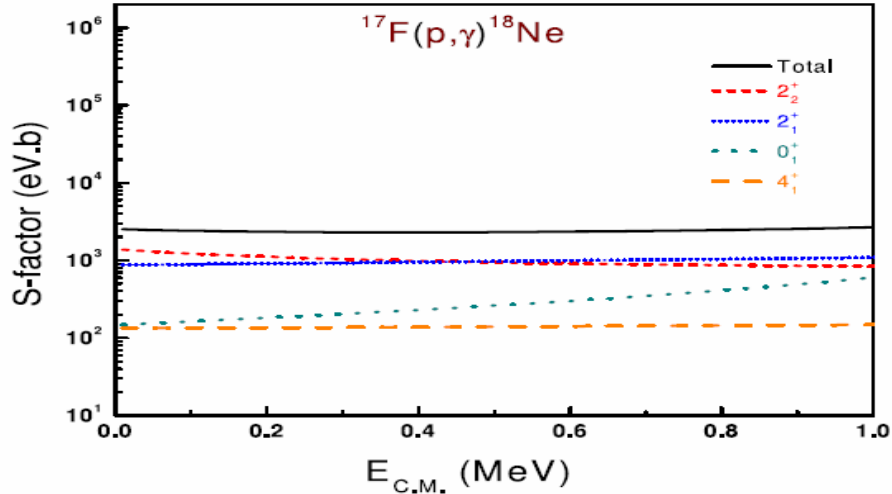


**Figure 2.** The  $S$ -factor components of the  ${}^{17}\text{F}(p,\gamma){}^{18}\text{Ne}$  reaction.  $S(\theta)$  of the  $J^\pi = 2_2^+$  state makes the major contribution to the reaction rate, and it is almost 50% larger than the  $J^\pi = 2_1^+$  contribution. The other components are one order of magnitude smaller than the major one. The total  $S_{1-17}(0) = 2.5 \pm 0.4$  keVb..

that the transitions to these states dominate the direct capture reaction over the other contributions. We find  $S_{1-17}(0) = 2.5 \pm 0.4$  keV b. The total direct capture rate is plotted in Fig. 3. The uncertainty in the reaction rate is related to the 20% overall uncertainty of the extracted ANCs. The resonant contribution through a proton capture to the resonance state  $J^\pi = 3^+ [E_r = 600$  keV,  $\Gamma_\gamma = (2.5 \pm 1.6) \times 10^{-5}$  keV ] [2] in  $^{18}\text{Ne}$  is calculated and plotted in the same figure to compare it with the direct capture reaction rate. The present results show that the thermonuclear reaction rate is dominated by the direct capture component by a factor up to  $10^4$  over the resonant contribution for  $T_9 = 0.2-0.4$ . The resonant contribution is more significant for temperatures in excess of  $T_9 \approx 0.5$  that characterize X-ray bursts or neutron stars.

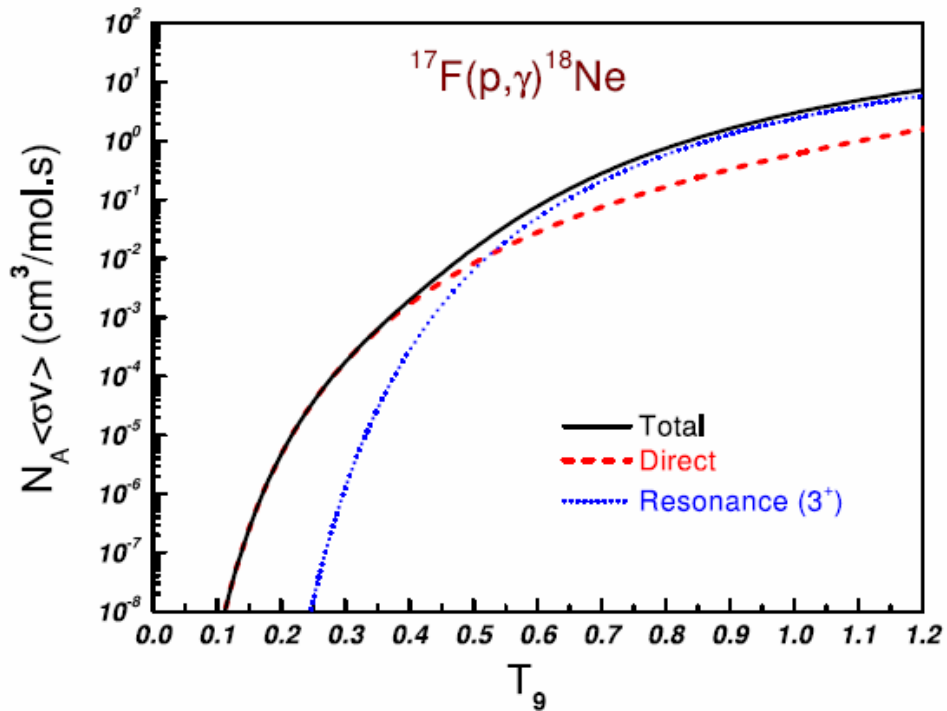


**Figure 3.** The (black) solid line represents the total rate for the  $^{17}\text{F}(p,\gamma)^{18}\text{Ne}$  reaction. The direct capture reaction, (red) dashed line, is evaluated using the extracted ANCs for the low-lying levels in  $^{18}\text{Ne}$  and the determined  $S$ -factors, while the (blue) dotted line shows the contribution from the resonant  $3^+$  state in  $^{18}\text{Ne}$ .

- [1] T. Al-Abdullah, *et al.*, *Progress in Research*, Cyclotron Institute, Texas A&M University (2005-2006), p. I-13.
- [2] D. W. Bardayan, *et al.*, *Phys. Rev. Lett.* **83**, 45 (1999).
- [3] A. Garcia, *et al.*, *Phys. Rev. C* **43**, 2012 (1991).

## Study of low-lying resonant states in $^{16}\text{F}$ using an $^{15}\text{O}$ radioactive ion beam

V. Z. Goldberg, D. W. Lee,<sup>1,2</sup> K. Peräjärvi,<sup>1</sup> J. Powell,<sup>1,3</sup> J. P. O'Neil,<sup>3</sup>

D. M. Moltz,<sup>4</sup> and Joseph Cerny<sup>1,4</sup>

<sup>1</sup> Nuclear Science Division, Lawrence Berkeley National Laboratory, Berkeley, California 94720

<sup>2</sup> Department of Nuclear Engineering, University of California, Berkeley, California 94720

<sup>3</sup> Life Sciences Division, Lawrence Berkeley National Laboratory, Berkeley, California 94720

<sup>4</sup> Department of Chemistry, University of California, Berkeley, California 94720

A 120 MeV  $^{15}\text{O}$  radioactive ion beam with an intensity on target of  $4.5 \times 10^4$  pps has been developed at the 88-inch cyclotron at the Lawrence Berkeley National Laboratory [1]. This beam has been used to study the level structure of  $^{16}\text{F}$  at low energies via the  $p(^{15}\text{O},p)$  reaction using the thick target inverse kinematics method [2] on a polyethylene target. The experimental excitation function was analyzed using R-matrix calculations. Significantly improved values for the level widths of the four low-lying states in  $^{16}\text{F}$  are reported. The spectroscopic factors are obtained using the experimental level widths and on the basis of the Coulomb shifts of the mirror levels in  $^{16}\text{N}$  and  $^{16}\text{F}$ . Good agreement with the theoretical spectroscopic factors is also obtained. Fig.1 presents the excitation function for the  $^{15}\text{O}+p$  elastic scattering at  $180^\circ$  ( $0^\circ$  in the laboratory system).

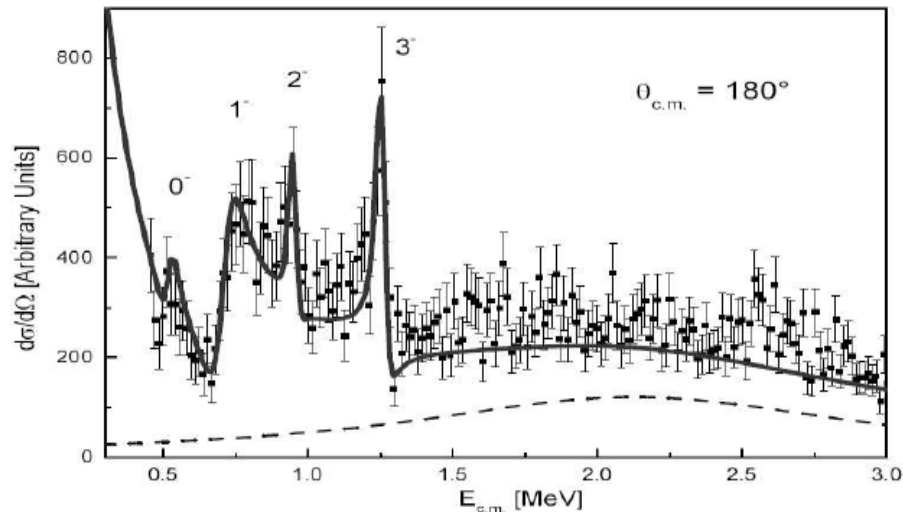


**Figure 1.** The R-matrix fit for the low-lying states in  $^{16}\text{F}$ . The solid line represents the R-matrix calculation added to the background; the background function is shown as a dashed line.

[1] F. Q. Guo *et al.*, Phys. Rev. C **72**, 034312 (2005).

[2] K. P. Artemov *et al.*, Sov. J. Nucl. Phys. **52**, 408 (1990).

## Study of the $^{20}\text{O}+p$ interaction

Changbo Fu, V. Z. Goldberg, G. G. Chubarian, M. McCleskey, Y. Zhai,  
T. Al-Abdullah, G. Tabacaru, and R. E. Tribble

Data on  $^{21}\text{O}$  level scheme are scarce and all spin parity assignments for the excited states were made just by comparison of the excitation energies with shell model calculations. The detailed data on the structure of the  $^{21}\text{O}$  levels are important to understand the way single-particle energies evolve when one goes away from stable nuclei to neutron and proton drip lines, specifically for the new  $N=14$  magic number [1], and for astrophysics [2]. The study of the  $^{20}\text{O}+p \rightarrow ^{21}\text{F}(T=5/2) \rightarrow ^{20}\text{O}+p$  reaction should provide a test of a possibility of investigating neutron rich nuclei through their analog states, which are populated in the resonance reactions of neutron rich nuclei with protons [3]. Our estimations show that in spite of the high binding energy of  $^{21}\text{O}$ ,  $\sim 3.8$  MeV, all isobar analogs of the  $^{21}\text{O}$  excited states can be populated in the resonance scattering in question. In a test experiment, we obtained the  $^{20}\text{O}$  beam with intensity about  $10^4$  pps, using the  $^4\text{He}(^{18}\text{O}, ^{20}\text{O})$  reaction and MARS facilities [4]. The main contaminants were  $^{20}\text{F}^{8+}$ , and  $^{15}\text{N}^{6+}$  (Fig. 1) with the same  $q/m$  values as  $^{20}\text{O}^{8+}$ . These contaminants could be identified and separated by an ionization chamber (Fig. 2). The working gas of the ionization chamber was the target material, methane gas. In a short test experiment we also could observe recoil protons from the interaction of  $^{20}\text{O}$  with hydrogen.

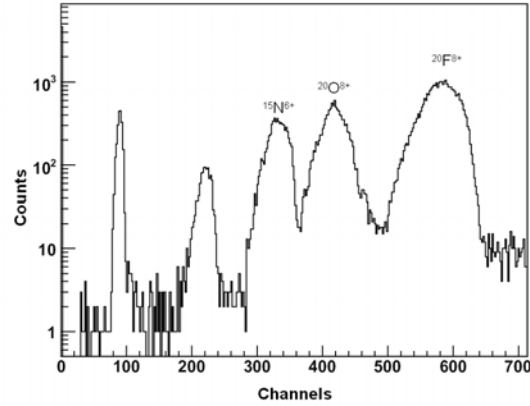


**Figure 1.** Composition of the beam by energy loss in the ionization chamber.

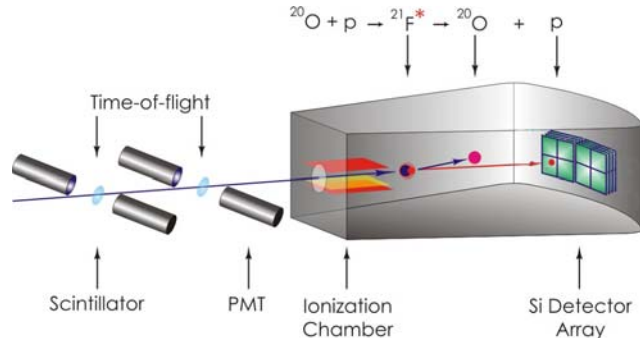


**Figure 2.** The setup of the experiment.

[1] M.Stanoiu *et al.*, Phys.Rev. **C 69**, 034312 (2004).

[2] H.Herndl *et al.*, Phys. Rev. **C 60**, 064614 (1999).

[3] V.Z. Goldberg, Exotic Nuclei and Atomic Masses, edited by B. M. Sherrill, *et al.*, (AIP, Woodbury, NY, 1998).

[4] R. E. Tribble *et al.*, Nucl. Instrum. Methods Phys. Res. **A285**, 441 (1989).

**Search for violation of the spin-parity and isospin conservation law  
in the decay of the 3.56 MeV  $0^+$  level in  ${}^6\text{Li}$**

V. Z. Goldberg, J. C. Hardy, A. Mukhamedzhanov, G. Tabacaru, G. Chubarian, R. E. Tribble  
G. V. Rogachev,<sup>1</sup> E. Johnson,<sup>1</sup> C. Spitaleri,<sup>2</sup> S. Cherubini,<sup>2</sup> S. Romano,<sup>2</sup> M. Gulino,<sup>2</sup>  
A. Tumino,<sup>2</sup> R. G. Pizzone,<sup>2</sup> M. La Cognata,<sup>2</sup> L. Lamia,<sup>2</sup> N. Shulgina,<sup>3</sup> and W.H. Trzaska<sup>4</sup>

<sup>1</sup>*Department of Physics, Florida State University, Tallahassee, Florida 32306*

<sup>2</sup>*Laboratori Nazionali del Sud-INFN, Italy*

<sup>3</sup>*Kurchatov Institute, R-123182 Moscow, Russia*

<sup>4</sup>*University of Jyvaskyla, Jyvaskyla, Finland*

Among nuclear processes for which spatial parity is not conserved (PNC processes), a distinguished role is played by those with changing isospin,  $\Delta T=1$ . These are initiated due to the existence of only weak neutral currents which are of paramount interest in developing unification schemes of gauge fields.

Parity nonconservation in nuclei is commonly analyzed in terms of parity violating nucleon-nucleon potential, based on one-boson exchange. The parameters of the potential (weak nucleon-meson couplings) are determined theoretically with large uncertainty (around 300%), depending on the model assumptions

Although the PNC effects in heavy nuclei are quite large owing to the enhancement mechanisms, exploration of the PNC transitions should preferably be carried out in few nucleon systems as for these the PNC effects can be separated (theoretically) from the nuclear interaction background.

Search for  $T=1$  levels in  ${}^{10}\text{B}$ , which can populate  $T=1, 0^+$  (3.56 MeV) level in  ${}^6\text{Li}$  as a result of  $\alpha$  decay, was made in the  ${}^9\text{Be}+p$  resonance interaction at LNS-INFN, Italy. (The search for the parity violating  $\alpha$  decay of the 3.56 MeV level in  ${}^6\text{Li}$  was a well known challenge for various experimental groups for many years [1,2].) The excitation function for the  ${}^9\text{Be}+p \rightarrow \alpha+{}^6\text{Li}$  (3.56 MeV) was studied in the region of 20-55 MeV of the  ${}^9\text{Be}$  incident energies using  $\alpha+{}^6\text{Li}$  coincidence events. The  ${}^9\text{Be}+p$  elastic scattering, as well as other possible decay channels of the resonances in  ${}^{10}\text{B}$  were also studied.

It was found that a resonance at excitation energy of 8.9 MeV in  ${}^{10}\text{B}$  was the best candidate for the population of the 3.56 MeV level in  ${}^6\text{Li}$ , and this resonance should be used for future search of the  ${}^6\text{Li}$  decay. Resonances at higher excitation energies in  ${}^{10}\text{B}$  manifest also itself in the  $\alpha+{}^6\text{Li}$  (3.56) decay channel. After determination of their quantum characteristics, we hope to find evidence for the  $\alpha+\alpha+p+n$  structure.

[1] D. H. Wilkinson, Phys. Rev. **109**, 1603 (1958).

[2] B. G. H. Robertson *et al.*, Phys. Rev. **C 29**, 755 (1984).

## $T = 3/2$ states in $^{13}\text{C}$

V. Z. Goldberg, R. E. Tribble, B. B. Skorodumov,<sup>1</sup> G. V. Rogachev,<sup>2</sup> A. Aprahamian,<sup>1</sup> J. J. Kolata,<sup>1</sup>  
S. Almaraz,<sup>1</sup> H. Amro,<sup>3</sup> L. O. Lamm,<sup>1</sup> M. Quinn,<sup>1</sup> A. Teymurazyan,<sup>1</sup> and A. Woehr<sup>1</sup>

<sup>1</sup>*Institute for Structure and Nuclear Astrophysics, University of Notre Dame, Notre Dame, Indiana 46556*

<sup>2</sup>*Physics Department, Florida State University, Tallahassee, Florida 32306*

<sup>3</sup>*Physics Department, University of Michigan, Ann Arbor, Michigan 48109*

The level scheme of  $T = 3/2$  states in  $A = 13$  nuclei is important to estimate the prediction quality of contemporary shell model calculations for exotic nuclei [1]. It also has impact on super massive star evolution [2]. It can be expected that several low-lying excited states with  $T = 3/2$  in this mass region should have substantial  $2s_{1/2}$  and  $1d_{5/2}$  single-particle reduced widths. However, a spin-parity assignment of  $J^\pi = 1/2^+$  has only recently been made for the first excited state in  $^{13}\text{O}$  [3], while other levels with large predicted single-particle widths were not observed in this work.

The intent of this experiment was to obtain data on  $T = 3/2$  states in  $A=13$  nuclei over a broader energy region than was available in Ref. [3]. In the present work, the first results from an investigation of  $^{12}\text{B}+p$  resonance elastic scattering are given.

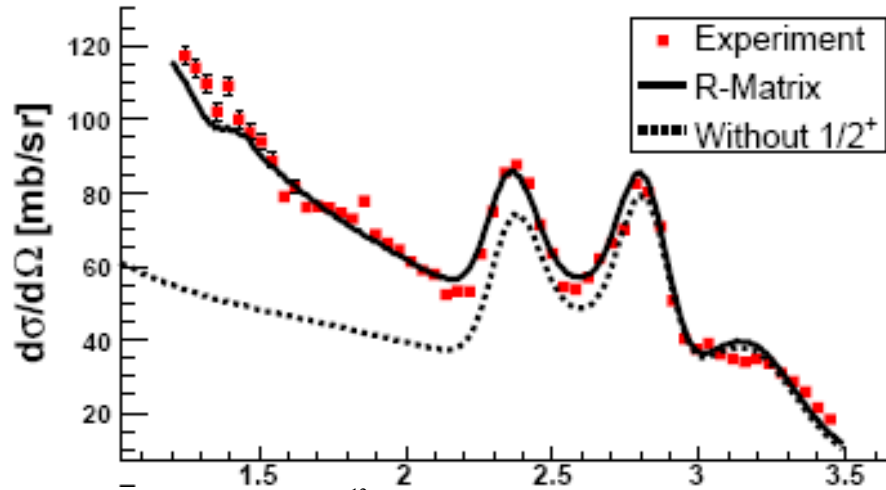


**Figure 1.** The excitation functions for  $^{12}\text{B}+p$  elastic resonance scattering. The dotted curve shows an R-matrix fit without the  $1/2^+$  resonance. To convert the *c.m.* energy to the excitation energy in  $^{13}\text{C}$ , add 17.53 MeV.

Fig.1 presents cm excitation function for the  $^{12}\text{B}+p$  elastic scattering obtained at  $7.5^0$  lab. system ( $165^0$  c.m.) at the N. D. tandem. (Excitation functions were obtained and analyzed at different angles.) Table 1 presents the resonance parameters of the levels in the fit together with predictions of the shell

Table I: Resonance parameters for levels in  $^{13}\text{C}$ .

L	$J^\pi$	$E_{c.m.}$	$E_{ex}$	$\Gamma_{exp}$	$S_{s.p.}$	Shell	$SOXBASH$	$SOXBASH$
			MeV	MeV	keV		(WBT)	(PSDMK)
0	$1/2^+$	1.05	18.58	411	0.89	2s1/2	0.67	0.75
						1d3/2	0.013	0.014
(1)	$(1/2^-)$	1.36	18.89	10	0.07	1p1/2	0.06	0.009
	$(3/2^+)$	2.36	19.89	109				
0				71	0.04	2s1/2	0.27	0.47
2				40	0.51	1d3/2	0.09	0.03
						1d5/2	0.30	0.28
2	$(5/2^+)$	2.84	20.37	98	0.48	1d3/2	0.03	0.017
						1d5/2	0.21	0.49
(2)	$(7/2^+)$	3.24	20.77	457	0.99	1d5/2	0.29	0.48

model (Oxbash) calculations. As a result of the investigation, we can state the following. Evidence was found for five new  $T = 3/2$  resonances in this region, and tentative spin-parity assignments were given for all these states. All have very small widths for decay through isospin violating channels. The dominant configurations of the levels are in qualitative agreement with shell-model predictions. However, disagreements with theoretical predictions of the non-dominant configurations, as well as with the relative excitation energies of the levels, were observed. We have considered existing data on  $T = 3/2$  states in the mirror nuclei,  $^{13}\text{C}$  and  $^{13}\text{N}$ , obtained in T-violating resonance scattering. Several unreliable  $T = 3/2$  assignments were noted. No anomalies related to the manifestation of  $T = 1/2$  states were observed. Still a mystery should be solved: the known density of levels (of unknown spins) in  $^{13}\text{B}$  is much higher than what we found for  $T=3/2$  states in  $^{13}\text{C}$ .

[1] A. Volya and V. Zelevinsky, Phys. Rev. Lett. 94, 052501 (2005).

[2] G. M Fuller *et al.*, Astrophys. J. **307**, 675 (1986); M. Wiesher *et al.*, Astrophys. J. **343**, 312 (1989).

[3] B. Skorodumov *et al.*, Phys. Rev. C **75**, 024607 (2007).

## Superallowed beta decay

J. C. Hardy, I. S. Towner, V. E. Jacob, N. Nica, V. Golovko, H. I. Park, J. Goodwin,  
C. A. Gagliardi, L. Trache and R. E. Tribble

Superallowed  $0^+ \rightarrow 0^+$  beta decay between  $T=1$  analogue states has been a subject of continuous and often intense study for five decades. The  $ft$  values of such transitions are nearly independent of nuclear-structure ambiguities and depend uniquely on the vector part of the weak interaction. Their measurement gives us access to clean tests of some of the fundamental precepts of weak-interaction theory, and, over the years, this strong motivation has led to very high precision being achieved in both the experiments and the theory used to interpret them. We have a major program at the Cyclotron Institute to study superallowed beta decay.

To obtain the  $ft$  value for any transition, three quantities must be measured: the half life of the parent, the  $Q_{EC}$  value for the transition of interest and the branching ratio for that transition. We produced a complete survey of existing data on these superallowed decays two years ago [1, 2]. There, all the experimental data for each transition were critically evaluated and final  $ft$  values obtained; then, small radiative and isospin-symmetry-breaking corrections [3] were applied and a final set of “corrected  $ft$  values”, denoted  $\overline{ft}$ , were obtained.

In the two years since our review was published, a number of new experimental results have appeared, some from our group and some from a variety of other groups worldwide. Furthermore, the largest radiative correction – the “inner” one – was revisited and its uncertainty reduced by a factor of two [4]. Figure 1 shows the raw  $ft$  values and corrected  $\overline{ft}$  values for the most precisely known superallowed  $0^+ \rightarrow 0^+$  transitions as they are now known in mid 2007. The constancy of the  $\overline{ft}$  values is evident, their average being 3073.9(8) s, with a normalized  $\chi^2$  of 0.9.

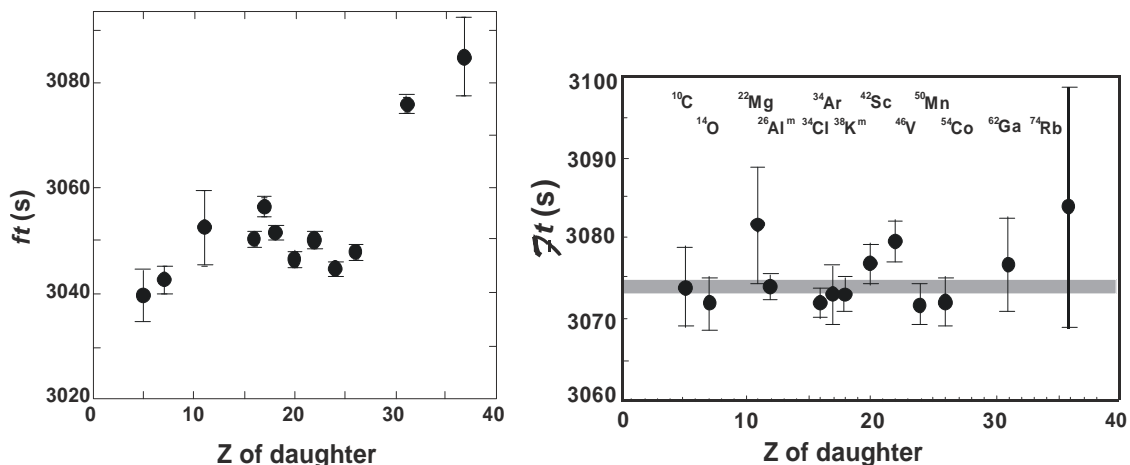


**Figure 1.** Results from the 2005 survey [1] updated with more recent published results. The uncorrected  $ft$  values for the thirteen best known superallowed decays (left) are compared with the same results after corrections have been applied (right). The grey band in the right-hand panel is the average  $\overline{ft}$  value, including its uncertainty.

Since these corrected  $\overline{ft}$  values are inversely proportional to the square of the vector coupling constant,  $G_V$ , the constancy of  $G_V$  is demonstrated to 1.3 parts in  $10^4$ . Not only is this an important confirmation of the Conserved Vector Current (CVC) hypothesis but it sets the stage for using the average value of  $G_V$  to test a fundamental principle of the electroweak standard model, the unitarity of the Cabibbo-Kobayashi-Maskawa (CKM) matrix. The up-down quark mixing element of that matrix,  $V_{ud}$ , is given by  $V_{ud} = G_V / G_F$ , where  $G_F$  is the weak interaction constant for the purely leptonic muon decay. The value of  $V_{ud}$  is a key component of the most demanding test available for the unitarity of the CKM matrix, the sum of squares of its top-row elements [1]. As explained elsewhere in this Progress Report [5], superallowed nuclear beta decays provide by far the most precise and reliable value for  $V_{ud}$  and, in fact, that element now is also the most precisely known one in the CKM matrix – by an order of magnitude! Its current value is 0.97378(27)

For several decades, the top-row unitarity sum has differed from unity by several standard deviations but, over the past several years, new results from kaon decay have demonstrated that the value of another element of the top row,  $V_{us}$ , was not correct. There is still some dispute over the exact theoretical correction terms to use in determining  $V_{us}$ , but the consensus at the moment favors a value for  $V_{us}$ , which, when combined with the nuclear value for  $V_{ud}$ , yields a unitarity sum of 0.9992(11). This confirmation of CKM unitarity is not only a significant verification of the standard model but the uncertainty quoted on the sum provides a tight limit on any possible new physics beyond the standard model.

In short, superallowed  $0^+ \rightarrow 0^+$  beta decay provides a high-profile application of nuclear-physics measurements to the study of fundamental symmetries, a subject of vital interest to both nuclear and particle physicists. Although much has already been achieved in this field by nuclear physicists, improvements are still possible. Reducing the uncertainty on the unitarity sum – and, with it, the scope for new physics – remains the primary goal of our research program.

The principal difference between the left and right panels of Fig 1, is the inclusion of the nuclear-structure-dependent corrections,  $\delta_{NS}$  and  $\delta_C$ , in the derivation of the  $\overline{ft}$  values in the latter. Since these corrections were determined [3] completely independently of the superallowed decay data, the consistency of the  $\overline{ft}$  values is also a powerful validation of these calculated corrections: obviously they act very well to remove the considerable “scatter” that is apparent in the left panel and is effectively absent in the right one.

The 2005 survey [1, 2], which considered a body of world data comprised of more than 125 individual measurements, presented a remarkably consistent picture for the nuclear results. Even so, it is still possible for well selected experiments to make real improvements. For example, the validation of the nuclear-structure-dependent correction terms can be improved by the addition of new transitions selected from amongst those with large calculated corrections. If the  $ft$  values measured for cases with large calculated corrections also turn into corrected  $\overline{ft}$  values that are consistent with the others, then this must verify the calculations' reliability for the existing cases, which have smaller corrections. At TAMU we have just completed half-life [6] and branching-ratio [7] measurements for  $^{34}\text{Ar}$  decay. This adds  $^{34}\text{Ar}$  to the select group of transitions whose  $\overline{ft}$  values are known to 0.1% or better. Its nuclear-structure-dependent correction is also larger than for any other well known transition with  $A < 40$ , where the nuclear

models used in the calculation are expected to be the most reliable. Conformity of the corrected  $\mathcal{F}t$  value for  $^{34}\text{Ar}$  with the average result from the other cases provides strong confirmation of the validity of the correction calculations.

We are also studying another superallowed decay with a large calculated correction,  $^{38}\text{Ca}$ . We have made some preliminary measurements of both its half-life [8] and branching ratio. Measurements of other new cases with large calculated corrections, such as  $^{18}\text{Ne}$  and  $^{30}\text{S}$ , are planned.

Another area of potential improvement is in the limit set on scalar currents, the presence of which would manifest themselves as a curvature either up or down in the locus of  $\mathcal{F}t$  values at low  $Z$ . Thus this limit, currently  $f_S < 0.0013$  in electron rest-mass units, is particularly sensitive to the  $\mathcal{F}t$ -value for  $^{10}\text{C}$ . We have re-measured and improved the half-life of  $^{10}\text{C}$  [9], with the goal of improving the scalar-current limit.

The nuclear-structure-dependent correction terms can also be tested by tightening the uncertainties on already well-known transitions. Considering the overall quality of world data on superallowed decays, no dramatic surprises were expected as new data appeared. However, two years ago came our measurement with the CPT Penning trap at Argonne National Lab of the  $Q_{\text{EC}}$  value of the  $^{46}\text{V}$  superallowed beta-decay branch [10]. This was the first time a Penning trap had been used for any of the well-known superallowed transitions and the one chosen was the transition whose  $Q_{\text{EC}}$  value was least precisely known, with the expectation that it would simply improve the precision of the average. Indeed, it shrunk the error bar but it also changed the result considerably.

This raised the question of whether there could be a systematic difference between on-line Penning-trap and reaction-based measurements? In collaboration with the JYFLTRAP Penning-trap group at the University of Jyväskylä we have settled this issue. We measured the  $Q_{\text{EC}}$  values for  $^{46}\text{V}$ ,  $^{42}\text{Sc}$  and  $^{26}\text{Al}^{\text{m}}$ [11], confirming the Savard *et al.* [10] result for  $^{46}\text{V}$  but finding that the  $Q_{\text{EC}}$  values for  $^{42}\text{Sc}$  and  $^{26}\text{Al}^{\text{m}}$  agree well with the survey results, which depend entirely on reaction-based measurements. Thus there is no indication of a systematic shift between Penning-trap and reaction measurements.

There still remains the fact that the corrected  $\mathcal{F}t$  value for  $^{46}\text{V}$  is now significantly higher than that for any other well known superallowed transition (see Fig. 1). The most obvious explanation of its unusual value is that the correction for isospin symmetry-breaking, which depends upon the nuclear structure of the parent and daughter nuclei, is missing some important components, and we have begun to examine this possibility theoretically [12]. What we have found so far is that by including the  $sd$ -shell with the  $fp$ -shell in our configuration space, we could remove the shift in the  $^{46}\text{V}$  result but not without introducing shifts in the  $\mathcal{F}t$  values for  $^{50}\text{Mn}$  and  $^{54}\text{Co}$  as well. The currently accepted  $Q_{\text{EC}}$  values for  $^{50}\text{Mn}$  and  $^{54}\text{Co}$  are averages, each with an important contribution from a 30-year-old ( $^3\text{He,t}$ )  $Q$ -value measurement, which appeared in the same paper in which the now-discredited value for the  $^{46}\text{V}$   $Q_{\text{EC}}$  value also appeared. Perhaps their results for  $^{50}\text{Mn}$  and  $^{54}\text{Co}$  were wrong as well. With the Jyväskylä group, we have re-measured the  $Q_{\text{EC}}$  values for  $^{50}\text{Mn}$  and  $^{54}\text{Co}$  [13].

- [1] J. C. Hardy and I. S. Towner, Phys. Rev. C **71**, 055501 (2005).
- [2] J. C. Hardy and I. S. Towner, Phys. Rev. Lett. **94**, 092502 (2005).
- [3] I. S. Towner and J. C. Hardy, Phys. Rev. C **66**, 035501 (2002).
- [4] W. J. Marciano and A. Sirlin, Phys. Rev. Lett. **96**, 032002 (2006).

- [5] J. C. Hardy, *Progress in Research*, Cyclotron Institute, Texas A&M University (2006-2007), p. I-46.
- [6] V. E. Iacob *et al.*, Phys. Rev. C **74**, 045810 (2006) and *Progress in Research*, Cyclotron Institute, Texas A&M University (2006-2007), p. I-48.
- [7] V. E. Iacob *et al.*, *Progress in Research*, Cyclotron Institute, Texas A&M University (2006-2007), p. I-51.
- [8] H. I. Park *et al.*, *Progress in Research*, Cyclotron Institute, Texas A&M University (2006-2007), p. I-58.
- [9] V. E. Iacob *et al.*, *Progress in Research*, Cyclotron Institute, Texas A&M University (2006-2007), p. I-55.
- [10] G. Savard, F. Buchinger, J. A. Clark, J. E. Crawford, S. Gulick, J. C. Hardy, A. A. Hecht, J. K. P. Lee, A. F. Levand, N. D. Scielzo, H. Sharma, I Tanihata, A. C. C. Villari, and Y. Wang, Phys. Rev. Lett. **95**, 102501 (2005).
- [11] T. Eronen, V. Elomaa, U. Hager, J. Hakala, A. Jokinen, A. Kankainen, I. Moore, H. Penttilä, S. Rahaman, A. Saastamoinen, T. Sonoda, J. Äystö, J. C. Hardy, and V. Kolhinen, Phys. Rev. Lett. **97**, 232501 (2006).
- [12] I. S. Towner and J. C. Hardy, *Progress in Research*, Cyclotron Institute, Texas A&M University (2006-2007), p. III-29 and III-31.
- [13] J. C. Hardy, *Progress in Research*, Cyclotron Institute, Texas A&M University (2006-2007), p.I-61.

## The status of $V_{ud}$

J. C. Hardy

The up-down quark mixing element,  $V_{ud}$ , of the Cabibbo Kobayashi Maskawa (CKM) matrix can be determined via three  $\beta$ -decay routes: superallowed  $0^+ \rightarrow 0^+$  nuclear decays, neutron decay and pion decay. Historically, the nuclear decays have yielded the most precise measurements, but the resultant value for  $V_{ud}$  was often thought to be severely limited in accuracy by the calculated nuclear-structure-dependent corrections that were required to extract it from the data. The neutron measurements, though free of nuclear corrections, are experimentally challenging and have therefore been less precise, not to mention occasionally inconsistent with one another. Pion  $\beta$  decay, being a  $10^{-8}$  decay branch, is even more challenging experimentally and has produced larger uncertainties for  $V_{ud}$  than either of the other two approaches.

All three decay modes require that small radiative corrections be applied to the primary experimental data in the process of obtaining a value for  $V_{ud}$ , and naturally there are uncertainties associated with these calculated corrections. In fact, in the case of the superallowed nuclear decays, the experimental uncertainties have become so well controlled that it is these theoretical uncertainties that dominate the uncertainty quoted on  $V_{ud}$ . However, it may be a surprise to some readers that the nuclear-structure-dependent correction is *not* the main contributor. Instead, the dominant theoretical uncertainty originates from the so-called inner radiative correction, which is a correction that is common to all three decay modes and, unless it is improved, will ultimately limit the precision with which  $V_{ud}$  can be determined by any route.

As more and more superallowed  $0^+ \rightarrow 0^+$  nuclear transitions are measured with high precision, the nuclear-structure-dependent corrections continue to prove their validity. The calculations themselves are based on well-established nuclear structure information derived from nuclear measurements that are totally independent of the superallowed decay experiments. The magnitude of the calculated correction for each transition, though always less than 1.5%, differs considerably from transition to transition. The measured superallowed transition strengths, which are an order of magnitude more precise than that, actually reproduce these predicted differences and, as a result, lead to completely consistent values of  $V_{ud}$ . All evidence points to the nuclear-structure-dependent corrections being completely reliable within their quoted uncertainties.

The current status of  $V_{ud}$  as determined by the three different experimental routes, has been assessed and summarized [1,2]. The up-to-date values are:

$$\begin{aligned} V_{ud} = & 0.97378(27) && [\text{superallowed nuclear decays}] \\ & 0.9766(20) && [\text{neutron decay}] \\ & 0.9751(27). && [\text{pion beta decay}] \end{aligned} \tag{1}$$

The corresponding error budgets for these three methods are given in Figure 1, from which it can be seen that uncertainties in the theoretical corrections currently limit the nuclear result, while the neutron and pion decays are limited to a much larger uncertainty by experimental factors.

As of now, superallowed  $0^+ \rightarrow 0^+$  nuclear  $\beta$  decay clearly dominates in the determination of  $V_{ud}$ . A weighted average of the three results quoted in Eq. 1, yields a result that differs only in the fifth place of decimals from the nuclear result alone; and, considering the experimental ambiguities present in the other decays, especially in that of the neutron, it seems best for the time being to rely simply upon the un-averaged nuclear result. Although this result is now limited by uncertainties originating in the theoretical corrections applied to the data, the largest theoretical uncertainty is not due to the nuclear-structure-dependent corrections,  $\delta_C$  and  $\delta_{NS}$ , and but rather to the “inner” radiative correction,  $\Delta_R$ , which actually is common to all three  $\beta$  decays: nuclear, neutron and pion. Clearly it would be beneficial to have confirmation of the nuclear  $V_{ud}$  by results of comparable precision from the other two  $\beta$ -decay modes, but one should not anticipate that either of the latter will actually surpass the nuclear result in the near future.

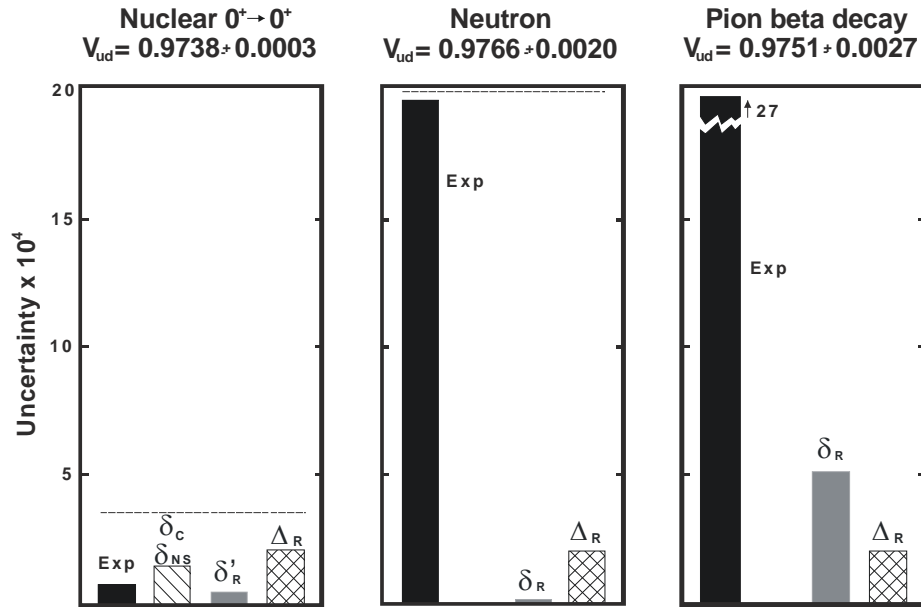


**Figure 1.** Error budgets for the three different methods to determine  $V_{ud}$ , illustrating the relative importance of experimental uncertainties (exp) and theoretical ones ( $\delta_C$ ,  $\delta_{NS}$ ,  $\delta_R$  and  $\Delta_R$ ).

[1] J. C. Hardy, *Intersections of Particle and Nuclear Physics 2006: 9<sup>th</sup> Conference*, ed. T.M. Liss, AIP Conference Proceedings, Vol. 1441, pp. 1-10, 2006.

[2] J. C. Hardy, *Proceedings of the CKM2006 Workshop*, to be published as a KEK report; see arXiv:hep-ph/0703165v1.

## Precise half-life measurements for the superallowed $\beta^+$ emitters $^{34}\text{Ar}$ and $^{34}\text{Cl}$

V. E. Iacob, J. C. Hardy, J. F. Brinkley, C. A. Gagliardi, V. E. Mayes, N. Nica, M. Sanchez-Vega,  
G. Tabacaru, L. Trache and R. E. Tribble

As part of our program to test the Standard Model *via* the unitarity of the Cabibbo-Kobayashi-Maskawa (CKM) matrix [1] we have measured the half-lives of  $^{34}\text{Ar}$  and  $^{34}\text{Cl}$  with the principal aim of extracting a precise  $ft$  value ( $\pm 0.1\%$  or better) for the superallowed  $0^+ \rightarrow 0^+$   $\beta$  branch of  $^{34}\text{Ar}$ . The  $ft$  value is determined from three experimental quantities: the half-life, branching ratio and  $Q_{\text{EC}}$  value. For the experimental results to contribute significantly to the CKM unitarity test, the required precision for each quantity must be better than 0.1%, making the experiment very demanding.

Before the measurement reported here, the half-life of  $^{34}\text{Ar}$  was only known to 0.4% and its branching ratio to 0.3% [2]. Our new branching-ratio measurement, which has a precision of 0.08%, is described elsewhere in this report [3]. The half-life measurement described here has a precision of 0.05%. It has already been published [4].

The  $^{34}\text{Ar}$  radioactive beam was produced from the  $^{35}\text{Cl}(p,2n)$  reaction with the primary beam at 30A MeV impinging on a liquid-nitrogen cooled gas target at 1.6 atm. A  $^{34}\text{Ar}$  beam at 26A MeV was separated by the Momentum Achromat Recoil Spectrometer (MARS). The beam exited the vacuum chamber through a thin Kapton window and then passed through a 0.3-mm-thick plastic scintillator and a series of Al degraders, which were adjusted to ensure the implantation of the  $^{34}\text{Ar}$  nuclei at the center of a 76- $\mu\text{m}$ -thick aluminized Mylar tape, part of our fast tape transport system. With an  $^{34}\text{Ar}$  beam intensity of about  $3 \times 10^4$  particles/s, we collected a radioactive sample ( $>99.8\%$  pure) for either 0.7 or 1 s, then turned off the beam and transported the activity in 180 ms to the center of our  $4\pi$  proportional gas counter. Signals from the counter were multiscaled for a period of 12 s. These cycles were repeated until the desired statistics were achieved.

We collected a total of about 400 million decay events in two separate experiments. The first one included about 180 million events from 20,800 tape cycles, which were split into 40 separate runs. In the second experiment another 220 million events were collected in 14,700 cycles split into 24 separate runs. For both experiments, each run was characterized by different settings of the adjustable detection parameters: dead-times, detector biases and discrimination thresholds. The main difference between the two experiments was the purity of the beam in the focal plane of MARS: the only significant impurity,  $^{33}\text{Cl}$  ( $t_{1/2} = 2.51$  s) -- as identified by a position-sensitive detector at the MARS focal plane -- was at a level of 0.3% relative to  $^{34}\text{Ar}$  in the first experiment, but increased to 0.7% in the second. A series of runs with longer collection times determined how much of this  $^{33}\text{Cl}$  impurity actually survived the range-purification of the degrader. From these runs, we determined that we had 0.1%  $^{33}\text{Cl}$  in the collected samples in the first experiment and 0.2% in the second. This was incorporated into our analysis.

We processed the data run-by-run by summing the dead-time-corrected spectra from all the cycles included in each run. The total time-decay spectrum obtained from the combined experiments is presented in Fig. 1, where we also show the separate contributions from the  $^{34}\text{Ar}$  parent and  $^{34}\text{Cl}$  daughter. This breakdown into components comes from a calculation based upon our final analysis and is presented

here simply to illustrate the problems we faced in analyzing the data. Clearly the decay of  $^{34}\text{Ar}$  is almost completely masked by the growth of its daughter. The experimental decay curve only differs very slightly from a single exponential with the daughter's half-life. We can easily understand this situation by examining the coupled decay equations for combined parent-daughter decays. The combined  $^{34}\text{Ar}$  and  $^{34}\text{Cl}$  activity is given by

$$\Lambda_{tot} = C_1 e^{-\lambda_1 t} + C_2 e^{-\lambda_2 t}, \quad (1)$$

where

$$C_1 = N_1 \lambda_1 \frac{2\lambda_2 - \lambda_1}{\lambda_2 - \lambda_1}$$

$$C_2 = \left( N_2 - \frac{N_1 \lambda_1}{\lambda_2 - \lambda_1} \right) \lambda_2, \quad (2)$$

where  $t$  is the time elapsed after the end of the collect period,  $N_{1,2}$  are the numbers of  $^{34}\text{Ar}$  and  $^{34}\text{Cl}$  nuclei present in the source at  $t = 0$ , and  $\lambda_{1,2}$  are the corresponding decay constants. Note that when  $\lambda_1 = 2\lambda_2$  the coefficient  $C_1$  vanishes, leaving a single exponential term having the decay constant of  $^{34}\text{Cl}$ . Although not related exactly by a factor of 2, the actual half-lives of  $^{34}\text{Ar}$  and  $^{34}\text{Cl}$  are close enough that, for our measurements, the coefficient  $C_1$  was more than six times smaller than the coefficient  $C_2$ , and was negative. This is a serious limitation for any conventional two-component fit of the data.

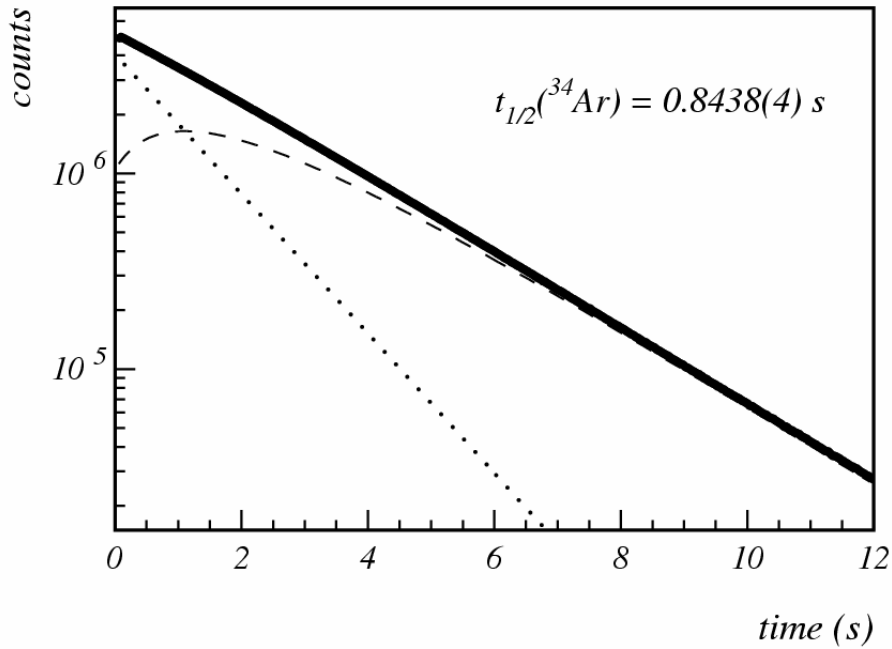


**Figure 1.** Total time-decay spectrum obtained for the  $\beta^+$  decay of  $^{34}\text{Ar}$  and its daughter  $^{34}\text{Cl}$ . The dotted/dashed lines represent the calculated  $^{34}\text{Ar}/^{34}\text{Cl}$  contributions.

Instead, we recognized that the near cancellation of the  $C_I$  coefficient could actually be turned to our advantage: instead of solving for the two components independently, we could focus on the difference between the experimental data and a one-component decay, and use that difference to determine the amount by which the ratio of the two half-lives deviates from 2. However, for this type of analysis to be effective, we needed an independent determination of the value of  $N_2/N_1$  from our experiment. If the  $^{34}\text{Ar}$ -sample collection rate had been constant, this ratio could have been determined from a simple calculation of the production of  $^{34}\text{Cl}$  (via  $^{34}\text{Ar}$  decay) over the collection period.

Unfortunately, although the collection rate was very nearly constant over most of the collection period, it was evident from the measured rate in the scintillator at the exit of MARS, which detected the separated  $^{34}\text{Ar}$  ions as a function of time, that there were noticeable variations at the beginning of the collection period. With the collection profile actually measured, however, we could perform numerical integrations over the measured  $^{34}\text{Ar}$  accumulation and the calculated decay-production of  $^{34}\text{Cl}$  during the collection period in order to obtain the  $N_2/N_1$  ratio for each cycle.

Naturally the half-life used for  $^{34}\text{Cl}$ , also influenced the result we extracted for  $^{34}\text{Ar}$  from fitting the data. We therefore dedicated another independent experiment to measuring its half-life. We produced it directly with a 25A-MeV  $^{35}\text{Cl}$  beam initiating the  $^{35}\text{Cl}(p,pn)$  reaction; no significant impurities were observed and otherwise conditions were similar to the  $^{34}\text{Ar}$  measurement. Our result,  $t_{1/2}(^{34}\text{Cl}) = 1.5268(5)$  is consistent with the most precise previous results cited in a recent survey of world data [5], but its precision is more than a factor of two better than any of them.

In our analysis of the experimental data collected in both the  $^{34}\text{Cl}$  and  $^{34}\text{Ar}$  experiments, we tested for the stability of the fitted half-lives as a function of various detection settings: the results showed no systematic dependence on detector bias, discriminator threshold or circuit dead time. Our final result for  $^{34}\text{Ar}$  thus represents a self-consistent analysis of more than 400 million combined  $^{34}\text{Ar}$  and  $^{34}\text{Cl}$  decay events. We determine the final half-life to be  $t_{1/2}(^{34}\text{Ar}) = 843.8(4)$  ms, a result that is consistent with, but significantly more precise than, the only comparable previous result for the  $^{34}\text{Ar}$  half-life, 844.5(34) ms [2].

- [1] J. C. Hardy *et al.*, *Progress in Research*, Cyclotron Institute, Texas A&M University (2006-2007), p. I-42.
- [2] J.C. Hardy *et al.*, *Nucl. Phys.* **A223**, 157 (1974).
- [3] V.E. Iacob *et al.*, *Progress in Research*, Cyclotron Institute, Texas A&M University (2006-2007), p. I-51.
- [4] V.E. Iacob *et al.*, *Phys. Rev. C* **74**, 045810 (2006).
- [5] J. C. Hardy and I. S. Towner, *Phys. Rev. C* **71**, 055501 (2005); *Phys. Rev. Lett.* **94**, 092502 (2005).

## Folding model analysis for 240MeV ${}^6\text{Li}$ elastic scattering on ${}^{28}\text{Si}$ and ${}^{24}\text{Mg}$

X. Chen, Y. -W. Lui, H. L. Clark, Y. Tokimoto, and D. H. Youngblood

In order to study giant resonance induced by  ${}^6\text{Li}$  scattering, optical model (OM) analysis of  ${}^6\text{Li}$  elastic scattering is necessary to get the optical parameters. OM has been widely used to analyze the heavy ion scattering data in term of empirical Woods-Saxon (W-S) parameterizations of the nuclear potential. However, it was found that a satisfactory microscopic understanding of heavy ion scattering can be obtained if one relates the optical potential to a fundamental nucleon-nucleon (NN) interaction through the double folding (DF) approach by folding this interaction with the nuclear matter distributions of both the target and projectile nuclei [1]. Since  ${}^6\text{Li}$  is a loosely bound nucleus, breakup has a large contribution to the real part of the nuclear potential and is responsible for the substantial renormalization factor  $N_R$  for the real folded potential [2].  ${}^6\text{Li}$  elastic scattering itself is very interesting.  ${}^6\text{Li}$  is in the mass number range  $A=4-12$ , where the elastic scattering show a transition between characteristics of light ions ( $A\leq 4$ ) and characteristics of heavy ion ( $A\geq 12$ ). Such data could provide a stronger test of the validity of any model for heavy ion potentials [3,4].

A beam of 240MeV  ${}^6\text{Li}$  ions from the Texas A&M University K500 superconducting cyclotron bombarded self-supporting  ${}^{28}\text{Si}$  and  ${}^{24}\text{Mg}$  target foil in the target chamber of the multipole-dipole-multipole spectrometer. Elastic scattering and inelastic scattering to the low-lying states were measured from  $5^\circ$ - $35^\circ$ . The calibration procedures were described in details in Refs. [5,6]. The experimental cross sections were obtained from the charge collected, target thickness, dead time and known solid angle. The cumulative uncertainties in target thickness, solid angle, etc., result in about a  $\pm 10\%$  uncertainty in absolute cross section.

Two different  $NN$  effective interactions (M3Y[7] and JLM[8]) were used to get the folded potential. Folding calculation **I** (FCI) used density dependent M3Y  $NN$  interaction and was described in detail by D.T. Khoa [9], while folding calculation **II** (FCII) with JLM effective interaction was described and discussed by F. Carstoiu *et al.* [10], L. Trache [11] and the references in these two papers. Two different density forms, Fermi distribution and Hartree Fork (HF) density [12], were used for target ground density during the folding procedures and are listed in Table I. The cluster-orbital shell-model

**Table I.** Density parameters for different density choices. Den1 and Den2 are Fermi distributions.  $R_p$ ,  $R_n$ ,  $R_m$ ,  $R_{ch}$  means the root mean square radii of the calculated proton, neutron, mass and charge distributions respectively.

target	Density choice	$\rho_0$	c	a	$R_p$	$R_n$	$R_m$	$R_{ch}$
${}^{24}\text{Mg}$	Den1 <sup>18</sup> <sub>1</sub>	0.17	2.995	0.478	2.922	2.922	2.922	3.040
	Den2 <sup>19</sup> <sub>1</sub>	0.166	2.979	0.523	3.017	3.017	3.017	3.040
	HF	-----	-----	-----	2.928	2.906	2.917	3.000
${}^{28}\text{Si}$	Den1 <sup>18</sup> <sub>1</sub>	0.175	3.15	0.475	3.010	3.010	3.010	3.875
	Den2 <sup>19</sup>	0.167	3.155	0.523	3.123	3.123	3.123	3.154

	I								
	HF	-----	-----	-----	3.059	3.031	3.045	3.132	

**Table II.** Optical model parameters obtained from fits of elastic scatterings with folding calculation I.  $N_r$  is renormalization factor for real potential.  $S_r$  is scaling factor for real potential radius.  $W, r_{i0}, a_i$  are W-S parameters for imaginary potentials.  $J_v$  and  $J_w$  are the volume integral per nucleon pair for real and imaginary potentials respectively.  $\sigma_r$  is total reaction cross section.

Target	N-N int	Target densit y	$N_r$	$S_r$	W	$r_{i0}$	$a_i$	$J_v$	$J_w$	$\sigma_r$	$\chi^2$
$^{24}\text{Mg}$	CDM3Y 6	Den1	0.824	1.062	58.7	0.731	1.204	242	154	179 9	1.038
	CDM3Y 5	Den1	0.823	1.062	58.67	0.731	1.204	242	154	179 9	1.039
	CDM3Y 4	Den1	0.822	1.062	58.73	0.731 1	1.204	242	154	179 9	1.039
	CDM3Y 5	HF	0.766	1.055	59.14	0.728	1.208	240	155	180 3	1.042
	CDM3Y 5	Den2	0.846	1.079	57.92	0.737	1.198	242	154	179 3	1.032
$^{28}\text{Si}$	CDM3Y 5	Den1	0.887	1.062 4	41.33	0.904 9	1.048	256	136	175 7	1.461
	CDM3Y 5	Den2	0.924	1.083	41.38	0.904 9	1.046	258	136	175 5	1.439
	CDM3Y 5	HF	0.933	1.059	41.85	0.901 1	1.051	257	137	176 1	1.485

approximation [13] form was used for  ${}^6\text{Li}$  ground dens

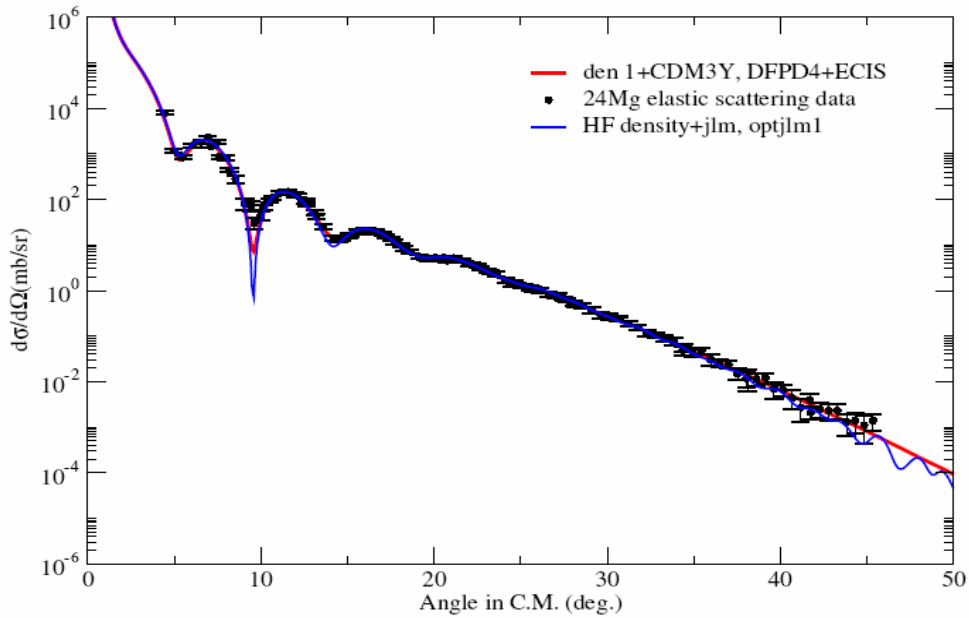


**Figure 1.** Angular distribution for  ${}^6\text{Li}+{}^{24}\text{Mg}$  elastic scattering cross section. The red line shows the calculation using real folded potential with CDM3Y5 NN interaction and a W-S imaginary term. The blue line shows the calculation using both real and imaginary potential folded with JLM interaction.

ity with FCI. FCI was carried out with code DFPD4 [14] and elastic scattering data were fitted with code ECIS[15]. The optical parameters obtained are listed in Table II. FCI and the elastic scattering fit were carried out with code OPTJLM1[16]. HF densities were used for both target and projectile. The optical parameters are listed in Table III. The angular distributions of the calculated cross-section are plotted along with data in Fig.1 for  ${}^{24}\text{Mg}$  and

**Table III.** Optical potential parameters obtained from the fit of elastic scatterings with folding calculation **II**.  $N_r$  and  $N_w$  are the normalization factor for real and imaginary potential respectively.  $t_r$  and  $t_w$  are range parameters for real and imaginary potential respectively.

Target	N-N int.	target densit y	$N_r$	$t_r$	$N_w$	$t_w$	$J_v$	$J_w$	$\sigma_r$	$\chi^2$
$^{24}\text{Mg}$	JLM	HF	0.519	0.955 9	0.862	2.586	237	144	180 3	1.6
$^{28}\text{Si}$	JLM	HF	0.546	0.916 5	0.825	2.427 5	248	137	173 4	1.94

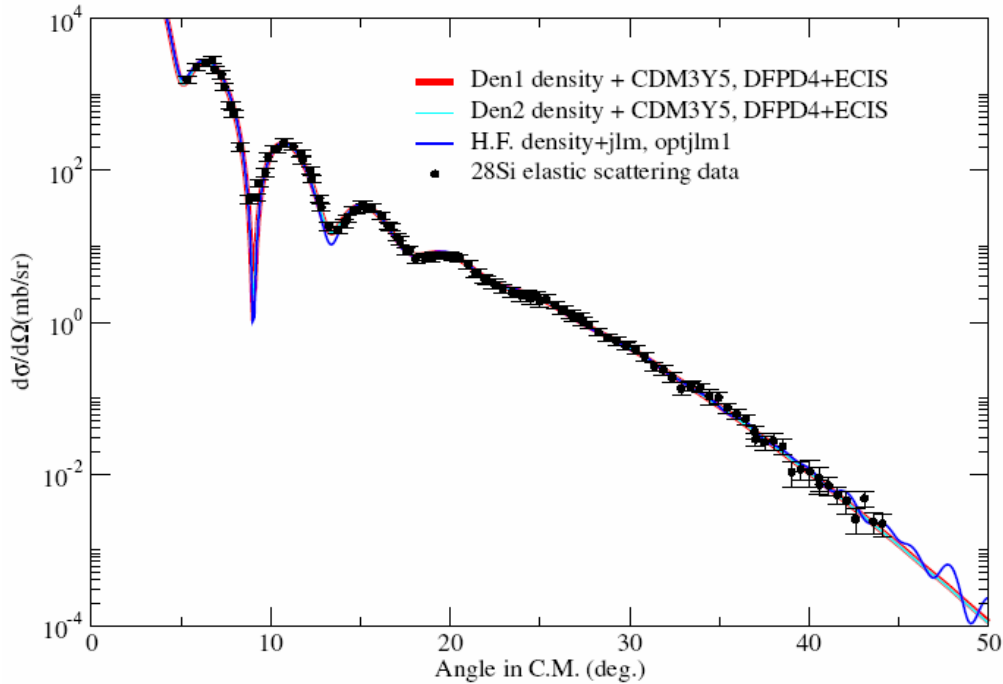


**Figure 2.** Angular distribution for  $^6\text{Li}+^{28}\text{Si}$  elastic scattering cross section. Both red and cyan lines show the calculation using real folded potential with CDM3Y5 N-N interaction and a W-S imaginary term. Den1 density is used for red line and Den2 density is used for cyan line. The blue line shows the calculation using both real and imaginary potential folded with JLM interaction.

Fig.2 for  $^{28}\text{Si}$ . Both **FCI** and **FCII** give almost the same quality fits for each nucleus. The **FCII** fit has large oscillations at large angles than the **FCI** fit.

A scaling factor on radius of the real optical potential is necessary to fit the elastic scattering for both  $^{24}\text{Mg}$  and  $^{28}\text{Si}$  when **FCI** is used. Different densities choices (as shown in Table I) will slightly change the value of the scaling factor (as shown in Table II.), but it can not eliminate the factor. Different types of density dependent M3Y interactions such as CDM3Y4, CDM3Y5, CDM3Y6 [17] give almost the same scaling factors for  $^{24}\text{Mg}$  elastic scattering. One possible reason for this factor could be the density used in the density dependent function. The density is defined as the sum of the densities of target and projectile, which may over-estimate the nuclear matter density at certain point.

DWBA calculations for  ${}^6\text{Li}$  inelastic scattering to the low-lying  $2^+$  state of  ${}^{24}\text{Mg}$  and to low-lying  $2^+$  and  $3^-$  states of  ${}^{28}\text{Si}$  were carried out with the optical parameter sets obtained by folding model I. CDM3Y5 density dependent NN interaction was used here and the Den1 form (as shown in Table I) was chosen as target density for both  ${}^{24}\text{Mg}$  and  ${}^{28}\text{Si}$ . The transition potentials were calculated with DFPD4 and the cross sections were calculated with ECIS. Deformation parameters for  $2^+$  and  $3^-$  states were obtained from electromagnetic B(EL) values by assuming the mass deformation length and coulomb deformation length are the same. The calculated angular distribution for the  $2^+$  state in  ${}^{24}\text{Mg}$  is plotted in Figure 3 along with the data. The calculated angular distributions for  $2^+$  and  $3^-$  states of  ${}^{28}\text{Si}$  are plotted in Figure 4 and Figure 5 along with data. All the calculations of  $2^+$  states agree well with the data. However, the DWBA calculation for the  $3^-$  state of  ${}^{28}\text{Si}$  does not agree well with the data as the calculated cross sections are slightly higher than the data.

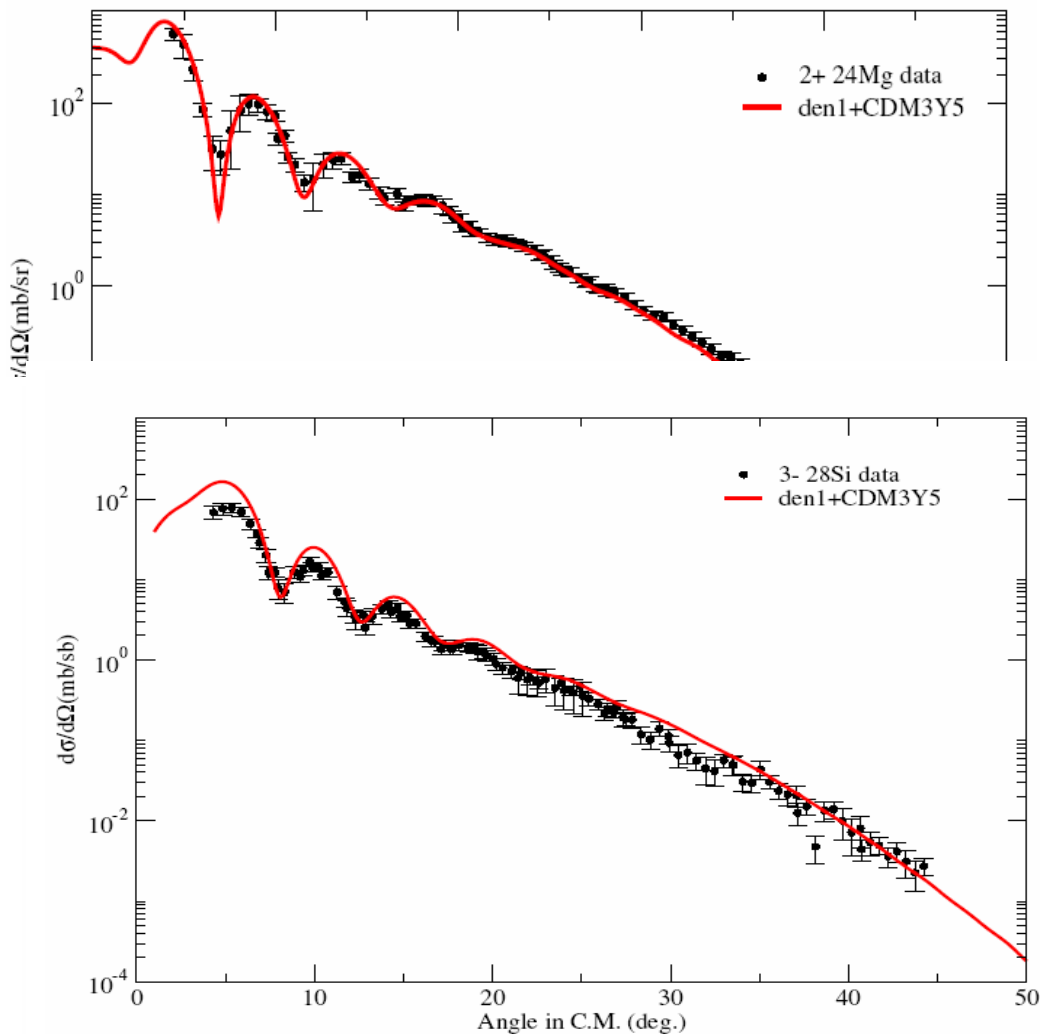


Figure 5. The line shows the calculated differential cross section using CDM3Y5 NN interaction for inelastic scattering to the 6.879MeV  $3^-$  state in  ${}^{28}\text{Si}$  plotted versus average center-of-mass angle along with the data points. Τη ηλεκτρομαγνητιχ B(E3) [21] παλυε ωασ υσεδ ηερε ανδ τη χορρεσπονδιγ

We thank Dr. Livius Trache and Dr. Florin Carstoiu for their help in JLM folding calculation. We thank Dr. D.T.Khoa and Mr. Hoang Sy Than for their help and offer of the computer codes to do the CDM3Yn folding calculation and cross-section calculation.

- [1] G. R. Satchler and W. G. Love, Phys. Rep. **55**, 183(1979).
- [2] Y. Sakuragi, Phys. Rev. C **35** 2161 (1987); Y. Sakuragi, M. Yahiro, M. Kmimura, Prog. Theor. Phys. Suppl. **89** (1986) 136; Y. Sakuragi, M. I. Hirabayashi, M. Kamimura, Prog. Theor. Phys. **98** 521(1997).
- [3] R.M. DeVries, *et al.*, Phys. Rev. Lett. **39** 450 (1977).
- [4] M. El-Azab Farid, M.A. Hassanain, Nucl. Phys. **A678**, 39 (2000).
- [5] D. H. Youngblood, Y. -W.Lui, H. L. Clark, P. Oliver, and G. Simler, Nucl. Instrum. Methods Phys. Res. **A361**, 539 (1995).
- [6] H. L. Clark, Y. -W.Lui, and D. H. Youngblood, Nucl. Phys. **A589**, 416 (1995).
- [7] G. Bertsch, J. Borysowicz, H. McManus and W. G. Love, Nucl. Phys. **A284**, 399 (1977).
- [8] J. P. Jeukenne, A. Lejeune, and C. Mahaux, Phys. Rev. C **16**, 80(1977).
- [9] Dao T. Khoa and G. R. Satchler, Nucl. Phys. **A668**, 3 (2000).
- [10] F. Carstoiu, L. Trache, R. E. Tribble and C. A. Gagliardi, Phys. Rev. C **70**, 054610 (2004).
- [11] L. Trache, *et al.*, Phys. Rev. C **61**, 024612 (2000).
- [12] M. Beiner and R. J. Lombard, Ann. Phys. **86**, 262 (1974); F. Carstoiu and R. J. Lombard, *ibid.* **217**, 279 (1992).
- [13] A. Korshenninnikov, *et al.*, Nucl. Phys. **A617**, 45 (1997).
- [14] D.T. Khoa, unpublished.
- [15] Jacques Raynal, Computing as a Language of Physics, ICTP International Seminar Course, Trieste, Italy, Aug. 2-10, 1971 (IAEA,1972), p281; M.A. Melkanoff, T. Sawada and J. Raynal, Methods in Computational Physics. **6**: Nuclear Physics (Academy Press, New York, 1966) p1.
- [16] F. Carstoiu, unpublished.
- [17] D. T. Khoa, G. R. Satchler and W. von Oertzen, Phys. Rev. C **56**,954 (1997).
- [18] M. Pignanelli *et al.*, Phys. Rev. C **33** 40(1986).
- [19] G. Fricke *et al.*, Atomic Data and Nuclear Data Tables **60**, 177 (1995).
- [20] S. RAMAN, C. W. NESTOR, JR., and P. TIKKANEN, At. Data Nucl. Data Tables **78**, 1 (2001).
- [21] T. KIBEDI and R. H. SPEAR, At. Data Nucl. Data Tables **80**, 35 (2002).

## Precise $\beta$ branching ratios in $^{34}\text{Ar}$ from $\beta$ - $\gamma$ coincidences

V. E. Iacob, J. C. Hardy, and V. Golovko

As part of our program to test the Standard Model *via* the unitarity of the Cabibbo-Kobayashi-Maskawa (CKM) matrix [1] we have measured the  $\beta$ -branching ratios in the decay of  $^{34}\text{Ar}$  with the aim of extracting a precise  $ft$  value (0.1% or better) for the superallowed  $0^+ \rightarrow 0^+$   $\beta$  branch. The  $ft$  value is determined from three experimental quantities: the half-life, branching ratio and  $Q_{\text{EC}}$  value. For the experimental results to contribute significantly to the CKM unitarity test, the required precision for each quantity must be better than 0.1%, making the experiment very demanding.

In the case of  $^{34}\text{Ar}$ , precise measurements now exist for the  $Q_{\text{EC}}$  value [2] and half-life [3], which lead to contributions to the  $ft$ -value uncertainty of 0.04% and 0.05% respectively. However, the branching ratio for the superallowed transition is only known to 0.26% based on a measurement published more than 30 years ago [4]. Thus, a more precise measurement of the branching ratio would add this nucleus to the list of superallowed  $\beta$  emitters whose corrected  $\mathcal{F}t$  values contribute to tests of CVC and CKM unitarity [5]. More important still is that the calculated correction for isospin symmetry breaking [6] in the  $^{34}\text{Ar}$  decay is larger than the comparable correction for any other well known transition with  $A < 40$ , where the nuclear models used in the calculation are expected to be the most reliable. Conformity of the corrected  $\mathcal{F}t$  value for  $^{34}\text{Ar}$  with the average result from the other cases [5] would provide strong confirmation of the validity of the correction calculations.

The  $^{34}\text{Ar}$  radioactive beam was produced from the  $^{35}\text{Cl}(p,2n)$  reaction with the primary beam at 30A MeV impinging on a liquid-nitrogen-cooled gas target at 1.6 atm. An  $^{34}\text{Ar}$  beam at 26A MeV was separated by the Momentum Achromat Recoil Spectrometer (MARS) [7]. The beam exited the vacuum chamber through a thin Kapton window and then passed through a 0.3-mm-thick plastic scintillator and a series of Al degraders, which were adjusted to ensure the implantation of the  $^{34}\text{Ar}$  nuclei at the center of a 76- $\mu\text{m}$ -thick aluminized Mylar tape, part of our fast tape transport system. With an  $^{34}\text{Ar}$  beam intensity of about  $3 \times 10^4$  particles/s, we collected a radioactive sample ( $> 99.7\%$  pure) for 2 s, then turned off the beam and transported the activity in 180 ms to a well-shielded counting location 90 cm away from the beam line. At the counting location the collected sample stopped between a 70% HPGe detector for  $\gamma$  rays and a 1-mm-thick plastic scintillator for  $\beta$ 's, the former being 151 mm away on one side of the source and the latter 5 mm away on the opposite side. We then recorded  $\beta$  singles and  $\beta$ - $\gamma$  coincidences for a 2-s period before repeating the collect-move-count cycle. These cycles were repeated until the desired statistics were achieved.

The total  $\gamma$ -ray spectrum we obtained for the decay of  $^{34}\text{Ar}$  is presented in Figure 1. Even though only about 5% of the  $^{34}\text{Ar}$  decays populate excited states in  $^{34}\text{Cl}$ , the relatively weak  $\gamma$ -rays from the de-excitation of these states appear as prominent peaks in this spectrum. The only notable peak not related to the  $^{34}\text{Ar}$  decay is the 1779 keV peak, which was generated by neutron activation of the Al structural materials surrounding the detectors.

From our data, we could obtain the  $\beta$ -branching ratio  $BR_i$  for a particular transition populating state  $i$ , which decays by emitting  $\gamma$  ray,  $\gamma_i$ . If the total number of  $\beta$  singles is  $N_\beta$  and the total number of  $\beta$ - $\gamma$  coincidences measured in the  $\gamma_i$  peak is  $N_{\beta\gamma_i}$ , then the branching ratio  $BR_i$  is given by

$$BR_i = \frac{N_{\beta\gamma_i}}{N_\beta \epsilon_{\gamma_i}} k, \quad (1)$$

where  $\epsilon_{\gamma_i}$  is the detector efficiency for  $\gamma$  ray,  $\gamma_i$ , and  $k$  is a small correction factor (*i.e.*  $k \sim 1$ ) that, among other things, takes into account the differences in the  $\beta$ -detector efficiency for the different transitions participating in  $^{34}\text{Ar}$  decay. This relation highlights the importance of a precise absolute efficiency calibration for the  $\gamma$ -ray detector and a reasonable knowledge of relative efficiencies in the beta detector. Our HPGe absolute efficiency is accurately known (to  $\pm 0.2\%$  for 50-1400 keV and  $\pm 0.4\%$  up to 3500keV) from source measurements and Monte Carlo calculations [8]. The relative efficiency as a function of  $\beta$  energy in the plastic scintillator was determined by Monte Carlo calculations using the DOSRZNR code from the EGS package [9] and checked by comparison with conversion-electron sources and with  $^{22}\text{Mg}$   $\beta$ -decay data [10].

The components of the correction factor  $k$  have been described in detail in Ref. [11]. In the present measurement, they are:

- differences in the total  $\beta$ -detection efficiency induced by the low-energy threshold set in the plastic-scintillator electronics; since the threshold is fixed, a different (small) fraction of the  $\beta$ 's will be lost for transitions with different  $\beta$  end-point energies. This contributes 0.2% to  $k$ ;
- dead time corrections in the  $\beta$  singles and  $\beta$ - $\gamma$  coincidence channels, which give a combined effect of 0.5%;
- real coincidence summing of the positron-annihilation radiation with the observed  $\gamma$  rays, which accounts for 0.1%; and
- random coincidence summing, a 0.3% effect.

Including all these small corrections we determine the sum of all branching ratios for transitions populating excited states in  $^{34}\text{Cl}$  to be:

$$\sum BR^* = 5.64(8)\% \quad (2)$$

These branches are all Gamow-Teller in character, and it is the ground-state transition that is the superallowed one. Subtracting the sum of excited-state transitions from 100%, we obtain the superallowed branching ratio to be:

$$BR_{GS} = 94.36(8)\% \quad (3)$$

Although the uncertainty quoted in Eq. (2) on the measured sum of branching ratios is  $\pm 1.4\%$ , because of the subtraction from 100%, the superallowed branch uncertainty in Eq. (3) is  $\pm 0.08\%$ . The former was principally determined by counting statistics on these relatively weak transitions. In detail, the error budget comprises:

- the peak-areas counting statistics ( $\pm 1.3\%$ );

- the uncertainty in  $\varepsilon_\gamma$  ( $\pm 0.7\%$ ), which is dominated here by the uncertainty in the position of the tape along the detector axis ( $\pm 0.5\text{mm}$ ); and
- the uncertainty in the relative efficiency of the beta detector ( $\pm 0.3\%$ ).

Using the branching ratio in Eq. (3) for the superallowed branch together with the known half life [3] and  $Q_{\text{EC}}$  value [2], we find a corrected  $\bar{t}_\beta$  value of 3072.3(32) s. This is in good agreement with the current world average,  $\bar{t}_\beta = 3073.9(8)$  s [5]. However, our result should still be considered as preliminary, since we want to confirm the techniques employed here with a similar measurement of the  $\beta$ -decay of  $^{10}\text{C}$ , where the population of the 718-keV excited state in  $^{10}\text{B}$  must yield a branching ratio of exactly 100%. Currently we are processing the data from a  $^{10}\text{C}$  measurement and, if the results agree with expectations and confirm our approach, we will publish the  $^{34}\text{Ar}$  branching ratio very shortly.

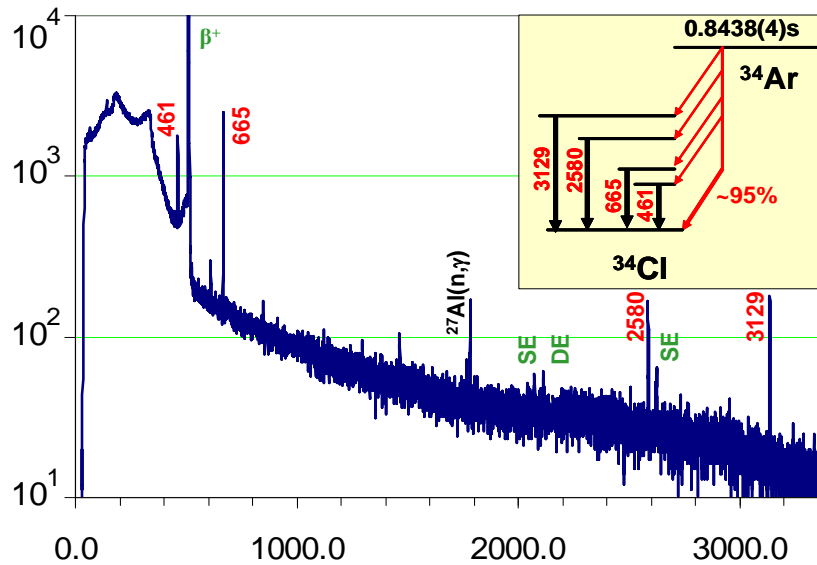


**Figure 1.** Spectrum of  $\beta$ -delayed  $\gamma$ -rays observed in coincidence with positrons following the decay of  $^{34}\text{Ar}$ . The decay scheme is shown in the inset.

- [1] J. C. Hardy *et al.*, *Progress in Research*, Cyclotron Institute, Texas A&M University (2006-2007), p. I-42.
- [2] F. Herfurth *et al.*, *Eur. Phys. J. A* **15**, 17 (2002).
- [3] V. E. Jacob *et al.*, *Phys. Rev. C* **74**, 055502 (2006).
- [4] J. C. Hardy *et al.*, *Nucl. Phys.* **A223**, 157 (1974).
- [5] J. C. Hardy and I. S. Towner, *Phys. Rev. C* **71**, 055501 (2005); *Phys. Rev. Lett.* **94**, 092502 (2005).

- [6] I. S. Towner and J. C. Hardy, Phys. Rev. C **66**, 035501 (2002).
- [7] R. E. Tribble *et al.*, Nucl. Phys. **A701**, 278 (2002).
- [8] J.C. Hardy *et al.*, Applied Radiation and Isotopes **56**, 65 (2002); R.G. Helmer *et al.*, Nucl. Instrum. Methods Phys. Res. **A511**, 360 (2003) and Appl. Radiat. Isot. **60**, 173 (2004).
- [9] NRCC Report PIRS-701 and [www.irs.inms.nrc.ca/inms/irs/EGSsrc/EGSsrc](http://www.irs.inms.nrc.ca/inms/irs/EGSsrc/EGSsrc)
- [10] V. E. Jacob *et al.*, 2004 Fall Meeting of the APS DNP, Oct 28 – 30, Chicago IL.
- [11] V. E. Jacob *et al.*, Phys. Rev. C **74**, 015501 (2006).

## The half life of $^{10}\text{C}$

V. E. Iacob, J. C. Hardy, V. Golovko, J. Goodwin, N. Nica, H. I. Park,  
L. Trache and R. E. Tribble

Although the uncertainty in the  $\lambda t$  value for the  $0^+ \rightarrow 0^+$  superallowed transition from  $^{10}\text{C}$  is dominated by the uncertainty in its branching ratio, the half-life uncertainty actually does contribute significantly and has, in fact, a larger percent uncertainty than the half-life of any other “well-known” superallowed emitter [1]. The two previous measurements [2,3] are consistent with one another and average to 19.290(12) s, a precision that, with our current techniques, we should be able to improve by at least a factor of two.

In our first attempt to improve the half-life of  $^{10}\text{C}$  [4], we reported a value that was only marginally more precise than the accepted value. At that time, the precision of our result was limited to only  $\sim 0.1\%$  by a relatively high background/noise rate in our proportional gas counter and insufficient control over impurities in the collected sample. These problems prompted us to make a second measurement, in which we focused on three main objectives: (i) increasing the statistics, (ii) improving our control over the impurities and (iii) lowering the background/noise rate.

Our experimental setup was similar to the one used in Ref. [4]: the 18.5A MeV radioactive beam was produced in a  $^1\text{H}(^{11}\text{B},2\text{n})^{10}\text{C}$  reaction, then separated by our spectrograph MARS and ultimately extracted in air and implanted into a 76- $\mu\text{m}$ -thick aluminized mylar tape. The  $^{10}\text{C}$  nuclei were collected in the tape for 10 s, then the beam was turned off and the activity was moved rapidly to the center of a  $4\pi$  proportional gas counter. The gas counter was shielded against neutrons and gammas to reduce the background rate to a minimum. Once the activity arrived at the center of the gas counter, the emitted

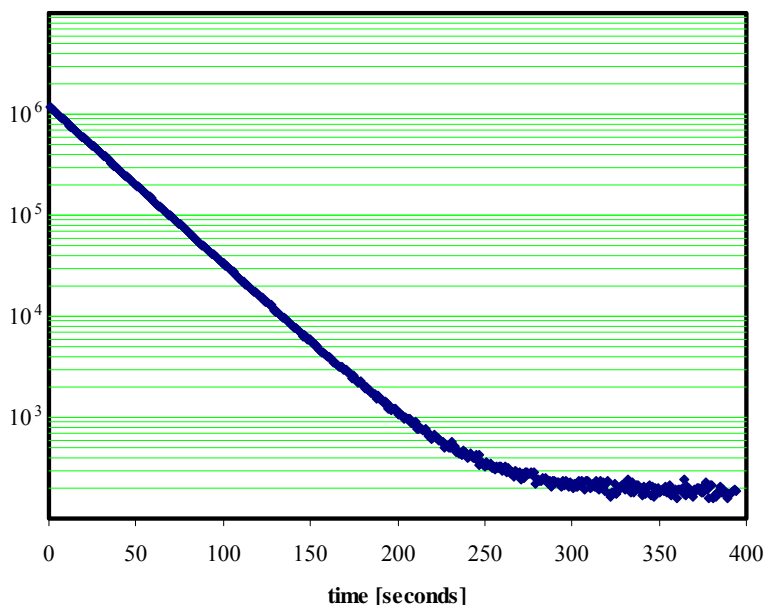


**Figure 1.** Total decay spectrum of  $^{10}\text{C}$

positrons were detected with >95% efficiency and their signals multiscaled for 400 s. Such collect-move-detect cycles were repeated until the desired statistics were achieved ( $8.5 \times 10^7$  decays). The total decay spectrum obtained in this experiment is presented in Fig. 1.

As with our previous experiment, we divided the total measurement into a number of separate runs, each with different critical settings in the acquisition chain: discriminator threshold, dead-time and detector bias. No evidence of a systematic bias was observed in the analysis of these runs, as evidenced by Fig. 2.

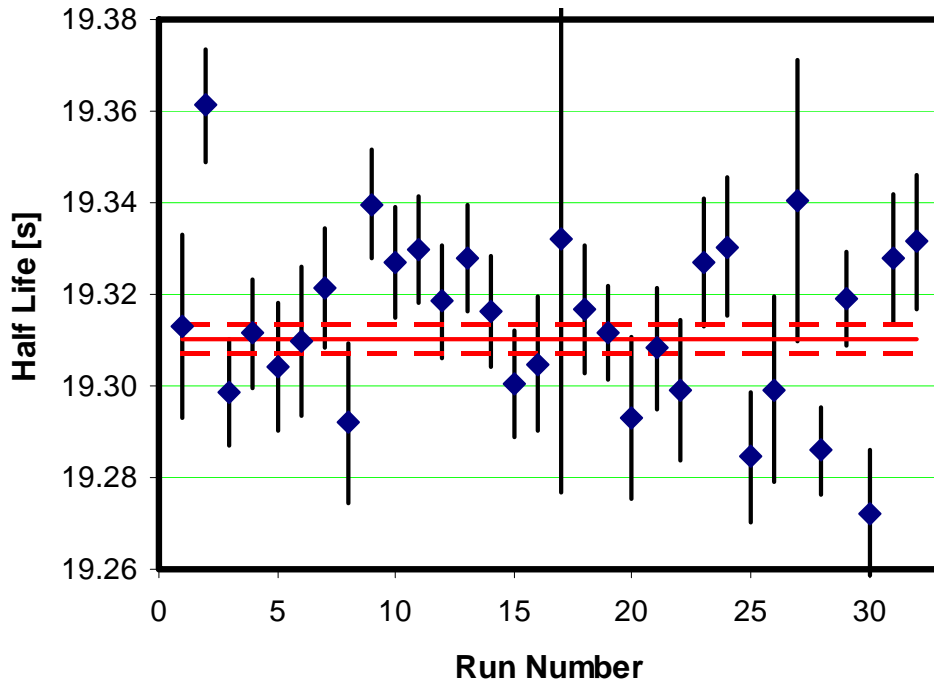


**Figure 2.** Scatter of the  $^{10}\text{C}$  half-life as extracted in the different runs, each having different detection settings: discriminator threshold, detector bias and major dead-time.

In order to gain more complete control over the long-lived impurities, we added to the “normal” runs, which had collect-move-detect intervals of 10s-0.180s-400s, two additional runs with collect-move-detect settings of 20s-0.180s-900s and 120s-0.180s-900s. Analyzing these latter runs we found that the main “impurity” was actually the result of neutron activation of the detector’s copper housing during the beam-on intervals. Only the  $^{65}\text{Cu}(n,\gamma)^{66}\text{Cu}$  component, with a half-life of  $t_{1/2} = 5.10$  min, had to be considered in the analysis since the  $^{63}\text{Cu}(n,\gamma)^{64}\text{Cu}$  activation leads to an activity with a half-life of 12.7 hours and thus serves only to increase slightly the constant background. We determined that the activity of  $^{66}\text{Cu}$  produced by activation was 0.078% of the activity of  $^{10}\text{C}$  implanted in the tape.

With provisions incorporated for the copper contaminant, we determined the half-life of  $^{10}\text{C}$  to be 19.312(4) s with a fit quality of  $\chi^2/\text{ndf}=44.9/31$ . When redoing the fit of our 2005 data [4], now including the same amount of  $^{66}\text{Cu}$  as observed in this experiment, we obtained a half-life of 19.313(7) s, in complete agreement with the more recent measurement. However, because there was additional noise

present in the earlier experiment, we have not averaged the two results; instead we keep only the result from the clean data obtained in the new experiment.

To make the result more definitive, we also tested the data for the possible presence of unidentified short-lived impurities and/or inconsistent dead-time corrections. We did this by applying the standard technique of successively removing early-time channels, where both effects would have the most significant contribution, and obtaining the fitted half-life with larger and larger numbers of early channels removed from the fit. The results are presented in Fig. 3, where it can be seen that the half life is statistically independent of the number of channels removed. There is no indication of any inconsistencies.

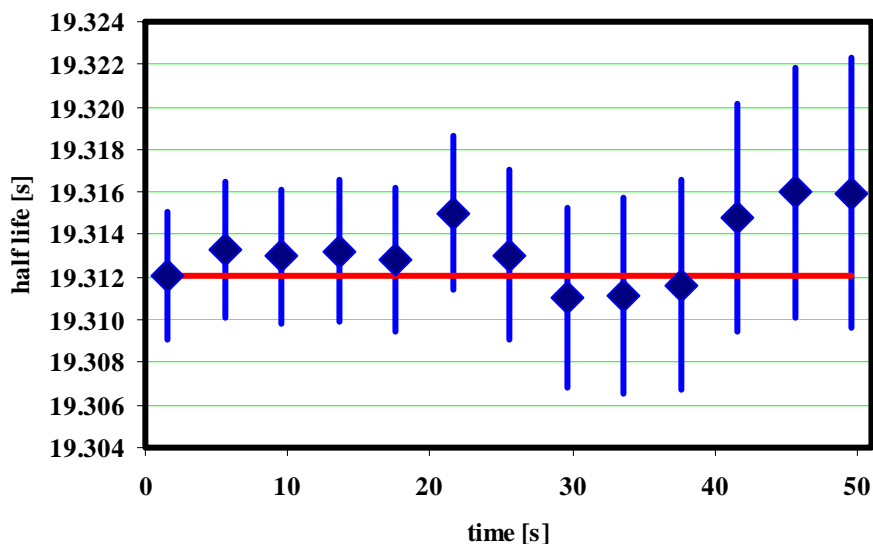


**Figure 3.** Scatter of the  $^{10}\text{C}$  half-life as extracted from subsets defined by gradually removing the early part of the decay spectrum. The abscissa represents the length of time for which data was removed from the first part of the decay spectrum

Our new half-life result,  $t_{1/2}(^{10}\text{C}) = 19.312(4)$  s, is nearly two standard deviations higher than the previously accepted average of  $19.290(12)$  s [1] but it is a factor of three more precise. It should be noted, though, that, of the two previous measurements, the most recent [3],  $19.295(15)$  s, does agree with our result and it is only the earliest one [2],  $19.280(20)$  s, that disagrees significantly. That value was measured more than 30 years ago.

[1] J. C. Hardy and I. S. Towner, *Phys. Rev. C* **71**, 055501 (2005).

[2] G. Azuelos, J. E. Crawford and J. E. Kitching, *Phys. Rev. C* **9**, 1213 (1974).

[3] P. H. Barker and G. D. Leonard, *Phys. Rev. C* **41**, 246 (1990).

[4] V. E. Jacob *et al.*, *Progress in Research*, Cyclotron Institute, Texas A&M University (2005-2006), p. I-28.

## High precision half-life measurement in $^{38}\text{Ca}$

H. I. Park, J. C. Hardy, V. V. Golovko, V. E. Iacob, N. Nica, A. Banu, L. Trache,  
R. E. Tribble, and Y. Zhai

It has been recently argued that the nuclear-structure-dependent corrections can be tested against experiment in the context of the unitarity test of the Cabibbo-Kobayashi-Maskawa (CKM) matrix [1]. The test is based on how well the calculated corrections convert the scatter in the uncorrected  $ft$  values for many transitions into a consistent set of corrected  $\mathcal{F}t$  values for all transitions, as required by CVC. The decay of  $^{38}\text{Ca}$  is a good case to investigate for this purpose since, for the superallowed transitions, the calculated nuclear-structure-dependent correction is larger than that of any of the nine well-known nuclei ( $^{10}\text{C}$ ,  $^{14}\text{O}$ ,  $^{26\text{m}}\text{Al}$ ,  $^{34}\text{Cl}$ ,  $^{38\text{m}}\text{K}$ ,  $^{42}\text{Sc}$ ,  $^{46}\text{V}$ ,  $^{50}\text{Mn}$ ,  $^{54}\text{Co}$ ) [2]. If the measured  $ft$  value with large calculated nuclear-structure-dependent corrections converts into the average  $\mathcal{F}t$  value established from these well-known cases, then it further demonstrates the calculation's reliability for the smaller corrections. For the  $ft$  value to be useful for this purpose, it is necessary to measure the half-life with a high precision of 0.1%.

The half-life of  $^{38}\text{Ca}$  was measured via the  $^1\text{H} (^{39}\text{K}, 2n)$  reaction at a primary beam energy of 30.4 MeV. The MARS spectrometer provided a pure  $^{38}\text{Ca}$  beam from the fully stripped reaction products at the extraction slits in the focal plane. This beam exited the vacuum system through a  $50\mu\text{m}$ -thick Kapton window, passed through a 0.3-mm-thick BC-404 scintillator and a stack of aluminum degraders, and finally stopped in the  $76\mu\text{m}$ -thick aluminized Mylar tape of a fast tape-transport system. We collected the activity of  $^{38}\text{Ca}$  on the tape for 0.5 s. At the end of the collection time, the beam was interrupted and the collected sample was moved in 196 ms to the center of a  $4\pi$  proportional gas counter. Signals from the counter were multiscaled for 15 s, and separate decay spectra were recorded. For the measurement of a highly precise half-life, this “collect-move-count” cycle must be repeated until high statistics are obtained. In a preliminary test run, over 18 million  $\beta$  events were recorded under various detecting conditions, with different settings for dominant dead time, bias voltage of the detector, and threshold of the discriminator. The data analysis is currently underway.

[1] I. S. Towner and J. C. Hardy, Phys. Rev. C **66**, 035501 (2002).

[2] J. C. Hardy, Nucl. Phys. **A752**, 101c (2005).

## TRIUMF E-823: Measurements of the $^{37,38\text{m}}\text{K}$ half-lives

V. E. Jacob and J. C. Hardy

The E-823 experiment was a collaboration between scientists from TRIUMF, Lawrence Berkeley National Laboratory, Simon Fraser University, Argonne National Laboratory, Queen's University and Texas A&M. It was designed to perform measurements of half-lives and branching ratios for superallowed  $0^+ \rightarrow 0^+$   $\beta$  decays in medium-mass ( $A > 60$ ) nuclei produced by the ISAC1 radioactive beam facility at TRIUMF. These data were to be used in testing the Standard Model via the unitarity of the Cabibbo-Kobayashi-Maskawa (CKM) matrix [1].

In its initial phase, more than eight years ago, we were testing the half-life detection equipment (electronics and tape-transport-system) and the fitting programs used to extract the half-lives. The experimental apparatus comprised a  $4\pi$  proportional gas-counter and a tape-transport system similar to the one in use by us at the Cyclotron Institute at Texas A&M. However, because of the low energy of the radioactive beam at TRIUMF, the ions were implanted in the mylar tape in vacuum, an arrangement that required two sets of slits with differential pumping between them for the tape to be withdrawn from the vacuum en route to the detector.

The test cases chosen were the decays of  $^{37,38\text{m}}\text{K}$ , nuclei readily available at the ISAC1 facility in its initial production phase. After our initial analysis of the  $^{38\text{m}}\text{K}$  data [2] we reported results consistent with previous measurements, thus confirming the reliability of our equipment and the data reduction techniques. Since  $^{38\text{m}}\text{K}$  ( $t_{1/2}=0.924$  s) was generated along with  $^{38}\text{K}$  ( $t_{1/2}=7.63$  min), the counting rate stayed at levels above the background for the whole detection cycle. However, in the case of  $^{37}\text{K}$  ( $t_{1/2}=1.235$  s), no other significant components were present in the radioactive beam so the counting rate had returned to background level during the 25-s counting period. Thus, for the  $^{37}\text{K}$  half-life, special care needed to be taken for the channels with few counts in them.

In preparing to publish these results, we have recently revisited the  $^{37}\text{K}$  data. The data-filtering procedure we used in the original analysis [2] included rejection of cycles that showed non-statistical noise anywhere in the spectrum. We have more recently come to realize that this filtering procedure has a bias: noise is more easily detected in the low rate region (at the end of the decay spectrum) than in the high rate region (at the beginning). This means that, after filtering, the data will tend to yield a fitted half life that is too short. In our new analysis we removed this filter and used only one that tested the  $\chi^2$  value of the fit of each individual cycle, rejecting those cycles with a confidence level below  $10^{-4}$ . In the new fits we found:

- a very small scatter associated with the detector bias – see Fig 1, in which  $\chi^2/\text{ndf} = 0.5$ ; but
- a higher scatter associated with the discriminator threshold – see Fig 2, in which  $\chi^2/\text{ndf} = 2.6$ .

It should be noted however that the values obtained in these fits have no provision for any  $^{37}\text{Ca}$  impurity in the collected samples. The extent of this contribution needs to be assessed by our colleagues at TRIUMF and then incorporated into the final data analysis. We anticipate this work to be completed within a few months.

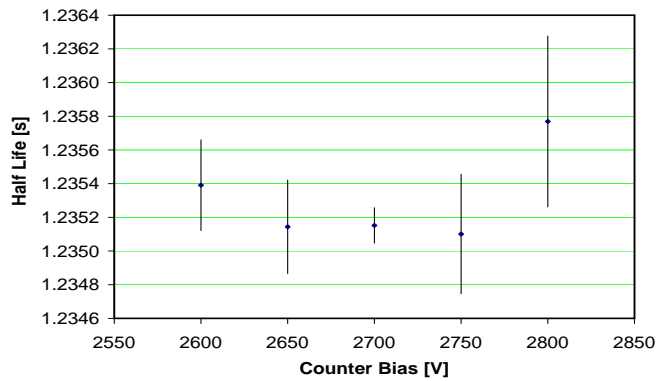


**Figure 1.** Half-life results for  $^{37}\text{K}$  from separate runs, plotted as a function of detector bias.

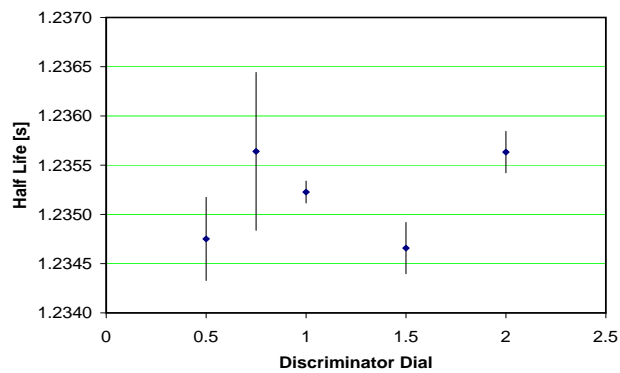


**Figure 2.** Half-life results for  $^{37}\text{K}$  from separate runs, plotted as a function of discriminator threshold.

- [1] J. C. Hardy and I. S. Towner, *Phys. Rev.C* **71**, 055501(2005) and *Phys. Rev. Lett.* **94**, 092502 (2005).  
 [2] J. C. Hardy and V. E. Jacob, *Progress in Research*, Cyclotron Institute, Texas A&M University (1998-1999), p. I-30

## JYFLTRAP : $Q_{EC}$ -values of the superallowed decays of $^{50}\text{Mn}$ and $^{54}\text{Co}$

J. C. Hardy

Following a successful measurement of the  $Q_{EC}$  values for  $^{26}\text{Al}^m$ ,  $^{42}\text{Sc}$  and  $^{46}\text{V}$  [1], our collaboration with JYFLTRAP, an on-line Penning trap mass spectrometer at the University of Jyväskylä cyclotron facility, has begun a second experiment, to measure the  $Q_{EC}$  values for the superallowed decays of  $^{50}\text{Mn}$  and  $^{54}\text{Co}$ . These cases have become particularly interesting after the discovery that the corrected  $\mathcal{F}t$  value for  $^{46}\text{V}$  was significantly higher than that for any other well known superallowed transition. The most obvious explanation of its unusual value is that the correction for isospin symmetry-breaking, which depends upon the nuclear structure of the parent and daughter nuclei, is missing some important components, and we have begun to examine this possibility theoretically [2]. What we have found so far is that by including the  $sd$ -shell with the  $fp$ -shell in our configuration space, we could remove the shift in the  $^{46}\text{V}$  result but not without introducing shifts in the  $\mathcal{F}t$  values for  $^{50}\text{Mn}$  and  $^{54}\text{Co}$  as well. The currently accepted  $Q_{EC}$  values for  $^{50}\text{Mn}$  and  $^{54}\text{Co}$  are averages, each with an important contribution from a 30-year-old ( $^3\text{He,t}$ )  $Q$ -value measurement published by Vonach et al. [3] in the same paper in which their now-discredited value for the  $^{46}\text{V}$   $Q_{EC}$  value appeared. Perhaps their results for  $^{50}\text{Mn}$  and  $^{54}\text{Co}$  were wrong as well.

As we did in our previous experiment, we produced  $^{50}\text{Mn}$  and  $^{54}\text{Co}$  via (p,n)-reactions. A powerful advantage of this approach is that, not only were the superallowed emitters of interest produced in the primary reactions but ions from the target material itself – the beta-decay daughters of these emitters – were also released by elastic scattering of the cyclotron beam. As explained in Ref. [1], with the JYFLTRAP system we can isolate a specific nuclide from the reaction products and measure the cyclotron frequency of its ions in the Penning trap. For each determination of a  $Q_{EC}$  value, the cyclotron frequency measurements were interleaved: first we recorded a frequency scan for the daughter, then for the mother, then for the daughter and so on. This way, most possible systematic effects could be reduced to a minimum or eliminated. For each measurement, data were collected in several sets, each comprising ~10 pairs of parent-daughter frequency scans taken under the same conditions.

The experimental data are still being analyzed.

- [1] T. Eronen, V. Elomaa, U. Hager, J. Hakala, A. Jokinen, A. Kankainen, I. Moore, H. Penttilä, S. Rahaman, A. Saastamoinen, T. Sonoda, J. Äystö, J. C. Hardy and V. Kolhinen, *Phys. Rev. Lett.* **97**, 232501 (2006).
- [2] I. S. Towner and J. C. Hardy, *Progress in Research*, Cyclotron Institute, Texas A&M University (2005-2006), p III-39.
- [3] H. Vonach *et al.*, *Nucl. Phys.* **A278**, 189 (1977).

## Branching ratios for the beta decay of $^{21}\text{Na}$

V. E. Jacob, J. C. Hardy, C. A. Gagliardi, J. Goodwin, N. Nica, H. I. Park, G. Tabacaru,  
L. Trache, R. E. Tribble, Y. Zhai and I. S. Towner

A recent publication by Scielzo *et al.*[1] reported a measurement of the  $\beta$ - $\nu$  angular correlation coefficient,  $\alpha_{\beta\nu}$ , for the  $\beta$ -decay transition between  $^{21}\text{Na}$  and the ground state of its mirror,  $^{21}\text{Ne}$ . The authors compare their result with the standard-model prediction for  $\alpha_{\beta\nu}$ , with a view to testing for scalar or tensor currents, the presence of which would signal the need for an extension of the standard model. Although they found a significant discrepancy – the measured value,  $\alpha_{\beta\nu} = 0.524(9)$  disagrees with the standard-model prediction of 0.558 – they stop short of claiming a fundamental disagreement with the standard model.

Scielzo *et al.* [1] offer two alternative explanations that would have to be eliminated before their result could begin to raise questions about the need for an extension to the standard model. One is that some  $^{21}\text{Na}_2$  dimers formed by cold photoassociation could also have been present in their trap, thus distorting the result; they themselves propose to do further measurements to test that possibility. The other is that the branching-ratio value they used for  $\beta$  decay to the first excited state of  $^{21}\text{Ne}$  might not be correct. Because Scielzo's measurement could not distinguish between positrons from the two predominant  $\beta$ -decay branches from  $^{21}\text{Na}$  (see Fig. 1), the adopted branching ratio for the  $\beta$  transition to the first excited state not only affects their data analysis but also helps determine the theoretical prediction for  $\alpha_{\beta\nu}$  itself, since the axial-vector component of the ground-state branch can only be determined from its  $ft$  value, which also depends on the branching ratio. This branching ratio is a key component of their standard-model test, yet the five published values [2-6] are between 25 and 45 years old, are quite inconsistent with one another and range from 2.2(3) to 5.1(2)%. To remedy this problem, we measured the excited-state branching ratio, for which we quote  $\pm 0.8\%$  relative precision, five times better than the best precision claimed in any previous measurement. This experiment has been published [7].

We produced 22.5-s  $^{21}\text{Na}$  using a 28A-MeV  $^{22}\text{Ne}$  to initiate the  $^1\text{H}(^{22}\text{Ne}, 2n)^{21}\text{Na}$  reaction on a  $\text{LN}_2$ -cooled hydrogen gas target. The ejectiles from the reaction were fully stripped and, after passing through the MARS spectrometer, produced a  $^{21}\text{Na}$  secondary beam of >99% purity at the extraction slits in the MARS focal plane. This beam, containing  $\sim 3 \times 10^5$  atoms/s at 24.4A MeV, then exited the vacuum system through a 50- $\mu\text{m}$ -thick Kapton window, passed successively through a 0.3-mm-thick BC-404 scintillator and a stack of aluminum degraders, finally stopping in the 76- $\mu\text{m}$ -thick aluminized Mylar tape of a tape transport system. Since the few impurities remaining in the beam had ranges different from that of  $^{21}\text{Na}$ , most were not collected on the tape; residual collected impurities were concluded to be less than 0.1% of the  $^{21}\text{Na}$  content.

In a typical measurement, we collected  $^{21}\text{Na}$  on the tape for a few seconds, then interrupted the beam and triggered the tape-transport system to move the sample in 180 ms to a shielded counting station located 90 cm away, where the sample was positioned between a 1-mm-thick BC404 scintillator to detect  $\beta^+$  particles, and a 70% HPGe detector for  $\gamma$  rays. We then recorded  $\beta$  singles and  $\beta$ - $\gamma$  coincidences for a pre-determined counting period. Two timing modes were used: in one, the collection and detection

periods were 3 and 30 s, respectively; in the other, they were 6 and 60 s. In both cases, after the detection period was complete, the cycle was repeated and, in all, some 3,200 cycles were completed over a span of 32 hours.

From our data, we could obtain the  $\beta$ -branching ratio  $BR_1$  for the transition populating the first excited state in  $^{21}\text{Na}$ , which decays by emitting a 351-keV  $\gamma$  ray. If the total number of  $\beta$  singles is  $N_\beta$  and the total number of  $\beta$ - $\gamma$  coincidences measured in the  $\gamma$  peak is  $N_{\beta\gamma}$ , then the branching ratio  $BR_1$  is given by

$$BR_1 = \frac{N_{\beta\gamma}}{N_\beta \varepsilon_\gamma} k, \quad (1)$$

where  $\varepsilon_\gamma$  is the detector efficiency at 351 keV and  $k$  is a small correction factor (*i.e.*  $k \sim 1$ ) that, among other things, takes into account the differences in the  $\beta$ -detector efficiency for the transitions to the ground and first excited states of  $^{21}\text{Ne}$ . This relation highlights the importance of a precise absolute efficiency calibration for the  $\gamma$ -ray detector and a reasonable knowledge of relative efficiencies in the beta detector. Our HPGe absolute efficiency is accurately known (to  $\pm 0.2\%$  for 50-1400 keV and  $\pm 0.4\%$  up to 3500keV) from source measurements and Monte Carlo calculations [10]. The relative efficiency as a function of  $\beta$  energy in the plastic scintillator was determined by Monte Carlo calculations using the DOSRZNR code from the EGS package [11] and checked by comparison with conversion-electron sources and with  $^{22}\text{Mg}$   $\beta$ -decay data [12].

Our measured branching-ratio value is compared with previous measurements in Table I. All previous experiments determined the branching ratio from a comparison of the area of the 351-keV peak to that of the annihilation radiation. This method has the advantage that only relative detector efficiencies are required, but it has three serious disadvantages: i) contaminant activities may well make an unknown contribution to the annihilation radiation; ii) most positrons do not annihilate at the source position, where the  $\gamma$  rays originate, so the relative detection efficiencies cannot be simply determined from calibration sources; and iii) the significant effect ( $\sim 5\%$ ) of positron annihilation in flight is a first-order correction that must be calculated and corrected for. All previous measurements except possibly reference [4] were susceptible to potential contaminants; only the last three references [4, 5, 6] mention accounting for a spatially distributed source of 511-keV radiation; and only the last two [5, 6] appear to have taken account of annihilation in flight.

**Table I.** Measurements of the branching ratio  $R_1$

Date	Reference	Result(%)
1960	Talbert & Stewart [2]	2.2(3)
1963	Arnell & Wernbom [3]	2.3(2)
1974	Alburger [4]	5.1(2)
1977	Azelos, Kitching & Ramavataram [5]	4.2(2)
1980	Wilson, Kavanagh & Mann [6]	4.97(16)
2006	This measurement	4.74(4)

Given the age of the previous measurements and the potential hazards associated with their experimental method – not to mention their mutual inconsistency – we choose not to average our result with them but instead to use our present result alone in extracting the properties of the  $^{21}\text{Na}$   $\beta$ -decay scheme.

Since there are only two significant  $\beta$ -decay branches from  $^{21}\text{Na}$  – to the ground and first excited states of the daughter – with  $BR_1$  determined, the branching ratio to the ground state,  $R_0$ , follows directly from it: *viz.*  $R_0 = 0.9526(4)$ . This result is actually determined to a precision of 0.04%. From this value for  $R_0$  we obtain the  $ft$  value for this transition, the relative contributions of axial-vector and vector components, and ultimately the standard-model expectation for its  $\beta$ - $\gamma$  angular correlation coefficient (see Ref. [7]). Our final computed result is  $\alpha_{\beta\nu} = 0.553(2)$ . This value can now stand as the “standard-model prediction” for  $\alpha_{\beta\nu}$ , against which the measured angular-correlation coefficient can be compared. It is 0.9% lower than the one originally used by Scielzo *et al.* [1] and still leaves that experimental result in disagreement with the prediction. However, the authors themselves expressed concern about the possible presence of  $^{21}\text{Na}_2$  dimers in their trapped samples; this would have caused a dependence of their result on the trapped-atom population and could easily reconcile their result with the standard model. With a precise branching ratio now determined, an investigation of the actual make-up of the trapped-atom samples in the Scielzo *et al.* experiment is essential if the  $^{21}\text{Na}$  result is to become a real test of the standard model.

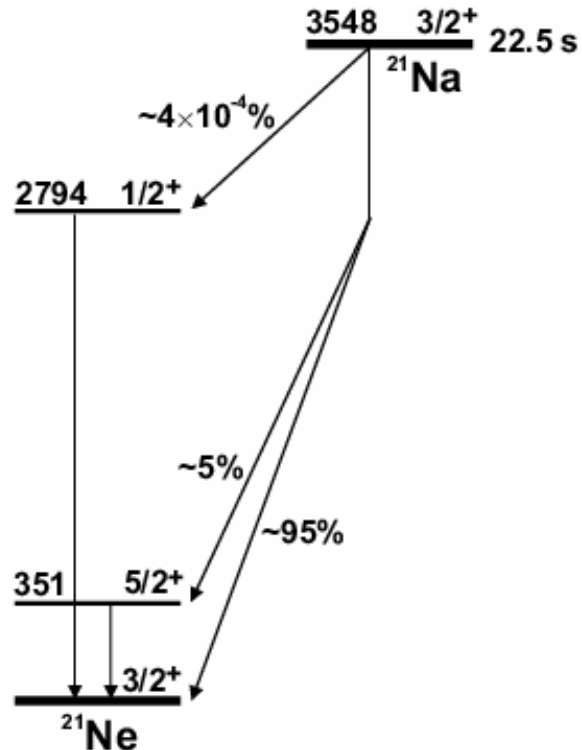


Figure 1.  $\beta$ -decay scheme for  $^{21}\text{Na}$

- [1] N. D. Scielzo, S. J. Freedman, B. K. Fujikawa and P. A. Vetter, Phys. Rev. Lett. **93**, 102501 (2004).
- [2] W. L. Talbert, Jr. and M. G. Stewart, Phys. Rev. **119**, 272 (1960).
- [3] S. E. Arnell and E. Wernbom, Arkiv für Fysik **25**, 389 (1963).
- [4] D. E. Alburger, Phys. Rev. C **9**, 991 (1974).
- [5] G. Azuelos, J. E. Kitching and K. Ramavataram, Phys. Rev. C **15**, 1847 (1977).
- [6] H. S. Wilson, R. W. Kavanagh and F. M. Mann, Phys. Rev. C **22**, 1696 (1980).
- [7] V. E. Iacob, J. C. Hardy, C. A. Gagliardi, J. Goodwin, N. Nica, H. I. Park, G. Tabacaru, L. Trache, R.E. Tribble, Y. Zhai and I.S. Towner, Phys. Rev. C **74**, 015501 (2006).
- [8] J. C. Hardy *et al.*, Applied Radiation and Isotopes **56**, 65 (2002); R.G. Helmer *et al.*, Nucl. Instrum. Methods Phys. Res. **A511**, 360 (2003) and Appl. Radiat. Isot. **60**, 173 (2004).

- [9] NRCC Report PIRS-701 and [www.irs.inms.nrc.ca/inms/irs/EGSnrc/EGSnrc](http://www.irs.inms.nrc.ca/inms/irs/EGSnrc/EGSnrc)
- [10] V. E. Jacob *et al.*, 2004 Fall Meeting of the APS DNP, Oct 28 – 30, Chicago IL.

**Tests of internal-conversion theory and efficiency calibration with precise  $\gamma$ - and x-ray spectroscopy:  $^{134}\text{Cs}^m$ ,  $^{137}\text{Ba}$ ,  $^{139}\text{La}$**

N. Nica, C. Balonek, J. C. Hardy, V. E. Jacob, J. Goodwin, H. I. Park,  
W. E. Rockwell and M. B. Trzhaskovskaya<sup>1</sup>

<sup>1</sup>*Petersburg Nuclear Physics Institute, Gatchina RU-188300, Russia*

Our program of precision measurements of internal conversion coefficients (ICC) continued with the completion of the  $^{134}\text{Cs}^m$  and  $^{137}\text{Ba}$  cases, and the measurement of a new case,  $^{139}\text{La}$ . This program was motivated by a comprehensive study published in 2002 by Raman *et al.* [1], in which various methods for calculating ICC's were reviewed and the results from each were compared with one hundred selected transitions whose experimentally determined ICC's were claimed to 6% precision or better. Of the various calculations examined, the best agreement with experiment was obtained by the "Relativistic Dirac-Fock" approach; surprisingly, though, the data showed a slight preference for a version of that calculation which completely ignored the presence of the atomic hole created by the conversion process. Since simple physical considerations show that the typical time for an electron to leave the atom is less than  $\sim 10^{-18}$  s, while the K-shell filling time is at least an order of magnitude longer ( $10^{-17}$  -  $10^{-15}$  s depending on Z) [2], one should expect the presence of the hole to have a non-negligible impact on the wave function of the outgoing electron, at least in cases where the transition energy is just above the atomic-shell binding energy and thus the electron energy is low.

Even so, it was decided at the time to adopt the calculations that appeared to agree best with experiment even though they incorporated a "non-physical" assumption, and the most recent published ICC tables [3], as well as the Evaluated Nuclear Structure Data Files (ENSDF) maintained by the National Nuclear Data Center (NNDC) at Brookhaven, used the "no hole" approximation. Being readily available and pre-evaluated, ENSDF in particular is intensively used by scientists and technologists, usually without any further critical judgment. Consequently, it is clearly important that the validity of the ICC calculations used throughout ENSDF be firmly established since significant differences in calculated ICC coefficients can arise depending on whether the atomic hole is included or not. As was originally pointed out by Raman *et al.* [1], there are cases where differences of up to 10% can be expected.

Three years ago we reported a precise measurement of the K-shell conversion coefficient for the 80.2 keV, M4 transition in  $^{193}\text{Ir}^m$  [4], a case originally suggested by Raman *et al.* [1] as providing the most sensitive test of the importance of the atomic hole. Our measurement,  $\alpha_K=103.0(8)$ , showed unequivocal agreement with the calculation that includes the "hole,"  $\alpha_K=103.5(1)$ , and disagreement with the "no-hole" result,  $\alpha_K=92.0(3)$ . Based on our result, NNDC changed its policy and adopted the ICC values calculated with the atomic hole included; the consequent change in the ENSDF data files has had considerable impact on the nuclear-data users' community.

There remains a serious question. The survey by Raman *et al.* [1] included ICCs from 100 transitions with quoted uncertainties spanning more than an order of magnitude, from 0.5% to more than 6%. Although the authors found the average difference between experiment and the Relativistic Dirac-Fock theory to be  $\sim 1\%$ , it is clear that their outcome was dominated by a few very precise measurements,

some of which were old and of dubious merit. A few of these ostensibly precise measurements in fact disagreed significantly with both the “hole” and “no-hole” version of the theory. Can we thus rely on even the best calculated ICCs to  $\pm 1\%$ ?

To begin to answer this question, we have measured two cases that disagreed significantly with both types of calculations in the Raman *et al.* survey [1]: the 127.5-keV, E3 transition in  $^{134}\text{Cs}^m$  and the 661.7-keV, M4 transition in  $^{137}\text{Ba}$ . We used the same measurement technique as we had used previously in the  $^{193}\text{Ir}^m$  experiment [4], where we determined the intensity ratio of conversion K X-rays to the  $\gamma$ -ray for a single transition and used the precisely known fluorescence yield [5] to obtain the  $\alpha_K$  ICC value at  $<1\%$  precision. The key to this type of measurement is our HPGe detector, the efficiency calibration of which is known to high precision [6,7]. However, the  $^{134}\text{Cs}^m$  and  $^{137}\text{Ba}$  decays produced K X-rays with energies below 50 keV, the lowest energy for which our detector efficiency is well known. As a result, we were forced initially to restrict our test to the ratio of the  $\alpha_K$  values for the two transitions.

Since this experiment was described in our last progress report [8], we have solved the problem of scattered radiation, which strongly affects the 30-37-keV K x-ray peaks from cesium and barium. Actually in this energy range the (lower energy) scattered radiation is not entirely separated from the K X-rays peaks themselves. With our energy resolution of  $\sim 1$  keV, the scattered continua extend only 3-4 keV below the x-ray energy and only a small fraction of it can be observed as a tail to the left side of the  $K_\alpha$ -group peak, while it is totally hidden for the  $K_\beta$  group. The effect is strongly dependent on the source design and surrounding materials of the source-detector assembly. Fortunately our sources were very similar and most of the effects of scattering could be expected to cancel out in the ratio.

Nevertheless, we carefully studied the correction using the  $^{137}\text{Cs}$  source, which was conveniently long lived and free of contaminants. We compared the observed low-energy tail of the  $K_\alpha$  peak with Monte-Carlo calculations using the Cyltran code [9], the same one we used so successfully for our efficiency calibration. We also modeled the source configuration and included a cylinder of air, 1 meter in diameter and 1 meter long, in front of the detector face and surrounding the source, which was located at 151 mm from the face. The comparison of experiment with calculation is shown in the upper part of Fig. 1; the agreement is quite reasonable. From the Monte Carlo calculation we could then determine that the scattered continuum continues to increase as it approaches the central peak energy (where it is hidden by the finite width of the observed peak). The shape of the simulated spectrum, especially the increase of scattered photons as the central energy is approached, was qualitatively checked by a measurement of the same source with a 30-mm<sup>2</sup> Si(Li) detector, which has higher resolution than our HPGe detector. The result is shown in the lower part of Fig. 1, where the continuing increase in scattering is clearly evident. (Since we did not have a model for the Si(Li) detector, we did not attempt a Monte Carlo calculation for it.)

From the Monte Carlo calculation we determined the ratio of observed-to-hidden scattering tail for each source and used the results to calculate the total effect of scattering in each case based on the observed low-energy tail. The result was 2.1(3)% for  $^{137}\text{Ba}$ , and 2.8(4)% for  $^{134}\text{Cs}^m$  respectively, which gave a 0.8(3)% correction on the  $\alpha_K$  ratio of the transitions studied here.

With this – and other – corrections in hand we determined the ratio of ICCs to be  $\alpha_K(^{134}\text{Cs}^m)/\alpha_K(^{137}\text{Ba}) = 30.01(15)$ . This result agrees well with 29.96, the Dirac-Fock ICC calculation in which the hole is accounted for in the “frozen orbital” approximation, and disagrees with the “no hole” calculation by more than three standard deviations. Our result also disagrees with the experimental ratio, 28.8(5), obtained from the data in Raman *et al.* [1], a result that was inconsistent with both calculations. The results of this study have been published [10].

The  $^{139}\text{La}$  experiment, which was also completed during the year reported here, was undertaken as a means of turning the  $^{134}\text{Cs}^m$ - $^{137}\text{Ba}$   $\alpha_K$ -ratio measurement into independent determinations of  $\alpha_K(^{134}\text{Cs}^m)$  and  $\alpha_K(^{137}\text{Ba})$ . The calculated  $\alpha_K$  value for the 165.9-keV M1 transition in  $^{139}\text{La}$  is essentially independent of whether the “hole” or “no hole” assumption is used: the results differ by less than 0.2%. Thus we can use this reliable result, together with the measured ratio of K x rays to 165.9-keV  $\gamma$  rays, to determine our detector’s efficiency at the K x-ray energy. Since the K x rays of all three elements, Cs, Ba and La, are separated by only 1.2-1.3 keV of one another, this same calibration, with minor adjustments can be applied, to the earlier measurement of Cs and Ba. This measurement has the added benefit that it extends the range of our HPGe detector’s precision efficiency-calibration from 50 keV, its previous limit, down to  $\sim 20$  keV.

One of the main difficulties of this measurement came from the short-lived ( $t_{1/2} = 83$  m)  $^{139}\text{Ba}$  precursor of  $^{139}\text{La}$ . Its short half-life precluded our processing the source after neutron activation so we were forced to activate an enriched  $^{138}\text{Ba}$  sample that was already placed between thin mylar foils. Much care had to be taken to minimize impurities that could cause competing radioactivities. We prepared two sources of  $^{138}\text{Ba}$  from thin uniform layers,  $\sim 1$   $\mu\text{m}$  thick, of barium nitrate placed on 12- $\mu\text{m}$ -thick mylar, and covered by 4- $\mu\text{m}$ -thick mylar. In order to reduce the contamination coming from impurities in mylar, the diameter of the whole source assembly was reduced to only 12 mm. These sources were almost absorption free: the correction, including both the source material and the covering mylar, was  $< 0.2\%$ .

The sources were activated for 1.8 h and 1 h respectively, at a flux of  $\sim 7 \times 10^{12}$  n/cm<sup>2</sup>s at the Nuclear Science Center Triga reactor at Texas A&M. Even though our enriched isotope was claimed to be pure, we found  $^{152}\text{Eu}^m$  ( $t_{1/2} = 9.3$  h) and  $^{153}\text{Sm}$  ( $t_{1/2} = 46.5$  h), both of which have huge activation cross

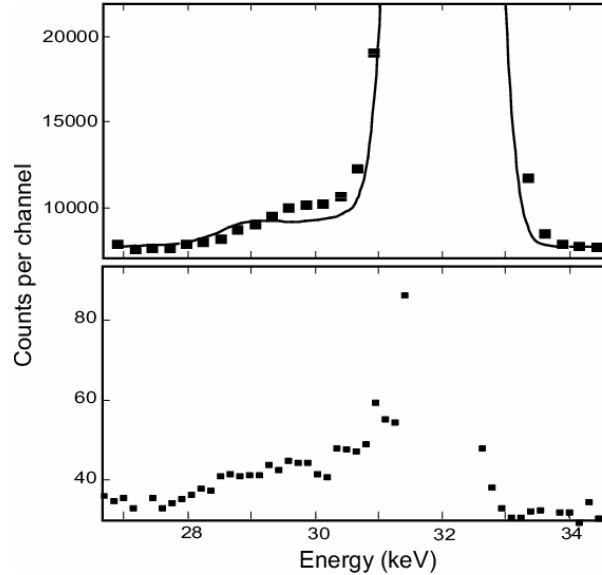


**Figure 1.** The top panel shows an expanded region of the HPGe spectrum at the base of the barium  $K_\alpha$  x-ray peak. The solid squares are the measured data from the  $^{137}\text{Cs}$  source; the curve is the result of a Monte Carlo simulation. The bottom panel gives the same region of the  $^{137}\text{Cs}$  spectrum as measured with a Si(Li) detector; the ordinate scale has been adjusted so that both panels display approximately the same fraction of the total K x-ray peak area.

sections, 3300 b for  $^{151}\text{Eu}$ , and 206 b for  $^{152}\text{Sm}$ , compared to 0.36 b for  $^{138}\text{Ba}$ . These activities affected lanthanum's  $K_{\beta}$  peaks at the level of several percent, depending on the time after activation. For this reason, we collected 8-9 spectra from each source over several days, long after  $^{139}\text{La}$  had decayed away, and used the measured decay curves to extract the contribution of both contaminants. The analysis is in progress.

- [1] S. Raman, C. W. Nestor, Jr., A Ichihara, and M. B. Trzhaskovskaya, *Phys. Rev. C* **66**, 044312 (2002).
- [2] J. C. Hardy, N. Nica, V. E. Iacob, M. B. Trzhaskovskaya and R. G. Helmer, *Appl. Radiat. Isot.* **64**, 1392 (2006).
- [3] I. M. Band, M. B. Trzhaskovskaya, C. W. Nestor, Jr., P. Tikkanen, and S. Raman, *At. Data Nucl. Data Tables* **81**, 1 (2002).
- [4] N. Nica, J. C. Hardy, V. E. Iacob, S. Raman, C. W. Nestor Jr., and M. B. Trzhaskovskaya, *Phys. Rev. C* **70**, 054305 (2004).
- [5] E. Schönfeld and H. Janssen, *Nucl. Instrum. Methods Phys. Res.* **A369**, 527 (1996).
- [6] J. C. Hardy, V. E. Iacob, M. Sanchez-Vega, R. T. Effinger, P. Lipnik, V. E. Mayes, D. K. Willis, and R. G. Helmer, *Appl. Radiat. Isot.* **56**, 65 (2002).
- [7] R. G. Helmer, J. C. Hardy, V. E. Iacob, M. Sanchez-Vega, R.G. Neilson, and J. Nelson, *Nucl. Instrum. Methods Phys. Res.* **A511**, 360 (2003).
- [8] N. Nica, J. C. Hardy, V. E. Iacob, H. I. Park, J. Goodwin, W. E. Rockwell and M. B. Trzhaskovskaya, *Progress in Research*, Cyclotron Institute, Texas A&M University (2005-2006), p. I-39.
- [9] J. A. Halbleib, T. A. Mehlhorn, *Nucl. Sci. Eng.* **92**, 338 (1986).
- [10] N. Nica, J. C. Hardy, V. E. Iacob, W. E. Rockwell, and M. B. Trzhaskovskaya, *Phys. Rev. C* **75**, 024308 (2007).

## Evaluated nuclear structure data file (ENSDF) at Texas A&M: A=140

N. Nica,<sup>1</sup> and J. C. Hardy

<sup>1</sup>*under contract with Brookhaven National Laboratory*

Work for the *Evaluated Nuclear Structure Data File (ENSDF)* started at the Cyclotron Institute in 2005 and is continuing. After about 1.5 years, our work already makes Texas A&M one of the significant contributors to the U.S. Nuclear Data Program, a national-interest activity sponsored by DOE and maintained by the National Nuclear Data Center (NNDC) at Brookhaven National Laboratory.

Information in the ENSDF files is grouped by *A* number and is obtained through the compilation and evaluation of virtually all data ever published on each nucleus. The data evaluation process depends on individual evaluators, each of whom works on one *A*-chain at a time, and involves painstaking inter-comparison and reconciliation of diverse published measurements. All available measurements are grouped into data sets, one for each nucleus and measurement technique; once reconciled, these sets are gathered into a single comprehensive data set, the *Adopted Levels, Gammas*, the unique repository where the “best known” data for each nucleus are made available for anyone to use. The evaluated results for each *A*-chain are published in the Nuclear Data Sheets by Academic Press, as well as being widely disseminated through the internet. Recently, NNDC reported more than one million database retrievals in FY2006 [1], a success of the entire nuclear-structure data-evaluation network.

Conceived as a service for the nuclear basic science community, ENSDF has become one of the most effective ways through which basic research renders service to society. Its beneficiaries include many other science and technology communities, such as biology, chemistry, environmental studies, pharmaceutical and medical industries, and various industries; recently this group has also included the Department of Homeland Security in its efforts to monitor terrorism-related activities.

Our evaluation work at the Cyclotron continued this past year with the mass chain *A*=140 which is one of the largest mass chains, comprising sixteen isobars (Te, I, Xe, Cs, Ba, La, Ce, Pr, Nd, Pm, Sm, Eu, Gd, Tb, Dy, Ho). In the preceding, 1994 evaluation [2] 67 data sets were included. Now there are 81 data sets [3], a 20% increase in the number of ways (different reactions or experimental methods) that the nuclei in this mass chain have been studied in the last 13 years. Most of the 80-character line records in the database (*ens* format) [4] are pure data records; the remaining ones are comment lines, which contain both data and explanations. Overall, the number of *ens* lines gives an idea about the quantity of data acquired per mass chain. For *A*=140 there are now almost 15000 lines, as compared with less than 7900 lines in 1994. This indicates that there has been a 90% increase in the data or, in other words, almost half of the data on *A*=140 nuclei has been obtained during the last 13 years.

The number of *ens* lines for each *A*=140 nucleus is plotted for both evaluations – 1994 and 2006 – in Figure 1. One can see that <sup>140</sup>La, <sup>140</sup>Nd, and <sup>140</sup>Eu together contribute half of all 2007 data, and they now contain three times more data than they did in 1994. These were not only the biggest data sets, but also the most discrepant ones, the evaluation of which was done in several layers and took about 3000 hours of work by the evaluator.

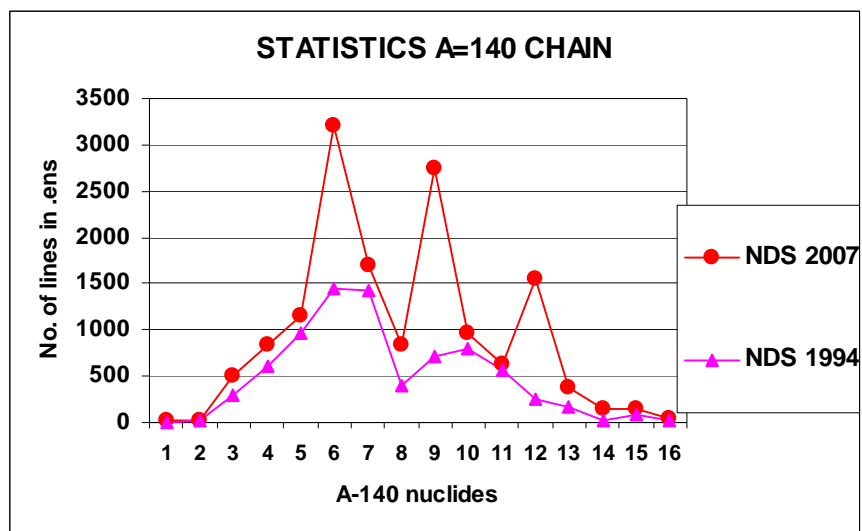


**Figure 1.** Comparison of A=140 data evaluated for NDS 2007 [3] and NDS 1994 [2], showing the number of ens lines for each nucleus in the mass chain.

[1] The Bulletin, vol. **60**, no. 36, Oct 20, 2006, published by Brookhaven National Laboratory

[2] L.K. Peker, Nucl. Data Sheet **73**, 261 (1994).

[3] N. Nica, Nucl. Data Sheet (to be published).

[4] <http://www.nndc.bnl.gov>

## TWIST: measuring the space-time structure of muon decay

C. A. Gagliardi, R. E. Tribble, K. Williams, and the TWIST Collaboration

This past year, TWIST published its first measurement of  $P_\mu \xi$ , where  $P_\mu$  is the polarization of the muon in pion decay and  $\xi$  is one of the four Michel parameters that characterize the energy and angular distributions of the positrons emitted in polarized muon decay. We find  $P_\mu \xi = 1.0003 \pm 0.0006(\text{stat.}) \pm 0.0038(\text{syst.})$  [1], consistent with the Standard Model expectation that  $P_\mu \xi = 1$  and a factor of two more precise than the previous best direct measurement [2]. The measurement was based on an analysis of muon decay data that TWIST recorded during Fall, 2004.

In parallel, Mr. Robert MacDonald of University of Alberta is reanalyzing the 2004 data to obtain improved measurements of  $\rho$  and  $\delta$ . Several significant improvements have been implemented in our Monte Carlo simulation and helix fitting codes. These improvements are expected to reduce the systematic uncertainties in  $\rho$  and  $\delta$  by a factor of  $\sim 2$ , compared to those in the analysis of the TWIST 2002 data [3,4]. They also permit an expansion of the experiment fiducial. This is illustrated in Fig. 1, which shows the difference between the measured downstream tracking efficiencies in data and Monte Carlo vs. polar angle. The match is excellent over the range  $0.5 < |\cos \theta| < 0.92$ , whereas previous TWIST analyses only considered  $0.5 < |\cos \theta| < 0.84$ . This leads to a significant reduction in the statistical uncertainty for the same number of recorded events. Mr. MacDonald is expected to complete his analysis this coming Fall. One of us (CAG) has been working with Dick Mischke and Art Olin of TRIUMF to advise Mr. MacDonald during his analysis.

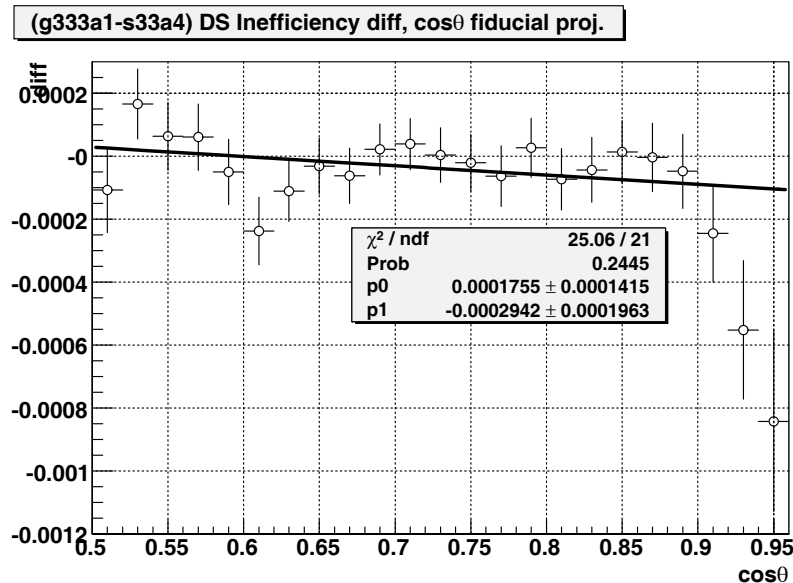


**Figure 1.** Difference between data and Monte Carlo for the efficiency of tracks in the downstream half of the detector as a function of polar angle. Each  $\cos \theta$  bin is integrated over the corresponding fiducial momentum range. The difference is essentially the same for upstream tracks.

During Summer, 2006, Ms. Kristen Williams, an REU student with our group, estimated the sensitivity of TWIST to a proposed non-local tensor interaction in muon decay [5]. The effects of this interaction are described in terms of a new muon decay parameter  $\kappa$ .  $\kappa$  makes a quadratic contribution to the normal Michel parameters  $\rho$ ,  $\delta$ , and  $P_\mu\xi$ , and also introduces additional linear terms in the unpolarized and polarized spectra. Previously, TWIST set a limit  $|\kappa| < 0.024$  with 90% confidence, based on its quadratic contribution to  $\delta$  [4]. Ms. Williams explored the contribution that  $\kappa$  would make to TWIST measurements of  $\rho$ ,  $\delta$ , and  $P_\mu\xi$  when both the linear and quadratic effects are considered. She found that TWIST is more sensitive to positive values of  $\kappa$  than had been realized previously, and less sensitive to negative values. Overall, she found the previous TWIST measurements of  $\rho$  and  $\delta$  limit  $\kappa$  to the 90% confidence range  $-0.031 < \kappa < 0.012$ . Ms. Williams' analysis procedures will be applied to determine  $\kappa$  in all future TWIST measurements.

TWIST expects to take its final data during 2006-07. We anticipate the final precisions for the Michel parameters  $\rho$  and  $\delta$  will be approximately  $\pm 0.0003$ . The final precision for  $P_\mu\xi$  will be  $\pm 0.001$  or better.

- [1] B. Jamieson *et al.* (TWIST Collaboration), Phys. Rev. D **74**, 072007 (2006).
- [2] I. Beltrami *et al.*, Phys. Lett. B **194**, 326 (1987).
- [3] J.R. Musser *et al.* (TWIST Collaboration), Phys. Rev. Lett. **94**, 101805 (2005).
- [4] A. Gaponenko *et al.* (TWIST Collaboration), Phys. Rev. D **71**, 071101R (2005).
- [5] M.V. Chizhov, hep-ph/0405073.

## Spin and low- $x$ physics with STAR at RHIC

J. L. Drachenberg, C. A. Gagliardi, T. W. Henry, M. Sarsour, R. E. Tribble,  
and the STAR Collaboration

During the past year, our primary focus has been on the analysis of inclusive jet data from longitudinally polarized p+p collisions to determine the contribution that gluons make to the proton spin. A long polarized proton run occurred in 2005. STAR devoted nearly the entire p+p run to longitudinally polarized proton collisions, with a mix of triggers that was designed to maximize our acceptance for high- $p_T$  jets. Since then, there has been a major effort within the STAR Spin PWG to extract the longitudinal double-spin asymmetry  $A_{LL}$  for inclusive jet production. Our group has played a major role in this effort. Initially, we identified a set of event and jet cuts that reduced our sensitivity to apparent false asymmetries. This led to the preliminary result shown in Fig. 1 [1]. These new results imply that the gluon polarization in the nucleon can't be much larger than the GRSV-std polarized parton distribution fit.

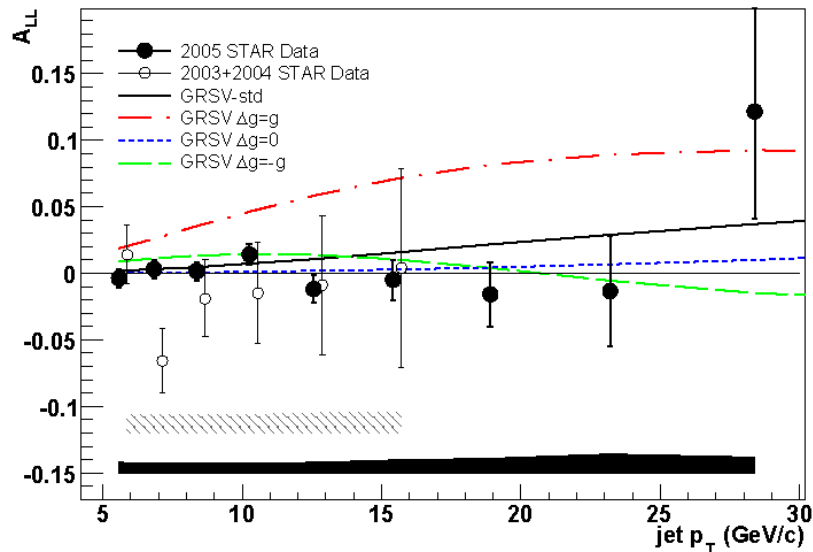


**Figure 1.** Preliminary STAR measurement of  $A_{LL}$  for inclusive jets from data recorded in 2005 [1], compared to previous STAR results from 2003-04 [2].

More recently, we have repeated many parts of the analysis. We repeated the run QA studies, which allowed us to increase the jet statistics by  $\sim 20\%$ . We also identified a problem with the relative luminosity study that had been performed by a post-doc from Caltech. Correcting that problem led to a significant reduction in the systematic uncertainties associated with relative luminosity and potential false asymmetries. These reduced uncertainties then motivated us to explore a new analysis procedure that involves a partial unfolding of instrumental effects to minimize jet reconstruction and trigger bias effects. The new analysis, which has been done in collaboration with R. Fatemi of MIT, has reduced the corresponding systematic uncertainty by a factor of 2 or more. It also allows us to make a quantitative

confidence level comparison between our data and the GRSV parameterization in a way that accounts properly for systematic uncertainties that are correlated across jet  $p_T$  bins. The results of this analysis are currently being written up for publication. M. Sarsour will be one of the principal authors of the paper.

In parallel, we have begun to analyze the inclusive jet data that STAR recorded during 2006. Improvements in detector acceptance, integrated luminosity, and beam polarization are expected to lead to a factor of 3 or more reduction in the statistical uncertainties for  $A_{LL}$  at high  $p_T$ , when compared to the 2005 results. The initial indications are very promising.

The STAR investigation of forward  $\pi^0$  production in p+p and d+Au collisions was published this past year [3]. One of us (CAG) was a principal author of this paper.

This past year, we completed our study of similarities and differences in mid-rapidity jet and di-jet production in p+p and d+Au collisions at RHIC energies, based on data that STAR recorded during 2003. Good agreement is found between Pythia+GEANT and data for the longitudinal ( $z$ ) and transverse ( $j_T$ ) jet shapes. The rms  $j_T$  is found to be  $612 \pm 12 \pm 30$  MeV/c for p+p collisions and  $630 \pm 13 \pm 30$  MeV/c in d+Au collisions. A new procedure has been developed to determine the intrinsic and nuclear  $k_T$ . We find the  $k_T$  Gaussian sigma is  $2.08 \pm 0.12 \pm 0.13$  GeV/c in p+p collisions. The additional nuclear  $k_T$  in d+Au collisions is consistent with zero to within 0.5 GeV/c. T. Henry received his Ph.D. for this work in December, 2006.

The STAR Forward Meson Spectrometer (FMS) is a new addition to the STAR electromagnetic calorimetry, providing complete coverage over the pseudorapidity region  $2.5 < \eta < 4$ , which is the deuteron forward direction when RHIC studies d+A collisions, and nearly complete EMC coverage over the range  $-1 < \eta < +4$ . The FMS will enable STAR to search for mono-jet production in d+Au collisions. It will also facilitate measurements of gluon polarization in the proton at low- $x$  and detailed studies of the dynamics that underlie the significant single-spin asymmetries that have been seen in forward  $\pi^0$  production at RHIC. This past year members of the group participated in the construction of the FMS and analysis of data that were taken during 2006 with the FPD++, an engineering prototype for the FMS.

We also carry administrative responsibilities related to STAR and RHIC. This past year, Dr. Gagliardi served as Deputy Spokesperson of the STAR Collaboration and co-chair, with A. Frawley of Florida State, of the RHIC II White Paper writing committee. Dr. Gagliardi also served on the STAR Advisory and Trigger Boards, and Drs. Gagliardi and Tribble participated on several STAR god-parent committees.

[1] M. Sarsour (for the STAR Collaboration), hep-ex/0612065.

[2] B.I. Abelev *et al.* (STAR Collaboration), Phys. Rev. Lett. **97**, 252001 (2006).

[3] J. Adams *et al.* (STAR Collaboration), Phys. Rev. Lett. **97**, 152302 (2006).

# Toward understanding relativistic heavy-ion collisions with the STAR detector at RHIC

M. Cervantes, R. Clarke, M. Codrington, L. Dunkelberger, A. Hamed, S. Mioduszewski,  
and the STAR Collaboration

## I. Charmonium and Bottomonium Measurement

Charmonium ( $c\bar{c}$ ) and bottomonium ( $b\bar{b}$ ) are measured via their decay to an electron-positron pair in the STAR detector [1]. The large background from hadrons in heavy-ion collisions, such as Au+Au, makes the measurement particularly challenging. To improve such measurements, we are working on better electron identification (*ie*, stronger hadron rejection). The Barrel Pre-Shower (BPRS) detector of the Barrel Electromagnetic Calorimeter (BEMC) was designed to identify particles that begin to shower already in the first 2 layers of the calorimeter [2], and thus is ideal for rejecting hadrons. We have made quite some progress commissioning and calibrating the BPRS in the past year. First there were issues with the software mapping of channels not matching the hardware configuration. Most of these problems have been identified. The pedestal values were checked and subtracted, and minimum-ionizing peaks (MIP's) were fit for each channel with associated tracks.

The improvement in electron identification can already be seen in the data from the current Au+Au RHIC run (see Fig.1 below).

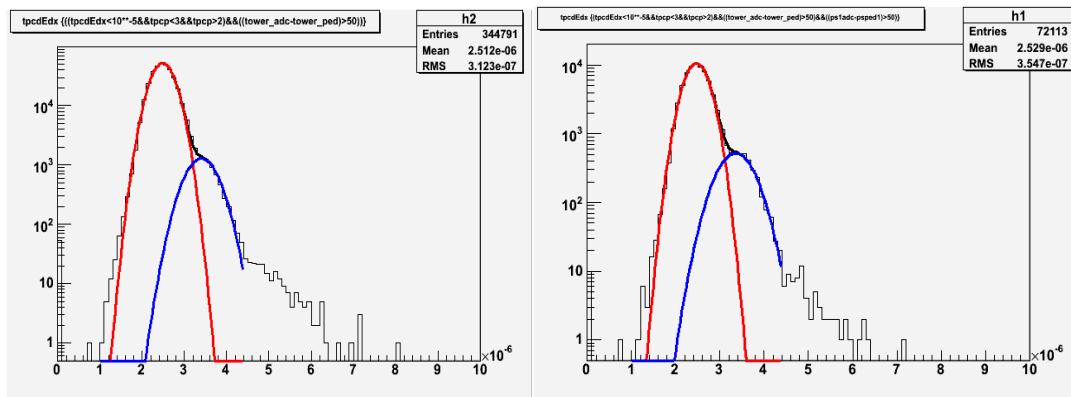


**Figure 1.** Ionization energy loss ( $dE/dx$ ) measured in the Time Projection Chamber (TPC) for tracks with momentum between 2 and 3 GeV/c and associated with a hit tower in the BEMC. In the left plot, the ADC measured in the tower is above the minimum ionizing peak for hadrons, and in the right plot the ADC measured by the Barrel Pre-Shower is also above the minimum ionizing peak. The distribution is fit with 2 gaussians, one for the hadrons (the red peak) and one for the electrons (the smaller, blue peak). The ratio of the integral of the blue gaussian to the integral of the red Gaussian (*ie*, the electron yield to hadron yield) increases from 3% to 7% by adding the cut on the Barrel Pre-Shower.

## II. Gamma-Jet Measurement

The “golden probe” of measuring parton energy loss in heavy-ion collisions is the  $\gamma$ -jet measurement [3]. The idea is to trigger on a “direct” photon, which originates directly from a hard

scattering and does not interact strongly with the medium, and measure the jet on the away-side which does suffer from parton energy loss. For the current Au+Au RHIC run, we have implemented a Level-2 gamma (L2Gamma) trigger to filter events that have a high energy cluster in the BEMC to an express stream (files that will be reconstructed earlier in order to yield results in time for the Quark Matter conference in 2008). The challenge is to separate the direct photons from those originating from  $\pi^0$  decays, particularly when the two decay photons from a  $\pi^0$  hit the same BEMC tower. For this case, the Barrel Shower-Max Detector (BSMD), a wire chamber after 5 layers within the BEMC, can help to distinguish between a single photon shower and 2 photon showers. A first look at the express stream files from the L2Gamma trigger shows a reasonable invariant mass reconstructed from photon pairs (see Fig. 2). The plot on the left is the invariant mass for photon pairs when the two photons hit different BEMC towers, and the right plot shows the case when the two photons hit the same tower (and are separated using the BSMD). The mass calculation is not as good for the right (not exactly at mass=0.135  $\text{GeV}/c^2$ ), presumably because the energy assignments for the separate photons is not perfect when they hit the same tower.

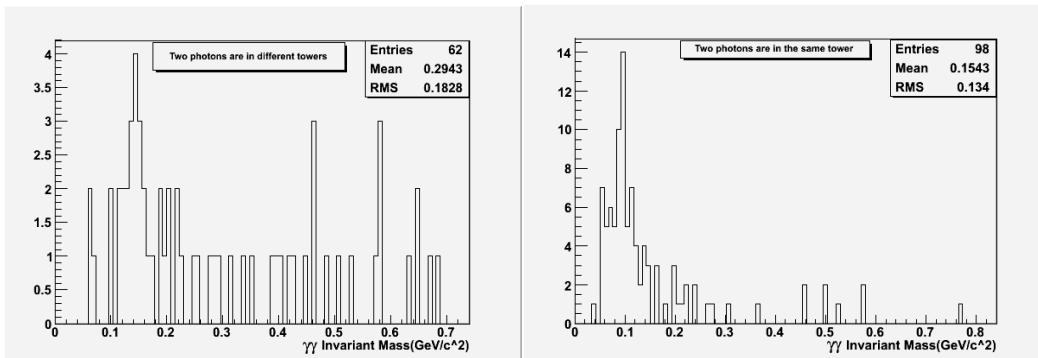


**Figure 2.** Reconstructed invariant mass from Level-2 triggered (L2Gamma) data.

To improve the identification of truly “direct” photons, we are currently running simulations, and comparing the response of the BEMC and BSMD in data to the simulation response. Establishing good agreement between the simulation and the data (see the  $\pi^0$  invariant mass peak in Fig. 3), we can use the

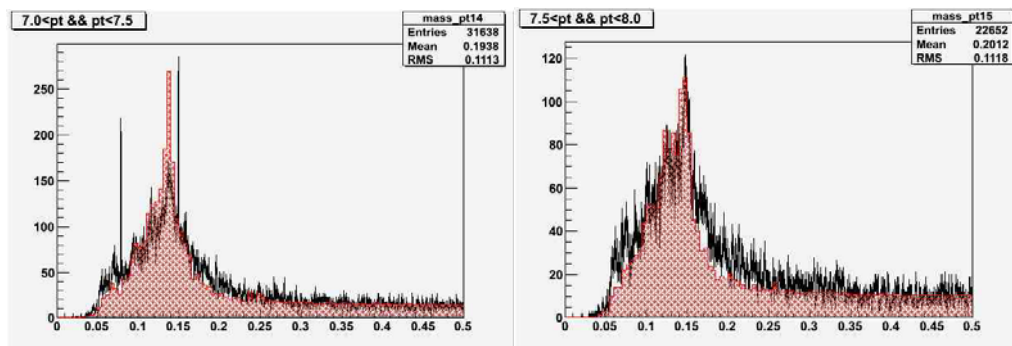


**Figure 3.** Comparison of the reconstructed invariant mass of photon pairs (in  $\text{GeV}/c^2$ ) between p+p data (2006 RHIC run) and simulation. The solid black line is the distribution calculated from the data, and the filled red histogram is from the simulation. The left plot is for the transverse momenta 7.0-7.5  $\text{GeV}/c$  and the right for 7.5-8.0  $\text{GeV}/c$ .

simulation to find stronger cuts to separate direct photons from decay photons.

- [1] Mauro R. Cosentino for the STAR Collaboration, e-Print: [arXiv:0706.0892](https://arxiv.org/abs/0706.0892) [nucl-ex].
- [2] M. Beddo *et al.* (STAR Collaboration), Nucl. Instrum. Methods Phys. Res. **A499**, 725 (2003).
- [3] X-N Wang, Z. Huang, and I. Sarcevic, Phys. Rev. Lett. **77**, 231 (1996).

**SECTION II**  
**HEAVY ION REACTIONS**

## Alternative mechanisms for heavy element production

P. K.Sahu, J. B. Natowitz, R. Wada, K. Hagel, T. Materna, Z. Chen, L. Qin, M. Barbui, S. Moretto, D. Fabris,<sup>1</sup> M. Lunardon,<sup>1</sup> M. Morando,<sup>1</sup> G. Nebbia,<sup>1</sup> S. Pesente,<sup>1</sup> V. Rizzi,<sup>1</sup> G. Viesti,<sup>1</sup> V. Bocci,<sup>2,3</sup> A. Andrighetto,<sup>3</sup> M. Cinausero,<sup>3</sup> G. Prete,<sup>3</sup> Z. Majka,<sup>4</sup> A. Wieloch,<sup>4</sup> and S. Kowalski<sup>5</sup>

<sup>1</sup>*Dipartimento di Fisica dell'Universita di Padova and INFN Sezione di Padova, Italy*

<sup>2</sup>*Dipartimento di Fisica dell'Universita di Brescia and INFN, Italy*

<sup>3</sup>*INFN Laboratori Nazionali di Legnaro, Italy*

<sup>4</sup>*Smoluchowski Institute of Physics, Jagiellonian University, Krakow, Poland*

<sup>5</sup>*Institute of Physics, Silesia University, Katowice, Poland*

The synthesis of superheavy elements (SHE) has been an important field in both theoretical and experimental nuclear physics for many years. Fusion of the doubly-magic neutron-rich <sup>48</sup>Ca projectiles with transuranium target nuclei has led during the past 6 years to the synthesis of elements with Z = 113-116 and 118 [1]. Our aim is to investigate possible alternative reactions to produce such elements. For example, one of the reactions might be one in which the fissile target nucleus (e.g. <sup>238</sup>U and <sup>232</sup>Th) would fission as the projectile approaches and where one of the fragments would fuse with the projectile nucleus. The fission fragments being neutron-rich and close to shell closure, they should enhance the fusion and survival probabilities of the formed superheavy nucleus [2].

The present experiments on BigSol beam line performed on August and December of 2006 are in continuation of the previous experiments carried out in 2003 and 2004 in collaboration with the Istituto Nazionale di Fisica Nucleare (INFN, Italy) and other university as listed in the headings. The superconducting solenoid BigSol was used to collect and focus the reaction products towards a segmented Ionization chamber (IC), with a back plane covered with scintillators, at about 4 meters from the magnet. Two position-sensitive PPACs and a multi-wire proportional counter were placed before the IC, allowing time of flight measurement and trajectory reconstruction. The IC is split into 8 segments. In addition another PPAC was placed near the target area to catch the complementary fragment.

In the experiment of 2003-04, a few tens of events consistent with the expected signature of superheavy ions, appeared mostly in systems at lower energy (7.5 A.MeV), in <sup>197</sup>Au + <sup>232</sup>Th and <sup>238</sup>U + <sup>64</sup>Zn reactions, therefore in the last experiment, we took the whole beam time with the more promising case of Au+Th at 7.5 A. MeV bombarding energy to produce a reasonable number of superheavy candidates.

The data analysis is in progress, we have calibrated all the detectors, and still optimizing the various methods for pileup rejection. The charge distributions were estimated from the time of flight between MWPC and PPAC separated by 1.05 meter and energy loss information in IC from direct beams (Ar, Kr, Xe, Yb, Au, and U) as shown in Figure.1, where the blue lines are the spline through the data that were used for charge estimation, these two lines were first used to reproduce the charge distributions of direct beams (Beam directly going to detectors without targets).

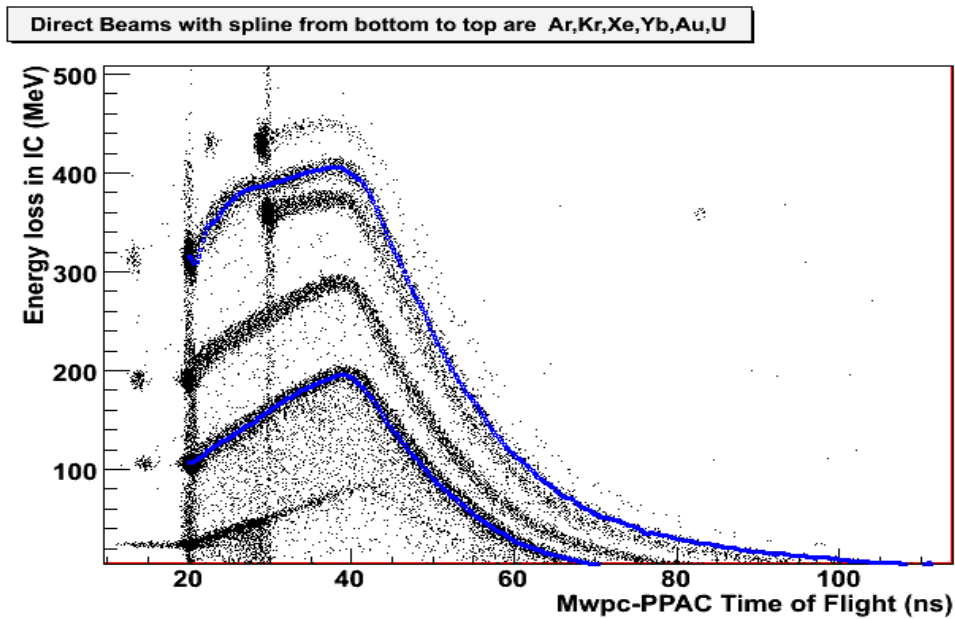


Figure 1. Time of flight versus Energy loss in IC.

- [1] Yu. Ts. Oganessian *et al.*, Phys. Rev. C **74**, 044602 (2006), Yu. Ts. Oganessian *et al.*, Phys. Rev. C **69**, R021601 (2004); Yu. Ts. Oganessian *et al.*, Nature **400**, 242 (1999); Yu. Ts. Oganessian *et al.*, Scientific American **282**, 45 (2000); Yu. Ts. Oganessian *et al.*, Phys. Rev. C **63**, R011301 (2001); Yu. Ts. Oganessian, “JINR Preprint and Communications”, D7-202-287, Dubna, 2002.
- [2] Y. Aritomo, Nucl. Phys. **A780**, 222 (2006), Y. Aritomo, T. Wada, M. Ohta, and Y. Abe, Phys. Rev. C **59**, 796 (1999).

## Z-dependence of isoscaling parameter in central heavy ion collisions at intermediate energy

Z. Chen, R. Wada, T. Keutgen, K. Hagel, J. Wang, L. May, L. Qin,  
J. B. Natowitz, T. Materna, S. Kowalski, and P.K. Sahu

The isoscaling of intermediate mass fragments (IMFs) has been studied in reactions between  $^{64,70}\text{Zn}$ ,  $^{64}\text{Ni}$  projectiles and  $^{58,64}\text{Ni}$ ,  $^{112,124}\text{Sn}$ ,  $^{197}\text{Au}$ ,  $^{232}\text{Th}$  targets at 40 MeV/nucleon. IMFs were detected by a telescope at  $20^\circ$ . The telescope consisted of four Si detectors and a CsI crystal. Each Si detector had 5 cm x 5 cm area. The thicknesses were 129, 300, 1000, 1000 micron, and each Si was segmented into four sections. Each quadrant section of Si was backed by a 3 cm thick CsI(Tl) crystal read by a photo multiplier tube. Isotopes of IMFs were clearly identified from  $Z=3$  up to  $Z=12$  with energy thresholds of 4-8 MeV/nucleon, depending on  $Z$  of the IMFs. In order to minimize the effect of the missing yields below the threshold, which becomes significant for heavier IMFs, the isotope yield ratios for two different reactions were examined as a function of IMF energy and the yield ratios were evaluated as an averaged value over the measured energy range of the given IMFs.

In Fig. 1, the results of isoscaling parameters  $\alpha$ , obtained by fitting yield ratios for different combinations of two reactions, are plotted as a function of  $\Delta(Z/A)^2$ .  $\Delta(Z/A)^2$  is given by

$$\Delta(Z/A)^2 = ((Z/A)_1)^2 - (Z/A)_2^2).$$

Where  $(Z/A)_i$  is the charge to mass ratio of the source of IMF in a given reaction system  $i$ . In the plot

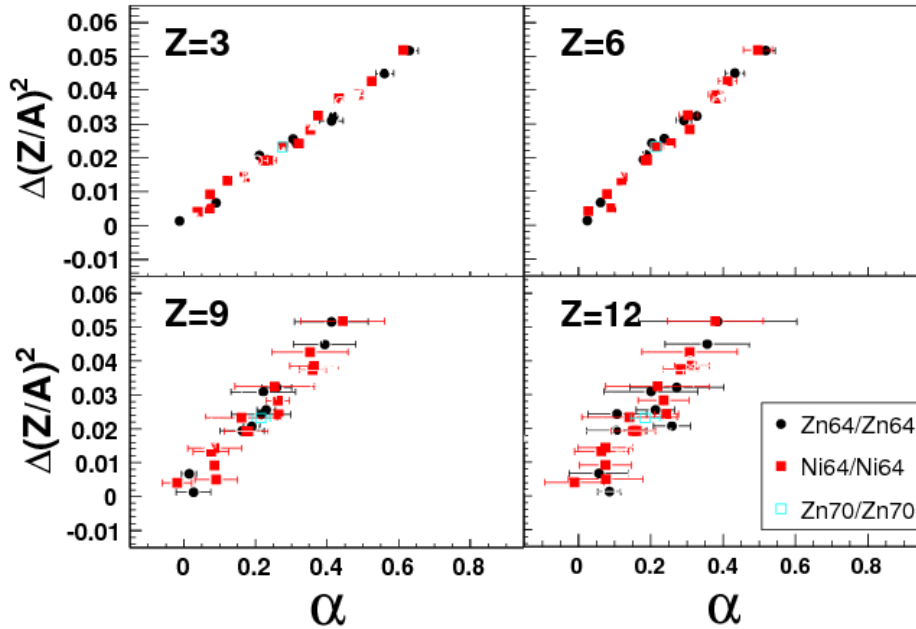


**Figure 1.**  $\alpha$  is plotted as a function of  $\Delta(Z/A)^2$  for different combinations of two reactions.

$\Delta(Z/A)^2$  is calculated from the  $Z/A$  of the compound system. One can clearly see that  $\alpha$  and  $\Delta(Z/A)^2$  are linearly correlated. In general  $\alpha$  can be represented as

$$\alpha = 4C(Z)/T \times \Delta(Z/A)^2.$$

$C(Z)$  is the symmetry energy coefficient and  $T$  is the temperature of the source. In Fig.1 it is also observed that the slope increases with the increase of  $Z$ . In order to study this  $Z$  dependence of  $\alpha$ ,  $\alpha$  is expressed by a linear function of  $Z$  as  $\alpha = a1 * Z + a0$ .

In Fig. 2,  $a1$  is plotted as a function of  $\Delta(Z/A)^2$ . It is found that the slope  $a1$  is also linearly correlated to  $\Delta(Z/A)^2$ . In order to understand the linear correlation of  $\alpha$  and  $a1$  as a function of  $\Delta(Z/A)^2$ , calculations of an anti-symmetrized molecular dynamics model (AMD) are being performed. Further detailed study is now underway.

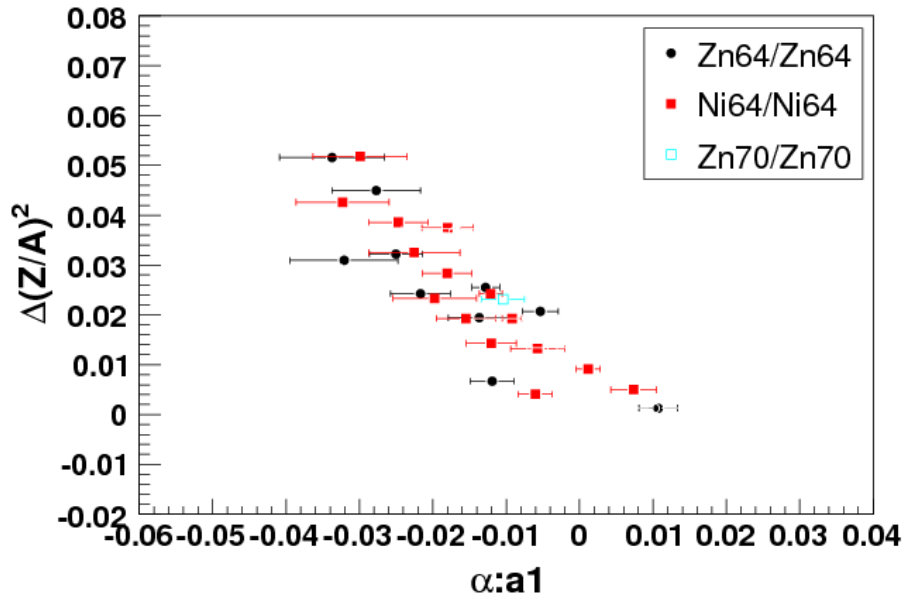


**Figure 2.** Linear coefficient  $a1$  is plotted as a function of  $\Delta(Z/A)^2$ , see detail in the text.

## Dynamical and statistical nature of heavy ion reactions at 47A MeV

L. J. Qin, R. Wada , K. Hagel , J. B. Natowitz, J. S. Wang, Y. Ma, T. Materna ,  
T. Keutgen, Z. Chen, and P. K Sahu

In order to investigate the dynamics and thermodynamics in light ion and heavy ion collisions near the Fermi Energy, we compared the yield, energy spectra and angular distribution of products observed from different reaction systems at the same incident energy. To do this, a series of heavy ion reaction systems have been studied using a  $4\pi$  detector array NIMROD at the Cyclotron Institute at Texas A&M University. The systems studied, all at an incident energy of 47A MeV, are shown in Table I.

**Table I.** Reaction List.

${}^1_1\text{H} + {}^{112}_{50}\text{Sn}$	${}^1_1\text{H} + {}^{124}_{50}\text{Sn}$
${}^2_1\text{H} + {}^{112}_{50}\text{Sn}$	${}^2_1\text{H} + {}^{124}_{50}\text{Sn}$
${}^3_2\text{He} + {}^{112}_{50}\text{Sn}$	${}^3_2\text{He} + {}^{124}_{50}\text{Sn}$
${}^4_2\text{He} + {}^{112}_{50}\text{Sn}$	${}^4_2\text{He} + {}^{124}_{50}\text{Sn}$
${}^{10}_5\text{B} + {}^{112}_{50}\text{Sn}$	${}^{10}_5\text{B} + {}^{124}_{50}\text{Sn}$
${}^{20}_{10}\text{Ne} + {}^{112}_{50}\text{Sn}$	${}^{20}_{10}\text{Ne} + {}^{124}_{50}\text{Sn}$
${}^{40}_{18}\text{Ar} + {}^{112}_{50}\text{Sn}$	${}^{40}_{18}\text{Ar} + {}^{124}_{50}\text{Sn}$
${}^{64}_{30}\text{Zn} + {}^{112}_{50}\text{Sn}$	${}^{64}_{30}\text{Zn} + {}^{124}_{50}\text{Sn}$

In the analysis, we separated emission resulting from nucleon-nucleon collisions from those resulting from the thermalized system using three source emission model. In order to obtain information, such as the temperature evolution, in-medium nucleon-nucleon cross sections, isospin effects, and symmetry energy for the dynamic evolution of the hot systems, particle multiplicity distributions at different velocities has been studied. Emphase has been made on the symmetry potential, including the density dependence, by comparing at different densities and different system N/Z ratios of emitting sources produced at the interaction region during the reaction process.

Several promising probes for the symmetry energy term at subnormal density have been proposed. One of these is the ratio between the yields of t and  ${}^3\text{He}$ . This ratio has been shown as a sensitive probe for the symmetry energy using different simulation codes [1-3,5,6].

We classify events into four different groups which correspond to different collision violence using the multiplicity distribution, as shown in Fig. 1 in the case for  ${}^{64}\text{Zn} + {}^{124}\text{Sn}$  reaction system. We currently focus on the most violent events in the 30% largest light particle multiplicity window.

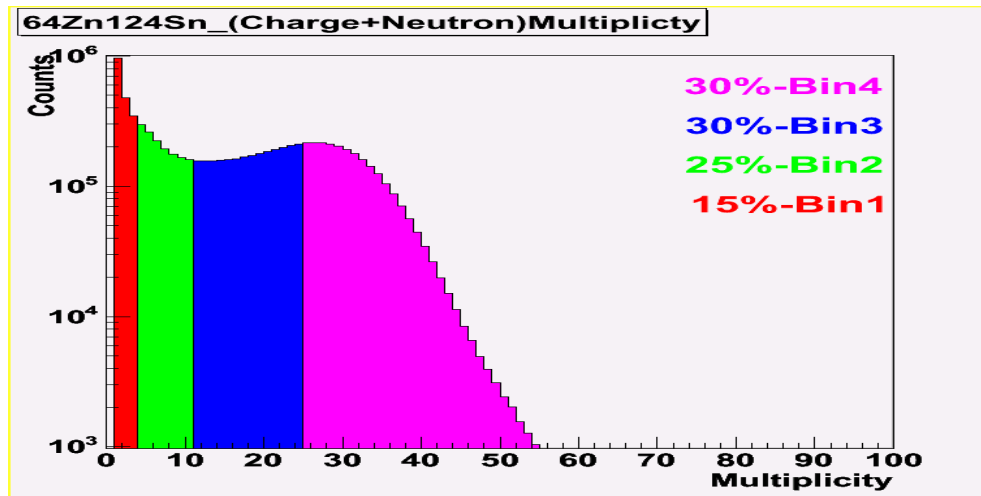


Figure 1. Multiplicity distribution of reaction system  $^{64}\text{Zn}+^{124}\text{Sn}$

Using those events we evaluated different observables in the invariant 2-D velocity plots for each reaction system, so that the physics quantities of interest can be studied in the different velocity regions.

In the following we show results of the evolution of  $t/{}^3\text{He}$  ratio, temperature and isoscaling parameters. In Fig.2 the  $t/{}^3\text{He}$  ratio is plotted for the systems  $^{40}\text{Ar}+^{112}\text{Sn}$  and  $^{40}\text{Ar}+^{124}\text{Sn}$  in the left and right panels, respectively. Both of the plots show that, from the low velocity region to the high velocity region, the  $t/{}^3\text{He}$  ratio is decreasing. Although the  $N/Z$  ratios of those two systems are different, the dynamic evolution of systems should be similar because of similar reaction systems and the same incident energy. The difference in the  $t/{}^3\text{He}$  ratio may, therefore, reflect the difference in the symmetry energy term [5].

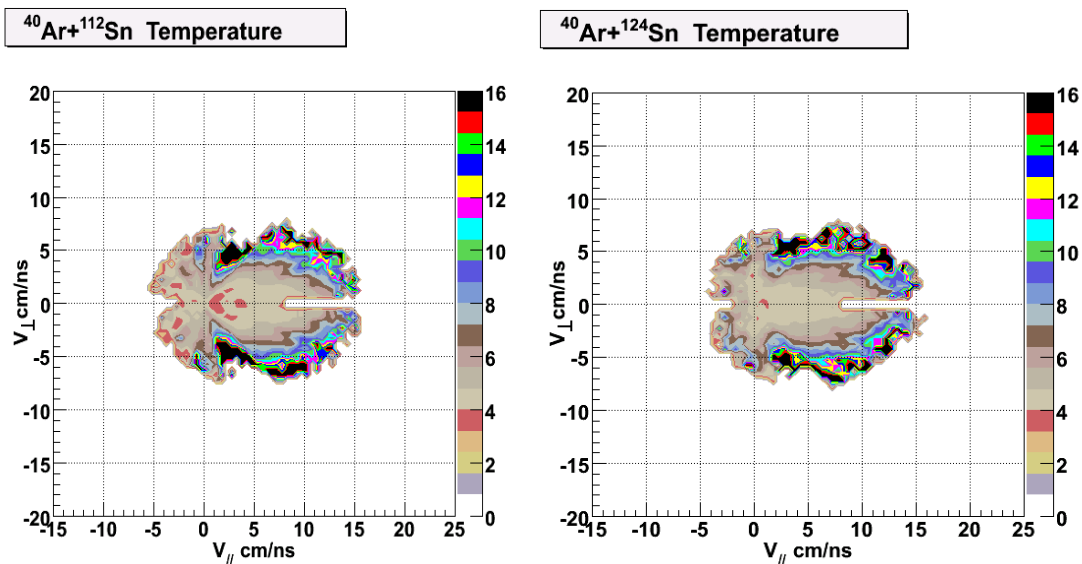
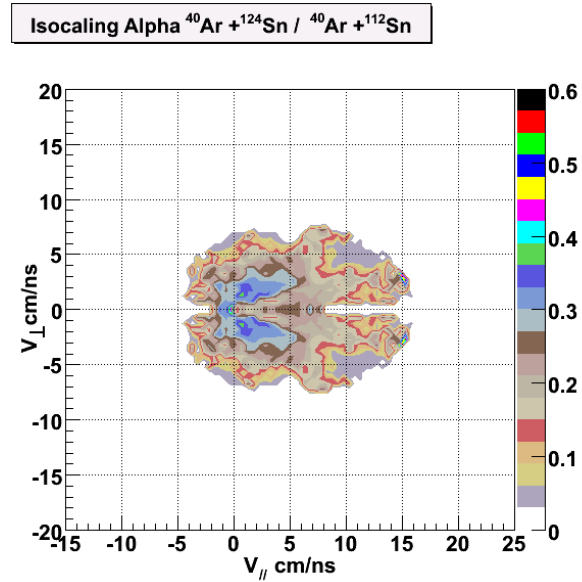


Figure 3. Temperature evolution in invariant velocity plot.

To characterize the temperature evolution of the system, the double isotope temperature has been calculated using the yields of d, t,  $^3\text{He}$ , and  $^4\text{He}$  clusters in each segment of the invariant velocity plot. The results for the systems  $^{40}\text{Ar}+^{112}\text{Sn}$  and  $^{40}\text{Ar}+^{124}\text{Sn}$  are shown in Fig. 3. At the same velocity regions, the temperature in both of the systems looks very similar and increases as the velocity increases, which indicates that high velocity particles are emitted at higher temperatures and, therefore, at an early stage of the reaction.

The isoscaling parameter of the two systems was also calculated for  $Z = 1$  and  $Z = 2$  particles. Isotope or isotone yield ratios were fitted globally to obtain  $\alpha$  and  $\beta$ . In Fig.4, the isoscaling parameters  $\alpha$  are plotted in 2-D invariant surface velocity frame [7]. Alpha values are different in the different velocity regions. The alpha values are high in low velocity regions, and gradually decrease toward high velocity regions which may reflect the  $N/Z$  ratios of different sources. The alpha parameter at a given velocity segment is related to the local temperature and symmetry energy. Further detailed study to determine the symmetry energy is now underway.



**Figure 4.** Alpha parameters extracted from systems  $^{40}\text{Ar}+^{112}\text{Sn}$  and  $^{40}\text{Ar}+^{124}\text{Sn}$ .

We also use AMD model for better understanding of the reaction mechanics and the nature of hot nuclear matter. We continue our analysis of symmetry free energy and density evolution in the invariant velocity frame.

- [1] Jian-Ye Liu *et al.*, Phys. Rev. Lett. **86**, 975 (2001).
- [2] Lie-Wen Chen *et al.*, Phys. Rev. Lett. **90**, 162701 (2003).
- [3] Ph. Chomaz *et al.*, Phys. Lett. **B447**, 221 (1999).
- [4] K. Hagel *et al.*, Phys. Rev. C **62**, 034607 (2000).
- [5] Y. Zhang *et al.*, Phys. Rev. C **71**, 024604 (2005).
- [6] <http://cyclotron.tamu.edu/nimrod.htm>
- [7] S. Kowalski *et al.*, Phys. Rev. C **75**, 014601 (2007).

## Progress in BRAHMS

K. Hagel, R. Wada, J. B. Natowitz and the BRAHMS Collaboration

BRAHMS completed the baseline program in June, 2006 with the measurement of  $p + p$  collisions having  $\sqrt{s_{nn}} = 63$  GeV during RHIC Run-VI. The  $p + p$  measurement at  $\sqrt{s_{nn}} = 63$  provides both a baseline measurement for the RAA studies at  $\sqrt{s_{nn}} = 63$  as well as information of the Single Spin Asymmetry studies that a number of researchers in the BRAHMS Collaboration are pursuing.

The BRAHMS collaboration completed the analysis of several topics and submitted results for publication. An example of such analysis is shown in figure 1 where we plot the nuclear modification factor for negative pions and anti-protons at mid-rapidity and forward pseudorapidity ( $\eta=2.2$ ) [1]. We note the well known suppression for the pions, but the anti-protons are not suppressed. Furthermore the stronger pion suppression at forward pseudorapidity suggests that other nuclear effects such as gluon saturation may contribute. The differences in suppression have been noted to depend on whether the hadron is a baryon or a meson. [2] The observations are consistent with a picture of forming a strongly interacting partonic matter with strong collective flow over a large rapidity range that boosts protons to

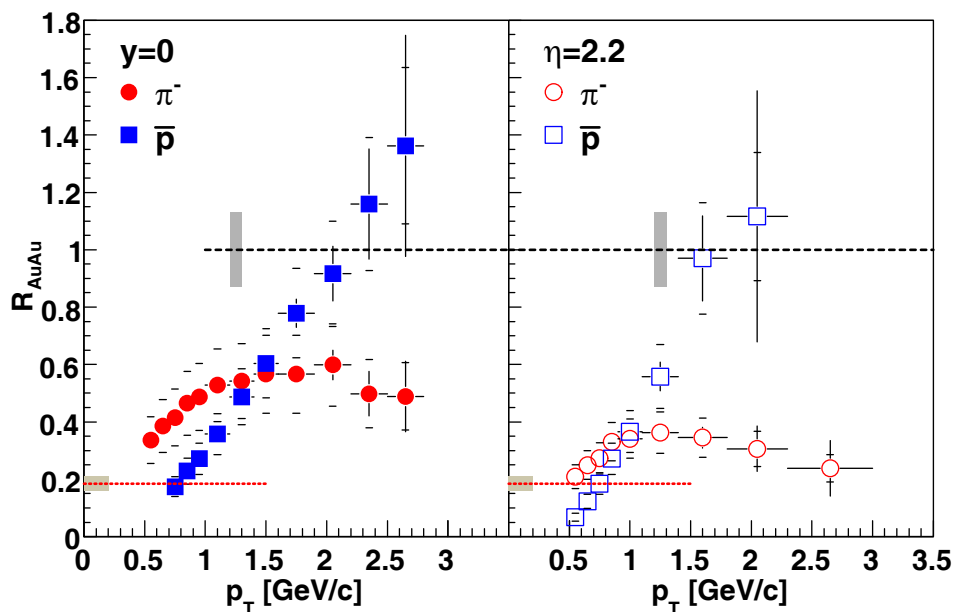


**Figure 1.** Nuclear modification factor for negative pions and anti-protons at mid-rapidity (left panel) and  $\eta=2.2$ .

higher transverse momenta and is responsible for the strong suppression of pions.

There is also a study on high  $p_T$  baryon and meson production in  $p + p$  collisions at  $\sqrt{s_{nn}} = 200$  GeV [3] as well as the report of a study on the rapidity dependence of high  $p_T$  suppression at  $\sqrt{s_{nn}} = 63$  GeV [4].

The local group at Texas A & M is working on the soft physics analysis of the Run V  $p + p$ . The calibration of the time of flight hodoscopes as well as the vertex counters is basically complete and preliminary versions of the spectra at rapidities less than 1 have been extracted. Preliminary spectra of the 90 deg setting of the mid-rapidity spectrometer are shown in figure 2. We are in the process of refining the details of these spectra as well as generating spectra for the other settings of the mid-rapidity spectrometer, namely the 34, 40, 45, 52.5 and 60 deg settings.

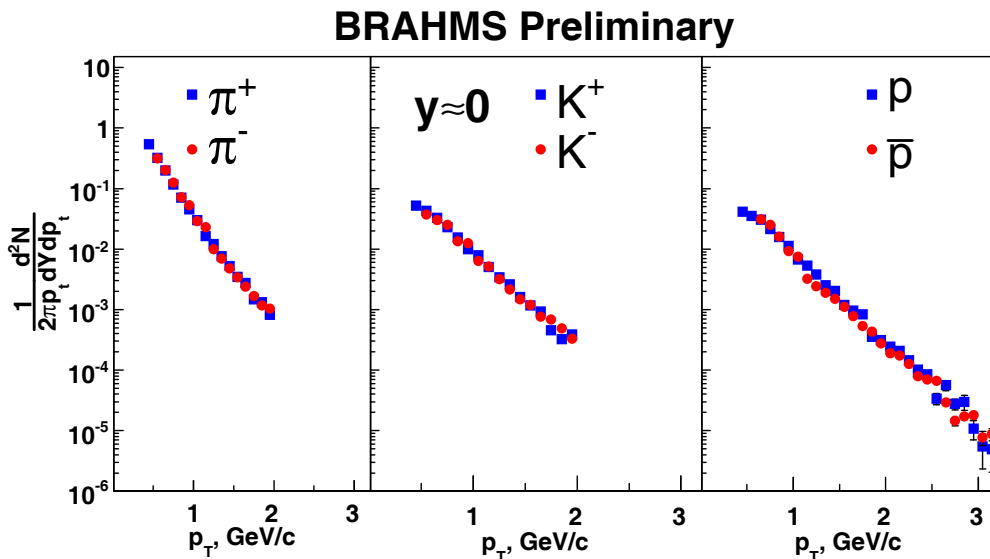


**Figure 2.** Preliminary spectra at  $y=0$  for positive (solid squares) and negative (solid circles) pions, kaons and protons.

- [1] I. Arsene *et al.*, nucl-ex/0602018; Phys. Lett. B (accepted).
- [2] P. Jacobs and Xin-Nian Wang, hep-ph/0405125 (2004).
- [3] I. Arsene *et al.*, hep-ex/0701041nucl-ex/0602018; Phys. Rev. Lett. (accepted).
- [4] I. Arsene *et al.*, nucl-ex/0602018 (2006).

## N/Z equilibration in deep inelastic collisions

A. L. Keksis, M. Veselsky, G. A. Souliotis, D. V. Shetty, M. Jandel, E. Bell, A. Ruangma, E. M. Winchester, J. Garey, S. Parketon, C. Richers, and S. J. Yennello

When target and projectile nuclei have a difference in N/Z, the quasiprojectiles formed in deep inelastic collisions should have a mean N/Z between that of the N/Z of the target and the N/Z of the projectile. This depends on the amount of N/Z equilibration that has occurred. Six reaction systems at two beam energies, 32 and 45 MeV/nucleon, were studied. The systems, in order of increasing difference between target and projectile N/Z (shown in parentheses), were  $^{40}\text{Ar} + ^{112}\text{Sn}$  (0.018),  $^{48}\text{Ca} + ^{124}\text{Sn}$  (0.080),  $^{48}\text{Ca} + ^{112}\text{Sn}$  (0.160),  $^{40}\text{Ca} + ^{112}\text{Sn}$  (0.240),  $^{40}\text{Ar} + ^{124}\text{Sn}$  (0.258) and  $^{40}\text{Ca} + ^{124}\text{Sn}$  (0.480). The projectiles were produced in the advanced electron cyclotron resonance ion source and accelerated by the Texas A&M University Cyclotron Institutes K500 superconducting cyclotron. The fragments from the reactions were measured with FAUST, the Forward Array Using Silicon Technology, which was composed of 68 Si-CsI telescopes that had 90% angular coverage between 2 and 33 degrees [1, 2].

Two techniques were used to determine the quasiprojectile N/Z. The first technique used the isotopically resolved fragments to reconstruct the quasiprojectile N/Z. Reconstruction also provided a route for source determination by requiring that the quasiprojectile charge equaled the projectile charge plus or minus 2. This reconstruction was affected by neutron loss, which made the apparent quasiprojectile N/Z lower than the true value. Reconstruction is described in detail in the appendix of [3]. The second technique, developed in this study, is not neutron dependent. Fragments form in the quasiprojectile source experiencing the N/Z of the source. The fragments therefore retain a memory of the N/Z of the quasiprojectile source.

Using yield ratios, such as the isobaric yield ratios, from a variety of systems that have a range in N/Z of the quasiprojectile source, coupled with a simple equation:

$$\frac{N}{Z}_{\text{Quasiprojectile}} = X \frac{N}{Z}_{\text{Target}} + Y \frac{N}{Z}_{\text{Projectile}}$$

are used to simultaneously fit the fragment yield ratios of all six systems to determine the quasiprojectile N/Z. The X value is the target contribution and the Y value is the projectile contribution. These were found to be 39% and 61%, respectively. The global fitting using all isobaric yield ratios for all systems at 32 MeV/nucleon at  $7^\circ$  is shown in Figure 1. Table I shows the results from both techniques on experimental and theoretical data for all 12 systems. Compared to a fully N/Z equilibrated quasiprojectile, the quasiprojectiles formed in this study are 54% equilibrated [3].

The quasiprojectile N/Z values determined by the yield ratio technique were much larger than those determined by the reconstruction technique. The question arose whether this is caused purely from neutron loss. This question was resolved by using simulations to form (DIT of Tassan-Got) and de-excite (SMM of Botvina) quasiprojectiles. The fragments formed were filtered to the acceptance of FAUST and

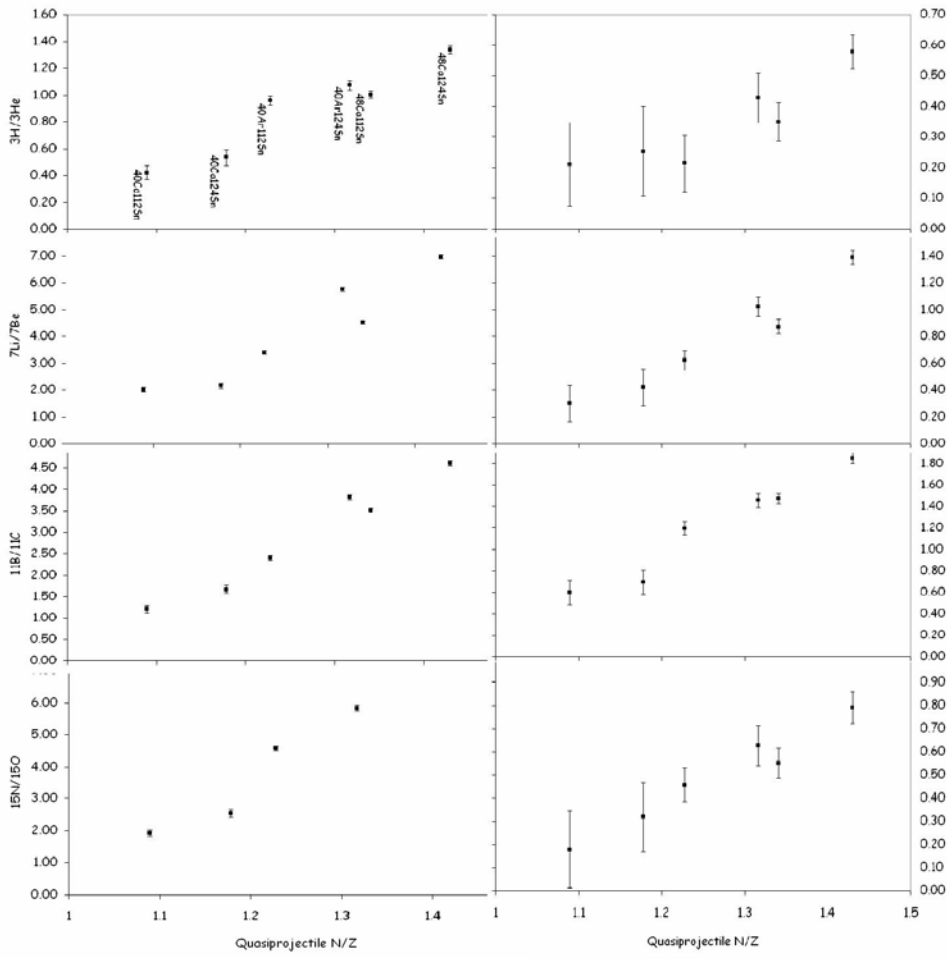


**Figure 1.** Results of global fitting of the isobaric yield ratios of all six systems at 32 MeV/nucleon at 7°.

then analyzed like experimental fragments, yielding similar results. In the simulations the quasiprojectile N/Z was known and compared to the results that used the yield ratio technique. The comparison showed that the yield ratio technique approximated the quasiprojectile N/Z [3]. Further modification of the equation used in the yield ratio technique, such as taking into account masses of target and projectile, might improve the approximation. Since the quasiprojectile N/Z was known, the neutron loss was calculated and was shown that the more neutron rich systems lose more neutrons (See Table 1). This accounts for the differences between the reconstruction and yield ratio techniques.

**Table I.** Summary of the results from experiment and DIT/SMM calculations using both techniques. 32 MeV/nucleon systems on top and 45 MeV/nucleon systems on bottom. The calculations have a known N/Z of the quasiprojectile and can be back tracked to study the neutron loss.

System	N/Z		N/Z	N/Z	N/Z	N/Z	N/Z	N/Z	Neutron Loss
	Tar.	Proj.	Comp. Sys.	Exp. Recon.	Exp. Fit.	Sim. Recon.	Sim. Fit.	DIT Back Track	
$^{40}\text{Ar} + ^{112}\text{Sn}$	1.24	1.22	1.24	1.00	1.23	1.03	1.23	1.17	3.36
$^{40}\text{Ar} + ^{124}\text{Sn}$	1.48	1.22	1.41	1.02	1.32	1.08	1.34	1.27	4.08
$^{40}\text{Ca} + ^{112}\text{Sn}$	1.24	1.00	1.17	0.98	1.09	0.97	1.11	1.04	2.31
$^{40}\text{Ca} + ^{124}\text{Sn}$	1.48	1.00	1.34	0.99	1.19	1.00	1.22	1.12	2.86
$^{48}\text{Ca} + ^{112}\text{Sn}$	1.24	1.40	1.29	1.03	1.34	1.08	1.33	1.27	5.19
$^{48}\text{Ca} + ^{124}\text{Sn}$	1.48	1.40	1.46	1.05	1.43	1.13	1.44	1.39	6.10
$^{40}\text{Ar} + ^{112}\text{Sn}$	1.24	1.22	1.24	0.99	1.23	1.02	1.23	1.17	3.73
$^{40}\text{Ar} + ^{124}\text{Sn}$	1.48	1.22	1.41	1.01	1.32	1.06	1.30	1.25	4.21
$^{40}\text{Ca} + ^{112}\text{Sn}$	1.24	1.00	1.17	0.95	1.09	0.94	1.08	1.03	2.59
$^{40}\text{Ca} + ^{124}\text{Sn}$	1.48	1.00	1.34	0.96	1.18	0.98	1.15	1.10	2.97
$^{48}\text{Ca} + ^{112}\text{Sn}$	1.24	1.40	1.29	0.91	1.34	1.07	1.35	1.27	5.57
$^{48}\text{Ca} + ^{124}\text{Sn}$	1.48	1.40	1.46	0.89	1.43	1.12	1.43	1.38	6.20

- [1] F. Gimeno-Nogues, D. J. Rowland, E. Ramakrishnan, S. Ferro, S. Vasal, R.A. Gutierrez, R. Olsen, Y.-W. Lui, R. Laforest, H. Johnston and S. J. Yennello, Nucl. Instrum. Methods Phys. Res. **A399**, 94 (1997).
- [2] D. J. Rowland, Ph. D Thesis, Texas A&M University, 2000.
- [3] A. L. Keksis, Ph. D. Thesis, Texas A&M University, 2007.

## The fragmentation of quasiprojectiles

A. L. Keksis, M. Veselsky, G. A. Souliotis, D. V. Shetty, M. Jandel, E. Bell, A. Ruangma, E. M. Winchester, J. Garey, S. Parketon, C. Richers, and S. J. Yennello

Fragments emitted from quasi projectile formed from the reactions of  $^{40}\text{Ca}$ ,  $^{40}\text{Ar}$ ,  $^{48}\text{Ca}$  with  $^{112,124}\text{Sn}$ , were studied using the FAUST array. Isobaric, isotopic, fractional and mean N/Z yield comparisons were made between systems [1]. These comparisons showed that the neutron richness of the system affected the fragment yields, with the neutron-rich nuclides populated preferentially by the neutron-rich systems; the neutron-poor nuclides populated preferentially by the neutron-poor systems. This trend is observed at all angles and all nuclides. For an example figure 1 shows the carbon fractional yields at both energies at  $7^\circ$ .

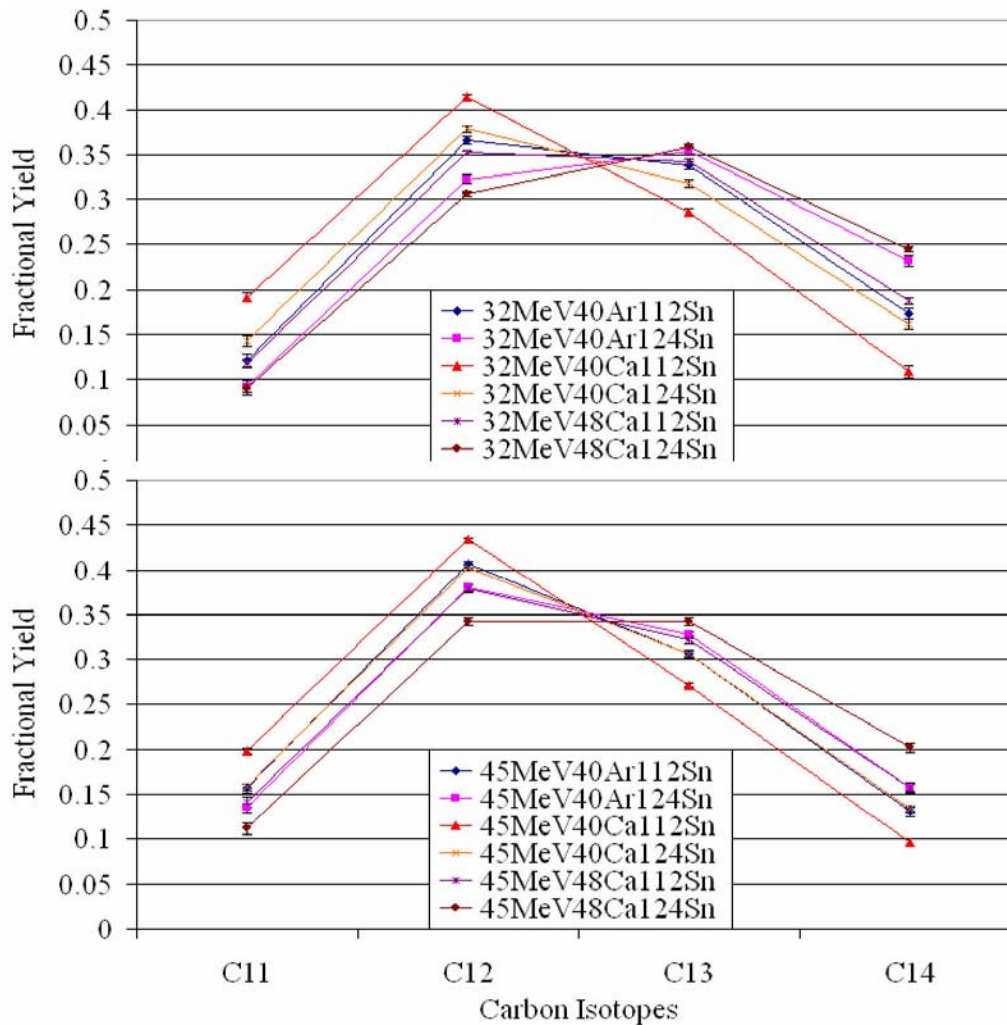


**Figure 1.** Carbon fractional yields for the 32 MeV/nucleon systems top and 45 MeV/nucleon systems bottom at the lab angle of  $7^\circ$ .

The  $N/Z$  distribution of the fragment yields was studied to observe an inhomogeneous  $N/Z$  distribution between the LCP's (Light Charged Particles:  $Z < 3$ ) and IMF's (Intermediate Mass Fragments:  $Z > 2$ ) [1]. Figure 2 shows the multiplicity of LCP's, IMF's and Total. The results showed a new trend. Previous studies had shown that increased proton richness increases the LCP multiplicity dramatically, while the IMF multiplicity remained nearly constant [2]. For increasing neutron richness the previous studies suggested that the neutron-rich LCP multiplicity would increase; however, this work showed that the IMF multiplicity increases, while the LCP multiplicity stays nearly constant with increasing neutron richness.

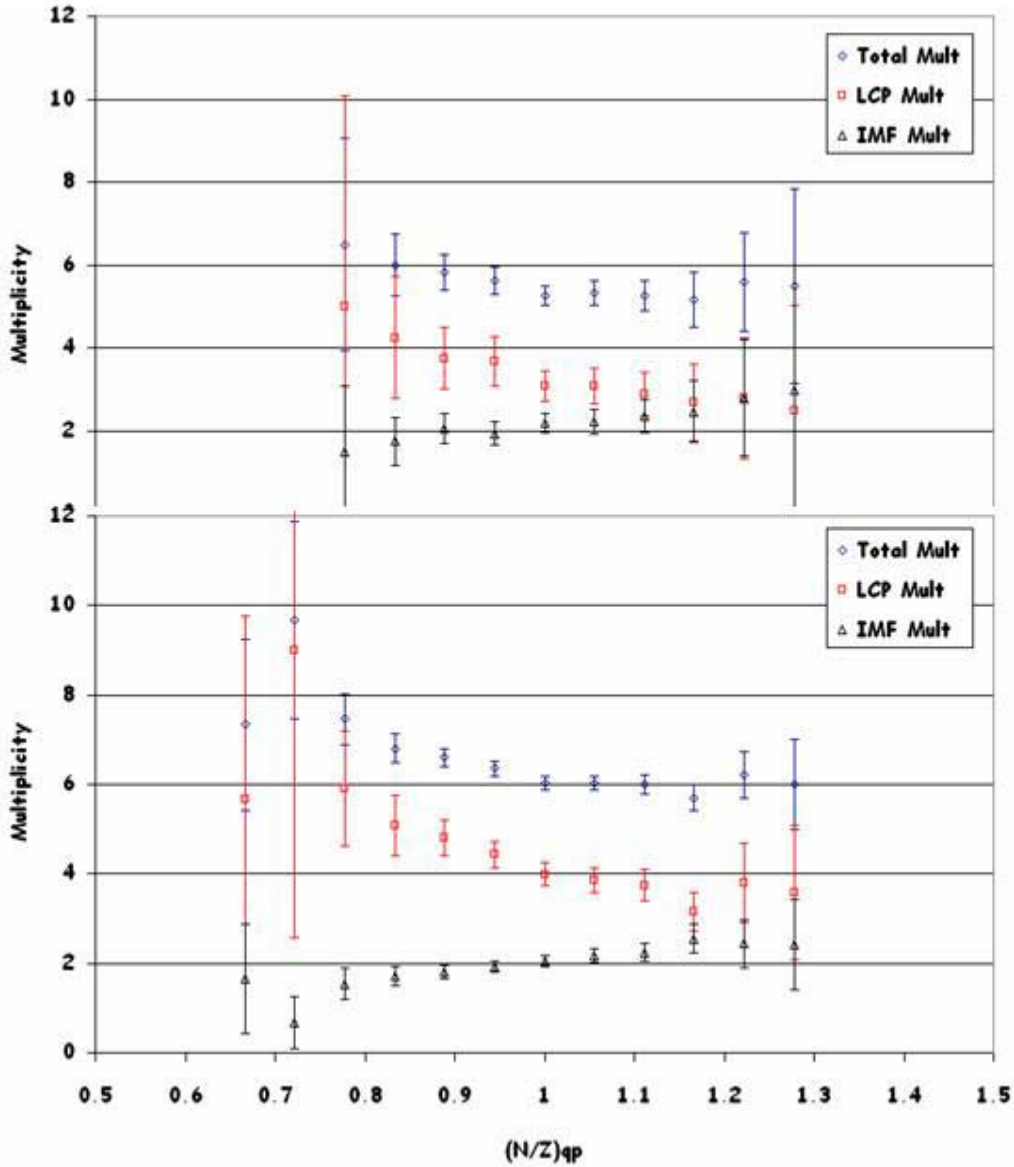


**Figure 2.** Multiplicity of LCP's, IMF's and Total as a function of  $N/Z$  of the quasiprojectile source for the  $^{40}\text{Ar}$  on  $^{112}\text{Sn}$  systems. 32 MeV/nucleon on top and 45 MeV/nucleon on bottom. Error bars are statistical.

The inhomogeneous distribution of N/Z was also studied using the mean N/Z of the IMF divided by the mean N/Z of the LCP shown in figure 3 [1]. The results were in accord with previous studies, however this work went further and showed that there was a dependence of the mean N/Z of the IMF on the quasiprojectile N/Z [1, 2].

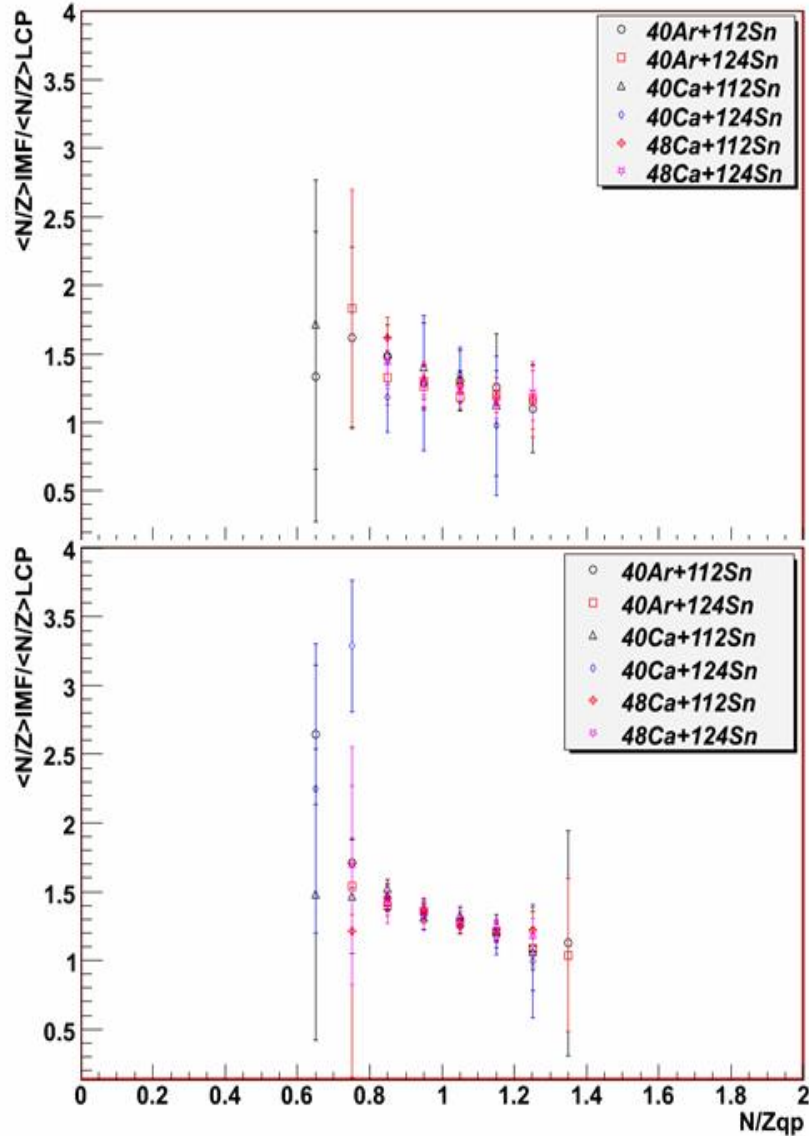


**Figure 3.** The ratio of the mean N/Z of the IMF and the mean N/Z of the LCP versus the N/Z of the quasiprojectile. 32 MeV/nucleon systems on top and 45 MeV/nucleon systems on bottom.

Finally the inhomogeneous distribution of N/Z was studied using the mirror nuclei ratios  ${}^3\text{H}/{}^3\text{He}$ ,  ${}^7\text{Li}/{}^7\text{Be}$ ,  ${}^{11}\text{B}/{}^{11}\text{C}$  and  ${}^{15}\text{N}/{}^{15}\text{O}$  [1]. Figure 4 shows the  ${}^{11}\text{B}/{}^{11}\text{C}$  ratio. Previous studies had only used the  ${}^3\text{H}/{}^3\text{He}$  ratio and observed an increase of the ratio with increasing quasiprojectile N/Z [2]. This work demonstrated that all of the mirror ratios increased with increasing quasiprojectile N/Z [1].

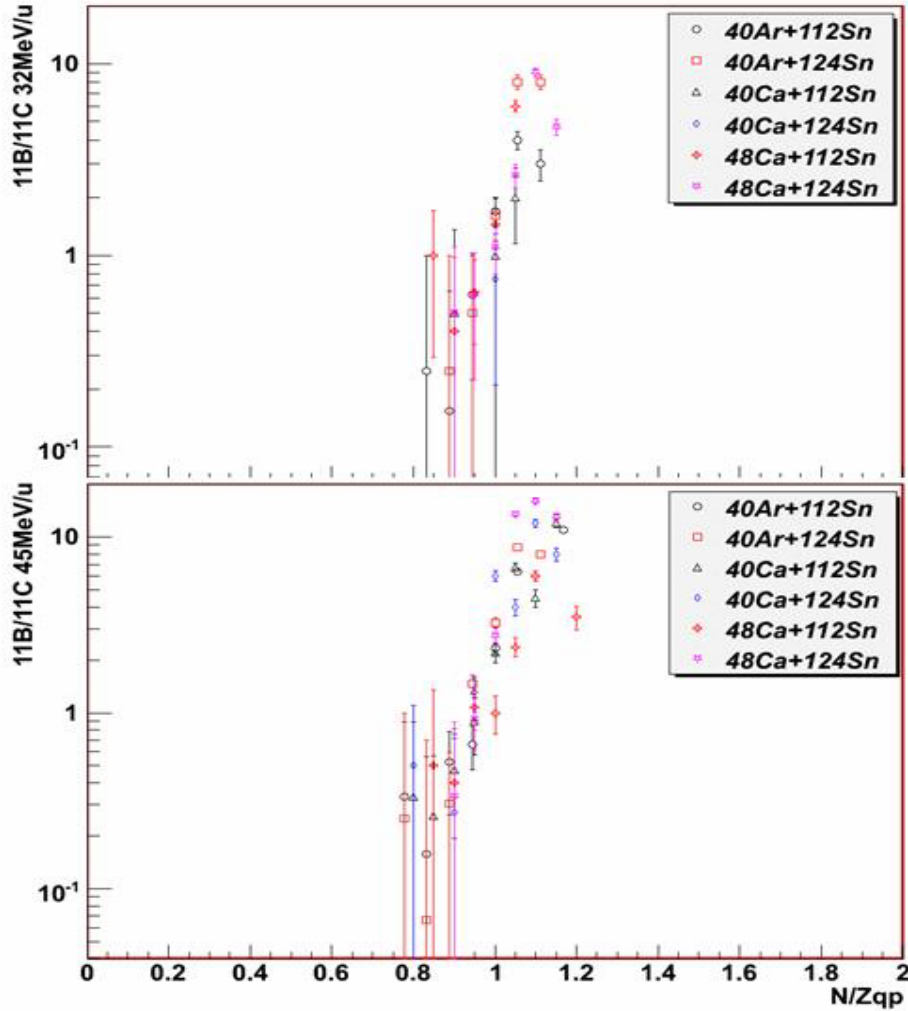


**Figure 4.** The  ${}^{11}\text{B}/{}^{11}\text{C}$  ratio as a function of quasiprojectile N/Z. 32 MeV/nucleon systems on top and 45 MeV/nucleon systems on bottom.

[1] A. L. Keksis, Ph. D. Thesis, Texas A&M University, 2007.

[2] M. Veselsky, R. W. Ibbotson, R. Laforest, E. Ramakrishnan, D. J. Rowland, A. Ruangma, E. M. Winchester, E. Martin, and S. J. Yennello. Phys. Rev. C **62**, 041605R (2000).

## Nucleon transfer calculations using HIPSE model

Z. Kohley, D. Lacroix, G. A. Souliotis, A. L. Keksis, B. Stein, D. V. Shetty,  
S. Soisson, and S. J. Yennello

The HIPSE (heavy-ion phase-space exploration) model, by Lacroix *et al.*, has been used to examine nucleon transfer during the interaction of the projectile and target [1]. The results of the HIPSE model were compared to experimental data obtained on the FAUST array (Forward Array Using Silicon Technology) for  $^{20}\text{F} + ^{108}\text{Ag}$ ,  $^{20}\text{F} + ^{197}\text{Au}$ ,  $^{20}\text{Na} + ^{197}\text{Au}$ , and  $^{20}\text{Ne} + ^{197}\text{Au}$  at 32 MeV/u [2]. The apparent mass change of the projectile was calculated for fully reconstructed events, in which the total detected charge was equal to the charge of the beam ( $\sum Z_{\text{detected}} = Z_{\text{beam}}$ ) [2]. Since neutrons were not detected, the mass change of projectile,  $\Delta N$ , represents the change in the number of neutrons between the projectile and the reconstructed quasiprojectile, as shown in equation 1:

$$\Delta N_{\text{app}} = A_{\text{beam}} - \sum_i^{\text{CP Mult}} A_{\text{fragment},i} \quad (1)$$

The  $\Delta N$  is a product of two mechanisms: the transfer of neutrons between the target and projectile and the evaporation of neutrons from the excited QP.

DIT/GEMINI and DIT/SMM was originally used for comparison of  $\Delta N$  with the experimental data, as shown in Ref. [2]. However, both DIT/GEMINI and DIT/SMM underestimated the transfer of neutrons to the projectile for the less neutron rich systems,  $^{20}\text{Na} + ^{197}\text{Au}$ , and  $^{20}\text{Ne} + ^{197}\text{Au}$ . These results suggested that DIT was incorrectly accounting for the change in nucleon transfer with respect to the changing N/Z of the system.

HIPSE provides another model in which the interaction, or transfer, stage of the reaction can be examined. HIPSE was used to generate quasiprojectiles for the aforementioned systems. The quasiprojectiles were then de-excited using the SIMON or SMM codes and the resulting fragments were filtered according to the geometrical and energetic acceptances of the FAUST array. The results, shown in Figure 1, demonstrate that the HIPSE calculations are in agreement with the experimental data for the more neutron rich systems. However, for the less neutron rich  $^{20}\text{Na}$  and  $^{20}\text{Ne}$  systems the HIPSE results overestimate the neutron loss from the projectile. These results could be attributed to an incorrect amount of transfer between the target and projectile or an overestimate of the loss of neutrons through the pre-equilibrium emission of HIPSE and the free neutron evaporation of SIMON and SMM.

The HIPSE code has a parameterized input for the amount of nucleon transfer between the target and projectile that occurs inside the interaction region. At 32 MeV/u the percent of nucleon transfer was set to 40%. The HIPSE model does not differ in its treatment of neutron or proton transfer. The fact that HIPSE seems to compare better with the more neutron rich systems might eventually be an indication that the nucleon transfer is isospin dependent. Therefore, the HIPSE model was modified, by Lacroix, in order to allow for the percent transfer of neutrons and protons to be input independently. As shown in Figure 1, when the percent transfer for protons and neutrons are set to 30% and 50%, respectively, only a slight

difference is observed. Also shown in Figure 1, is the results of changing the level density parameter,  $A$ , in the de-excitation code SIMON. The default value of the level density parameter in SIMON was changed from 10 to 8. The results, again, show no significant changes in the distribution.

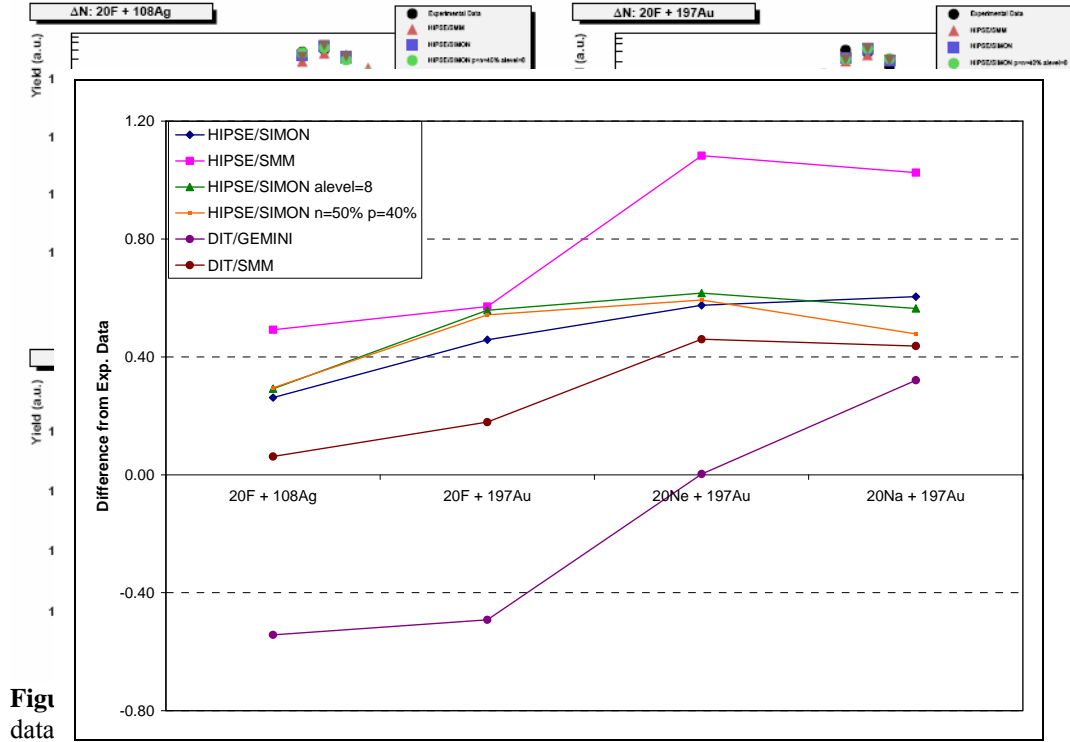


**Figure 2.** The differences between the simulated and the experimental mean values of the  $\Delta N$  plots. DIT/SMM and DIT/GEMINI results taken from Ref. [2].

A more quantitative comparison of the different simulation methods used is shown below in Figures 2 and 3. In Figure 2, the differences in the mean values of the experimental data versus the simulation results are shown. It is evident that for the neutron rich systems DIT/SMM is the most accurate, while DIT/GEMINI has the best agreement with the less neutron rich systems. The HIPSE code is clearly overestimating the mean value of the neutron transfer. In Figure 3, the difference between the experimental and simulated distribution widths are plotted. The distribution width is represented by the sigma value from a Gaussian fit of the  $\Delta N$  plot. It is interesting to note that even though the DIT/SMM results were able to better reproduce the mean values, the HIPSE/SIMON results provide the best overall agreement with the width of the distributions. This suggests that HIPSE is able to better reproduce the amount of reactions in which a large transfer of nucleons is observed, while DIT underestimates the number of large nucleon transfer reactions. The results in Figures 2 and 3 also demonstrate that both the mean values and distribution widths of the  $\Delta N$  plots are sensitive to the interaction code as well as the de-excitation code. Further examination of the HIPSE code with different variations of the level density parameter, percent transfer of neutrons and protons, and the de-excitation code may provide a better description of the  $N/Z$  dependence of the nucleon transfer.

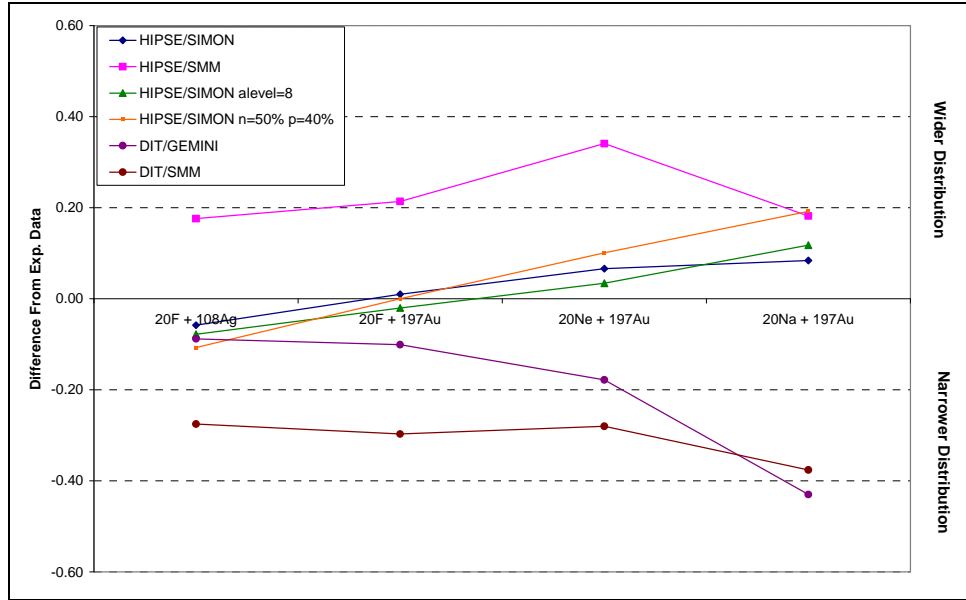


**Figure 3.** The differences between the simulated and the experimental sigma values of the  $\Delta N$  plots. The sigma value was extracted from a Gaussian fit of the  $\Delta N$  plot. DIT/SMM and DIT/GEMINI results taken from Ref. 2.

[1] D. Lacroix *et al.*, Phys. Rev. C **69**, 054605 (2005).

[2] D. Rowland, Ph.D. Thesis, Texas A & M University, 2000.

## Using light cluster production to determine the density dependence of the nuclear symmetry energy

S. N. Soisson, L. W. Chen, E. Bell, B. A. Li, D. V. Shetty, G. A. Souliotis, A. L. Keksis,  
S. J. Yennello and the NIMROD Collaboration

Using a coalescence model for treating cluster production from an isospin dependent transport model, it has been shown that the multiplicities and the energy spectra of light clusters produced is sensitive to the density dependence of the nuclear symmetry energy but not to the isospin-independent part of the nuclear equation of state or the in-medium cross sections [1,2]. Using an isospin-dependent Boltzmann-Uehling-Uhlenbeck (IBUU) transport model [2] coupled to a coalescence model the comparison of the energy spectra, multiplicities and the ratio of  ${}^3\text{H}$  and  ${}^3\text{He}$  production for the systems of  ${}^{58}\text{Fe} + {}^{58}\text{Fe}$  and  ${}^{58}\text{Ni} + {}^{58}\text{Ni}$  at 45 MeV/nucleon has been studied.

Previously, we have shown that the measured  ${}^3\text{H}$  to  ${}^3\text{He}$  ratio shows no significant dependence on centrality and that the iBUU-coalescence model does not reproduce the production ratio of  ${}^3\text{H}$  to  ${}^3\text{He}$  well [3]. In recent studies [4], a constraint of the  $x$  parameter, found in the momentum and isospin-dependent single nucleon potential [5] in the iBUU calculation has been proposed to be between 0 and -1. These values correspond to parameterization of the symmetry energy of  $E_{sym}(\rho) \approx 31.6(\rho/\rho_o)^{0.69}$  to  $E_{sym}(\rho) \approx 31.6(\rho/\rho_o)^{1.1}$ . We have run the iBUU-coalescence model to reflect this constraint. In Figure 1 we see the experimental double ratio of  $({}^3\text{H}/{}^3\text{He})_{\text{FeFe}}/({}^3\text{H}/{}^3\text{He})_{\text{NiNi}}$  compared to four different  $x$  values for a momentum dependant iBUU calculation. In Table I we see the slope of the best fit line for

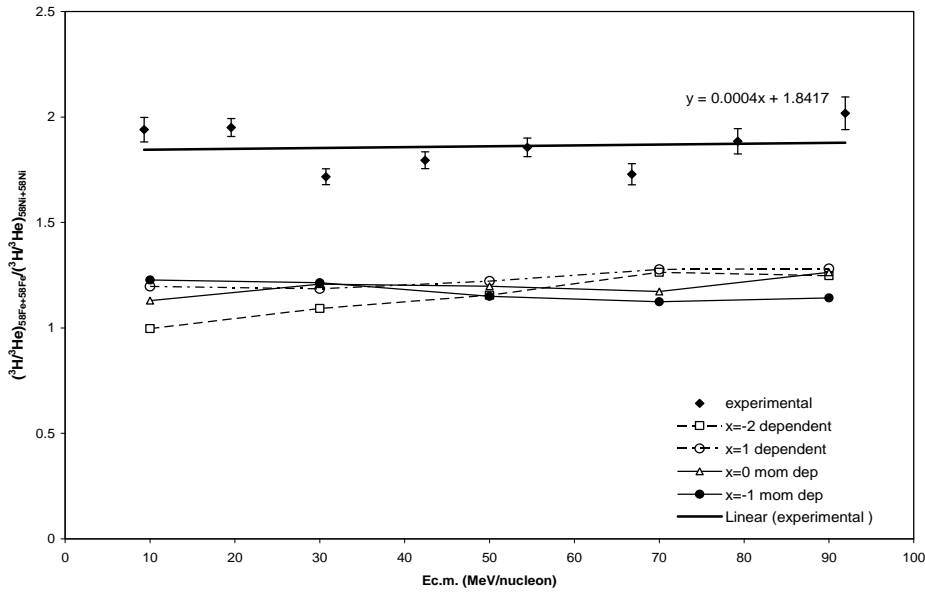


**Figure 1.** The double ratio of  $({}^3\text{H}/{}^3\text{He})_{\text{FeFe}}/({}^3\text{H}/{}^3\text{He})_{\text{NiNi}}$  compared to 4 different iBUU-coalescence calculations.

each  $x$  value. The slope of the experimental best fit straight line is 0.0004 for the energy range of 0 to 100 MeV/nucleon. The double ratio is nearly flat which signals that there is no energy dependent differential production of  ${}^3\text{H}$  and  ${}^3\text{He}$  due to the  $N/Z$  of the parent system. When comparing this to the iBUU-coalescence extracted double ratio best fit slopes for this energy region we find that it lies between  $x = -1$  and  $x = 0$ . However, the slopes of the lines for all calculations are similar and no definitive conclusion can be made through this type of analysis. The under prediction of the double ratio could reflect the distillation of the systems that is not being accounted for in the calculation. For this to be a good observable, it is possible that a greater  $N/Z$  difference is needed.

**Table I.**  $x$  value used in iBUU calculation with its corresponding slope of the best fit line for the double yield ratio.

$x$ value	Slope
-2	0.0034
-1	-0.0013
0	0.0012
1	0.0013

- [1] L. W. Chen, C. M. Ko, B. A. Li, Phys. Rev. C **68**, 01601 (2003).
- [2] L. W. Chen, C. M. Ko, B. A. Li, Nucl. Phys. **A739**, 809 (2003).
- [3] S. N. Soisson *et al.*, *Progress in Research*, Cyclotron Institute, Texas A&M University (2004-2005), p.II-23.
- [4] B. A. Li, L. W. Chen, G. C. Yong, W. Zuo, Phys. Lett. B **634**, 378 (2006).
- [5] C. B. Das, S. Das Gupta, C. Gale and B. A. Li, Phys. Rev. C **67**, 034611 (2003).

## An update to the dual-axis dual-lateral upgrade to the FAUST detector array

S. N. Soisson, B. C. Stein, and S. J. Yennello

In the last several years advances in silicon strip technology and continuous position sensitive detectors have allowed for more precise measurement of the emission angle of fragments from heavy-ion reactions. By achieving a greater understanding of the emission pattern of fragments from heavy-ion collisions, it is possible that the different modes of disassembly of excited nuclei can be differentiated [1]. Because of the success of FAUST due to its reconstruction capabilities it is a prime candidate for a move towards greater position sensitivity to allow for a greater understanding of multifragmentation processes.

We have continued work with the dual-axis dual-lateral position sensitive detector (DADL PSD) design in conjunction with Micron Semiconductor [2]. A second prototype was delivered with a resistivity of 3.5 k $\Omega$  on the front surface and 1.71 k $\Omega$  on the back surface of the detector. It was chosen to allow the resistivity of each side to be more equal and lower than the first prototype (with a front resistivity of 6.8 k $\Omega$  and a back resistivity of 22 k $\Omega$ ) because it is believed that the higher resistivity back side gives an uneven implantation depth since the time of implantation is extremely small. An uneven implantation depth can describe the behavior that was observed with the first prototype of an increasing leakage current with increasing bias with independent fluctuations with the leakage current regardless of applied conditions.

In testing the second-prototype of the DADL PSD we have determined that there is a design flaw in the masking process during the manufacture of the detectors. This is observed during prolonged testing of the detectors as observed in Figure 1. Figure 1 shows the reconstructed energy off of the back side of the detector. We clearly see an energy spectrum that is expected from a normal silicon detector if it is being hit by particles of all energies. On top of this spectrum we can see a  $^{228}\text{Th}$  source spectrum. This indicates that there is charge leakage occurring. In conjunction with this, when the back guard ring is monitored, it is observed that the back guard ring leakage current increases with increasing the bias on the detector itself. This behavior is seen whether the detector is biased from the front or the back side. The design of the detector allows for the surface and the guard ring to be isolated from each other and this clearly is not the case. It is believed that the back guard ring and the back surface of

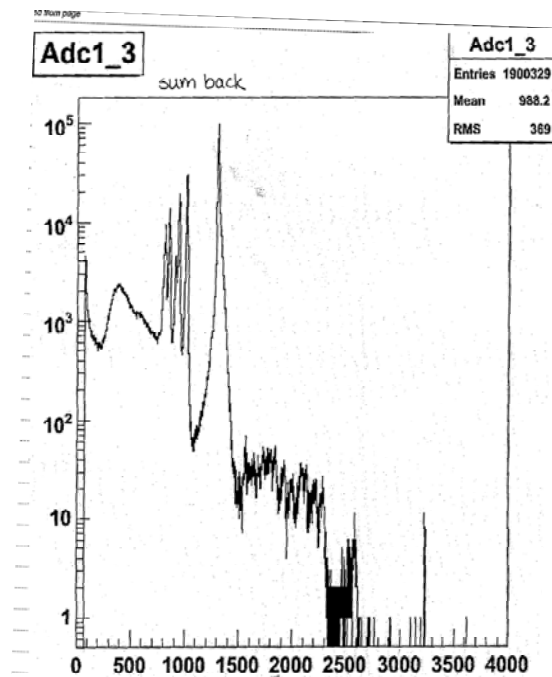


**Figure 1.** Summed energy spectra from the back surface

the detector are joined in some fashion that allows for some type of random charge to be detected in conjunction with a signal. Micron Semiconductor has delivered a third prototype that addresses this issue and further testing will begin shortly.

[1] R. J. Charity *et al.*, Phys. Rev. C **46**, 1951 (1992).

[2] S. N. Soisson *et al.*, *Progress in Research*, Cyclotron Institute, Texas A&M University (2005-2006), p. II-23

## Comparisons of microscopic calculations with experimental heavy residue distributions and the sensitivity to the density dependence of the nuclear symmetry energy

G. A. Souliotis, D. V. Shetty, and S. J. Yennello

During the last several years we have undertaken a systematic study of heavy residues formed in quasi-elastic and deep-inelastic collisions near and below the Fermi energy. The original motivation of these studies was the understanding and the optimization of the production of very neutron-rich rare isotopes in these collisions [1,2,3]. In parallel, we became motivated to pursue these studies further in hopes of extracting information on the properties of the nuclear effective interaction as manifested in the mechanism of nucleon exchange and the course towards  $N/Z$  equilibration [4]. In addition, studying specifically those heavy residues produced near the nuclear multifragmentation threshold, we investigated the possibility of obtaining the symmetry energy coefficient of the binding energy of the hot fragments [5,6].

Recently, we focussed our interest on the possibility of extracting information on the dynamics and the nuclear equation of state (EOS) by comparing our heavy residue data to detailed calculations using microscopic models of heavy-ion collisions at these energies [7].

Our initial efforts with transport-type codes (BUU, BNV) have not been successful in describing the details of the heavy residue distributions. We believe that this may be due, in part, to the inability of these types of models to provide an accurate estimate of the primary fragment excitation energy in peripheral and semiperipheral collisions.

We subsequently turned our attention to the quantum molecular dynamics approach (QMD). At present, we are performing detailed calculations of the QMD type using a recent version of the constrained molecular dynamics code CoMD of M. Papa [8,9]. This QMD code is especially designed for reactions near and below the Fermi energy. It implements an effective interaction corresponding to a nuclear-matter compressibility of  $K=200$  (soft EOS) with several forms of the density dependence of the nucleon-nucleon symmetry potential. While not specifically using antisymmetrized  $N$ -body wave functions, CoMD imposes a constraint in the phase space occupation for each nucleon, thus effectively restoring the Pauli principle at each time step of the collision. This constraint preserves the fermionic nature of the interacting nuclei in a satisfactory manner [8]. The latest version (CoMD-II) also fully preserves the total angular momentum along with linear momentum and energy [9].

Preliminary results of the calculations and comparisons with our residue data are shown in Figs. 1-4. Fig. 1 shows the calculated average quasiprojectile angle (upper panel) and excitation energy per nucleon (lower panel) as a function of the mass of the (primary) quasiprojectiles. The black line corresponds to the prediction of the deep-inelastic transfer (DIT) code of Tassan-Got that has been extensively used in our studies of quasiprojectile formation near the Fermi energy [10]. The light blue curve shows the prediction of the heavy-ion phase-space exploration (HIPSE) model [11]. The remaining four lines are the results of CoMD calculations with four symmetry potential options referred to as: “a-soft” (blue line), “linear” (red line), “a-stiff” (green line) and “no-symm” (grey line). The above characterizations refer to the form of the density dependence of the nucleon-nucleon symmetry potential

$V_{\text{symm}}$ , whereas, in the last case (“no-symm”) this potential is set to zero (thus, only the kinetic part of the symmetry energy plays a role in this case). The CoMD calculation was stopped at  $t=300$  fm/c. We observe differences between the predictions of DIT, HIPSE and CoMD that we will try to further investigate and understand in the near future. Regarding CoMD, despite the observed fluctuations of the mean values, we may tentatively conclude that the mean quasiprojectile angle is not sensitive to the choice of the symmetry potential. However, the mean excitation energy shows some sensitivity in the choice that deserves further exploration.

In Fig. 2, the distributions of the mean angle, mean velocity and yield as a function of the mass of the (final) observable fragments are shown. The deexcitation of the primary fragments was done with the sequential decay code GEMINI. The meaning of the curves is as before: black line: DIT, coloured lines: CoMD. The top panel shows, along with the calculations, the angular acceptance of the MARS separator  $\Delta\theta=3^\circ\text{-}6^\circ$  for our measurements (dashed horizontal lines). In the middle and lower panels, the MARS data [1] are shown with solid symbols. The calculations in both cases are filtered with the angular acceptance of the separator. Additionally, in the lower panel, the thin lines show the calculations of the total residue yields. We observe an overall satisfactory agreement of the CoMD calculations

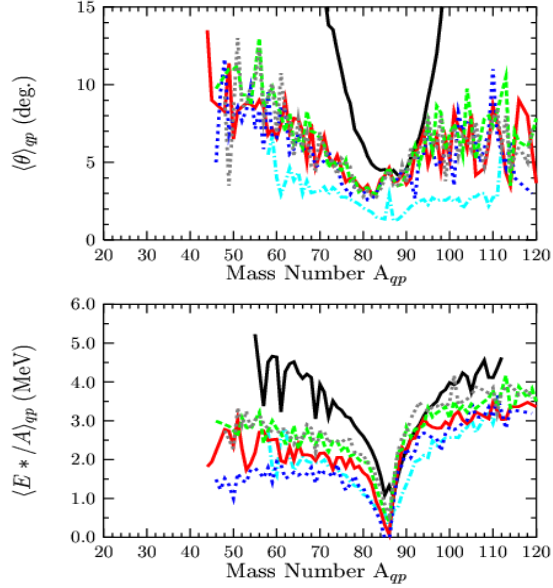


**Figure 1.** Mean quasiprojectile angle (upper panel) and excitation energy per nucleon (lower panel) as a function of quasiprojectile mass for the reaction  $^{86}\text{Kr}(25\text{MeV/nucleon}) + ^{124}\text{Sn}$ . Black line: DIT. Light-blue line: HIPSE. Blue (a-soft), red (linear), green (a-stiff) and grey (no-symm): CoMD calculations (see text).

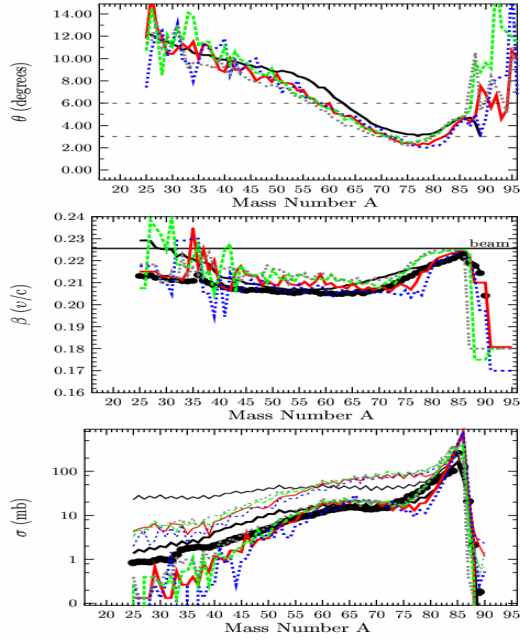


**Figure 2.** Mean angle (upper panel), mean velocity (middle panel) and yield (lower panel) as a function of projectile residue mass for the reaction  $^{86}\text{Kr}(25\text{MeV/nucleon}) + ^{124}\text{Sn}$ . Black line: DIT. Blue (a-soft), red (linear), green (a-stiff) and grey (no-symm): CoMD calculations (see text). Black points: MARS data [1]

with the data and again, in the CoMD calculations, an insensitivity to the choice of the symmetry potential. The situation is similar for the comparison of the mean  $Z/A$  values of the observed residues with the CoMD calculations shown in Fig. 3.

Finally, in Fig. 4, upper panel, we show the calculated mean  $N/Z$  of the primary quasiprojectiles as a function of the excitation energy per nucleon. The meaning of the curves is as in Fig. 1. The upper set of curves is for the  $^{86}\text{Kr}(25\text{MeV/nucleon}) + ^{124}\text{Sn}$  reaction and the lower set is for the  $^{86}\text{Kr}(25\text{MeV/nucleon}) + ^{112}\text{Sn}$  reaction. The solid horizontal line corresponds to the  $N/Z$

of the projectile, whereas the upper and lower dashed lines give the  $N/Z$  of the fully equilibrated systems in the two cases. In the lower panel of the figure we show the difference of the calculated mean  $N/Z$  values, along with our data (solid and open points) from the heavy-residue isoscaling analysis of [4]. It is interesting to note that the CoMD calculations show some sensitivity in the choice of the symmetry potential. However, this observation may be subject to the inherent uncertainty in the determination of the excitation energy of the quasiprojectiles. In the present calculations, the excitation energy has been determined from the difference of the binding energy of the (hot) quasiprojectiles as given by the CoMD code and the corresponding binding energy taken from mass tables. We plan to investigate the issues of the excitation energy determination in a systematic way.

Finally, we plan to explore the  $N/Z$  equilibration process (e.g. Fig. 4) in greater detail via comparisons of CoMD

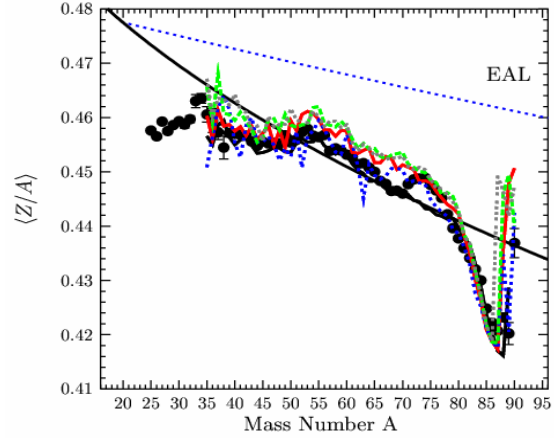


**Figure 3.** Mean projectile residue  $Z/A$  as a function of residue mass for the reaction  $^{86}\text{Kr}$  (25MeV/nucleon) +  $^{124}\text{Sn}$ . Black line tracing the data: DIT. Blue (a-soft), red (linear), green (a-stiff) and grey (no-symm): CoMD calculations (see text). Black points: MARS data [1]. Black line: line of stability.

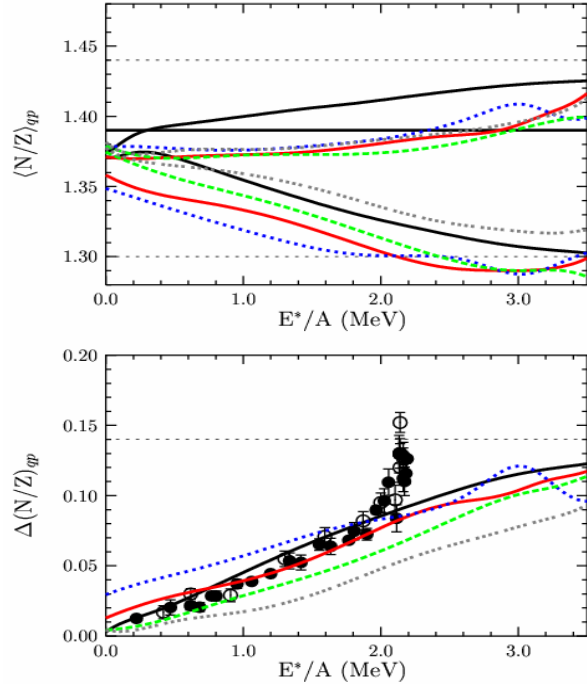


**Figure 4.** Upper panel: Mean  $N/Z$  of primary quasiprojectiles as a function of excitation energy per nucleon for the 25 MeV/nucleon reactions:  $^{86}\text{Kr} + ^{124}\text{Sn}$  (upper set of curves) and  $^{86}\text{Kr} + ^{112}\text{Sn}$  (lower set of curves). Black lines DIT. Blue (a-soft), red (linear), green (a-stiff) and grey (no-symm): CoMD calculations (see text). Lower panel: Difference in quasiprojectile mean  $N/Z$ . Lines as above. Black points: residue isoscaling data from [4].

calculations with our residue data from other reactions at 25 MeV/nucleon [5,6], as well as new experimental measurements at 15 MeV/nucleon that we plan to undertake in the near future.

- [1] G.A. Souliotis *et al.*, Phys. Rev. Lett. **91**, 022701 (2003).
- [2] G.A. Souliotis *et al.*, Nucl. Instrum. Methods Phys. Res. **B204**, 166 (2003).
- [3] M. Veselsky, and G.A. Souliotis, Nucl.Phys. **A765**, 252 (2006).
- [4] G.A. Souliotis *et al.*, Phys. Lett. B **588**, 35 (2004).
- [5] G. A. Souliotis *et al.*, Phys. Rev. C **73**, 024606 (2006).
- [6] G. A. Souliotis *et al.*, Phys. Rev. C **75**, 011601 (2007).
- [7] A. Ono and J. Randrup, Eur. Phys. J. A **30**, 109 (2006).
- [8] M. Papa *et al.*, Phys. Rev. C **64**, 024612 (2001).
- [9] M. Papa *et al.*, J. Comp. Phys. **208**, 403 (2005).
- [10] L. Tassan-Got and C. Stephan, Nucl. Phys. **A524**, 121 (1991).

## Production and separation of rare isotope beams at K150 energies ( $E/A=10-15$ MeV/nucleon)

G. A. Souliotis, B. C. Stein, Z. Kohley, S. Galanopoulos, A. L. Keksis, D. V. Shetty, S. N. Soisson, S. Wuenschel, and S. J. Yennello.

A substantial part of our recent efforts has been directed in acquiring experience in the production and separation of RIBs in peripheral collisions in the energy range expected from the refurbished K150 cyclotron. The Institute's RIB upgrade plan comprises the implementation of a large-bore superconducting solenoid as a preseparator before a heavy-ion gas stopper [1]. Our recent measurements and calculations indicate that the application of the deep-inelastic transfer mechanism [2,3,4] seems to be a very effective way to obtain rare isotopes at the K150 energies.

Along these lines, we recently performed a preliminary experiment with a 15 MeV/nucleon  $^{40}\text{Ar}^{9+}$  beam striking a natural Ni ( $5\text{ mg/cm}^2$ ) target. The projectile fragments were collected and identified using the BigSol superconducting solenoid. A schematic diagram of the experimental setup is shown in Fig. 1. The Ar beam, after interaction with the target was collected on an on-axis beam blocker. Behind the beam blocker, a PPAC provided X,Y position measurements and a start signal for the time-of-flight measurement. The fragments were focused at the end of the device ("RIB diagnostics" box in Fig. 1). At the entrance to the box, a circular aperture selected a range of fragment magnetic rigidities. The fragments were then passed through a PPAC providing X,Y position and stop-time information. Finally the fragments were collected in a  $5 \times 5\text{ cm}^2$   $\Delta E$ -E Si detector telescope (50 and 1000  $\mu\text{m}$  thickness). Following standard techniques of Bp- $\Delta E$ -E-TOF (magnetic rigidity, energy-loss, residual energy and time-of-flight, respectively), the atomic number Z, the mass number A, the velocity and the ionic charge of the fragments were obtained on an event-by-event basis (see, e.g [3]).

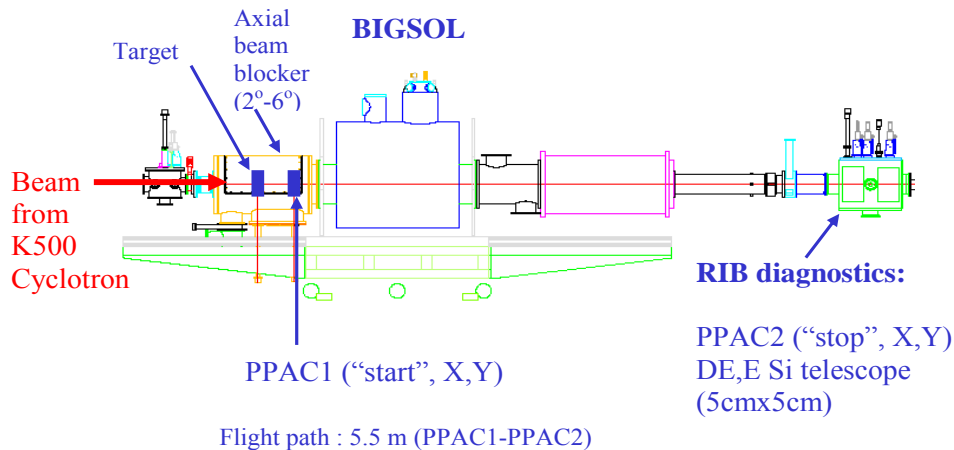


**Figure 1.** Schematic diagram of BigSol setup and the detector system for RIB production.

Fig. 2 shows a typical on-line  $\Delta E$ -E spectrum indicating the group of fragments along with intense background of elastics. Fig. 3 shows the corresponding particle identification (Z,A) spectrum after calibration of the on-line measured quantities. Even if the TOF resolution was not fully optimized, the

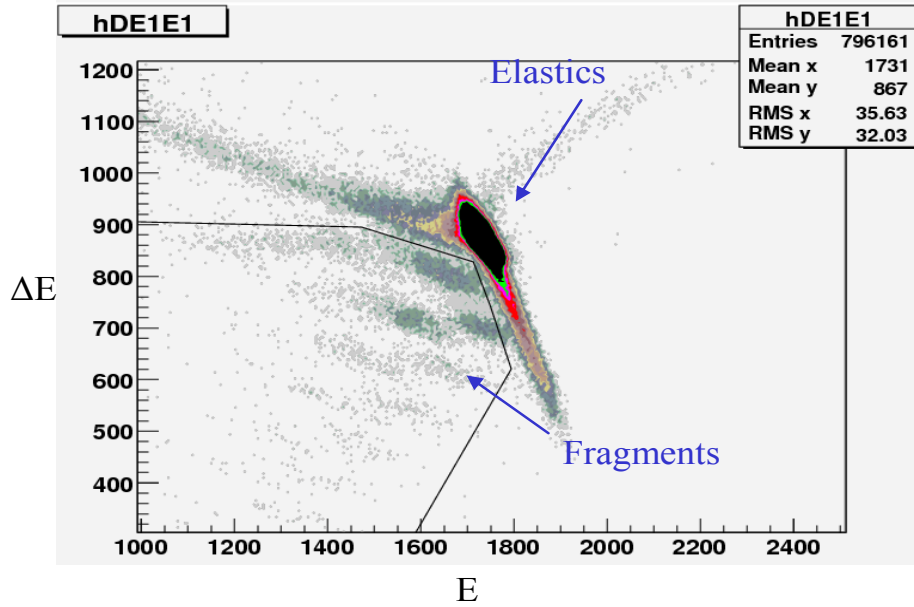


**Figure 3.** Example of an on-line  $\Delta E$ -E plot showing a group of projectile fragments from  $^{40}\text{Ar}(15\text{MeV/nucleon}) + ^{\text{nat}}\text{Ni}$ , along with elastically scattered beam.

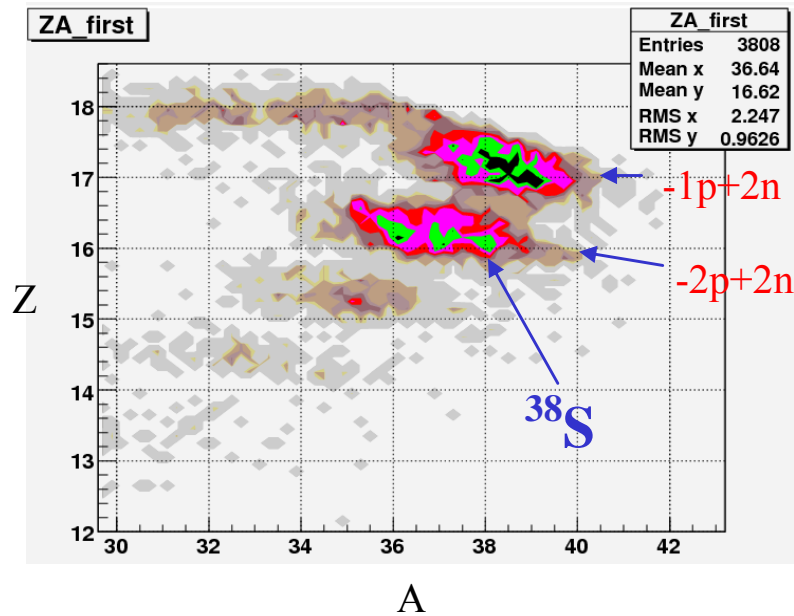


**Figure 2.** Particle identification (Z vs A) plot of the group of fragments shown in Fig. 1. The magnetic rigidity of this run was  $B\rho = 1.28$  Tesla-meter (corresponding to a 84.1 A current in the BigSol magnet). A narrow angular acceptance of 3.0-3.5 degrees was selected for this run.

mass of the fragments was obtained with a resolution of approximately 1.2 units (FWHM). The figure shows that along with proton-removal products (e.g.  $^{38}\text{S}$ ), neutron-pickup products are produced in substantial yields, as expected from a deep-inelastic transfer mechanism at these energies. Using the reaction simulation procedure described in our previous works [2,3,4] and filtering the events through BigSol (and the subsequent experimental apparatus) using the beam-optics code RAYTRACE, we found that the yields of the observed neutron-rich products are in overall agreement with the model expectations. We plan to extend the RIB production tests in the near future and investigate ways to separate the RIB mixtures from the elastically scattered beam using, e.g., a degrader after the target or an iris-like aperture at the diagnostic chamber.

- [1] “A Proposed Facility Upgrade for the Texas A&M University, Cyclotron Institute”, <http://cyclotron.tamu.edu>
- [2] G. A. Souliotis *et al.*, Phys. Rev. Lett. **91**, 022701 (2003).
- [3] G. A. Souliotis *et al.*, Nucl. Instrum. Methods Phys. Res. **B204**, 166 (2003).
- [4] M. Veselsky, and G. A. Souliotis, Nucl.Phys. **A765**, 252 (2006).

## Study of projectile multifragmentation in the reactions $^{24}\text{Mg} + ^{112,124}\text{Sn}$ and the effect of system N/Z at 32 MeV/u

S. Galanopoulos, G. A. Souliotis, A. L. Keksis, M. Veselsky, M. Jandel, D. V. Shetty, S. Soisson, B. Stein, S. Wuenschel, and S. J. Yennello

The relationship between the entrance channel isospin (N/Z) and the isotopic distribution of the reaction products has been found to be a sensitive observable in the study of the charge asymmetry term in the nuclear equation of state, (nEOS) [1]. A number of recent studies have revealed that the yield ratio of a given fragment coming from a neutron-rich vs a neutron deficient fragmenting system follows an exponential dependence with respect to the neutron and proton number of the fragments, an effect termed isoscaling (e.g. [2-4]).

In the present study, we are investigating projectile multifragmentation reactions in the collisions of  $^{24}\text{Mg} + ^{112,124}\text{Sn}$ . The measurements were performed at the K500 Cyclotron accelerator of Texas A&M University using a  $^{24}\text{Mg}$  beam at 32 MeV/u. The produced reaction fragments were detected by the Forward Array Using Silicon Technology (FAUST) [5]. The data are presently under analysis. Preliminary results of the isotopic yield ratio of projectile fragments from the two reactions are depicted in Fig. 1. In this plot, the isotopic yields have resulted from the integration of all the individual yields detected within the angular acceptance of FAUST detector. The rapid growth of the neutron-rich vs the neutron-deficient isotopic yield ratio is evident for each element.

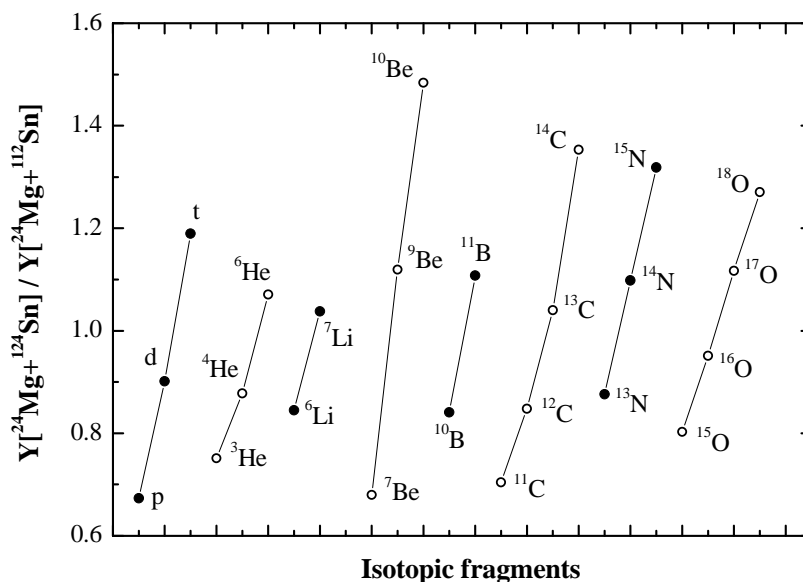


**Figure 1.** Isotopic neutron rich to neutron deficient yield ratios of the fragments (solid and open dots) emitted in the  $^{24}\text{Mg} + ^{112,124}\text{Sn}$  collisions.

From the present data, we plan to obtain reconstructed quasiprojectiles and to study systematically their angular distributions, excitation energy and N/Z. We also plan to compare the experimental results to detailed calculations using a) phenomenological models like DIT [6] and HIPSE [7] and b) microscopic models, e.g. the quantum molecular dynamics code CoMD [8]. It's our hope that via such systematic comparisons, information on the underlying dynamics and the nEOS, especially the asymmetry term, may be obtained.

- [1] M. Colonna and M. B. Tsang, *Eur. Phys. J. A* **30**, 165, (2006).
- [2] M. B. Tsang *et al.*, *Phys. Rev. Lett.* **86**, 5023 (2001).
- [3] D. V. Shetty *et al.*, *Phys. Rev. C* **68**, 021602 (2003).
- [4] G. A. Souliotis *et al.*, *Phys. Rev. C* **73**, 024606 (2006).
- [5] F. Gimeno-Nogues, D. J. Rowland, E. Ramakrishnan, S. Ferro, S. Vasal, R. A. Gutierrez, R. Olsen, Y. -W. Lui, and S. Y. Yennello, *Nucl. Instrum. Methods Phys. Res.* **A399**, 94 (1997).
- [6] L. Tassan-Got and C. Stephan, *Nucl. Phys.* **A524**, 121 (1991).
- [7] D. Lacroix *et al.*, *Phys. Rev. C* **69**, 054604 (2004).
- [8] M. Papa *et al.*, *Phys. Rev. C* **64**, 024612 (2001); *J. Comp. Phys.* **208**, 403 (2005).

## Status of the NIMROD upgrade

S. Wuenschel, K. Hagel, Z. Kohley, L. May, J. B. Natowitz, R. Wada, and S. J. Yennello

The upgrade to the 4pi detector NIMROD has made great progress since the last report [1]. The forward rings (~3 to 45 degrees) have been augmented with the appropriate Si detectors ranging in thicknesses between 150 and 500 microns. From 45 to 90 degrees CsI coverage is completed and some Si installed for energy calibration. Efforts have begun to estimate the cost of completing Si coverage in this angular region. The ISiS detector (~90-177 degrees) has been installed.

New fabrication methods are being investigated for construction of the ion chambers. The new construction procedures will provide better grounding for the windows thus yielding better shaping of the field within the chamber.

The installation of Indiana motherboards for the ISiS detectors has been modified to allow the neutron ball to be opened and closed without dismounting of the motherboards. In the new configuration Faraday cages are provided for the motherboards to minimize the baseline noise.

The Si bias power supply system for the ISiS detectors has been installed and is operational. The system allows control of the bias online and is able to read the leakage current of each detector. Adapting this system for use on the detectors in the forward rings failed due to the lack of flexibility in voltage polarity. In its place a system of passive distribution boxes has been incorporated.

Significant effort was put forth to bias the target ladder assembly to reduce electrons impinging on the Si detectors. At  $10^{-5}$  vacuum the HV assembly will hold approximately up to 30kV without significant sparking.

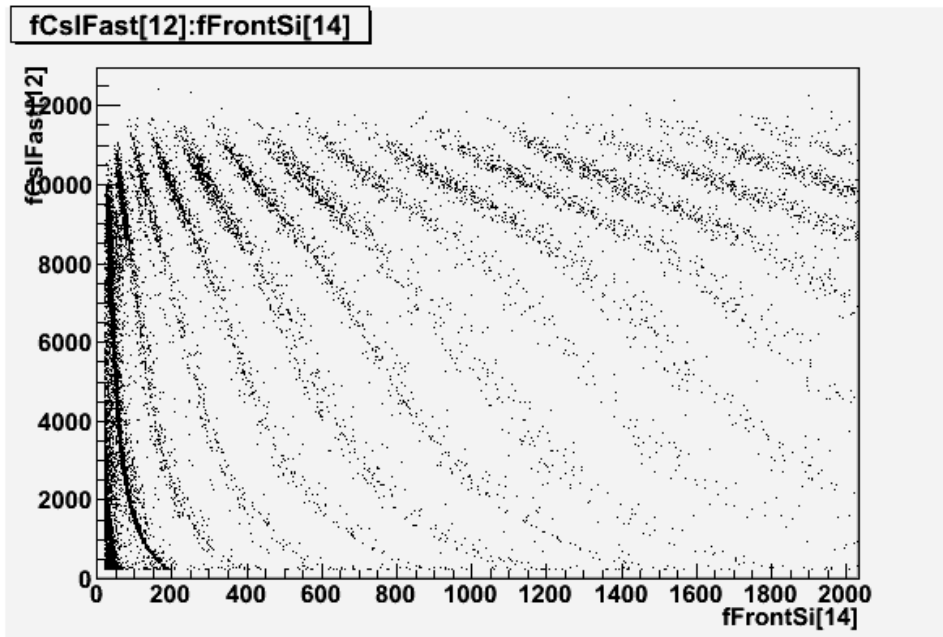


Figure 1. Si(x-axis) vs CsI (y-axis) showing isotopic resolution.

Experiments have been successfully conducted to rigorously test the apparatus. In the most forward ring (ring 2) silicon detectors yield excellent elemental resolution. However, they do not have isotopic resolution as they appear to have suffered some radiation damage. Isotopic resolution on Si-CsI telescopes can be easily seen for all of the other rings [Figure 1&2].

The neutron ball surrounding the vacuum chamber is operational. The efficiency in its new configuration has been calibrated with a  $^{252}\text{Cf}$  source. The observed efficiency agrees with GEANT calculations which give the efficiency for low energy neutrons at approximately 70 percent.

The analysis tools based on the CERN ROOT software, including a software filter for the NIMROD, has been incorporated into the Cyclotron Application software tools, Cycapps. All software has begun to be updated for the new detector configuration. The software filter will allow simulation data to be compared with the experimental data directly. The NIMROD experimental campaign has started. Several systems of experiments have been proposed. The first data set will be taken in April with the others to follow starting during the summer.

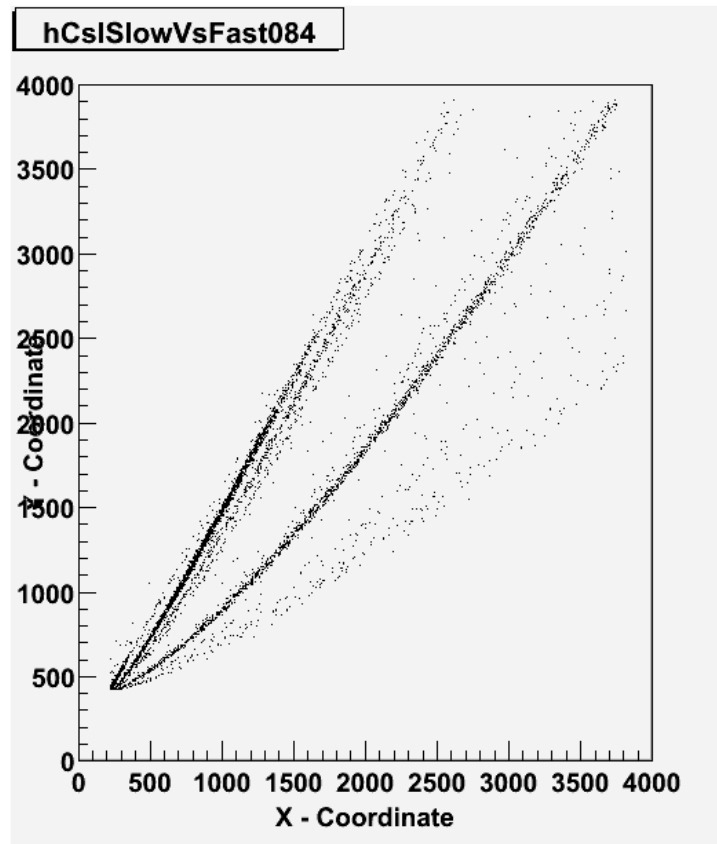


Figure 2. CsI fast vs slow.

[1] S. Wuenschel *et al.*, *Progress in Research*, Cyclotron Institute, Texas A&M University (2005-2006), p.II-17

## Density dependence of the symmetry energy and the nuclear equation of state : A dynamical and statistical model perspective

D. V. Shetty, S. J. Yennello, and G. A. Souliotis

The density dependence of the symmetry energy is a key unknown in the equation of state of isospin asymmetric nuclear matter. Due to its direct relevance to the structure and stability of systems as diverse as the neutron stars and neutron-rich nuclei, there is a significant interest in determining this quantity. Theoretical studies based on microscopic “ab-initio” calculations predict a variety of different forms of the density dependence of the symmetry energy. Experimental measurements on the density dependence of the symmetry energy are still scarce and difficult. In the past, we have tried to study the density dependence of the symmetry energy using the fragment isotope yields in multifragmentation reactions compared to the dynamical model Antisymmetrized Molecular Dynamic (AMD). We have now investigated the same using the statistical model approach of multifragmentation reaction. We report here a comparison between the two approaches along with several other independent studies to obtain a constraint on the form of the density dependence of the symmetry energy. We also report several predictions that follow from the constraint.

Fig. 1 shows the density dependence of the symmetry energy obtained from the statistical model approach using the experimentally measured isoscaling parameter (red and green circle symbols) [1]. The green solid curve corresponds to the density dependence of the symmetry energy obtained from the Gogny-AS interaction in our previous analysis using the dynamical AMD approach [2,3], assuming the sequential decay effect to be small. The red dashed curve corresponds to the one obtained from an accurately calibrated relativistic mean field interaction, used for describing the Giant Monopole Resonance (GMR) in  $^{90}\text{Zr}$  and  $^{208}\text{Pb}$ , and the IVGDR in  $^{208}\text{Pb}$  by Piekarewicz *et al.* [4]. The light-blue dashed curve correspond to the one used to explain the isospin diffusion results of NSCL-MSU using the isospin dependent Boltzmann-Uehling-Uhlenbeck (IBUU) model by Tsang *et al.* [5]. The blue dot-dashed curve also corresponds to the one used for explaining the isospin diffusion data of NSCL-MSU by Chen *et al.* [6], but with the momentum dependence of the interaction included in the IBUU calculation. This dependence has been further modified to include the isospin dependence of the in-medium nucleon-nucleon cross-section by Li *et al.* [7], and is in good agreement with the present study. The shaded region in the figure corresponds to that obtained by constraining the binding energy, neutron skin thickness and isospin analogue state in finite nuclei using the mass formula of Danielewicz [8]. The yellow solid curve corresponds to the parameterization adopted by Heiselberg *et al.* [9] in their studies on neutron stars. By fitting earlier predictions of the variational calculations by Akmal *et al.* [10], where the many-body and special relativistic corrections are progressively incorporated, Heiselberg and Hjorth-Jensen obtained a value of  $C_{\text{sym}}^0 = 32$  MeV and  $\gamma = 0.6$ , similar to those obtained from the present measurements. A similar result is also obtained from the relativistic Dirac-Brueckner calculation, with  $C_{\text{sym}}^0 = 32.9$  MeV and  $\gamma = 0.59$  [11]. The Dirac-Brueckner is an “ab-initio” calculation based on nucleon-nucleon interaction with Bonn A type potential instead of the AV18 potential used in the variational calculation of Ref. [10]. The density dependence of the symmetry energy has also been studied in the framework of an expanding

emitting source (EES) model by Tsang *et al.* [12], where a power law dependence of the form  $C_{\text{sym}}(\rho) = 23.4(\rho/\rho_0)^\gamma$ , with  $\gamma = 0.6$ , was obtained. This dependence (shown by the pink dashed curve) is significantly softer than other dependences shown in the figure. The pink square point in the figure correspond to the value of symmetry energy obtained by fitting the experimental differential cross-section data in a charge exchange reaction using the isospin dependent CDM3Y6 interaction of the optical potential by Khoa *et al.* [13].

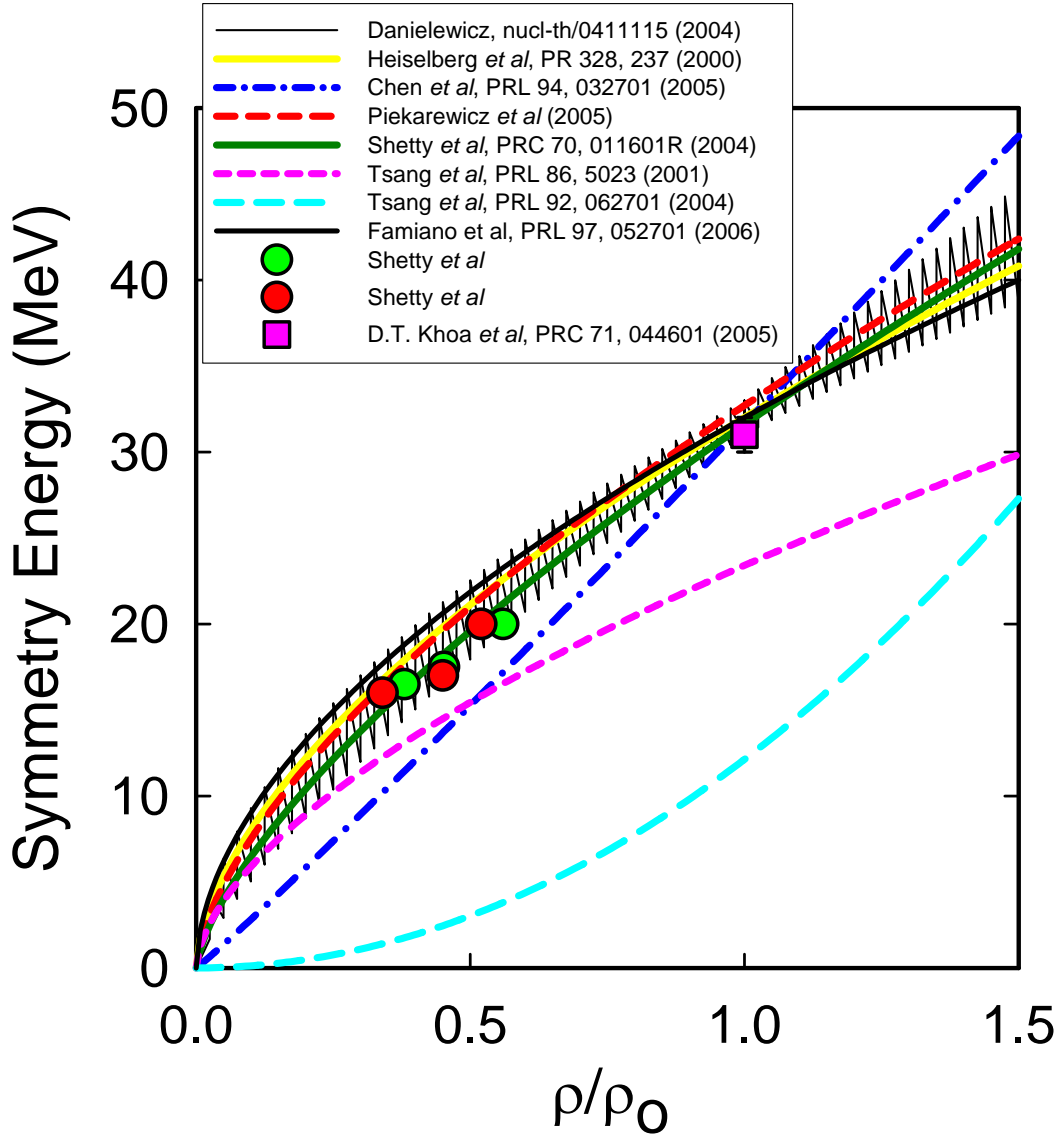


**Figure 1.** Comparison between the results on the density dependence of the symmetry energy obtained from various different studies. The different curves and symbols are described in the

An alternate observable, the double neutron/proton ratio of nucleons taken from two reaction systems using four isotopes of the same element, has recently been proposed as a probe to study the density dependence of the symmetry energy [14]. This observable is expected to be more robust than the isoscaling observable. It was shown recently [14] that the experimentally determined double-ratio for the  $^{124}\text{Sn} + ^{124}\text{Sn}$  reaction to that for the  $^{112}\text{Sn} + ^{112}\text{Sn}$  reaction, results in a dependence with  $\gamma = 0.5$  (shown by black solid curve), when compared to the predictions of the IBUU transport model calculations. This observation is in close agreement with other studies discussed above. However, this dependence has been obtained by using the momentum independent calculation of Ref. [15]. A more recent calculation [16] using a BUU transport model that includes momentum dependent interaction shows significantly lower values for the double neutron/proton ratio of free nucleons compared to the one reported by Famiano *et al.*

The parameterized form of the density dependence of the symmetry energy obtained from all the above studies are as shown in Table I. The close agreement between various independent studies therefore suggests that a constraint on the density dependence of the symmetry energy, given as  $C_{\text{sym}}(\rho) = C_{\text{sym}}^0(\rho/\rho_0)^\gamma$ , where  $C_{\text{sym}}^0 \sim 31 - 33$  MeV and  $\gamma \sim 0.55 - 0.69$  can be obtained. This rules out extremely “stiff” and “soft” dependences predicted by theory.

**Table I.** Parameterized form of the density dependence of the symmetry energy obtained from various independent studies

Reference	Parameterization	Studies
<b>Fuchs <i>et al.</i> [11]</b>	<b><math>32.9(\rho/\rho_0)^{0.59}</math></b>	<b>Relativistic Dirac-Bruckner cal.</b>
<b>Heiselberg <i>et al.</i> [9]</b>	<b><math>32.0(\rho/\rho_0)^{0.60}</math></b>	<b>Variational calculation</b>
<b>Danielewicz <i>et al.</i> [8]</b>	<b><math>31(33)(\rho/\rho_0)^{0.55(0.79)}</math></b>	<b>BE, Skin, Isospin analogue states</b>
<b>Tsang <i>et al.</i> [5]</b>	<b><math>12.125(\rho/\rho_0)^2</math></b>	<b>Isospin diffusion</b>
<b>Chen <i>et al.</i> [6]</b>	<b><math>31.6(\rho/\rho_0)^{1.05}</math></b>	<b>Isospin diffusion</b>
<b>Li <i>et al.</i> [7]</b>	<b><math>31.6(\rho/\rho_0)^{0.69}</math></b>	<b>Isospin diffusion</b>
<b>Piekarewicz <i>et al.</i> [4]</b>	<b><math>32.7(\rho/\rho_0)^{0.64}</math></b>	<b>GMR, IVGDR</b>
<b>Shetty <i>et al.</i> [1,2]</b>	<b><math>31.6(\rho/\rho_0)^{0.69}</math></b>	<b>Isotopic distribution</b>
<b>Famiano <i>et al.</i> [14]</b>	<b><math>32.0(\rho/\rho_0)^{0.55}</math></b>	<b>Neutron-proton emission ratio</b>
<b>Tsang <i>et al.</i> [12]</b>	<b><math>23.4(\rho/\rho_0)^{0.6}</math></b>	<b>Isotopic distribution</b>

We draw following conclusions from the above comparisons :

1) Assuming a negligibly small sequential decay effect, the form of the density dependence of the symmetry energy obtained from the dynamical model analysis is in good agreement with the one obtained from the statistical model analysis.

2) The result of the statistical model analysis is in good agreement with other independent studies.

3) The isoscaling parameter probes the property of infinite nuclear matter : The symmetry energy obtained from the dynamical model analysis corresponds to the volume part of the symmetry energy as in infinite nuclear matter, whereas, the symmetry energy obtained from the statistical model analysis corresponds to the fragments that are finite and have a surface contribution. The similarity between the two can probably be understood in terms of the weakening of the surface symmetry free energy when the

fragments are being formed. During the density fluctuation in uniform low density matter, the fragments are not completely isolated and continue to interact with each other, resulting in a decrease in the surface contribution. Using the constraint obtained for the volume part of the symmetry energy from the present study, and following the expression for the symmetry energy of finite nuclei, the general expression for the density dependence of the symmetry energy can be given as,

$$S_A(\rho) = \alpha(\rho/\rho_0)^\gamma/[1 + (\alpha(\rho/\rho_0)^\gamma/\beta A^{1/3})]$$

Where  $\alpha = C_{\text{sym}}^0 = 31 - 33$  MeV,  $\gamma = 0.55 - 0.69$  and  $\alpha/\beta = 2.6 - 3.0$ . The quantities  $\alpha$  and  $\beta$  are the volume and the surface symmetry energy at normal nuclear density. The above equation reduces to the volume symmetry energy for infinite nuclear matter in the limit of  $A$  tending to infinity, and to the symmetry energy of finite nuclei for  $\rho = \rho_0$ . The ratio  $\alpha/\beta$ , is related to the neutron skin thickness, the measurement of which should provide a tighter constraint on the surface-volume correlation.

4) *The density dependence of the symmetry energy obtained using the statistical model approach is consistent with other experimentally determined observables* : In the past, attempts have been made to study the density dependence of the symmetry energy by looking at specific observables and comparing them with predictions of the dynamical models. Such an approach attempts to explain the observable of interest without trying to simultaneously explain other properties, such as, the temperature, density and excitation of the fragmenting system. The present statistical model approach simultaneously explains the isoscaling parameter, caloric curve, and the density as a function of excitation energy to arrive at the density dependence of the symmetry energy.

5) *Symmetry energy determined from the present study is lower than that of normal nuclei* : The present statistical model analysis yields volume contribution of the symmetry energy of the order of 18 – 20 MeV at half the normal nuclear density.

6) *The obtained constraint on the density dependence of the symmetry energy has important implications for astrophysical and nuclear physics studies* :

- a) *Neutron skin thickness* : It has been shown that an empirical fit to a large number of mean field calculations yield neutron skin thickness for  $^{208}\text{Pb}$  nucleus,  $R_n - R_p \sim (0.22 \gamma + 0.06)$  fm, where  $\gamma$  is the exponent that determines the stiffness of the density dependence of the symmetry energy. From the above comparison, one obtains a neutron skin thickness of 0.18 – 0.21 fm.
- b) *Neutron star mass and radius* : The constraint also predicts a limiting neutron star mass of  $M_{\text{max}} = 1.72$  solar mass and a radius,  $R = 11 - 13$  km for the “canonical” neutron star. Recent observations of pulsar-white dwarf binaries at the Arecibo observatory suggest a pulsar mass for PSRJ0751+1807 of  $M = 2.1(+0.4, -0.5)$  solar mass at a 95% confidence level.
- c) *Neutron star cooling* : The constraint obtained predicts a direct URCA cooling for neutron stars above 1.4 times the solar mass. In such a case the enhanced cooling of an  $M = 1.4$  solar mass neutron star may provide strong evidence in favor of exotic matter in the core of a neutron star.

[1] D. V. Shetty *et al.*, Phys. Rev. C (submitted); nucl-ex/0606032 (2006).

[2] D. V. Shetty *et al.*, Phys. Rev. C **75**, 034602 (2007).

- [3] D. V. Shetty *et al.*, Phys. Rev. C **70**, 011601 (2004).
- [4] J. Piekarewicz, Proc. of the International conf. on current problems in nuclear physics and atomic energy, Kyiv, Ukraine, (2006).
- [5] M. B. Tsang *et al.*, Phys. Rev. Lett. **92**, 062701 (2004).
- [6] L. W. Chen *et al.*, Phys. Rev. Lett. **94**, 032701 (2005).
- [7] B. A. Li *et al.*, Phys.Rev. C **72**, 064611 (2005).
- [8] P. Danielewicz *et al.*, Nucl.Phys. **A727**, 233 (2003).
- [9] H. Heiselberg *et al.*, Phys. Rep. **328**, 237 (2000).
- [10] A. Akmal *et al.*, Phys. Rev. C **56**, 2261 (1997).
- [11] C. Fuchs, Private Communication; E. N. E. van Dalen *et al.*, Nucl.Phys. **A744**, 227 (2004).
- [12] M. B. Tsang *et al.*, Phys. Rev. Lett. **86**, 5023 (2001).
- [13] D. T. Khoa *et al.*, Phys. Rev. C **71**, 044601 (2005).
- [14] M. A. Famiano *et al.*, Phys. Rev. Lett. **97**, 052701 (2006).
- [15] B. A. Li *et al.*, Phys. Rev. Lett. **78**, 1644 (1997).
- [16] B. A. Li *et al.*, Phys. Lett. B **634**, 378 (2006).

## Symmetry energy, temperature, density and isoscaling parameter as a function of excitation energy in A ~ 100 mass region

D. V. Shetty, S. J. Yennello, G. A. Souliotis, A. L. Keksis, S. N. Soisson,  
B. C. Stein, and S. Wuenschel

Continuing our investigation on the density dependence of the symmetry energy from previous years, we have now investigated the same from an alternate point of view – the statistical model approach. Previously, we had studied the density dependence of the symmetry energy by comparison to the dynamical model Antisymmetrized Molecular Dynamic (AMD). The present statistical model approach combines the features of the Statistical Multifragmentation Model (SMM) and the expanding Fermi gas model to obtain a systematic correlation between the temperature, density and symmetry energy of a multifragmenting system as it evolves with the excitation energy. The advantage of this approach is that unlike the dynamical model approaches, where the effect of sequential decay on isoscaling parameter remains controversial, the sequential decay effect in statistical models are well established and known to have negligible effect.

To build the correlation between the temperature, density, and symmetry energy of a multifragmenting system as it evolves with the excitation energy, we have made use of the fragment yield distributions measured in  $^{58}\text{Ni}$ ,  $^{58}\text{Fe} + ^{58}\text{Ni}$ ,  $^{58}\text{Fe}$  reactions at 30, 40 and 47 MeV/nucleon. The yield distributions were used to obtain the isoscaling parameter  $\alpha$ , as a function of the excitation energy of the fragmenting source. The parameter  $\alpha$  was obtained from the ratios of the isotopic yields for two different pairs of reactions,  $^{58}\text{Fe} + ^{58}\text{Ni}$  and  $^{58}\text{Ni} + ^{58}\text{Ni}$ , and  $^{58}\text{Fe} + ^{58}\text{Fe}$  and  $^{58}\text{Ni} + ^{58}\text{Ni}$ . Fig. 1(a) shows the experimental isoscaling parameter  $\alpha$  as a function of the excitation energy for Fe + Fe and Ni + Ni, and Fe + Ni and Ni + Ni pairs of reactions. A systematic decrease in the absolute values of the isoscaling parameter with increasing excitation energy is observed for both pairs. The  $\alpha$  parameters for the  $^{58}\text{Fe} + ^{58}\text{Fe}$  and  $^{58}\text{Ni} + ^{58}\text{Ni}$  are about twice as large compared to those for the  $^{58}\text{Fe} + ^{58}\text{Ni}$  and  $^{58}\text{Ni} + ^{58}\text{Ni}$  pair of reactions. The experimental isoscaling parameters were compared with the predictions of the Statistical Multifragmentation Model (SMM) to study their dependence on the excitation energy and the isospin content. The break-up density in the calculation was taken to be multiplicity-dependent and was varied from approximately 1/2 to 1/3 the saturation density. This was achieved by varying the free volume with the excitation energy. The form of the dependence was adopted from the work of Bondorf *et al.* [1,2], (and shown by the solid curve in Fig. 1(d)). It is known that the multiplicity-dependent break-up density, which corresponds to a fixed inter-fragment spacing and constant pressure at break-up, leads to a pronounced plateau in the caloric curve [1,2]. A constant break-up density would lead to a steeper temperature versus excitation energy dependence. The symmetry energy in the calculation was then varied until a reasonable agreement between the calculated and the measured  $\alpha$  was obtained. Fig. 1(a) shows the comparison between the SMM calculated and the measured  $\alpha$  for both pairs of systems. The dashed curves correspond to the calculation for the primary fragments and the solid curves to the secondary fragments. The width in the curve is the measure of the uncertainty in the inputs to the SMM calculation.

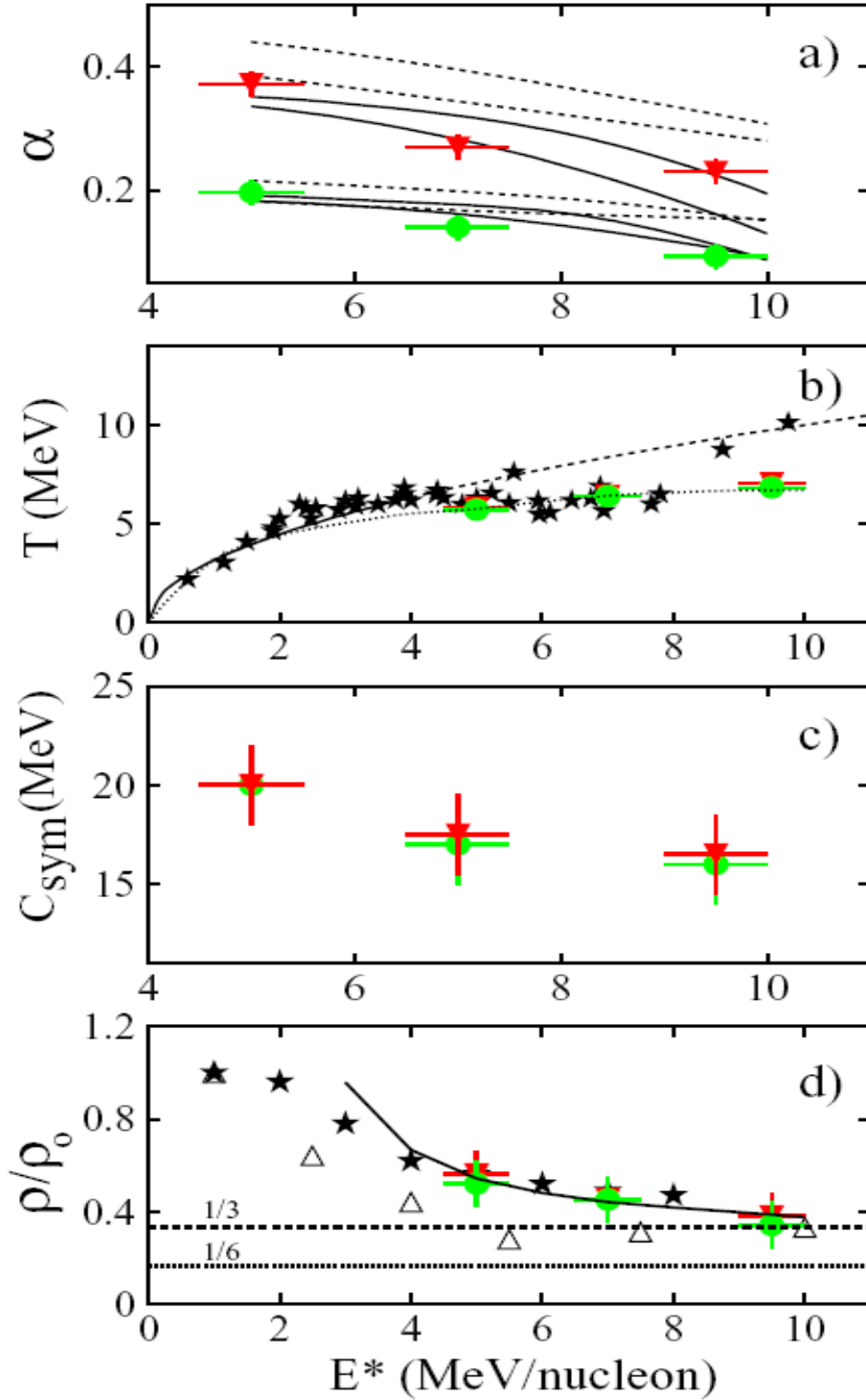


**Figure 1.** Isoscaling parameter  $\alpha$ , temperature, symmetry energy and density as a function of excitation energy for the  $^{58}\text{Fe} + ^{58}\text{Fe}$  and  $^{58}\text{Ni} + ^{58}\text{Ni}$  (inverted triangles), and  $^{58}\text{Fe} + ^{58}\text{Ni}$  and  $^{58}\text{Ni} + ^{58}\text{Ni}$  (circles) reactions. a) Experimental  $\alpha$  as a function of excitation energy. The solid and the dashed curves are the SMM calculations. b) Temperature as a function of excitation energy. The solid stars correspond to the measured values taken from the literature. The solid-and-dashed curve corresponds to the Fermi-gas relation. c) Symmetry energy as a function of excitation energy. d) Density as a function of excitation energy.

Fig. 1(b) shows the temperature as a function of excitation energy (caloric curve) obtained from the above SMM calculation that uses the excitation energy dependence of the break-up density to explain the observed isoscaling parameters. These are shown by the solid and inverted triangle symbols. Also shown in the figure are the experimentally measured caloric curve data compiled by Natowitz *et al.* [3], from various measurements for this mass range. The data from these measurements are shown collectively by solid star symbols and no distinction is made among them. The Fermi-gas model predictions with inverse level density parameter  $K_0 = 10$  (solid-and-dashed curve) is also shown. It is evident from the figure that the temperatures obtained from the SMM calculations are in good agreement with the overall trend of the caloric curve. The symmetry energies obtained from the statistical model comparison of the experimental isoscaling parameter  $\alpha$ , are shown in Fig. 1(c). A steady decrease in the symmetry energy with increasing excitation energy is observed for both pairs of systems.

The phase diagram of the multifragmenting system is two dimensional and hence the excitation energy dependence of the temperature (the caloric curve) must take into account the density dependence too. Often this dependence is neglected while studying the caloric curve. It has been shown by Sobotka *et al.* [4], that the plateau in the caloric curve could be a consequence of the thermal expansion of the system at higher excitation energy and decreasing density. By assuming that the decrease in the breakup density, as taken in the present statistical multifragmentation calculation, can be approximated by the expanding Fermi gas model, the density as a function of excitation energy was extracted using the relation,

$$T^2 = K_0(\rho/\rho_0)^{2/3} E^*$$

In the above expression, the momentum and the frequency dependent factors in the effective mass ratio were taken to be one as is expected at the high excitation energies and low densities studied in this work.

The resulting densities for the two pairs of systems are shown in Fig. 1(d) by the solid circles and inverted triangles. For comparison, the figure also shows the break-up densities obtained from the analysis of the apparent level density parameters required to fit the measured caloric curve by Natowitz *et al.* [3], and those obtained by Viola *et al.* [5], from the Coulomb barrier systematics of the measured intermediate mass fragment kinetic energy spectra. One observes that the present results, obtained by requiring a fit to both the measured isoscaling parameters and the caloric curve, are in good agreement with those obtained by Natowitz *et al.* The figure also shows the fixed freeze-out density of 1/3 (dashed line) and 1/6 (dotted line) of the saturation density assumed in various statistical model comparisons. The caloric curve obtained using the above densities and excitation energies (shown by solid stars, circles and the triangles) with  $K_0 = 10$  in the above equation, is shown by the dotted curve in Fig. 1(b). The small discrepancy between the dotted curve and the data (solid stars) below 4 MeV/nucleon is due to the approximate nature of the equation being used. It is evident from Figure 1(a), (b), (c) and (d) that the decrease in the experimental isoscaling parameter  $\alpha$ , symmetry energy, break-up density, and the flattening of the temperature with increasing excitation energy are all correlated. One can thus conclude that the expansion of the system during the multifragmentation process leads to a decrease in the isoscaling parameter, a decrease in the symmetry energy and density, and the flattening of the caloric curve.

From the above correlation between the symmetry energy as a function of excitation energy and the density as a function of excitation energy, we have obtained the symmetry energy as a function of density. This is shown by the inverted triangles and solid circles in Fig. 2 for the  $^{58}\text{Fe} + ^{58}\text{Fe}$   $^{58}\text{Ni} + ^{58}\text{Ni}$ , and the  $^{58}\text{Fe} + ^{58}\text{Ni}$   $^{58}\text{Ni} + ^{58}\text{Ni}$  pair of reactions. The solid curve in Fig. 2 corresponds to the dependence  $C_{\text{sym}}(\rho) = 31.6(\rho/\rho_0)^{0.69}$  MeV, obtained from the dynamical Antisymmetrized Molecular Dynamic (AMD) calculation, as discussed in our previous work [6].

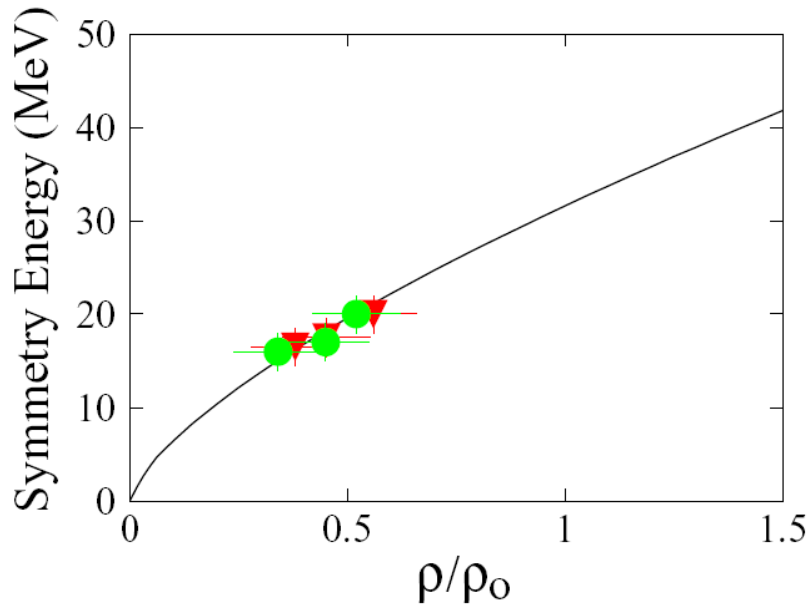


**Figure 2.** Symmetry energy as a function of density for the  $^{58}\text{Fe} + ^{58}\text{Fe}$  and  $^{58}\text{Ni} + ^{58}\text{Ni}$  pair of reaction (inverted triangles), and  $^{58}\text{Fe} + ^{58}\text{Ni}$  and  $^{58}\text{Ni} + ^{58}\text{Ni}$  pair of reactions (solid circles) or the 30, 40 and 47 MeV/nucleon. The solid curve is the dependence obtained from the dynamical model analysis.

In the past, attempts have been made to study the density dependence of the symmetry energy by looking at specific observables and comparing them with the predictions of the dynamical models. Such an approach attempts to explain the observable of interest without trying to simultaneously explain other properties, such as, the temperature, density and excitation of the fragmenting system. This has led to a variety of different dependences without accurate knowledge of what density is being probed. While it might not be straightforward to distinguish different equations-of-state using dynamical models, due to uncertainties in the sequential decay effects, the allure of extracting information on the symmetry energy from the point of view of the basic nucleon-nucleon interaction is very appealing. On the other hand, the determination of the density dependence of the symmetry energy from statistical model analysis by simultaneously explaining the isoscaling parameter, caloric curve and the density as a function of excitation energy is a reverse approach. This approach attempts to explain the experimental observables without any prior knowledge of the governing interaction and arrives at a dependence which can then be compared with those predicted from the basic interactions.

- [1] J. P. Bondorf *et al.*, Nucl. Phys. **A444**, 460 (1985).
- [2] J. P. Bondorf *et al.*, Phys. Rev. C **58**, 27 (1998).
- [3] J. B. Natowitz *et al.*, Phys. Rev. C **65**, 034618 (2002).
- [4] L. G. Sobotka *et al.*, Phys. Rev. Lett. **93**, 132702 (2004).
- [5] V. E. Viola *et al.*, Phys. Rev. Lett. **93**, 132701 (2004).
- [6] D. V. Shetty *et al.*, Phys. Rev. C **75**, 034602 (2007).

## Thermal expansion, effective mass and nuclear caloric curve

D. V. Shetty, S. J. Yennello, G. A. Souliotis, S. Galanopoulos, A. L. Keksis,  
S. N. Soisson, B. C. Stein, S. Wuenschel, and Z. Kohley

The experimentally observed “plateau” in the nuclear “caloric curve” (temperature versus excitation energy) has long been seen as a signature of liquid-gas phase transition, similar to that in water. Recently [1], it has been argued that the plateau in nuclear caloric curve is a consequence of a combined effect of decreasing density due to thermal expansion and the evolution of in-medium nucleon effective mass, rather than an indication of liquid-gas phase coexistence. A pseudo plateau, in variance with the one expected from the simple Fermi gas relation, is to be expected in the nuclear caloric curve with or without a multifragmentation-like phase transition. Furthermore, the inclusion of the surface expansion degree of freedom (surface diffuseness) along with the self-similar expansion degree of freedom, leads to a plateau [2] even flatter than the one obtained using just the self-similar expansion degree of freedom. The caloric curve for finite mononuclear system therefore exhibits not simply a pseudo plateau but a real one.

The above schematic model for describing the caloric curve is based on the relaxation of density profile of the mononucleus that results in maximum entropy under a local density approximation for the level density parameter. The plateau in the caloric curve from this model is however established at a rather modest excitation energy (about 2 MeV/nucleon), well before where one usually considers the liquid-gas phase transition to occur. The evolution of effective mass with density and excitation in the above prescription is included in a schematic fashion as they are currently unknown.

In this report, we show that a plateau in the caloric curve can also be obtained under various different assumptions regarding the role of effective mass as a function of excitation energy, and the collective expansion energy. The caloric curve thereby obtained exhibits a plateau at somewhat higher excitation energy compared to those obtained by Sobotka *et al.* [2], and in better agreement with the experimental data. Fig. 1 shows a comparison between the caloric curve obtained from the present study and the experimental data. The inverted triangle symbols corresponds to the experimentally measured caloric curve data for the mass range of  $A = 100 - 140$ , compiled by Natowitz *et al.* [3], from various measurements. The data from all different measurements are shown here collectively and no distinction is made between them. The black dashed curve is the simple Fermi gas relation, with the inverse level density parameter  $K_0 = 10$ . The Fermi gas relation explains the data at low excitation quite well, but fails at higher excitation energies. The brown dashed curve corresponds to the expanding Fermi gas relation,

$$T^2 = K_0(\rho/\rho_0)^{2/3}E^* \quad (1)$$

The density  $\rho/\rho_0$  as a function of excitation energy  $E^*$  in the above equation was assumed to be similar to that adopted by Bondorf *et al* [4]. This form of dependence is also similar to that obtained by Natowitz *et al* [5], for the break-up densities obtained from the analysis of the apparent level density parameters. This equation does not include the momentum and the frequency dependent factors in the effective mass ratio that are important at lower excitation energies. As a result of which, this relation

does a poor job of reproducing the data at excitation energies below 4 – 5 MeV/nucleon. At higher excitation energies, the effective mass ratio reduces to one, and hence shows good agreement with the

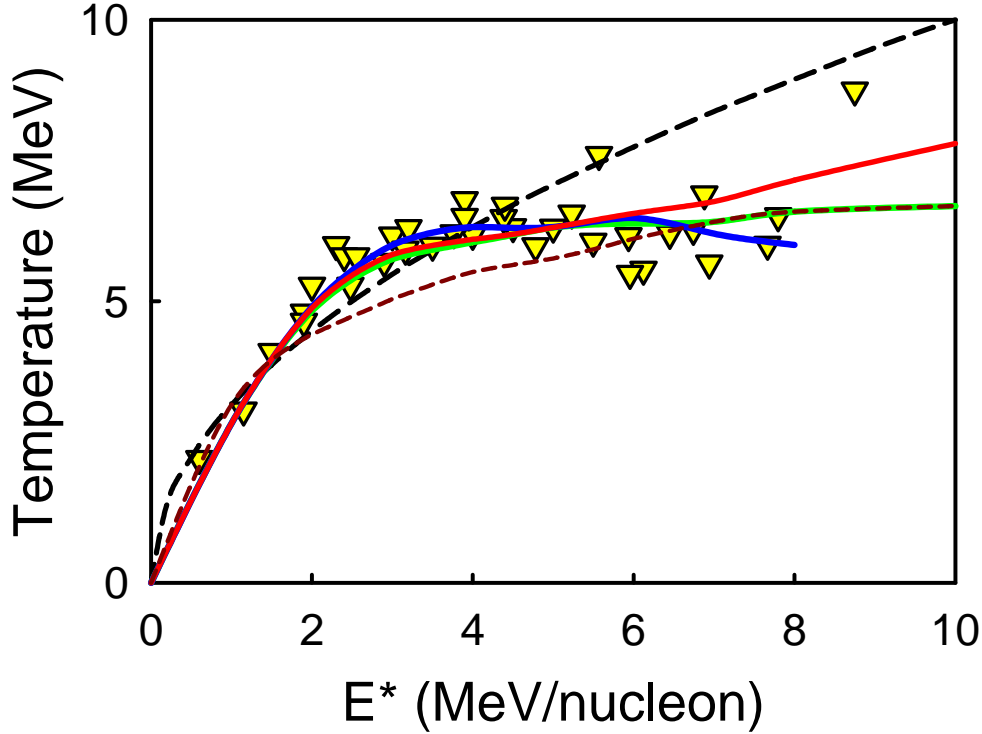


**Figure 1.** Temperature as a function of excitation energy for  $A = 100 - 140$ . The curves are from the present study. The data are taken from Ref. [3].

data. Accounting for the excitation energy dependence of the effective mass (as shown by the green curve in fig. 2) as discussed in Refs. [6] and [7] in the above equation as one obtains the relation,

$$T^2 = K_0(m^*/m)(\rho/\rho_0)^{2/3}E^* \quad (2)$$

The above equation results in a significant flattening of the caloric curve (shown by green curve in Fig. 1). Note the effective mass ratio  $m^*/m$ , in Fig. 2 reduces to one at higher excitation energy. The above expression for the temperature versus excitation energy with the effective mass dependence assumes a collective expansion energy of the form  $(1 - (\rho/\rho_0)^{2/3})$ . If the expansion energy is assumed to be a simple upside down bell shaped form, as suggested by Friedman [8],  $\epsilon_b(1 - \rho/\rho_0)^2$ , where  $\epsilon_b = 8$  MeV, one obtains a dependence given by,

$$T^2 = K_0(m^*/m)[E^* - 8(1 - \rho/\rho_0)^2] \quad (3)$$

This is shown by the red curve in Fig. 1. One observes that both the red and the green curve with different assumption of the collective expansion energy, but the same effective mass dependence, leads to

similar results at excitation energies below 6 MeV/nucleon, except for a small deviation at higher excitation energies. Both calculations show plateau at excitation energies in agreement with the data. A much stronger, but unphysical, effective mass dependence (shown by blue curve in Fig. 2) along with simple Fermi gas relation leads to significant flattening of the caloric curve as shown by the blue curve in Fig. 1.

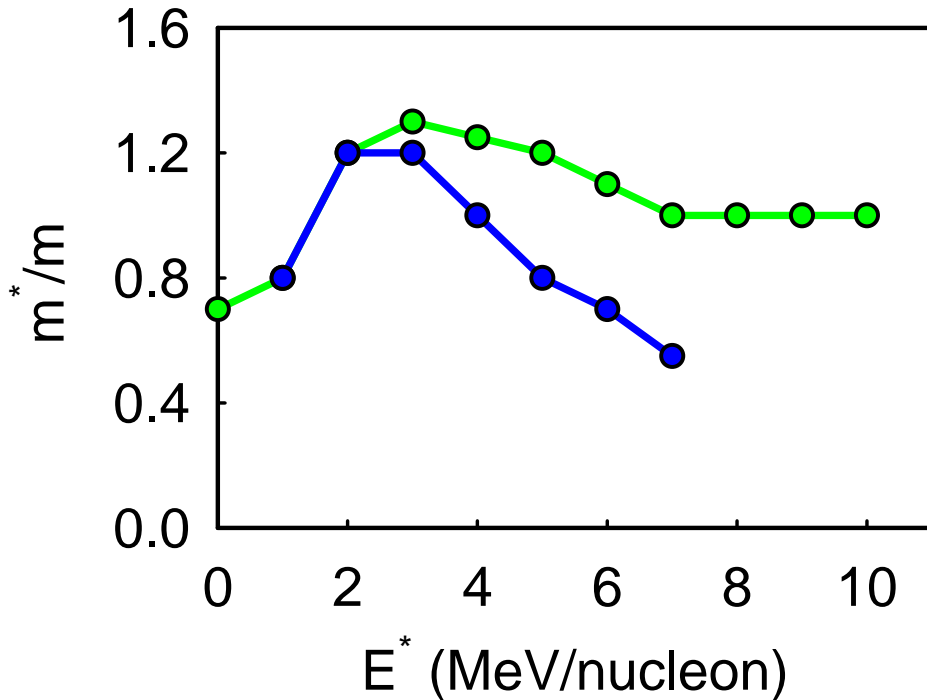


**Figure 2.** Effective mass ratio as a function of excitation energy.

- [1] L. G. Sobotka *et al.*, Phys. Rev. Lett. **93**, 132702 (2004).
- [2] L. G. Sobotka *et al.*, Phys. Rev. C **73**, 014609 (2006).
- [3] J. B. Natowitz *et al.*, Phys. Rev. C **65**, 034618 (2002).
- [4] J. P. Bondorf *et al.*, Nucl. Phys. **A444**, 460 (1985); Phys. Rev. C **58**, 27 (1998).
- [5] J. B. Natowitz *et al.*, Phys. Rev. C **66**, 031601 (2002).
- [6] M. Prakash *et al.*, Phys. Lett. B **128**, 141 (1983).
- [7] C. Mahaux *et al.*, Phys. Rep. **120**, 1 (1985).
- [8] W. A. Friedman, Phys. Rev. Lett. **60**, 2125 (1988).

## Investigating the symmetry and surface energy co-efficient from fragment isotope and charge yield distribution using statistical multifragmentation model

D. V. Shetty, A. E. Echeverria, S. J. Yennello, G. A. Souliotis, S. Galanopoulos, A. L. Keksis, S. N. Soisson, B. C. Stein, S. Wuenschel, and Z. Kohley

It has been shown [1] recently from the Statistical Multifragmentation Model (SMM) calculation that the symmetry energy term and the surface energy term in the free energy of the fragments, formed in multifragmentation reaction, are sensitive to the isotopic yield distribution and the charge distribution. The symmetry energy is shown to be sensitive to the fragment isotope yield distribution, and the surface energy to the fragment charge distribution.

a) **Influence of the symmetry energy in SMM:** The symmetry energy of the hot fragments with mass  $A$  and charge  $Z$  in SMM is parameterized as  $E^{\text{sym}}(A,Z) = \gamma(A - 2Z)^2/A$ . The parameter  $\gamma$ , known as the symmetry energy co-efficient, has a value of 25 MeV for the cold nuclei. For hot fragments, this value is unknown and is sensitive to the fragment isotopic yield distribution. It can be extracted from the experimental data via isoscaling phenomena in multifragmentation reaction.

b) **Influence of the surface energy in SMM:** The surface energy of the hot fragments in SMM is parameterized as  $E^{\text{sur}}(A,Z) = B(T)A^{2/3}$ , where  $B(T) = B_0[(T_c^2 - T^2)/(T_c^2 + T^2)]^{5/4}$ . The parameter  $B_0 = 18$  MeV is the standard surface energy co-efficient for cold nuclei. The production of new fragments leads to an increase in the surface contribution to the total energy of the system. A small variation of the surface energy can lead to big changes in fragment charge distribution.

In this work, we aim to constrain the values of the symmetry energy and the surface energy using them as free parameters in the SMM calculation. In the first stage of the calculation we will constrain the value of the symmetry energy using the fragment isotopic yield distribution and comparing them to the experimental yield distribution using the isoscaling technique. The value of the symmetry energy thus obtained can then be used to constrain the surface energy from the fragment charge distribution. Fig. 1 shows the calculated isotope yield distribution for  $Z = 4, 6, \text{ and } 8$  elements in  $^{58}\text{Fe} + ^{58}\text{Ni}$  and  $^{58}\text{Ni} + ^{58}\text{Ni}$ , and  $^{58}\text{Fe} + ^{58}\text{Fe}$  and  $^{58}\text{Ni} + ^{58}\text{Ni}$  reactions for two different values of the symmetry energy  $\gamma = 25$  and 14 MeV. These yield distribution were used to determine the isoscaling parameter  $\alpha$  for the primary and the secondary fragments. Fig. 2 shows the calculated primary (yellow curve) and secondary fragment (blue curve) isoscaling parameters as a function of system excitation energy. The solid red points show the experimentally determined isoscaling parameter. The figure shows the comparison between the experiment and the calculation for the  $^{58}\text{Fe} + ^{58}\text{Ni}$  and  $^{58}\text{Ni} + ^{58}\text{Ni}$  (left column), and the  $^{58}\text{Fe} + ^{58}\text{Fe}$  and  $^{58}\text{Ni} + ^{58}\text{Ni}$  (right column) pair of reactions. The calculations are shown for three different values of the symmetry energy,  $\gamma = 25, 20$  and 16 MeV. The surface energy co-efficient is kept constant at a standard value of  $B_0 = 18$  MeV. It is observed that the experimental isoscaling parameter for both the pairs of reactions could be explained using a symmetry energy value of about 16 MeV.

Having constrained the symmetry energy co-efficient  $\gamma$  from the fragment yield distribution, the surface energy co-efficient  $B_0$  was constrained using the charge yield distribution. Fig. 2 shows the comparison between the experimental (solid points) charge yield distribution and the SMM calculated

(curves) charge yield distribution, using different values of the surface energy co-efficient  $B_0$ , for  $^{58}\text{Fe} + ^{58}\text{Ni}$  (top) and  $^{58}\text{Fe} + ^{58}\text{Fe}$  (bottom) systems. The calculations were carried out for a constant value of  $\gamma = 16$  MeV, as obtained from the constraint on the yield distribution discussed above, and different values of the surface energy co-efficient  $B_0$ . Fig. 3 shows the preliminary results from this calculation for the  $^{58}\text{Fe} + ^{58}\text{Ni}$  (top) and  $^{58}\text{Fe} + ^{58}\text{Fe}$  (bottom) systems. Further investigation to understand the charge distribution is underway.

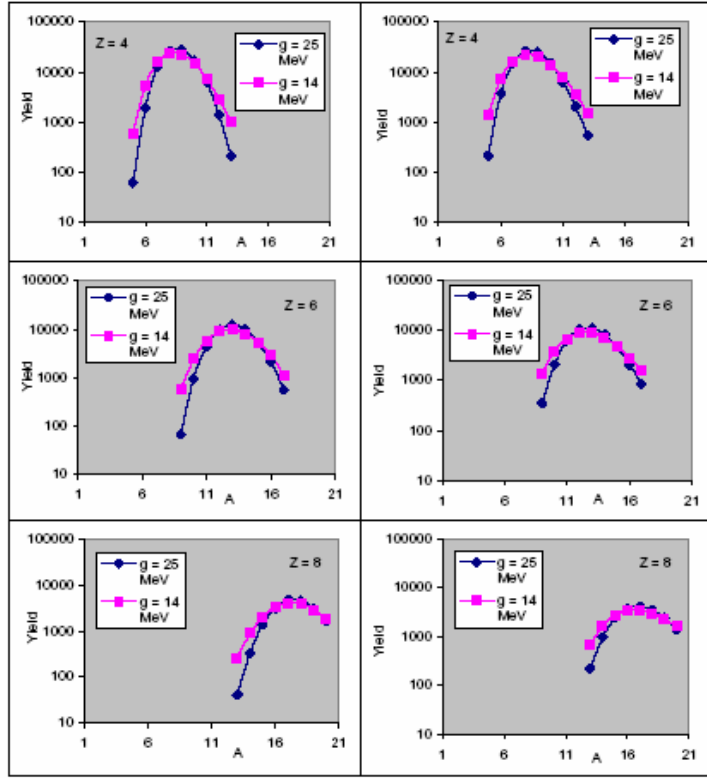


**Figure 1.** SMM calculated isotope yield distributions for Fe + Ni and Ni + Ni (left), and Fe + Fe and Ni + Ni (right) pair of reactions. The calculations are for two different values of symmetry energy  $\gamma = 25$  and 14 MeV.

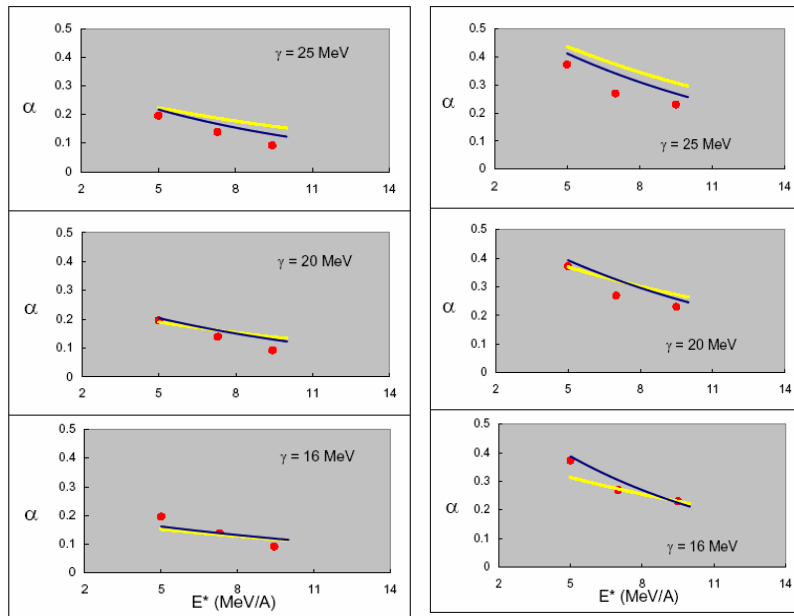


**Figure 2.** Isoscaling parameter as a function of excitation energy for the Fe + Ni and Ni + Ni, and Fe + Fe and Ni + Ni pair of reactions. The calculations (curves) are for different values of symmetry energy  $\gamma$ .

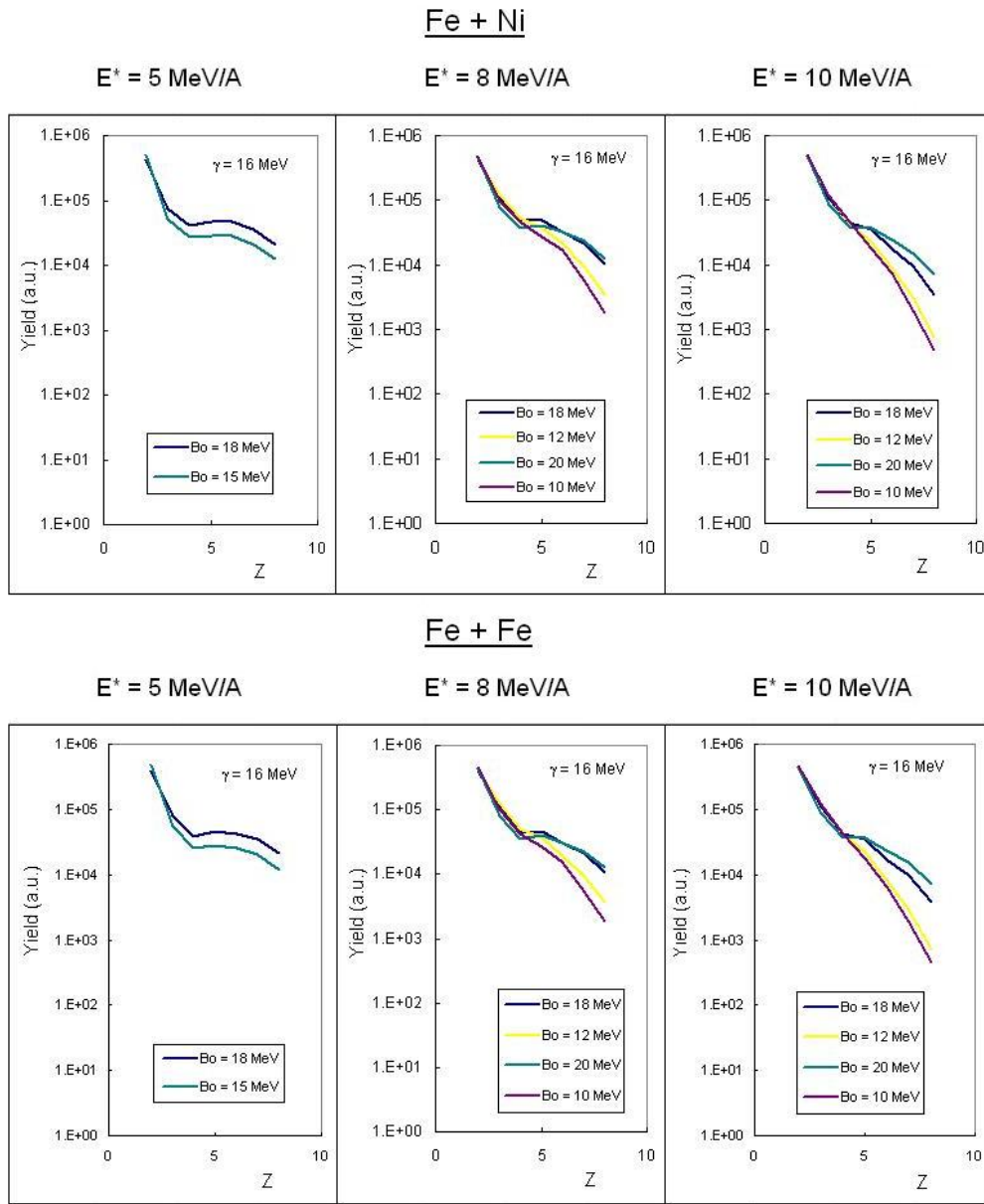


**Figure 3.** Comparison between the experimentally determined and SMM calculated charge distribution for Fe + Ni and Fe + Fe systems at different excitation energies, and using different values of the surface energy co-efficient.

[1] A. S. Botvina *et al.*, Phys. Rev. C **74**, 044609 (2006).

**Effect of symmetry energy evolution during sequential de-excitation on isoscaling parameter of the fragments produced in multifragmentation reaction**

D. V. Shetty, J. Iglío, A. E. Echeverria, S. J. Yennello, G. A. Souliotis, S. Galanopoulos,  
A. L. Keksis, S. N. Soisson, B. C. Stein, S. Wuenschel, and Z. Kohley

It has been argued [1] that the effect of sequential decay of the hot primary fragments produced in multifragmentation reactions on the isoscaling parameter  $\alpha$  depends not only on the excitation energy of the primary fragments but also on the evolution of the mass/symmetry energy of the primary fragments during the decay. The fragments produced in the primary stage of the multifragmentation reaction are usually hot and their properties (*i.e.* binding energy and mass) differ from those of cold nuclei. If hot fragments in the freeze-out configuration have smaller symmetry energy, their mass at the beginning of the sequential de-excitation will be different, and the isoscaling parameter of the experimentally determined cold fragments will be significantly different from those of the primary fragments. If such is the case, then the comparison between the theoretically calculated and the experimentally measured isoscaling parameter  $\alpha$  must be treated with caution.

In order to study the effect of symmetry energy evolution on the isoscaling parameter during the sequential de-excitation of the hot primary fragments, the Statistical Multifragmentation Model (SMM) calculation with a phenomenological approach of Buyuckcizmeci *et al* [2], was carried out. In this approach, one assumes liquid drop masses,  $m_{A,Z} = m_{ld}(\gamma)$ , for the light particles ( $n, p, d, t, {}^3\text{He}, \alpha$ ) if the internal excitation energy of the fragment is large ( $\xi = \beta E^*/A > 1$ ). For lower excitation energies ( $\xi < 1$ ), one assumes a smooth transition to standard experimental masses with shell effects ( $m_{exp}$ ), and having the following dependence,

$$m_{A,Z} = m_{ld}(\gamma)\xi + m_{exp}(1 - \xi)$$

The excitation energy is determined from the energy balance taking into account the mass  $m_{A,Z}$  at the given excitation.

Fig. 1(a) shows the primary and the secondary isoscaling parameter  $\alpha$  as a function of symmetry energy  $\gamma$  calculated from the statistical multifragmentation model with the symmetry energy of the hot primary fragments kept fixed. The calculation is for the  ${}^{40}\text{Ar} + {}^{58}\text{Ni}$  and  ${}^{40}\text{Ca} + {}^{58}\text{Ni}$ , and  ${}^{40}\text{Ar} + {}^{58}\text{Fe}$  and  ${}^{40}\text{Ca} + {}^{58}\text{Ni}$  pair of reactions. The various panels (from top to bottom) correspond to different excitation energies of the multifragmenting system. The dashed lines in each panel correspond to the isoscaling parameter for the primary fragments, and the solid lines to the secondary fragments (*i.e.* after sequential decay). It is observed that there is no significant difference between the primary and the secondary  $\alpha$ . Fig. 1(b) shows the result of the calculations when the symmetry energy is varied during the sequential de-excitation of the hot fragments. It is again observed that there is no significant change in the isoscaling parameter  $\alpha$  between the primary and the secondary fragments. The main difference, however, in the two figure (Fig 1(a) and 1(b)) is the rate at which isoscaling parameter decreases with decreasing symmetry

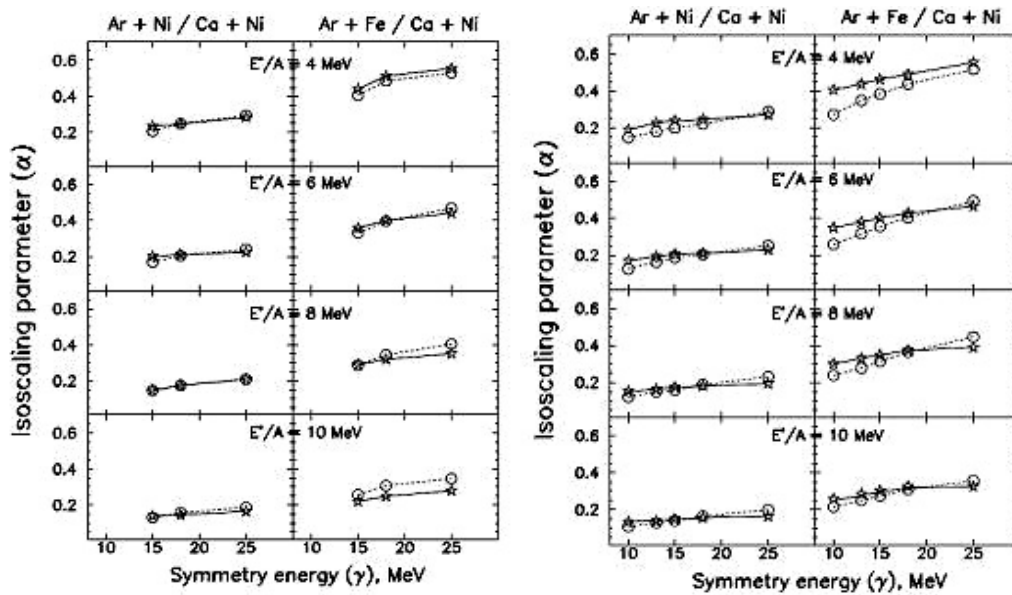


**Figure 2.** 1(a): Left, Isoscaling parameter  $\alpha$  as a function of symmetry energy for various excitation energies. The symmetry energy is kept fixed during the sequential decay of the primary fragments. Figure 1(b): Right, Isoscaling parameter as a function of symmetry energy with symmetry energy evolving during sequential decay of the primary fragments.

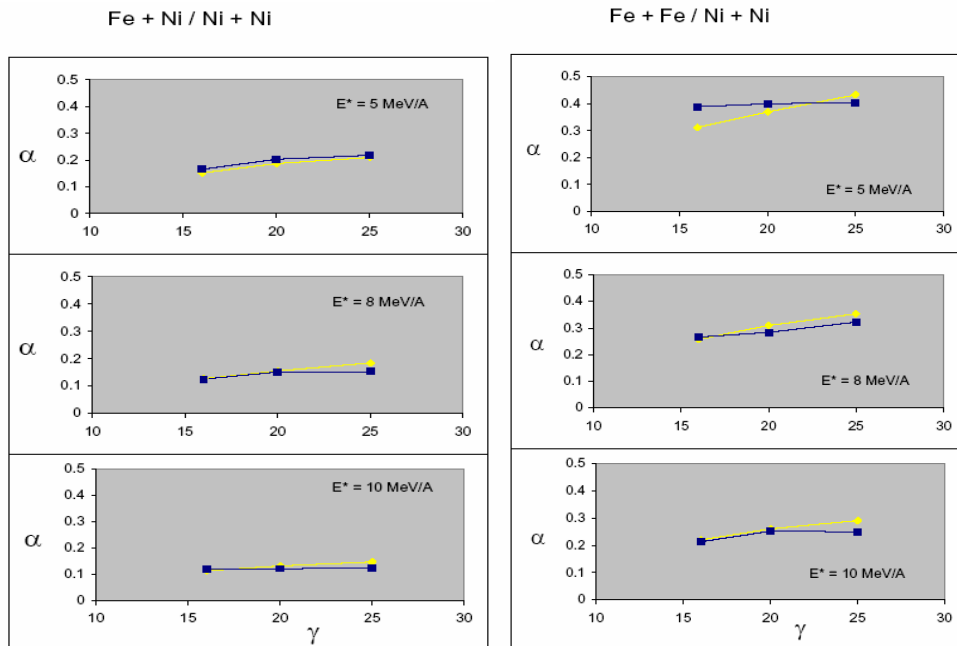


**Figure 1.** Same as in Fig. 1, but for  $^{58}\text{Fe} + ^{58}\text{Ni}$ ,  $^{58}\text{Ni} + ^{58}\text{Ni}$ , and  $^{58}\text{Fe} + ^{58}\text{Fe}$ ,  $^{58}\text{Ni} + ^{58}\text{Ni}$  pair of reactions.

energy. The decrease is much slower in the calculation where the symmetry energy dependence of the mass is taken into account during the secondary de-excitation. The slower decrease in the isoscaling parameter results in the calculation being able to reproduce the experimental isoscaling parameter at a slightly lower value of symmetry energy [3]. A similar feature (shown in Fig. 2) is also observed for the  $^{58}\text{Fe} + ^{58}\text{Ni}$ ,  $^{58}\text{Ni} + ^{58}\text{Ni}$ , and  $^{58}\text{Fe} + ^{58}\text{Fe}$ ,  $^{58}\text{Ni} + ^{58}\text{Ni}$  reactions.

- [1] M. Colonna and M. B. Tsang, *Eur. Phys. J. A* **30**, 165 (2006).
- [2] N. Buyukcizmeci, R. Ogul, and A. S. Botvina, *Eur. Phys. J.* **25**, 57 (2005).
- [3] J. Iglío *et al.*, *Phys. Rev. C* **74**, 024605 (2006).

**SECTION III**  
**NUCLEAR THEORY**

## Heavy quark three-body collisional energy loss in quark-gluon plasma

C. M. Ko and Wei Liu

Heavy quark drag coefficients due to three-body elastic scattering in a quark-gluon plasma are evaluated in the lowest order in QCD [1]. They are found to have similar values as those due to two-body elastic scattering, and both are larger than those due to two-body radiative scattering if the momenta of charm and bottom quarks are below about 4 and 9 GeV/ $c$ , respectively. Shown in Fig.1 is the nuclear modification factor for electrons from heavy quark decays in central Au+Au collisions at center of mass energy  $s_{NN}^{1/2}=200$  GeV. Results obtained from including two-body elastic scattering are given by the dotted line. Including also two-body radiative scattering gives the dashed line. Adding the contribution from three-body elastic scattering leads to the solid line. The dash-dotted line is obtained by using the strong QCD coupling constant from the lattice calculations in calculating all the drag coefficients. It is seen that including three-body elastic scattering increases the momentum degradation of heavy quarks in QGP, bringing the nuclear modification factor for electrons from the decays of produced heavy mesons closer to the measured one.

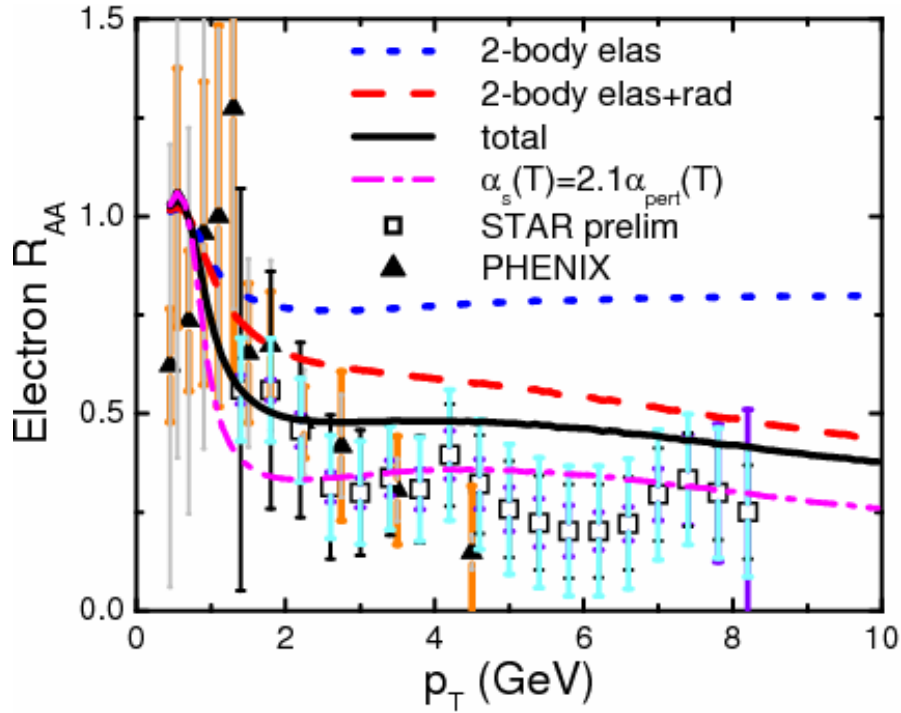


**Figure 1.** Nuclear modification factor  $R_{AA}$  for electrons from heavy quark decays in central Au+Au collisions at center of mass energy  $s_{NN}^{1/2}=200$  GeV for different heavy quark energy loss mechanisms.

[1] C.M. Ko and W. Liu, Nucl. Phys. **A783**, 233 (2007).

## Elliptic flow of deuterons in relativistic heavy ion collisions

Y. Oh and C. M. Ko

Using a dynamical model based on the  $NN \rightarrow d\pi$ ,  $NNN \rightarrow dN$ , and  $NN\pi \rightarrow d\pi$  reactions, we have studied the production of deuterons and their elliptic flow in heavy ion collisions at RHIC. Using measured nucleon transverse momentum spectrum and elliptic flow in minimum bias Au+Au collisions at center of mass energy  $s_{NN}^{1/2}=200$  GeV, the production rate of deuterons at freeze out is evaluated and is found to be dominated by the reaction  $NN \rightarrow d\pi$ . The predicted scaled deuteron elliptic flow  $v_2/A$  is shown by solid lines in Fig.1 as a function of scaled transverse momentum  $p_T/A$  in the left panel and scaled transverse kinetic energy  $E_{KT}/A$  in the right panel. Also shown by dashed lines are the scaled deuteron  $v_2$  from the coalescence model based on the overlap of the deuteron Wigner function with the nucleon distribution function. Compared to the nucleon  $v_2$ , given by dotted lines, the expected nucleon number scaling of deuteron  $v_2$  is slightly violated in both the coalescence model and the dynamical model. Both models give a reasonable description of measured deuteron  $v_2$  by the PHENIX and STAR collaborations, shown by filled circles and squares, respectively, except at low  $p_T$  and  $E_{KT}$ .

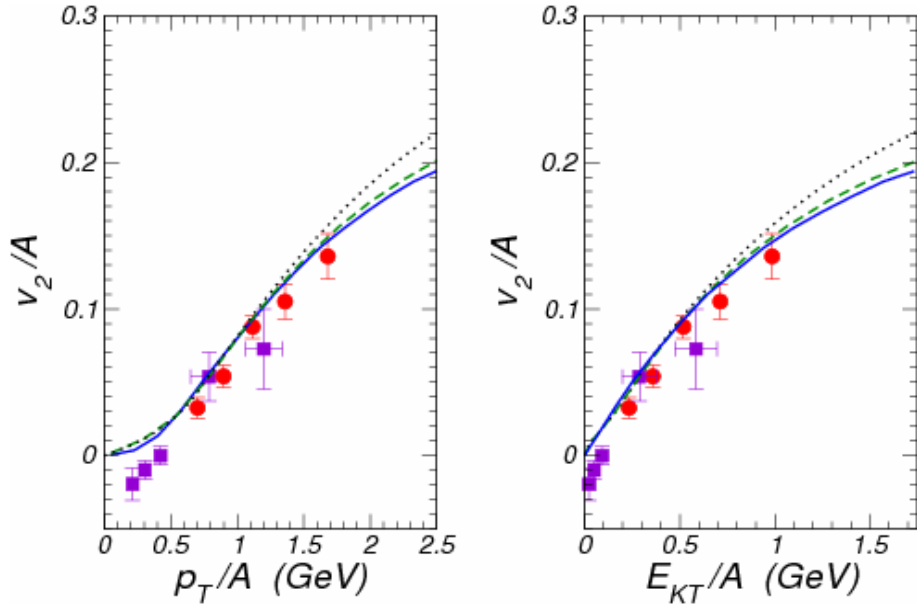


**Figure 1.** Scaled elliptic flow of deuterons as a function of (left panel)  $p_T/A$  and of (right panel)  $E_{KT}/A$  at midrapidity with the nucleon number  $A$ . The dotted line is the nucleon  $v_2$ , and the dashed and solid lines are the results of the coalescence model and the dynamical model. Experimental data are from PHENIX (filled circles) and STAR (filled squares) collaborations.

## Equation of state of the hot dense matter in a multiphase transport model

B. Zhang,<sup>1</sup> L. W. Chen,<sup>2</sup> and C. M. Ko

<sup>1</sup>*Department of Chemistry and Physics, Arkansas State University, State University, AR 72467*

<sup>2</sup>*Institute of Theoretical Physics, Shanghai Jiao Tong University, Shanghai 200240, China*

Within the framework of a multi-phase transport (AMPT) model [1], we have studied [2] the equation of state, given by the ratio of pressure to energy density, and the pressure anisotropy, given by the ratio of pressures in the longitudinal and transverse directions, of the hot dense matter produced in central relativistic heavy ion collisions. Both are found to depend on the hadronization scheme and the parton scattering cross sections. As shown in the left panel of Fig. 1, the equation of state in the default AMPT model with the partonic matter consisting of only mini jets is much softer in a wide energy density region than in the string melting model in which the partonic matter includes all valence quarks from produced hadrons. In the latter case, hardness of the equation of state further increases with increasing parton cross section. In both scenarios, the produced hot dense matter is not in thermal equilibrium as the pressure isotropy deviates significantly from unity during most of its evolution as a result of fast expansion as shown in the right panel of Fig.1.

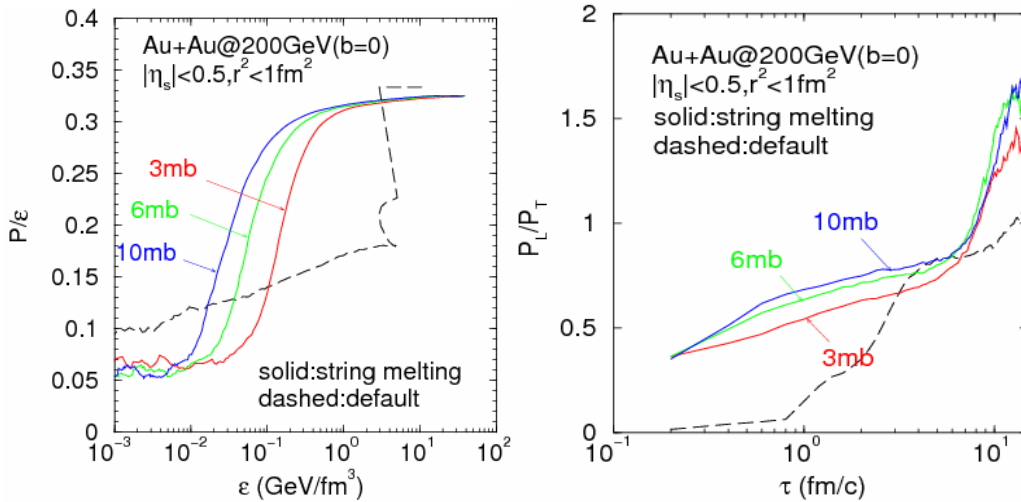


**Figure 1.** Equation of state  $P/\epsilon$  as a function of  $\epsilon$  (left panel) and the proper time evolution of the pressure anisotropy parameter (right panel) in both the default and the string melting AMPT

[1] Z. W. Lin, C. M. Ko, B. A. Li, B. Zhang, and S. Pal, Phys. Rev. C **72**, 064901 (2005).

[2] B. Zhang, L. W. Chen, and C. M. Ko, nucl-th/07053968.

## Jet flavor conversions in a quark-gluon plasma

W. Liu, C. M. Ko, and B. W. Zhang

We have studied the effect of both elastic ( $gq \leftrightarrow qq$ ) and inelastic ( $gg \leftrightarrow q \bar{q}$ ) two-body scatterings of quark and gluon jets in a quark-gluon plasma not only on their energy loss but also on the conversions between them [1]. To mimic the effect of radiative energy loss of quark and gluon jets in the quark-gluon plasma, we have multiplied the drag coefficients calculated from two-body scattering by a factor of four. We find that two-body conversion scatterings lead to a small net conversion of the quark jet to the gluon jet, resulting in a slightly larger  $p/\pi^+$  and  $p\bar{b}/\pi^-$  ratios compared to the case without conversions between gluon and quark jets, but they are not large enough to bring these ratios in central Au+Au collisions to that in p+p collisions at same energy as shown in Fig. 1. A large conversion enhancement factor  $K_C$  of more than four, similar to that needed for the jet drag coefficients to describe the jet energy loss, is needed to explain the experimental observations. Our results thus could be another indication for the strongly coupled QGP that has been produced in central heavy ion collisions at RHIC.

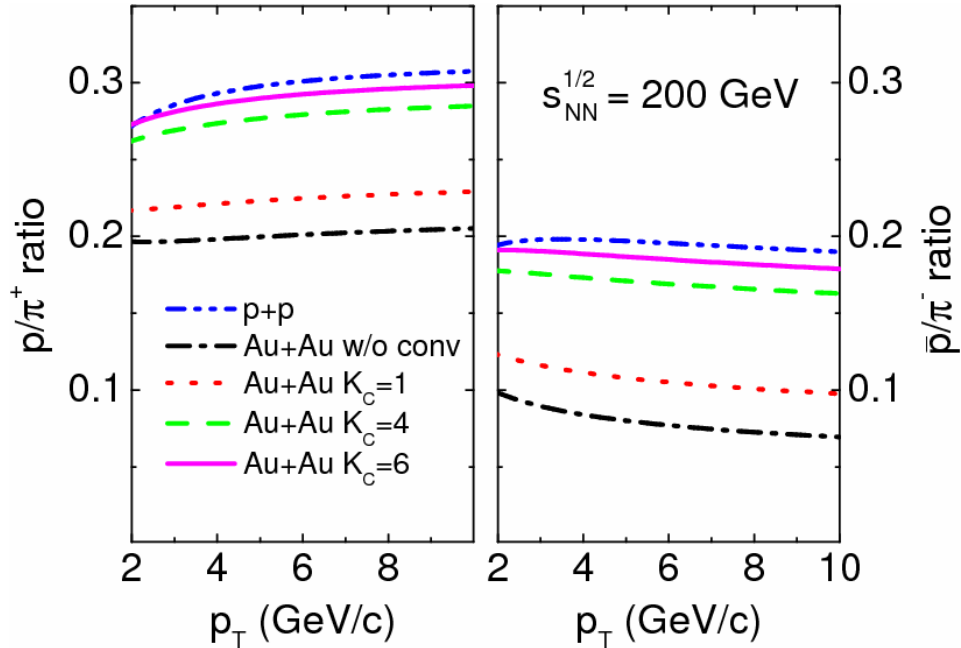


**Figure 1.**  $p/\pi^+$  (left panel) and  $p\bar{b}/\pi^-$  (right panel) ratios from quark and gluon jet fragmentation in p+p collisions and central Au+Au collisions at  $s_{NN}^{1/2}=200$  GeV as functions of momentum without or with different enhancement factor  $K_C$  for conversion scattering.

[1] W. Liu, C. M. Ko, and B. W. Zhang, Phys. Rev. C **75**, 051901(R) (2007).

## Charmonium absorption by nucleons in the meson-exchange model

Y. Oh, C. M. Ko, and W. Liu

We have reanalyzed and improved the meson-exchange model for  $J/\psi$ -nucleon reaction [1]. We find that vector-meson dominance and charm vector-current conservation lead to the universality of the  $J/\psi$  meson couplings, which can drastically change the ratio  $R_{D/D^*}$  of the cross sections of  $J/\psi+N \rightarrow D+\Lambda_c$  and  $J/\psi+N \rightarrow D^*+\Lambda_c$ . It is also found that this ratio is sensitive to the relative strengths of the coupling constants  $g_{DN\Lambda_c}$  and  $g_{D^*N\Lambda_c}$  as well as to the tensor couplings  $\kappa_{\psi\Lambda_c\Lambda_c}$  and  $\kappa_{D^*N\Lambda_c}$ . We further find that the Vector Meson Dominance (VDM) and vector-current conservation lead to a large value of  $R_{D/D^*}$ . This value can be further enhanced by the  $\psi\Lambda_c\Lambda_c$  tensor interaction. But the  $D^*N\Lambda_c$  tensor interaction has the opposite role by decreasing  $R_{D/D^*}$ . To match the quark-interchange model predictions of Ref.[2] with those from our effective Lagrangian approach leads us to conclude that  $g_{DN\Lambda_c}$  must be larger than  $g_{D^*N\Lambda_c}$  and  $\kappa_{D^*N\Lambda_c}$  must be small. The first condition contradicts with the QCD sum-rule predictions of Ref.[3] that prefers a similar strength for the two couplings. Instead, the SU(4) symmetry relations satisfy this condition. However, SU(4) symmetry gives a large value for  $\kappa_{D^*N\Lambda_c}$ , and thus does not fulfill the second condition. Since SU(4) symmetry must be broken by the heavy charm quark mass, it would be interesting to see how badly the SU(4) symmetry relations for  $g_{DN\Lambda_c}$ ,  $g_{D^*N\Lambda_c}$ , and  $\kappa_{D^*N\Lambda_c}$  are broken. Therefore, more rigorous studies on these couplings are required, which will eventually help to reconcile the predictions of the quark model and of the meson-exchange model. Nevertheless, the constraints used in our study, VMD and charm vector-current conservation, are found to have a nontrivial role to fill the gap between the quark-interchange model and meson-exchange model predictions to some extent.

[1] Y. Oh, W. Liu, and C. M. Ko, Phys. Rev. C **75**, 064903 (2007).

[2] J. P. Hilbert, N. Black, T. Barnes, and E. S. Swanson, nucl-th/0701087.

[3] F. O. Duraes, F.S. Navarra, and M. Nielsen, Phys. Lett. B **498**, 169 (2001).

## Heavy ion collisions at LHC in a multiphase transport model

C. M. Ko, L. W. Chen,<sup>1</sup> and B. W. Zhang

<sup>1</sup>*Institute of Theoretical Physics, Shanghai Jiao Tong University, Shanghai 200030, China*

To predict what one might observe in Pb+Pb collisions at  $s_{NN}^{1/2}=5.5$  TeV that will soon be available at the Large Hadron Collider (LHC), we have used a multiphase transport (AMPT) model that includes scattering in both initial partonic and final hadronic matters and the transition between these two phases of matter. Using a large parton scattering cross section of 10 mb, which is needed to describe observations in Au+Au collisions at  $s_{NN}^{1/2}=200$  GeV at the Relativistic Heavy Ion Collider (RHIC), we have studied the rapidity distributions and transverse momentum spectra of various hadrons, the elliptic flows of both light and heavy quarks as well as resulting hadrons from coalescence of quarks and antiquarks, and the two-pion correlation functions as well as the emission source function. For rapidity distributions, the total charge multiplicity in central Pb+Pb collisions at LHC is almost a factor of three larger than in central Au+Au collisions at RHIC. This value may, however, be subject to large uncertainty due to the nucleon structure functions at small  $x$  that is used in the model. Compared to those at RHIC, hadron transverse momentum spectra show even larger effective inverse slope parameters as a result of stronger collective transverse flow. For non-central collisions, the elliptic flows of quarks at LHC are stronger than those at RHIC. Although their values at low transverse momentum decrease with the masses of quarks, they reach similar peak values at higher transverse momenta. Using the quark coalescence model, the elliptic flows of hadrons including those consisting of heavy quarks can be related to those of quarks and thus provide the possibility to study the partonic dynamics in the collisions. From the emission function of pions in the AMPT model, two-pion correlation functions have been evaluated and are found to be smaller than those at RHIC. As at RHIC, the emission source is non-Gaussian in space and time. It shifts significantly to the direction along the pion transverse momentum and also has a strong correlation between this displacement and the emission time, leading to a radius in the direction along the pion momentum that is only somewhat larger than the radius in the direction that is perpendicular to the pion momentum and the beam direction. All radii of the emission source at LHC are, however, larger than those at RHIC. The emission function from the AMPT model also allows one to calculate the pair separation function of the source and to compare with the empirical one extracted from measured correlation function by the imaging method.

[1] C. M. Ko, L. W. Chen, and B. W. Zhang, *Braz. J. Phys.* (in press).

## $D_{sJ}(2317)$ meson production at RHIC

L. W. Chen,<sup>1</sup> C. M. Ko, W. Liu, and M. Nielsen<sup>2</sup>

<sup>1</sup>*Institute of Theoretical Physics, Shanghai Jiao Tong University, Shanghai 200030, China*

<sup>2</sup>*Instituto de Fisica, Universidade de Sao Paulo, C.P. 66318, 05315-970 Sao Paulo-SP, Brazil*

We have studied the production of  $D_{sJ}(2317)$  mesons in central Au+Au collisions at RHIC. The initial number of  $D_{sJ}(2317)$  mesons produced during hadronization of created quark-gluon plasma is determined by the quark coalescence model, and it depends sensitively on the quark structure of the  $D_{sJ}(2317)$  meson. An order-of-magnitude larger yield is obtained for a conventional two-quark than for an exotic four-quark  $D_{sJ}(2317)$  meson. Including the absorption and production of  $D_{sJ}(2317)$  mesons during the hadronic stage of heavy ion collisions via a kinetic model with cross sections evaluated in a phenomenological hadronic model, we find that the final yield of  $D_{sJ}(2317)$  mesons remains sensitive to its initial number produced from the quark-gluon plasma as shown in Fig. 1. Our results thus suggest that relativistic heavy ion collisions provides the possibility of studying both the quark structure of the  $D_{sJ}(2317)$  meson and its production mechanism.

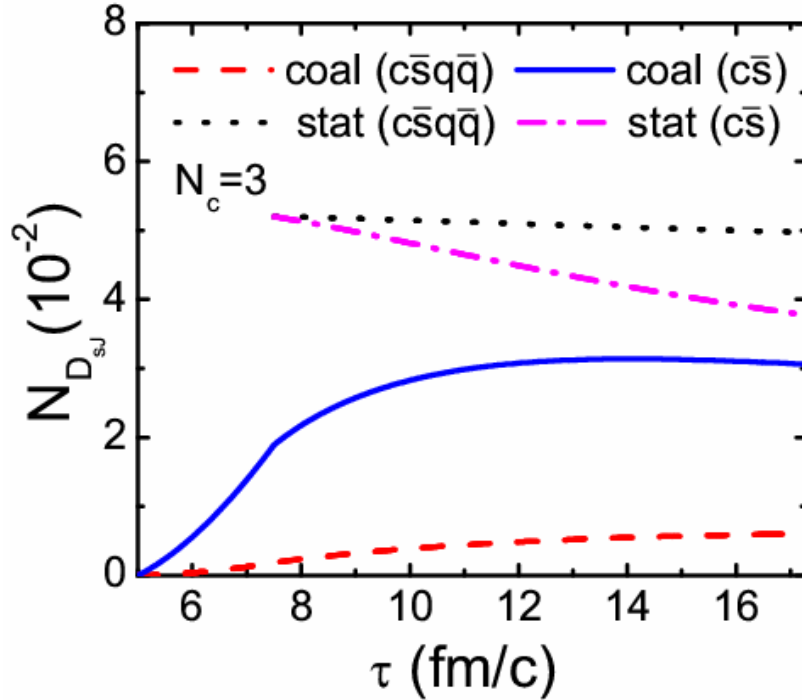


**Figure 1.** Time evolution of the  $D_{sJ}(2317)$  meson abundance in central Au+Au collisions at  $s_{NN}^{1/2}=200$  GeV for different initial numbers of  $D_{sJ}(2317)$  mesons produced from the quark-gluon plasma.

[1] L. W. Chen, C. M. Ko, W. Liu, and M. Nielsen, nucl-th/07051697.

## T-matrix approach to quarkonium correlation functions in the quark-gluon plasma

Daniel Cabrera and Ralf Rapp

Bound states of heavy quarks (charmonium and bottomonium) provide a rich laboratory for spectroscopy in QCD [1]. Potential models have been widely and successfully applied to charmonium and bottomonium spectra in vacuum, and the validity of the approach has received further support from lattice QCD (IQCD). It is therefore promising to extend the potential approach to finite temperatures,  $T$ . Medium modifications of heavy quarkonia have long been recognized as a valuable probe to characterize properties of the Quark-Gluon Plasma (QGP), such as color screening or deconfinement [2]. A good understanding of quarkonium properties in medium is a prerequisite to utilize them as diagnostic tools for the matter created in high-energy heavy-ion reactions.

Finite- $T$  IQCD computations of charmonium spectral functions suggest that low lying S-wave states ( $\eta_c, J/\Psi$ ) survive in the QGP up to  $\sim 2T_c$  ( $T_c$ : critical temperature) [3,4]. This has been confirmed in potential models based on IQCD heavy-quark free energies implemented into a Schrödinger [5] or Lippmann-Schwinger equation [6]. While the IQCD spectral functions are beset with significant uncertainty, direct (and more accurate) computations are available for the Euclidean correlation function,  $G(\tau, T)$  ( $\tau$ : Euclidean time) which is related to the spectral function,  $\sigma(\omega) \sim \text{Im}G(\omega)$ , via

$$G(\tau, T) = \int_0^{\infty} d\omega \sigma(\omega, T) K(\tau, \omega, T), \quad (1)$$

with a known temperature kernel,  $K$ . Rather than performing an inverse integral transform to extract spectral functions from Euclidean IQCD correlators, effective model calculations of spectral functions can be used to straightforwardly compute correlators and constrain them by IQCD results [7,8].

We have employed our earlier developed T-matrix approach [6] for quark-antiquark scattering to calculate charmonium and bottomonium spectral functions based on heavy-quark potentials extracted from IQCD [9]. The T-matrix approach allows for a comprehensive treatment of bound and scattering states which is essential for reliable computations of Euclidean correlators since the latter involve an integration over the entire spectrum (cf. Ref. [8] for calculations using the Schrödinger equation). Our results for S- and P-wave charmonium spectral functions and Euclidean correlation functions are summarized in Figs. 1 and 2. In line with IQCD spectral functions, we confirm that S-wave states survive in the QGP well above  $T_c$ , while P-wave ( $\chi_c$ ) states “melt” slightly above  $T_c$ . In addition, we find that nonperturbative rescattering effects lead to a large enhancement of strength around and beyond the quark-antiquark threshold, as highlighted by comparing to the perturbative (non-interacting) continuum (dashed line in the left panels of Fig.1, 2). The pertinent Euclidean correlators are calculated from Eq. (1) and normalized to a “reconstructed” correlator following from a schematic  $T=0$  spectral function (right panels in Figs. 1, 2). The decreasing trend with  $T$  for the S-wave correlator, and the enhancement over 1 in the P-wave, qualitatively agree with IQCD results [4], while the magnitude of the S-wave correlator and the  $T$ -dependence of the P-wave one are not consistent with IQCD. The plotted ratios are rather sensitive to the reconstructed correlator used for normalization. E.g., when normalizing to the S-wave correlator for  $1.5T_c$  (which according to IQCD is consistent with the free one), the agreement improves. The  $T$ -dependence of

the P-wave channel improves when using in-medium  $c$ -quark masses (as suggested by IQCD), reiterating the importance of threshold effects; finite width effects have little impact. Advanced studies are in progress and will hopefully provide a better understanding of charmonia in the QGP which can then be applied to high energy heavy-ion collisions.

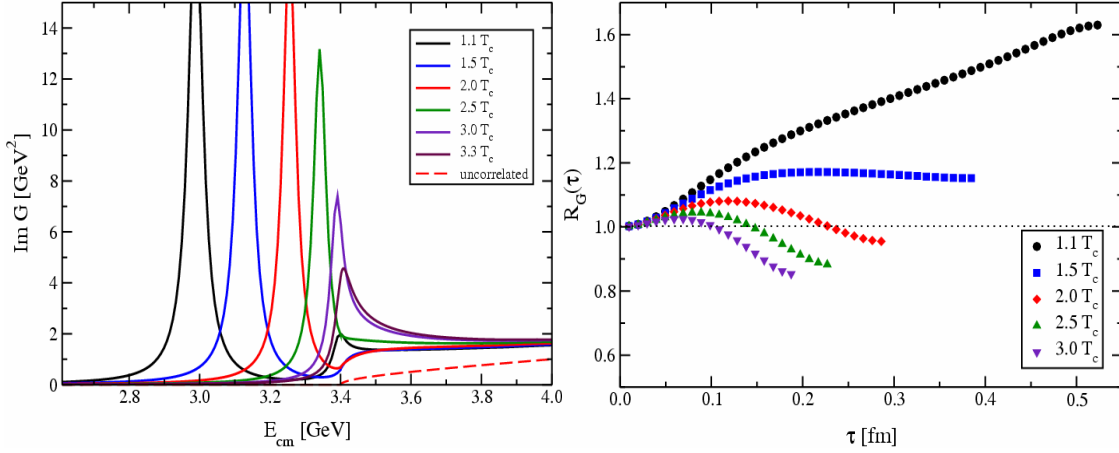


**Figure 1.** S-wave charmonium spectral function (left) and normalized Euclidean correlation function (right) [9].

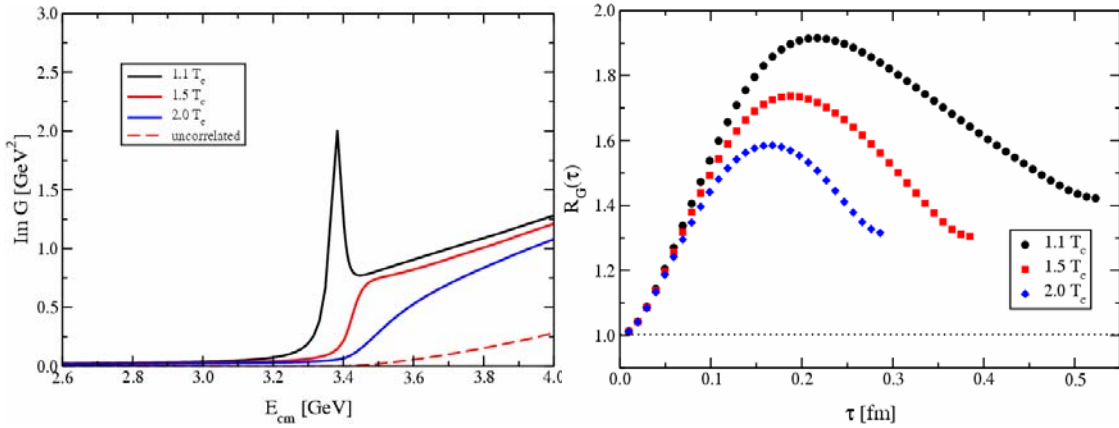


**Figure 2.** P-wave charmonium spectral function (left) and normalized Euclidean correlation function (right) [9].

[1] N. Brambilla *et al.*, *Heavy Quarkonium Physics*, arXiv:hep-ph/0412158.

[2] T. Matsui and H. Satz, *Phys. Lett.* **178B**, 416 (1986); R. Rapp and L. Grandchamp, *J. Phys. G* **30**, S305 (2004).

[3] Y. Asakawa and T. Hatsuda, *Phys. Rev. Lett.* **92**, 012001 (2004).

[4] S. Datta *et al.*, *Phys. Rev. D* **69**, 094507 (2004).

- [5] E. V. Shuryak and I. Zahed, Phys. Rev. C **70**, 021901 (2004); C.Y. Wong, Phys. Rev. C **72**, 034906 (2005); W.M. Alberico, A. Beraudo, A. de Pace, and A. Molinari, Phys. Rev. D **72**, 114011 (2005).
- [6] M. Mannarelli and R. Rapp, Phys. Rev. C **72**, 064905 (2005).
- [7] R. Rapp, Eur. J. Phys. A **18**, 459 (2003) [arXiv:nucl-th/0209081].
- [8] A. Mocsy and P. Petreczky, Phys. Rev. D **37**, 074007 (2006).
- [9] D. Cabrera and R. Rapp, arXiv:hep-ph/0611134; Eur. J. Phys. A **31**, 858 (2007).

## Transverse-momentum spectra of dilepton radiation at the CERN-SPS

Hendrik van Hees, Trenton Strong, and Ralf Rapp

Dilepton spectra are valuable probes of the strongly interacting matter as created in ultrarelativistic heavy-ion collisions (URHIC's), since the leptons, once produced, penetrate the medium without substantial final-state interactions [1]. Invariant-mass spectra encode rather direct information on medium modifications of the electromagnetic (e.m.) spectral function. Recent dimuon measurements in 158 AGeV In-In collisions by the NA60 collaboration at the CERN Super Proton Synchrotron (SPS) [2] have achieved much improved precision over existing dielectron data, providing rather stringent constraints for viable theoretical interpretations. The new data have confirmed a strong broadening of the  $\rho$ -meson as predicted several years ago by hadronic many-body theory [3]. However, the increased precision of the data requires further theoretical developments and the inclusion of sources beyond the dominant one from thermal emission via  $\rho$ -mesons.

In our previous work [4] it was shown that with a moderate modification of the underlying fireball model, together with contributions from in-medium  $\omega$  and  $\phi$  spectral functions, a quantitative description of the low-mass ( $M \leq 1\text{GeV}$ ) NA60 spectra emerges. In addition, with the source parameters fixed, the ensuing (parameter-free) prediction for thermal emission at intermediate masses ( $M > 1\text{GeV}$ ) satisfactorily reproduces the experimental excess in this regime, with the largest yield attributed to 4-pion type annihilation (with medium effects due to “chiral  $\rho$ -a1 mixing”), while emission from the Quark-Gluon Plasma is subleading.

In the present work we confront and refine our approach with newly released transverse pair-momentum ( $q_T$ ) spectra by NA60 [5]. The thermal sources which give a good description of the  $q_T$ -integrated mass spectra lead to good agreement with the momentum spectra up to  $q_T \approx 1\text{GeV}$ , reconfirming the prevalent role of thermal emission for soft momenta. At higher  $q_T$ , however, the data are significantly above the theoretical predictions. In a first step, we have re-evaluated  $\rho$  decays at thermal freezeout; it turns out that, due to the lack of regeneration (equilibrium can no longer be sustained), the kinematics for the  $\rho$ 's decaying at freezeout induce an extra time dilation (Lorentz) factor,  $\gamma$ , which entails a moderate hardening of their  $q_T$  spectra [6]. In a second step, we have included the contribution from primordially (hard) produced  $\rho$  mesons which do not thermalize with the medium, employing an estimate of the Cronin effect and a schematic surface emission [6] or jet quenching model [7]. Assuming a vacuum spectral line shape, their contribution is concentrated around the free  $\rho$  mass, and their  $q_T$  slope is substantially harder than any of the thermal or freezeout decays (cf. double-dashed line in the upper panels of Fig.1). Finally, we have evaluated primordial Drell-Yan annihilation using an extrapolation procedure to low mass by matching its  $q_T$  spectrum to the ( $M=0$ ) photon point. Below  $M=1\text{GeV}$ , the Drell-Yan yield is small up to  $q_T \approx 2\text{GeV}$ , while at  $M > 1\text{GeV}$  it becomes significant for  $q_T \geq 1.5\text{GeV}$ . In the lower panels of Fig. 1 we compare our calculations to NA60 invariant-mass spectra integrated over two bins in  $q_T$ . Again, we see that the additional hard sources are (very) small at low momenta ( $q_T < 0.5\text{GeV}$ , lower left panel) but essential at higher ones ( $q_T > 1\text{GeV}$ , lower right panel).

In summary, our earlier constructed model for thermal dilepton radiation based on an in-medium e.m. spectral function leads to fair agreement with new transverse-momentum spectra measured by NA60 up to  $q_T \approx 1\text{GeV}$ . Beyond, the inclusion of non-thermal sources, such as freezeout  $\rho$ 's, primordial  $\rho$ 's and

Drell-Yan annihilation are required, even though a quantitative comparison with a local slope analysis of experimental vs. theoretical spectra still reveals some discrepancies. Whether these can be resolved by a refined analysis, e.g. by improved estimates of the Cronin effect using p-A data, or whether additional effects, e.g. due to finite viscosity in the hydro-like fireball expansion, are necessary, remains to be seen.

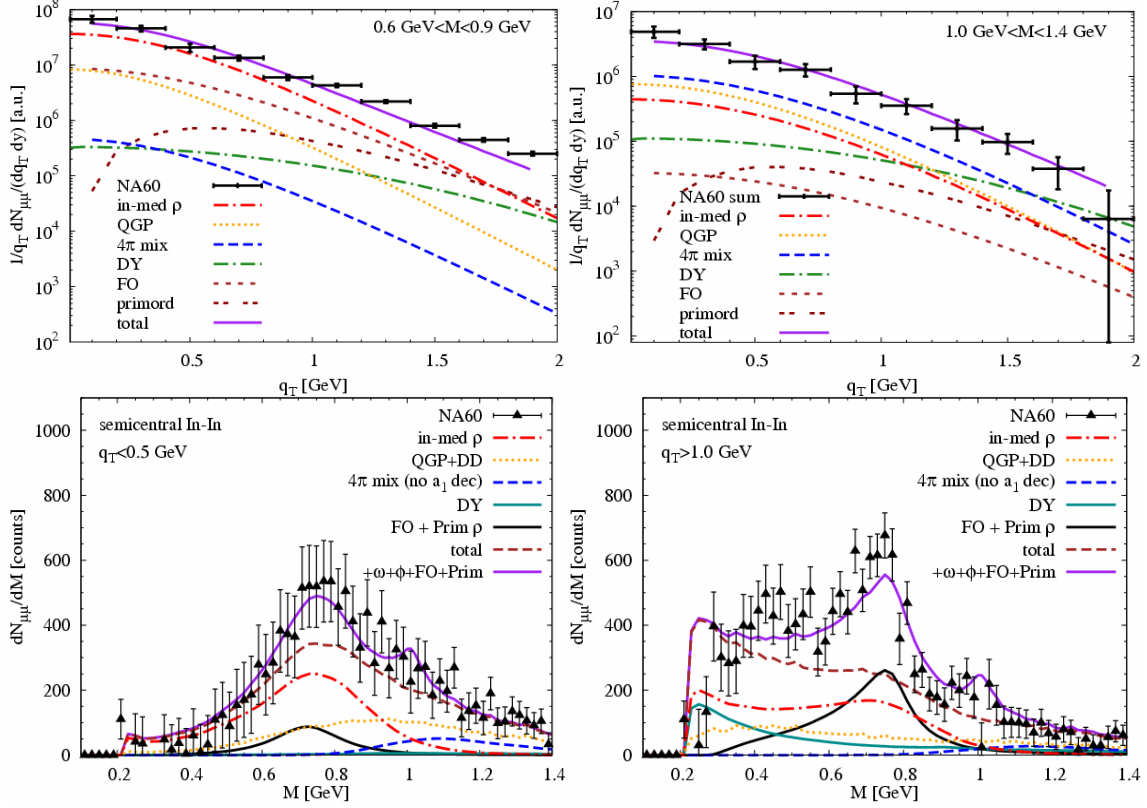


**Figure 1.** *Upper panels:* NA60 dimuon excess  $q_T$  spectra [2] in semicentral In(158A GeV)-In collisions compared to thermal dimuon radiation (based on in-medium  $\rho$ ,  $\omega$  and  $\phi$  spectral functions, QGP emission and 4-pion annihilation) supplemented with harder sources due to  $\rho$  decays at freezeout, primordial  $\rho$ 's including Cronin effect and quenching, as well as Drell-Yan annihilation [6,7]. *Lower panels:* NA60 dimuon excess spectra in invariant mass for two bins of transverse momentum (left:  $q_T < 0.5$  GeV, right:  $q_T > 1.0$  GeV) [2,5] compared to the same set of theoretical sources as in the upper panels [6,7].

- [1] R. Rapp and J. Wambach, *Adv. Nucl. Phys.* **25**, 1 (2000).
- [2] NA60 Collaboration [R. Araldi *et al.*], *Phys. Rev. Lett.* **96**, 163202 (2006).
- [3] R. Rapp and J. Wambach, *Eur. Phys. J. A* **6**, 415 (1999).
- [4] H. van Hees and R. Rapp, *Phys. Rev. Lett* **97**, 102301 (2006).
- [5] S. Damjanovic *et al.* [NA60 Collaboration], *Nucl. Phys.* **A783**, 327c (2007).
- [6] R. Rapp, H. van Hees and T. Strong, *Braz J. Phys.* (2007) in press [arXiv:hep-ph/0611339].
- [7] H. van Hees and R. Rapp, *J. Phys. G.* (2007) in press [arXiv:hep-ph/0701167]; and to be published.

## Quark coalescence based on a transport equation

Lorenzo Ravagli and Ralf Rapp

Hadron spectra measured at intermediate transverse momenta,  $p_T=2-6\text{GeV}$ , in 200A GeV Au-Au collisions at the Relativistic Heavy-Ion Collider (RHIC) have revealed a surprisingly large baryon-to-meson ratio  $\sim 1$  and a so-called constituent quark-number scaling (CQNS) of the elliptic flow,  $v_2(p_T)$ . Both phenomena are rather naturally explained within quark coalescence models (QCMs), where constituent quarks are combined into hadrons at the phase boundary between a Quark-Gluon-Plasma (QGP) and a hadron gas. QCMs are typically formulated in a collinear, instantaneous approximation which conserves 3-momentum but not total energy, limiting their applicability to sufficiently high  $p_T$  [1].

In the present work [2], we employ the Boltzmann equation to compute meson formation via resonant quark-antiquark scattering which improves previous QCMs in that energy is conserved and a proper thermal equilibrium limit can be established. This, in turn, allows a more controlled extension of the approach to low  $p_T$  and to address the experimentally observed transition from a hydrodynamic regime to CQNS, while  $2 \rightarrow 1$  scattering restricts the applicability to positive values of  $Q = m_M - 2m_q$  ( $m_M, m_q$ : meson, quark mass). We here focus on the  $\phi$  meson using input strange-quark distributions with collective properties characteristic for RHIC energies. Our results for  $\phi$  spectra are summarized in Fig. 1, illustrating that we recover CQNS of  $v_2$  at sufficiently high  $p_T$ , but with appreciable sensitivity to the  $Q$  value of the

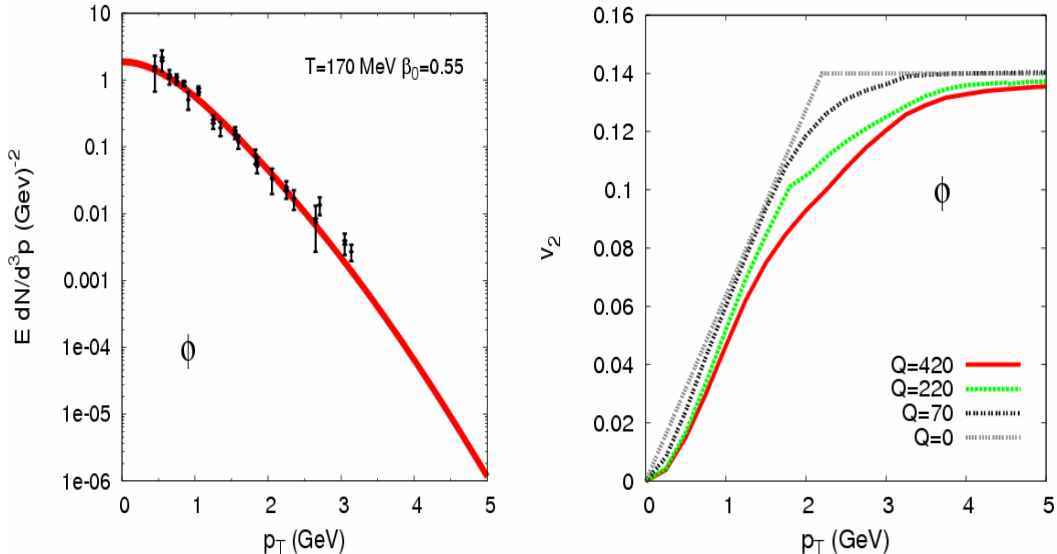


**Figure 1.**  $\phi$  meson  $p_T$ -spectra (left panel, with RHIC data for central 200A GeV Au-Au[3]) and elliptic flow (right panel) as evaluated from resonance formation via the Boltzmann equation in the quasi-stationary case. The right panel illustrates the sensitivity of  $v_2$  to the  $Q$ -value of the  $s\bar{s}$  fusion process. For  $Q \rightarrow 0$ , the input quark- $v_2$  is recovered.

meson fusion reaction. When extending the approach to include charm quarks, our results are indicative for a general CQNS for  $v_2$  in transverse kinetic energy, as recently found experimentally [4].

- [1] R.C. Hwa and C.B. Yang, Phys. Rev. C **67**, 034902 (2003); V. Greco, C.M. Ko and P. Levai, Phys. Rev. C **68**, 034904 (2003); R.J. Fries, B. Müller, C. Nonaka and S.A. Bass, Phys. Rev. C **68**, 044902 (2003).
- [2] L. Ravagli and R. Rapp, arXiv:hep-ph/0705.0021.
- [3] PHENIX Collaboration [S.S. Adler *et al.*], Phys. Rev. C **72**, 014903 (2005); STAR Collaboration, [J. Adams *et al.*], Phys. Lett. B **612**, 181 (2005).
- [4] PHENIX Collaboration [A. Adare *et al.*], arXiv :nucl-ex/0608033.

## The initial state of high energy nuclear collisions

R. J. Fries, J. Kapusta,<sup>1</sup> and Y. Li<sup>2</sup>

<sup>1</sup>*School of Physics and Astronomy, University of Minnesota, Minneapolis, Minnesota 55455*

<sup>2</sup>*Department of Physics and Astronomy, Iowa State University, Ames, Iowa 50011*

At asymptotically large energies hadrons and nuclei essentially appear as black disks with a large saturated gluon density. This state has been termed the color glass condensate and a rich literature about this phenomenon has been produced in recent years. For heavy ion collisions at RHIC and LHC this concept is believed to be very important. It governs the initial state of high energy nuclear collisions. One of the main questions in the field of heavy ion physics is how the colliding color glass evolves into a thermalized quark gluon plasma. In an ongoing effort with several collaborators R.J.Fries is working on two aspects of this question.

- (a) The McLerran-Venugopalan (MV) model was one of the first formulations of the color glass condensate. It uses the large gluon occupation numbers to justify a quasi-classical treatment of the gluon field. For nuclear collisions, no analytic solution to all orders in the coupling or the sources is known. In a recent publication [1] it has been shown that the field equations can be solved recursively using an expansion in the proper time  $\tau$  in the forward light cone. One of the outcomes has been the rediscovery of the strong longitudinal color fields immediately after the collision. This work is being continued. Currently the first few coefficients in the recursion are evaluated in detail. The goal is to obtain a space-time map of the energy momentum tensor at very early times in the collision.
- (b) Immediately following (a) is the question what can be learned about the initial energy density, pressure and flow in the plasma after thermalization. This is important to reliably determine the initial conditions for a further hydrodynamic evolution of the system. Currently techniques are being developed to derive constraints for the plasma phase from the initial phase of strong gluon fields.

Preliminary results have been reported at the Quark Matter 2006 Conference [2].

[1] R. J. Fries, J. Kapusta, and Y. Li, nucl-th/0604054.

[2] R. J. Fries, nucl-th/0702026.

## Perturbative QCD and multiple scattering in nuclear matter

R. J. Fries and A. Majumder<sup>1</sup>

<sup>1</sup>*Department of Physics, Duke University, Durham, North Carolina 27708*

Factorization theorems in perturbative QCD traditionally describe only a single scattering of partons in high energy hadron or nucleus collisions. This is not sufficient if the mean free path of a parton is smaller than the size of the nuclear matter. A rigorous way to treat multiple scattering within a factorized pQCD framework as so-called higher twist corrections has been laid out by J. Qiu and G. Sterman. In the past R.J. Fries has successfully applied this formalism to proton nucleus collisions, e.g. he was the first to carry out a resummation of higher twist contributions [1]. Renewed interest in this more rigorous approach comes from heavy ion physics where "pQCD inspired" calculations of jet energy loss have turned out to carry a large dependence on model assumptions. During the period under consideration R.J. Fries has started work with A. Majumder to further develop the higher twist formalism. Before applications in heavy ion collisions can be considered processes in well-defined environments are studied:

- (a) Transverse momentum broadening from multiple scattering for heavy quarks in deep inelastic scattering and p+A collisions. This work has the goal to resum nuclear enhanced higher twist corrections at leading order in the coupling (i.e. w/o radiation). This is a generalization of previous work of R.J. Fries [1]. A. Majumder and collaborators have recently added the insight that the results can be written as a diffusion in transverse momentum space.
- (b) Resummation of leading nuclear enhanced higher twist corrections at next-to-leading order (NLO) in the coupling. This is a generalization of project (a) to allow gluon radiation. At the same time it is also a generalization of previous work of Wang and Guo at NLO which has only twist-4 corrections but no resummation of arbitrary twist. The calculations are carried out for deep-inelastic scattering. Both energy loss and transverse momentum broadening will be studied.

[1] Rainer J. Fries, Phys. Rev. D **68**, 074013 (2003).

## The recombination model

R. J. Fries and collaborators

The recombination model has been a success story at RHIC. It describes certain features of hadron production at intermediate transverse momentum at RHIC energies by simply assuming coalescence of effective quarks into hadrons. R. J. Fries has been one of the main proponents of the recombination model in the past [1]. Currently efforts are focused on extended applications. More fundamental questions which remain open are under consideration as well and will be reported on in the future.

- (a) The so called Duke Recombination Model does only recombine thermal quarks at the hadronization temperature in heavy ion collisions. It has been suggested by other groups that recombination of thermal quarks with partons from jets may play an important role as well. A new project aims at implementing jet-thermal recombination into the Duke Recombination Model and to apply it to data. In the future this will also be matched with a jet fragmentation calculation.
- (b) The Duke Recombination Model has never been applied to energies and systems other than Au+Au at 200 GeV. Experimental collaborations have repeatedly asked for results from recombination models for lower energies, even down to the SPS region. This region is currently explored within the classical Duke Recombination Model and first results are to be expected soon.

[1] R. J. Fries, B. Muller, C. Nonaka, and S. A. Bass, Phys. Rev. Lett. **90**, 202303 (2003).

## Suppression of the Coulomb interaction in the off-energy-shell $p - p$ scattering from the $p + d \rightarrow p + p + n$ reaction

A. M. Mukhamedzhanov, A. Tumino,<sup>1</sup> C. Spitaleri,<sup>1</sup> G. G. Rapisarda,<sup>1</sup> S. Cherubini,<sup>1</sup>  
V. Crucillá,<sup>1</sup> M. Gulino,<sup>1</sup> M. La Cognata,<sup>1</sup> L. Lamia,<sup>1</sup> F. Mudó,<sup>1</sup> R. G. Pizzone,<sup>1</sup> S. Romano,<sup>1</sup>  
M. L. Sergi,<sup>1</sup> Z. Elekes,<sup>2</sup> Z. Fülöp,<sup>2</sup> G. Gyürky,<sup>2</sup> G. Kiss,<sup>2</sup> and E. Somorjai<sup>2</sup>

<sup>1</sup>*Dipartimento di Metodologie Fisiche e Chimiche per l'Ingegneria - Università di Catania, Catania and  
Laboratori Nazionali del Sud - INFN, Catania, Italy,*

<sup>2</sup>*ATOMKI - Debrecen, Hungary*

The proton-proton scattering has been extensively investigated in the past in order to gather more information on the nuclear force. Despite the simplicity of the  $p+p$  system, the analysis of such interaction is complicated by the presence of the Coulomb scattering that has to be considered in addition to the nuclear effects. There is a region at low  $p+p$  relative energy ( $E_{pp}$ ) in which the nuclear scattering amplitude in the 1S-state and the even part of the Coulomb scattering amplitude give destructive interference [1], leading to the deep minimum in the  $p+p$  cross section.

Such a strong signature has recently triggered the idea that an indirect study of the  $p-p$  scattering at low energy can provide another important test for the Trojan Horse Method (THM). Indeed the interference pattern should be missing if there is no sizeable Coulomb amplitude, and this is what the THM is for. In the present we address the study of the  $p+p$  elastic scattering through the  ${}^2H(p,pp)n$  reaction. The aim of the experiment is to investigate the suppression of the Coulomb amplitude also for scattering. This will be done by checking whether there is still evidence of the nuclear plus Coulomb interference pattern in the half-off-energy-shell (HOES)  $p+p$  cross-section extracted via the THM. This experimental cross-section will be compared with the calculated HOES one and with the on-energy-shell (OES) counterpart in the energy region where the Coulomb-nuclear interference occurs. We note that in the case of elastic scattering, the off-shell suppression mechanism of the Coulomb interaction is quite different from that of rearrangement reactions mentioned before. In particular, in the case of elastic scattering the total amplitude is given by the sum of Coulomb and Coulomb-modified nuclear parts. As we will show, the off-shell effects make the Coulomb amplitude suppressed compared to the nuclear part and the Gamow factor missing in the Coulomb modified nuclear amplitude. Thus leads to an additional enhancement of the nuclear scattering. The low energy  ${}^2H(p,pp)n$  reaction in the QF kinematics was measured several times before (see [2] and references therein), but not in the region where the  $p-p$  Coulomb-nuclear interference takes place. We made the first measurements of this reaction at 5 MeV of beam energy in the interference region at the ATOMKI, Debrecen (Hungary). In Fig. 1 we present the HOES  $p+p$  extracted from the measured  ${}^2H(p,pp)n$  reaction (black full dots from present work, red triangles and blue stars from our previous measurements [2,3]) compared with the theoretical OES  $p+p$  cross section (black solid line); dashed-dotted line is the HOES  $p+p$  cross section calculated using the HOES Coulomb scattering amplitude and HOES Coulomb-modified nuclear scattering amplitude generated by the Yamaguchi potential. We observe a striking disagreement between the THM (HOES) and free  $p+p$  (OES) cross sections throughout the region of the interference minimum, which is missing in

the THM data. Instead, the calculated HOES  $p+p$  cross section nicely fits the THM data. The reason for such a big difference in the energy dependence between low-energy OES and HOES cross sections is due to the suppression of the HOES Coulomb scattering amplitude. Due to this suppression the energy dependence of the HOES cross section is very similar to the energy dependence of the OES  $n+n$  and  $p+n$  cross sections. The effect of the suppression of the Coulomb effects is universal whether we consider reaction or scattering what provides another validation of the THM. The paper has been accepted for publication in Physical Review Letter (2007).

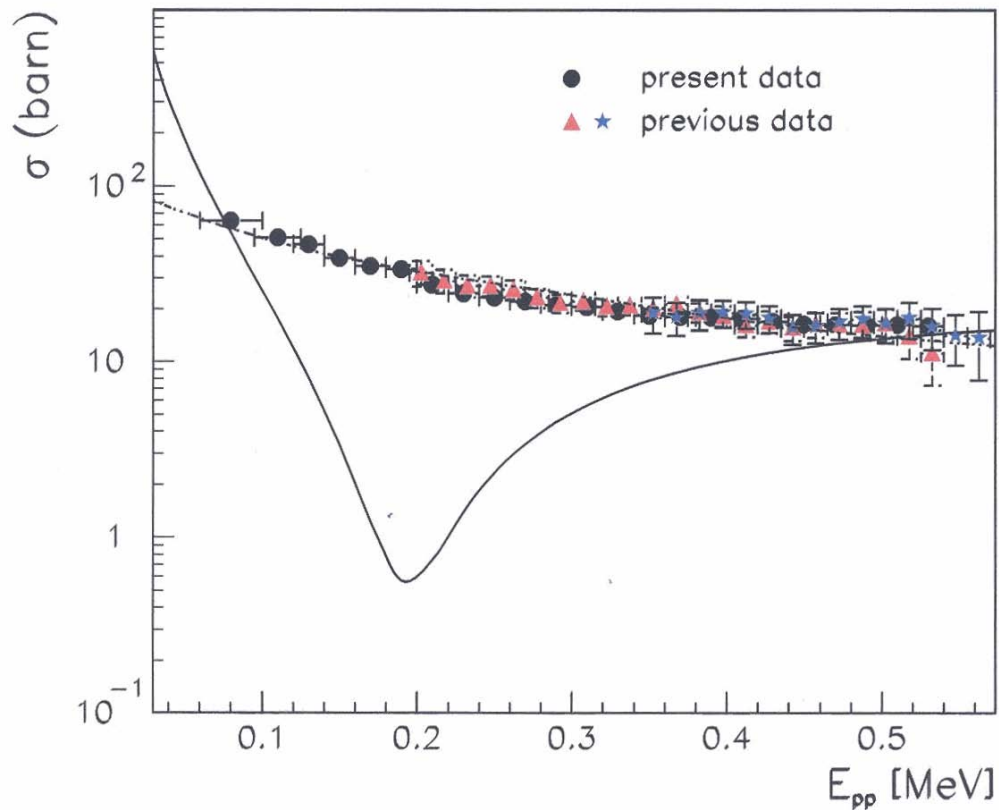


**Figure 1.** Red diamonds are the OES experimental  $p-p$  cross section [1] and black full dots are the THM  $p-p$  cross sections (from the present experimental work; red triangles and blue stars are our data from Ref. [3]). Solid line represents the theoretical OES  $p-p$  cross section and the dashed-dotted line is the HEOS  $p-p$  cross section calculated as explained in the text.

- [1] H. Dombrowski *et al.*, Nucl. Phys. **A619**, 97 (1997).
- [2] M. G. Pellegriti *et al.*, Prog. Theor. Phys. **154**, 349 (2004).
- [3] A. Tumino *et al.*, Nucl. Phys. **A787**, 337 (2007).

## Are spectroscopic factors from transfer reactions consistent with asymptotic normalization coefficients?

D. Y. Pang,<sup>1,2</sup> F. M. Nunes,<sup>2</sup> and A. M. Mukhamedzhanov

<sup>1</sup>*School of Physics and MOE Key Laboratory of Heavy Ion Physics, Peking University, Beijing, China,*

<sup>2</sup>*National Superconducting Cyclotron Laboratory and Department of Physics and Astronomy, Michigan State University, East Lansing, Michigan 48864*

It is extremely important to devise a reliable method to extract spectroscopic factors (SFs) from transfer cross sections. One would eventually like to have a very accurate probe that could test the predictions of the models and could disentangle the relevant elements of the NN force that are still missing, especially when moving toward the driplines. For exotic nuclei near or on the driplines, transfer reactions are a unique tool and, hence, can have a large impact in the programs of the new generation rare isotope laboratories. The standard framework for analysing transfer data with the intent of extracting SFs is the distorted-wave Born approximation (DWBA). Overall, it has been very successful in describing angular distributions at forward angles and less so for the larger angles where higher order become more important. The SF is the normalization needed for the calculated DWBA differential cross section to match the experimental one at forward angles. The uncertainty of the extracted SF resulting from the normalization of the DWBA cross section is assumed to be  $\sim 30\%$ , even if the statistical errors are low. The reasons for this inaccuracy are typically attributed to ambiguities in the optical potentials, the inadequacy of the DWBA reaction theory, or the dependence on the single-particle potential parameters.

In Ref. [1], a combined method of extracting SFs from transfer reactions was introduced. This method can also be applied to breakup and  $(e, e'p)$  reactions. The combined method, which is based on the introduction of the asymptotic normalization coefficients (ANC) into the transfer analysis, allows one to significantly reduce the uncertainty in the choice of the bound state potential parameters and to test the DWBA or other underlying reaction theory. In the combined method the ANC should be determined from an independent measurement of a peripheral reaction while the SF is determined from transfer reactions which are sensitive to the nuclear interior. In [1] we emphasize that fixing the ANC is absolutely necessary, since even when the beam energy is well above the Coulomb barrier, most of the reaction happens in the asymptotic region.

In this work, [2], we expand on the ideas of the combined method, and explore other uncertainties (such as optical potentials and higher order effects) to attempt a unification of the SF and the ANC, searching for a reaction description which is practical and gives reliable spectroscopic information. We have studied transfer reactions to states considered good single particles, with three different Q-values, namely  $^{14}\text{C}(d,p)^{15}\text{C}(g.s.)$  at the deuteron incident energy  $E_d = 14$  MeV,  $^{16}\text{O}(d,p)^{17}\text{O}(g.s.)$  at  $E_d = 15$  MeV and  $^{40}\text{Ca}(d,p)^{41}\text{Ca}(g.s.)$  at  $E_d = 11$  MeV. All these reactions are above the Coulomb barrier and therefore contain some information from the interior. The standard DWBA method, using global optical potentials and the typical single particle parameters, produces SFs in agreement with shell model predictions, however the corresponding ANCs are not consistent with those extracted from independent

measurements. If one imposes, within the DWBA formulation, ANCs that are consistent with the experimental values, the extracted SFs are significantly reduced compared to the shell model predictions. Some improvements on the SF/ANC mismatch can be obtained by using a deuteron optical potential fitted directly to the corresponding elastic data, at the relevant energy. In particular, for  $^{16}\text{O}(d,p)^{17}\text{O}(g.s.)$  we obtain SF/ANC consistency. However the problem for the other two cases is not resolved. The deuteron adiabatic potential, which takes into account breakup, can change the SF up to 30%. This improves the situation for  $^{14}\text{C}(d,p)^{15}\text{C}(g.s.)$  but fails to bring the  $^{41}\text{Ca}$  ANC.

Contrary to  $(e,e'p)$  measurements, transfer reactions are surface peaked and it is disconcerting that the traditional methods to handle higher order effects at the surface are not able to solve the SF/ANC discrepancy for one of our test cases. The very fact that, even when the energies are well above the Coulomb barrier, there is such a large contribution from the peripheral region, makes it extremely important to pin down the ANC input unambiguously. We cannot rule out the possibility of a problem in the  $^{41}\text{Ca}$  ANC we extracted from other data. Experiments to measure ANCs for this case are crucial to settle this matter. In the future we suggest that experiments be designed for the extraction of ANCs in parallel with the corresponding experiments aimed at extracting SFs. All three ANCs important for this analysis can be measured at the Cyclotron Institute, Texas A&M University. In particular, the  $^{15}\text{C}$  ANC is important for nuclear astrophysical reaction and will be measured in the near future.

[1] A. M. Mukhamedzhanov and F. M. Nunes, Phys. Rev. C **72**, 017602 (2005).

[2] D. Y. Pang, F. M. Nunes, and A. M. Mukhamedzhanov, Phys. Rev. C **75**, 024601 (2007).

## Deuteron elastic scattering and stripping processes off $^{12}\text{C}$ as a three-body problem

E. O. Alt,<sup>1</sup> L. D. Blokhintsev,<sup>2</sup> A. M. Mukhamedzhanov, and A. I. Sattarov

<sup>1</sup>*Institut für Physik, Universität Mainz, D-55099 Mainz, Germany*

<sup>2</sup>*Nuclear Physics Institute, Moscow State University, Moscow, Russia*

In this work we performed the first full-scale three-body calculations of the stripping reaction  $^{12}\text{C}(d,p)^{13}\text{C}$ . First deuteron elastic scattering and stripping processes off a target nucleus consisting of  $A$  nucleons are treated within the framework of the few-body integral equations theory. By projecting the  $(A+2)$ -body operators onto target states, matrix three-body integral equations are derived which allow for the incorporation of the excited states of the target nucleons. This approach is applied to deuteron scattering off  $^{12}\text{C}$  when the latter is in its ground state before and after the reaction. For the nucleon- $^{12}\text{C}$  subsystem three sets of (quasi-separable) potentials are employed. The first such potential is based on the one derived in Ref. [1] for orbital angular momentum states with  $L \leq 2$ , which is valid for low energies. As second set we use the potential of Miyagawa and Koike [2] which is fit to semiphenomenological higher-energy phase shifts for states up to  $L = 6$ . The third one finally consists for  $3 \leq L \leq 5$  of the potential set of Miyagawa and Koike while the potential parameters for  $L \leq 2$  are determined by simultaneously fitting the elastic-channel  $T$  matrix obtained as solution of multichannel two-body Lippmanr-Schwinger equations, to the experimental low-energy and the semi-phenomenological higher-energy phase shifts. For the nucleon-nucleon interaction we take one of the separable 3S1 – 3D1 potentials from Ref. [3]. Differential cross sections for the elastic scattering reaction  $d+^{12}\text{C} \rightarrow d+^{12}\text{C}$  and the transfer reaction  $d+^{12}\text{C} \rightarrow p+^{13}\text{C} (^{13}\text{C}^*)$  are

calculated at deuteron bombarding energies 4.66 and 15 MeV (up to 36-channel calculation), and at 56 MeV (up to 76-channel calculation) together with some selected analyzing powers, and are compared with experimental data. At the highest energy considered, the decomposition of the differential cross section into the near-side and the far-side components shows the appearance of nuclear rainbow scattering. In Figs 1 and 2 we present the calculated and experimental differential cross sections for the elastic scattering  $d+^{12}\text{C} \rightarrow d+^{12}\text{C}$  and transfer reaction  $d+^{12}\text{C} \rightarrow p+^{13}\text{C}$  at deuteron energy 4.66 MeV. The elastic scattering data are taken from Ref. [4] and the transfer data from Ref. [5]. The paper has been accepted for publication in Physical Review C (2007).

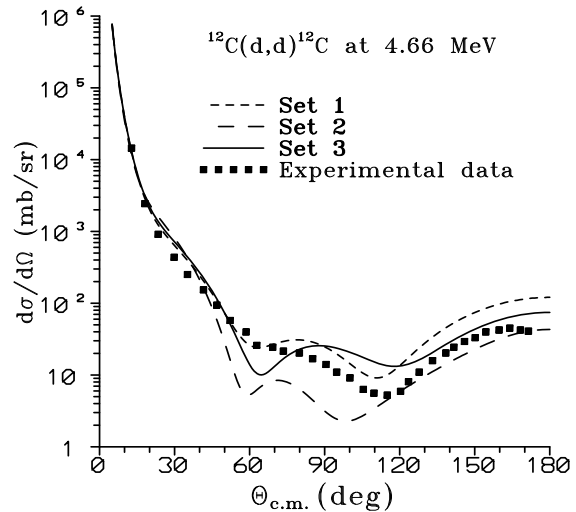


**Figure 1.** Differential cross section for the elastic  $(d,d)$  scattering. Experimental data are from Ref.[4].

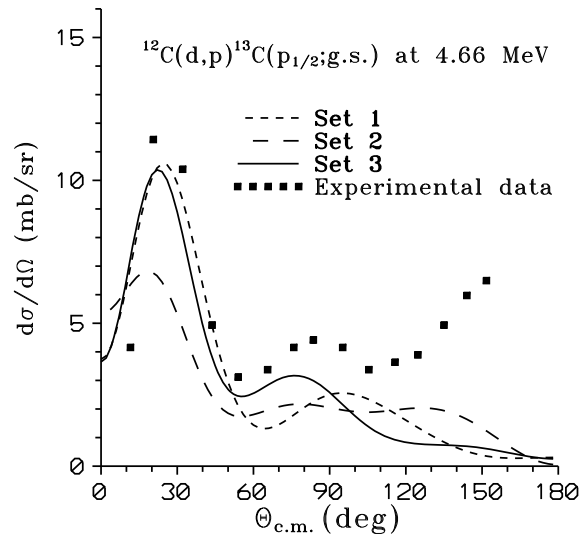


**Figure 2.** Same as Figure 1 but for the differential cross section for the  $^{12}\text{C}(d,p)^{13}\text{C}(p_{1/2})$  stripping reaction to the ground state of  $^{13}\text{C}$ . Experimental data are from Ref. [5].

- [1] G. Cattapan *et al.*, Nucl. Phys. **A241**, 204 (1975).
- [2] K. Miyagawa and Y. Koike, Prog. Theor. Phys. **82**, 329 (1989).
- [3] A. C. Phillips, Nucl. Phys. **A107**, 207 (1968).
- [4] R. L. A. Cottrell, J. C. Lisle, J. O. Newton, Nucl. Phys. **A109**, 288 (1968).
- [5] E. W. Hamburger, Phys. Rev. **123**, 619 (1961).

## Trojan horse for resonance reactions

A. M. Mukhamedzhanov, C. Spitaleri,<sup>1</sup> and R. E. Tribble

<sup>1</sup>*DMFCI, Universit di Catania, Catania, Italy and INFN - Laboratori Nazionali del Sud,  
Catania, Italy*

The presence of the Coulomb barrier for colliding charged particles makes nuclear reaction cross sections at astrophysical energies so small that their direct measurement in the laboratory is very difficult, or even impossible. Consequently indirect techniques often are used to determine these cross sections. The Trojan Horse (TH) method is a powerful indirect technique which allows one to determine the astrophysical factor for rearrangement reactions. The TH method involves obtaining the cross section of the binary  $x + A \rightarrow b + B$  process at astrophysical energies by measuring the two-body to three-body ( $2 \rightarrow 3$ ) process,  $a + A \rightarrow y + b + B$ , in the quasifree (QF) kinematics regime, where the "Trojan Horse" particle,  $a = (yx)$  is accelerated at energies above the Coulomb barrier. After penetrating through the Coulomb barrier, nucleus  $a$  undergoes breakup leaving particle  $x$  to interact with target  $A$  while projectile  $y$  flies away. From the measured  $a + A \rightarrow y + b + B$  cross section, the energy dependence of the binary subprocess,  $x + A \rightarrow b + B$ , is determined.

In this work we address the TH formalism for the resonant binary processes  $x + A \rightarrow b + B$ . In the TH method we determine the cross section for the binary process  $x + A \rightarrow b + B$  proceeding through an isolated resonance  $F$  which contains the DWBA amplitude of the direct transfer reaction  $a + A \rightarrow y + F$  rather than the partial width corresponding to the resonance formation  $x + A \rightarrow F$ . The DWBA amplitude takes into account the initial and final state interactions and the off-shell character of the transferred particle  $x$ . By simple renormalization the resonant TH amplitude can be reduced to the on-shell amplitude of the binary reaction  $x + A \rightarrow b + B$ . In the case of two or more interfering resonances the half-off-energy-shell (HOES) R matrix theory has been developed. We show why a simple plane wave approximation works. For example, for two interfering resonances the astrophysical factor determined from the TH reaction is given by

$$S^{TH}(E_{xA}) = \frac{\pi e^{2\pi\eta_{xA}}}{2\mu_{xA}} \Gamma_{xA(1)} \left| \frac{\Gamma_{bb(1)}^{1/2}(E_{bb})}{E_{xA} - E_{R_1} + i \frac{\Gamma_1(E_{xA})}{2}} + \frac{\Gamma_{bb(2)}^{1/2}(E_{bb}) M_{21}^{DW}}{E_{xA} - E_{R_1} + i \frac{\Gamma_2(E_{xA})}{2}} \right|^2, \quad (1)$$

where  $\Gamma_{xA(i)}$  and  $\Gamma_{bb(i)}$  are the partial width in the entry and exit channels of the resonance  $F_i$ ,  $\Gamma_i$  and  $E_{R_i}$  its total width and resonance energy,  $\eta_{xA}$  is the Coulomb parameter in the channel  $x + A$ ,  $M_{21}^{DW} = M_2^{DW} / M_1^{DW}$ , and  $M_i^{DW}$  is the DWBA amplitude for the reaction  $a + A \rightarrow y + F_i$ ,  $i = 1, 2$ , populating resonance  $F_i$ . The TH astrophysical factor is to be compared with the on-energy-shell (OES) S factor

$$S(E_{xA}) = \frac{\pi e^{2\pi\eta_{xA}}}{2\mu_{xA}} \Gamma_{xA(1)} \left| \frac{\Gamma_{bb(1)}^{1/2}(E_{bb})}{E_{xA} - E_{R_1} + i \frac{\Gamma_1(E_{xA})}{2}} + \frac{\Gamma_{bb(2)}^{1/2}(E_{bb}) \gamma_{(xA)21}}{E_{xA} - E_{R_1} + i \frac{\Gamma_2(E_{xA})}{2}} \right|^2. \quad (2)$$

Here  $\gamma_{(xA)21} = \gamma_{(xA)2} / \gamma_{(xA)1}$  is the ratio of the reduced widths of the resonance  $F_i$  in the entry channel  $x + A$ . In Fig. 1 we compare the calculated HOES astrophysical factor given by Eq. (1) (red dashed line) with the OES S factor (black solid line), Eq. (2), for reaction  $^{15}\text{N} + p \rightarrow ^{12}\text{C} + \alpha$ . An excellent agreement demonstrates the power of the TH method for resonance reactions. The paper has been submitted to Physical Review C.

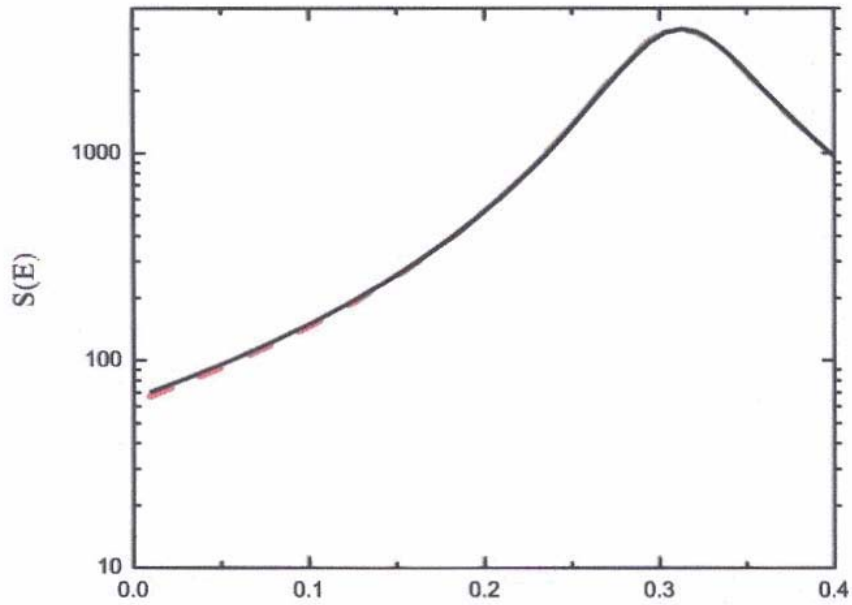


**Figure 1.** Comparison of the HOES S factor (red dashed line) with the OES one (black solid line) calculated using Eqs. (1) and (2), respectively;  $E \equiv E_{xA}$ .

## Asymptotic normalization coefficient and spectroscopic factor from $^{48}\text{Ca}(d,p)^{49}\text{Ca}$ and $^{48}\text{Ca}(n,\gamma)^{49}\text{Ca}$

A. M. Mukhamedzhanov, P. Mohr,<sup>1</sup> and F. M. Nunes<sup>2</sup>

<sup>1</sup>*Strahlentherapie, Diakoniekrankenhaus Schwäbisch Hall, D-74253 Schwäbisch Hall, Germany,*

<sup>2</sup>*National Superconducting Cyclotron Laboratory and Department of Physics and Astronomy, Michigan State University, East Lansing, Michigan 48864*

In our previous works [1,2] we have suggested a new combined method to determine the spectroscopic factors (SFs) from transfer reactions using the information about the asymptotic normalization coefficients (ANCs). Introduction of the ANC will allow us to determine the parameters of the bound state potential and obtain more accurate SF. The determined Sfs can be used to calculate the neutron radiative capture reactions.

To test our method we applied it for analysis of the direct radiative capture reaction  $^{48}\text{Ca}(n,\gamma)^{49}\text{Ca}$ . We note that  $^{48}\text{Ca}$  is considered to be a double magic nucleus, hence the  $^{49}\text{Ca}$  ground state is well described as a single-particle neutron wave function bound to the core  $^{48}\text{Ca}$  with the spectroscopic factor close to unity.

To apply our method first we determined the ANC for  $^{49}\text{Ca} \rightarrow ^{48}\text{Ca} + n$  from the sub-Coulomb transfer reaction  $^{48}\text{Ca}(d,p)^{49}\text{Ca}$  [3]. After that we determined the SF for the configuration  $^{48}\text{Ca} + n$ . Fortunately in the case under consideration direct measurements for  $^{48}\text{Ca}(n,\gamma)^{49}\text{Ca}$  are available [4] and we can compare the SF and ANC determined from the radiative capture process with the ones obtained from the  $^{48}\text{Ca}(d,p)^{49}\text{Ca}$  reaction. The sub-Coulomb  $^{48}\text{Ca}(d,p)^{49}\text{Ca}$  reaction is entirely peripheral and by normalizing the DWBA cross section to the experimental one at backward angles we determined the ANC for  $^{49}\text{Ca} \rightarrow ^{48}\text{Ca} + n$ ,  $C = 5.22 \text{ fm}^{-1/2}$ . To determine the single-particle ANC  $b$  we used the Woods-Saxon potential with standard geometry, the radius parameter  $r_o = 1.25 \text{ fm}$  and diffuseness  $a = 0.65 \text{ fm}$ . It gives the single-particle ANC  $b = 5.79 \text{ fm}^{-1/2}$  and the SF is  $S = C^2/b^2 = 0.81$ . Now we consider the  $^{48}\text{Ca}(n,\gamma)^{49}\text{Ca}$  data [4]. The neutron binding energy of the ground state of  $^{49}\text{Ca}$  is 5.148 MeV and capture cross section is determined by both ANC and SF. For the Woods-Saxon potential with parameters given above from the fit of the theoretical capture cross section to the experimental one we get SF=0.73 and the ANC  $C = 4.96 \text{ fm}^{-1/2}$ . Taking into account the systematic experimental uncertainties for the sub-Coulomb  $(d,p)$  and  $(n,\gamma)$  data 5% difference in the extracted ANCs and 10% difference in SFs is an excellent agreement. More accurate measurements of the sub-Coulomb  $(d,p)$  reaction, which can be done at the Cyclotron Institute, Texas A&M University, can even decrease this difference. Thus we can conclude that for  $^{49}\text{Ca}$  both  $(n,\gamma)$  and  $(d,p)$  provide very close ANC and SF, i. e.  $(d,p)$  reaction can be used to determine the SF and calculate direct radiative  $(n,\gamma)$  reaction cross sections.

This work is supported in part by the U. S. DOE-NNSA under Grant no. DE-FG52-06NA26207.

[1] A. M. Mukhamedzhanov and F. M. Nunes, Phys. Rev. C **72**, 017602 (2005).

[2] D. Y. Pang, F. M. Nunes, and A. M. Mukhamedzhanov, Phys. Rev. C **75**, 024601 (2007).

[3] J. Rapaport, A. Sperduto, and M. Salomaa, Nucl. Phys. **A197**, 337 (1972).

[4] H. Beer *et al.*, Phys. Rev. C **54**, 2014 (1996).

## Trojan horse for direct reactions

A. M. Mukhamedzhanov, C. Spitaleri,<sup>1</sup> and R. E. Tribble

<sup>1</sup>*DMFCI, Universit di Catania, Catania, Italy and INFN - Laboratori Nazionali del Sud,  
Catania, Italy*

In this work we address the Trojan Horse (TH) formalism for the direct binary processes  $x + A \rightarrow b + B$ . In the TH method the cross section for the binary process  $x + A \rightarrow b + B$  is determined from the TH reaction  $a + A \rightarrow y + b + B$ , where  $a = (yx)$ . The half-off-energy-shell (HOES) post-form amplitude of the direct binary reaction,  $x + A \rightarrow b + B$ , which is extracted from the TH reaction, is given by

$$M^{HOES} = \langle \psi_{bb}^{(-)} \varphi_b | \Delta V_{bb} | \varphi_x \varphi_A e^{i\mathbf{p}_{xA} \cdot \mathbf{r}_{xA}} \rangle \quad (1)$$

Here,  $\varphi_i$  is the bound state wave function of nucleus  $i$ ,  $\psi_{bb}^{(-)}$  is the scattering wave function of nuclei  $b$  and  $B$  in the final state,  $\Delta V_{bb} = V_{bb} - U_{bb}$ ,  $V_{bb}$  and  $U_{bb}$ , are the interaction potential of nuclei  $b$  and  $B$  and their optical potential, respectively;  $\mathbf{r}_{xA}$  and  $\mathbf{p}_{xA}$  are the radius-vector connecting nuclei  $x$  and  $A$  and their relative momentum.

The HOES amplitude contains the off-shell plane wave which describes the relative motion of the virtual  $x$  and  $A$  nuclei in the initial channel of the binary reaction rather than the distorted wave describing the initial state in the OES amplitude. Hence the HOES amplitude does not contain a Coulomb barrier factor. The on-energy-shell (OES) amplitude to be compared with the HOES one is

$$M^{OES} = \langle \psi_{bb}^{(-)} \varphi_b | \Delta V_{bb} | \varphi_x \varphi_A \chi_{xA}^{(+)} \rangle \quad (2)$$

Here,  $\chi_{xA}^{(+)}$  is the distorted wave describing the scattering of particles  $x$  and  $A$ . The only difference in the energy dependence between the HOES and OES astrophysical factors comes from the use of the HOES plane wave in the initial state in Eq. (1) and the OES distorted wave in Eq. (2). The distorted wave at low energies can be approximated by the pure Coulomb scattering wave function which contains the Gamow penetration factor, hypergeometric wave function and the OES plane wave. When calculating the astrophysical  $S$  factor the Gamow penetration factor is dropped. The energy dependence of the hypergeometric function is very weak. Hence one can expect that HOES and OES astrophysical factors should have similar energy behavior. From Fig. 1 it is clear that the results we calculated justify the TH method. The calculations have been done for two reactions,  ${}^6\text{Li}(d,\alpha){}^4\text{He}$  and  ${}^7\text{Li}(p,\alpha){}^4\text{He}$ . The corresponding TH reactions are  ${}^6\text{Li}({}^6\text{Li},\alpha\alpha){}^4\text{He}$  and  ${}^7\text{Li}(d,n\alpha){}^4\text{He}$ , respectively. The energy dependence of the HOES and OES astrophysical factors at low energies are practically identical. Since only the energy dependence is of interest, the HOES results in Fig. 1 have been normalized to the OES ones at a relative  $x$ - $A$  kinetic energy  $E_{xA} = 1$  keV for ease of comparison.

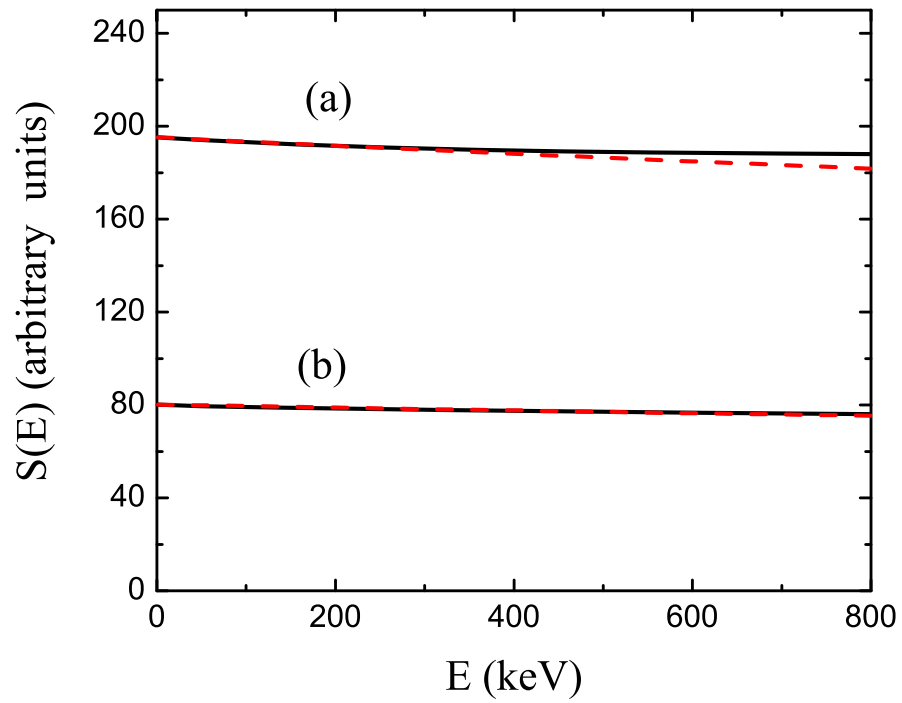


**Figure 1.** Energy dependence ( $E \equiv E_{xA}$ ) of the HOES (red dashed line) and OES (black solid line) astrophysical factor for (a)  ${}^6\text{Li}(d,\alpha){}^4\text{He}$  and (b)  ${}^7\text{Li}(p,\alpha){}^4\text{He}$  reactions.

## Superaligned Fermi beta decay: the isospin-symmetry-breaking correction

I. S. Towner and J. C. Hardy

For weak vector interactions in hadron states, the conserved vector current (CVC) hypothesis protects the decay amplitudes from strong-interaction corrections. However, there is a caveat. The CVC hypothesis requires the hadron state to be an exact eigenstate of  $SU(2)$  symmetry (isospin) in the case of nucleons and pions, and an exact eigenstate of  $SU(3)$  in the case of kaons.

In nuclei,  $SU(2)$  symmetry is always broken, albeit weakly, by Coulomb interactions between protons. There may be other charge-dependent effects as well. These influences shift the value of the hadron matrix element from its exact symmetry limit to a new value and this shift has to be evaluated before weak-interaction physics can be probed with hadrons. In the case of superallowed nuclear  $\beta$  decay, the hadron matrix element,  $M_F$ , is written

$$|M_F|^2 = |M_0|^2 (1 - \delta_C), \quad (1)$$

where  $M_0$  is the exact-symmetry value, and  $\delta_C$  is the correction we seek to evaluate. In our approach to these calculations [1] we have identified two contributions,

$$\delta_C = \delta_{C1} + \delta_{C2}, \quad (2)$$

where  $\delta_{C1}$  is the correction caused by adding charge-dependent terms to the shell-model Hamiltonian, and  $\delta_{C2}$  accounts for the difference in radial forms between the proton in the parent  $\beta$ -decaying nucleus and the neutron in the daughter nucleus. These radial forms are integrated together and, if there were no difference between them, the integral would just be the normalization integral of value one. Any departure of the square of this overlap integral from one represents the correction,  $\delta_{C2}$ . There is a strong constraint on the calculation: the asymptotic forms of the radial functions are matched to the separation energies,  $S_p$  and  $S_n$ , where  $S_p$  is the proton separation energy in the decaying nucleus and  $S_n$  the neutron separation energy in the daughter nucleus.

In the past year, we have revisited the calculation of the  $\delta_{C2}$  correction. In the shell model, the  $A$ -particle wave functions can be expanded into products of  $(A-1)$ -particle wave functions  $|\pi\rangle$  and single-particle functions  $|j\rangle$ . In terms of this expansion, the Fermi matrix element is given by:

$$M_F = \sum_{j,\pi} S_j^\pi \Omega_j^\pi, \quad (3)$$

$$\Omega_j^\pi = \int_0^\infty R_{\pi j}^p(r) R_{\pi j}^n(r) r^2 dr.$$

The expansion coefficients  $S_j^\pi$  are generalized fractional parentage coefficients and represent the spectroscopic overlap of the  $A$ - and  $(A-1)$ -particle wave functions; and  $R_{\pi j}^p(r)$  and  $R_{\pi j}^n(r)$  are proton and neutron radial functions, whose asymptotic forms are matched to the corresponding separation energies between the  $A$ - and  $(A-1)$ -particle states,  $\pi$ . The correction  $\delta_{C2}$  is then

$$\delta_{C2} \approx \frac{2}{M_0} \sum_{j,\pi} S_j^\pi (1 - \Omega_j^\pi), \quad (4)$$

which shows that a large contribution to  $\delta_{C2}$  requires both a large spectroscopic amplitude and a significant departure of the radial integral from unity.

We have focused our attention on the four superallowed cases in the  $fp$  shell: the decays of  $^{42}\text{Sc}$ ,  $^{46}\text{V}$ ,  $^{50}\text{Mn}$  and  $^{54}\text{Co}$ . The CVC hypothesis has the consequence that the corrected  $ft$  values for superallowed  $\beta$  decay should all be the same for all nuclei of the same isospin, after radiative and isospin-symmetry-breaking corrections have been applied: *i.e.*

$$\mathfrak{ft} = ft(1+\delta_R)(1-\delta_C) = \text{constant} \quad . \quad (5)$$

In the current data set, the  $\mathfrak{ft}$  values for both  $^{42}\text{Sc}$  and  $^{46}\text{V}$  are high and could be indicating that their calculated  $\delta_{C2}$  values should be larger. Up to now, we have restricted the summation over orbitals  $j$  in Eq. (4) to the shell-model space of  $d_{3/2}$ ,  $f_{7/2}$ ,  $p_{3/2}$  orbitals for  $^{42}\text{Sc}$ , and  $f_{7/2}$ ,  $p_{3/2}$  orbitals for  $^{46}\text{V}$ ,  $^{50}\text{Mn}$  and  $^{54}\text{Co}$ . This past year, we were able to include one additional  $sd$ -shell core orbital into the calculation. For  $^{42}\text{Sc}$ , this increased  $\delta_{C2}$  from 0.44% to 0.52% and decreased its  $\mathfrak{ft}$  from 3076.5 to 3074.0s. Similarly in  $^{46}\text{V}$ ,  $\delta_{C2}$  increased from 0.34% to 0.49% such that its  $\mathfrak{ft}$  value reduced from 3079.4 to 3074.8s. Both these are highly desirable results as the  $\mathfrak{ft}$  values are then much closer to the average,  $\mathfrak{ft} = 3073.8s$ . However, similar increments of 0.08% and 0.06% in  $\delta_{C2}$  for the  $^{50}\text{Mn}$  and  $^{54}\text{Co}$  transitions was detrimental, reducing the  $\mathfrak{ft}$  value of  $^{50}\text{Mn}$  from 3071.6 to 3069.1s, and for  $^{54}\text{Co}$  from 3071.9 to 3070.0s.

We conclude that enlarging the model space of the shell-model calculations for  $\delta_{C2}$  to include the next available core orbital will give an increment to  $\delta_{C2}$  that on the whole improves the CVC test. However, this raises the question: why just include the next available core orbital? Why not include all core orbitals? We have evaluated the effect of doing so in the extreme  $jj$  model and the result for the heavier nuclei, such as  $^{62}\text{Ga}$  and  $^{74}\text{Rb}$ , is a correction to the  $\delta_{C2}$  value that is far too large. In this extreme limit, the CVC test would be severely compromised. More work needs to be done to evaluate the effect of core orbitals in a more realistic model.

[1] I. S. Towner and J. C. Hardy, Phys. Rev. C **66**, 035501 (2002).

## Superallowed Fermi beta decay: the radiative correction

I. S. Towner and J. C. Hardy

Precision studies of superallowed beta decay are used to determine the Cabibbo-Kobayashi-Maskawa (CKM) matrix element  $V_{ud}$  and to study the matrix's unitarity. To reach this goal, however, the experimental  $\beta$ -decay rates need to be corrected for radiative and isospin-symmetry-breaking effects. The radiative correction, which in total is around 4%, is conveniently divided into terms that are nucleus dependent, the 'outer' radiative correction  $\delta_R$ , and terms that are nucleus independent, the 'inner' radiative correction  $\Delta_R$ . The outer correction is fairly unambiguous and is given by a QED calculation. The inner correction is more troublesome. Since nuclear  $\beta$  decay involves hadronic states, uncertainties arise from the presence of strong interactions. To minimize these effects, attention is focused on superallowed transitions between  $0^+$  states where the conserved vector current (CVC) hypothesis protects the decay amplitudes at the tree level from strong-interaction corrections. However, radiative corrections go beyond the tree level and introduce loop corrections that can involve the weak axial-vector interaction that is not protected by CVC. These effects require a model-dependent calculation.

At the time of our 2005 survey [1], the inner radiative correction was taken from [2] to be

$$\Delta_R = (2.40 \pm 0.08)\%, \quad (1)$$

where the error was an estimate of the uncertainty of the axial-vector contribution to the loop diagram. This uncertainty in fact dominated the accuracy with which  $V_{ud}$  could be determined from nuclear  $\beta$  decays. In our survey we quoted:

$$|V_{ud}|^2 = 0.9482 \pm 0.0008. \quad (2)$$

The total quoted uncertainty, which is 0.00083 if the next significant figure is included, is dominated by the uncertainty arising from  $\Delta_R$ , *viz.* 0.00074.

In 2006, Marciano and Sirlin [3] reevaluated the loop correction paying particular attention to the causes of the uncertainty. They divided the loop integration into three energy regimes. At low energy the interactions are with structureless nucleons (but with nucleus-modified coupling constants) and the loop diagram reduces to the easily evaluated Born graphs. At the other extreme of high energies the interactions are with quarks yielding a leading-log term and QCD corrections, which are related to a Bjorken sum rule and hence are under control. At intermediate energies Marciano and Sirlin introduced an interpolation function inspired by vector meson dominance models and matched it to the low-energy and high-energy loop contributions. By assuming a 100% error in the interpolator and a 10% error in the low-energy contribution, Marciano and Sirlin [3] reduced the uncertainty on  $\Delta_R$  by a factor of two, from 0.08% (see Eqn. 1) to 0.038%.

We have now adopted these new calculations into our analysis of the superallowed  $\beta$  transitions but in doing so we have moved one small term from the inner to the outer correction. This reorganization is prompted by the estimate of Czarnecki, Marciano and Sirlin [4] of the order  $\alpha^2$  correction. Their estimate is based on a renormalization-group analysis of the leading log extrapolation: in the high-energy regime, this extrapolation remains an inner correction; but at low energies, the leading log depends on the maximum electron energy and is thus nucleus dependent. Consequently we place its extrapolation in the outer correction. This leads to the result we now use for the inner radiative correction:

$$\Delta_R = (2.361 \pm 0.038)\%. \quad (3)$$

At the same time, we must of course update our outer radiative corrections to incorporate the transferred contributions. Our division of the total radiative correction,  $RC$ , now is

$$\begin{aligned} RC &= \delta_R + \Delta_R \\ \text{where } \delta_R &= \delta_{R'} + \delta_{\alpha^2} + \delta_{NS}. \end{aligned} \quad (4)$$

Here  $\delta_{R'}$  has our usual definition [5] and includes the corrections to order  $\alpha$ ,  $Z\alpha^2$  and  $Z^2\alpha^3$ . The second component of  $\delta_R$  incorporates the new order- $\alpha^2$  corrections, and the third,  $\delta_{NS}$ , is the nuclear-structure dependent term, which comes from the low-energy Born graphs and is slightly changed by the new reorganized arrangement.

In Table I we give some sample results, comparing 2005 values for the radiative corrections with today's values. The new values for the total radiative corrections,  $RC$ , differ from the 2005 values by 0.01 to 0.02%. This shift is very small and has no impact on the central value of  $V_{ud}$ . The reduction in the error, on the other hand, gives a significant improvement in the accuracy of  $V_{ud}$  and in the sharpness of the CKM unitarity test.

**Table I.** Contributions to the radiative correction in percent units.

Parent	2005					2006				
	$\delta_{R'}$	$\delta_{\alpha^2}$	$\delta_{NS}$	$\Delta_R$	RC	$\delta_{R'}$	$\delta_{\alpha^2}$	$\delta_{NS}$	$\Delta_R$	RC
$^{10}\text{C}$	1.652	0.000	-0.360	2.400	3.692	1.652	0.027	-0.357	2.361	3.683
$^{26}\text{Al}^m$	1.458	0.000	0.009	2.400	3.867	1.458	0.020	0.012	2.361	3.851
$^{54}\text{Co}$	1.428	0.000	-0.029	2.400	3.799	1.428	0.015	-0.025	2.361	3.779
$^{74}\text{Rb}$	1.485	0.000	-0.065	2.400	3.820	1.485	0.013	-0.061	2.361	3.798

- [1] J.C. Hardy and I.S. Towner, Phys. Rev. C **71**, 055501 (2005).
- [2] W.J. Marciano and A. Sirlin. Phys. Rev. Lett. **56**, 22 (1986).
- [3] W.J. Marciano and A. Sirlin. Phys. Rev. Lett. **96**, 032002 (2006).
- [4] A. Czarnecki, W.J. Marciano and A. Sirlin. Phys. Rev. D **70**, 093006 (2004).
- [5] I.S. Towner and J.C. Hardy, Phys. Rev. C **66**, 035501 (2002).

## Renormalized self consistent continuum random phase approximation

Vuong Kim Au, Nguyen Dinh Dang,<sup>1</sup> and Shalom Shlomo

<sup>1</sup>*RIKEN, Wako-shi, Japan*

The random-phase approximation (RPA) has been widely used in the theoretical study of nuclei within the valley of  $\beta$ -stability. The success of the RPA is mainly based on the use of the quasiboson approximation (QBA), which considers fermion pairs as boson operators, just neglecting the Pauli principle between them. As a result, a set of linear equations, called the RPA equations, was derived, which reveals the physics of collective excitations generated by the RPA boson like modes. The simplicity of the RPA equations allows a feasible treatment of a number of many-body problems, which would be computationally intractable otherwise. However, this approach suffers a drawback: It breaks down at a certain critical value of the interaction's parameter, where the RPA yields imaginary solutions. The reason of this well-known RPA instability is the violation of Pauli principle within the QBA.

In  $\beta$ -stable medium and heavy nuclei, the QBA is a good approximation, and the RPA is a very powerful tool for the description of several important quantities such as the ground state and excited-state energies, electro-magnetic transition probabilities and their distribution, transition densities, etc. However, with the decrease of particle number, the concept of collective excitations, which are described by the RPA modes, becomes less and less firm. The ground-state correlations (GSC) that are beyond the RPA become stronger in light systems. This feature makes the validity of the QBA, and therefore of the RPA itself, questionable in systems with small particle numbers. Several approaches were developed to take into account the GSC beyond RPA in a simple way in order to restore the Pauli principle among the fermion pairs, from which the RPA operators are constructed. The popular one, known as the renormalized RPA (RRPA) [1,2], includes the expectation values over the ground state of the diagonal elements of the commutator between two fermion-pair operators, which are neglected in the QBA. In this way the Pauli principle is approximately taken care of. The inclusion of GSC beyond RPA within the RRPA eventually renormalizes the interaction in such a way that the collapse of RPA is avoided, and the RRPA has solutions at any values of the interaction's parameter.

By approaching the drip line the Fermi level is getting closer to zero. The continuum starts to be involved into the phase space around the Fermi surface, where the particle correlations are strongest. This means that the coupling between bound states and the continuum becomes more and more important. The discretized RPA approaches, which are constructed using discrete single-particle states, should be replaced with the continuum RPA (CRPA), where the effect of coupling to continuum is properly taken into account.

Therefore, for a proper study of unstable light nuclei one should take into account simultaneously both effects of the GSC beyond RPA and the coupling to the continuum. This is the aim of our research work. We will apply the method of renormalizing RPA proposed by Catara, Dang, and Sambataro [2] to renormalize the selfconsistent CRPA (SCRPA) developed by Shlomo and Bertsch [3]. As a result of such renormalized SCRPA (RSCRPA), we obtain a set of equations for the single-particle transition densities, which should be solved self-consistently with the equations for the Green functions

within the RSCRPA. The developed approach will be applied to calculate the properties of electromagnetic excitations such as pygmy and giant resonances in stable and unstable nuclei.

- [1] K. Hara, Prog. Theor. Phys. **32**, 88 (1964); K. Ikeda, T. Udagawa, and H. Yamamura, *ibid.* **33**, 22 (1965); D. J. Rowe, Phys. Rev. **175**, 1283 (1968).
- [2] F. Catara, N. D. Dang, and M. Sambataro, Nucl. Phys. **A579**, 1 (1994).
- [3] S. Shlomo and G. Bertsch, Nucl. Phys. **A243**, 507 (1975).

## Constraining the symmetry energy from nuclear giant resonances

Tapas Sil,<sup>1</sup> and Shalom Shlomo

<sup>1</sup>*Department of Physics, VIT University, Vellore 632 014, TN, India*

The nuclear symmetry energy appearing in the equation of state (EoS) of nuclear matter is essential in understanding many aspects of nuclear physics as well as astrophysical phenomena. The structure of neutron star, supernovae explosion, heavy-ion collision dynamics etc. depend on the structure of EoS, i.e., in turn on the bulk properties of nuclear matter like symmetry energy ( $J$ ) and incompressibility modulus ( $K$ ). Empirical liquid-drop mass formula predicts the value of  $J$  around normal nuclear density to be of the order of 30 MeV. Nuclear giant resonances provide much important information about the nuclear structure and the bulk properties of the nuclear matter. The value of another important bulk property of nuclear matter, i.e., the value of  $K$  for symmetric matter is constrained to be  $230 \pm 20$  MeV from the nuclear isoscalar giant monopole resonance (ISGMR) data. The uncertainty of 20 MeV is mainly due to the uncertainty in the value of  $J$ .

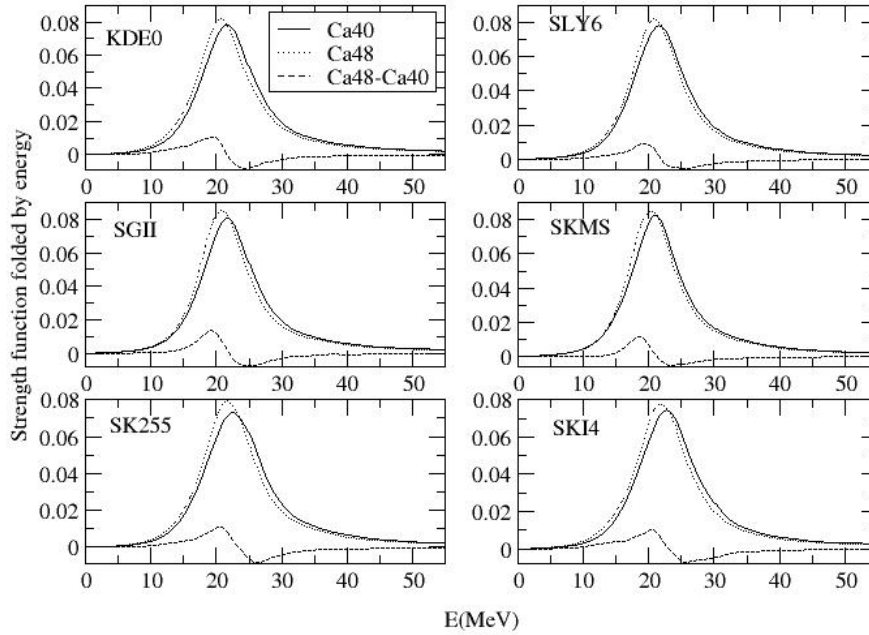


**Figure 1.** ISGMR strength distributions for  $^{40}\text{Ca}$  and  $^{48}\text{Ca}$ .

It has been shown in Ref. [1] that the distribution of the strength of ISGMR in  $^{208}\text{Pb}$  is sensitive to the density dependence of the symmetry energy. This motivates us to study the force dependence of the ISGMR strength distribution for calcium isotopes. Experimental data for ISGMR for the symmetric nucleus  $^{40}\text{Ca}$  is already available and it is possible now to do experiment with the asymmetric nucleus  $^{48}\text{Ca}$ . In the figure, we plot the ISGMR strength functions for  $^{40}\text{Ca}$  and  $^{48}\text{Ca}$ , obtained from highly accurate and fully self-consistent Hartree-Fock based RPA [2] calculations using various forces having different values of J and K. We also plot the difference of the strength functions of  $^{40}\text{Ca}$  and  $^{48}\text{Ca}$ . By comparing these theoretical values with experimental data we hope to constrain the value of the symmetry energy.

[1] J. Piekarewicz, Phys. Rev. C **69**, 041301 (2004).

[2] T. Sil, S. Shlomo, B. K. Agrawal and P.-G. Reinhard, Phys. Rev. C **73**, 034316 (2006).

## Effects of long range correlations on nuclear charge radii in fully self-consistent Hartree-Fock RPA method

Tapas Sil,<sup>1</sup> and Shalom Shlomo

<sup>1</sup>*Department of Physics, VIT University, Vellore 632 014, TN, India*

Mean field model is very successful in describing various nuclear ground state properties. But there are many observed phenomena, such as the parabolic shape of isotopic shifts in the calcium chain ( $^{40}\text{Ca}$  to  $^{48}\text{Ca}$ ), for which one needs to consider correlation effects beyond the mean field. Systematic study of nuclear charge radii sheds light on nuclear structure and forces between nucleons. Highly accurate experimental data of nuclear charge radii are presently available which demand very accurate theoretical calculations. Random phase approximation (RPA) is one of the commonly used ways to take into account the ground state long range correlations (LRC) which are interpreted as zero point oscillations of collective vibrations.

We have employed highly accurate and fully self consistent Hartree-Fock (HF) based RPA calculations [1] to evaluate the corrections to the charge root mean square (rms) radii due to the LRC for several spherical nuclei ( $^{16}\text{O}$ ,  $^{40}\text{Ca}$ ,  $^{48}\text{Ca}$ ,  $^{56}\text{Ni}$ ,  $^{90}\text{Zr}$  and  $^{208}\text{Pb}$ ). We plot in the left panel of the figure,

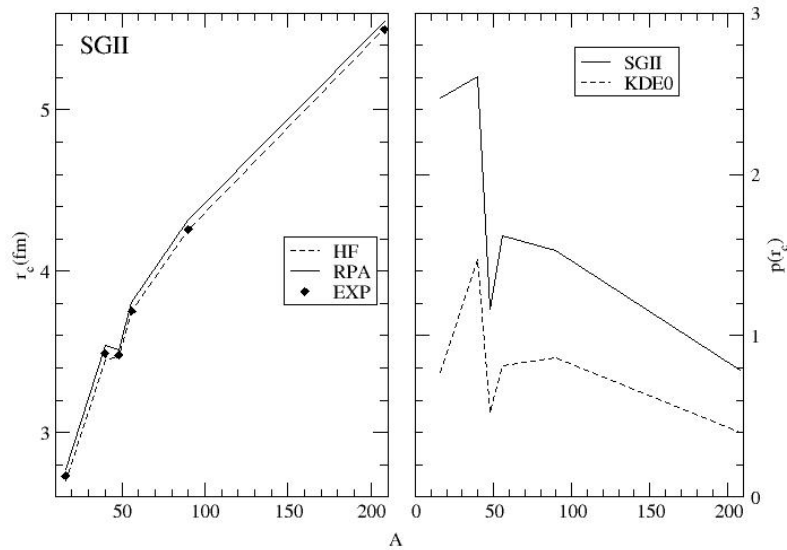


**Figure 1.** Long range correlation effects in charge radii

the charge rms radii calculated from HF ground state and compare them with those considering the LRC corrections. HF calculations in, over all, better agreement with the experimental values whereas those obtained from HF-RPA calculations overestimate the experimental data. This is because of that in the

fitting process for the interaction parameter sets within HF, these experimental values are used. But the qualitative trend of experimental data ( $r_c$  of  $^{48}\text{Ca}$  is slightly smaller than that of  $^{40}\text{Ca}$ ) is better reproduced by the HF-RPA calculations. The percentage of the change of charge rms radii  $\{p(r_c) = 100[r_c(\text{RPA}) - r_c(\text{HF})] / r_c(\text{HF})\}$  for the same nuclei are plotted in the right panel for the SGII and KDE0 forces. Qualitative trends are similar for both of the forces but the quantitative values of the corrections are somewhat different for different force [2].

[1] T. Sil, S. Shlomo, B. K. Agrawal and P.-G. Reinhard, Phys. Rev. C **73**, 034316 (2006).

[2] T. Sil, and S. Shlomo, (submitted).

## **SECTION IV**

# **ATOMIC, MOLECULAR AND MATERIALS SCIENCE**

## A semiempirical scaling law for target K x-ray production in heavy ion collisions

R. L. Watson, Y. Peng, V. Horvat, and A. N. Perumal

In view of the fact that reliable theoretical methods for predicting cross sections for K x ray production in heavy ion-atom collisions have yet to be developed, and because these cross sections are of practical use in analytical applications and for beam monitoring in experiments with heavy ions, it is desirable to examine scaling relations that might provide a means for their estimation. First-order descriptions of inner-shell ionization based on the PWBA as well as the classical binary encounter approximation (BEA) predict that target K-shell ionization cross sections are proportional to the square of the projectile effective charge ( $Z_{\text{eff}}^2$ ) divided by the square of the target electron binding energy ( $B_K^2$ ) times a function that defines the V dependence of the collision process (where V is the projectile speed divided by the K-electron average speed). Therefore, a plot of the K-shell ionization cross section multiplied by  $B_K^2/Z_{\text{eff}}^2$  versus V should define a universal function that depends only on V. This type of scaling has been found to work reasonably well for proton and alpha particle projectiles with  $Z_{\text{eff}}$  taken to equal the projectile atomic number ( $Z_1$ ) [1].

In order to develop a scaling method applicable to heavy ions, cross sections were measured for K x-ray production in targets of Al, Ti, Cu, Zr, Ag, Sm, and Ta by Ar, Kr, and Xe ions ranging in energy from 2.5 to 25 MeV/amu. In addition, the degree of simultaneous L-shell ionization and the enhancement of the  $K\alpha$  diagram lines due to secondary ionization processes were assessed by performing high-resolution spectral measurements on Al, Ti, V, Co, and Cu targets. This information was used to correct for the  $K\alpha$  x-ray yield produced by secondary electron bombardment and photoionization, and to calculate the fluorescence yields needed to convert the  $K\alpha$  x-ray production cross sections into K vacancy production cross sections. The results of these measurements are described in Ref. [2].

In the case of heavy ion projectiles, the goal of providing a convenient scaling method for estimating K x-ray production cross sections is obscured by the fluorescence yield factor (which depends on the degree of multiple ionization) since its calculation is difficult and relies on a number of untested approximations and assumptions. Therefore, in the present treatment, it was decided to replace the calculated fluorescence yield  $\omega_{K\alpha}$  with the single vacancy fluorescence yield  $\omega_0$  and, in effect, consider it to be part of the overall scaling factor. It was found that the  $B_K^2/\omega_0$  scaling factor is quite effective in accounting for the target dependence of the cross sections.

In seeking to account for the projectile dependence of the  $K\alpha$  x-ray production cross sections, the following procedure was found to provide values for  $Z_{\text{eff}}$  that gave reasonably good projectile scaling. Because the Al data points sampled the highest V region, where the V dependence is nearly constant, the four cross sections measured at 10, 15, 20, and 25 MeV/amu were chosen to establish the average  $Z_{\text{eff}}$  normalization factors, which were defined as

$$Z_{\text{eff}} = \{\sigma_{K\alpha}(Z_1)/[\omega_0\sigma_K(1)]\}^{1/2}, \quad (1)$$

where  $\sigma_{K\alpha}(Z_1)$  is the measured Al  $K\alpha$  x-ray production cross section for a projectile with atomic number  $Z_1$  and  $\sigma_K(1)$  is the Al K-shell ionization cross section predicted by the ECPSR theory for protons. The fully scaled cross sections are shown in Fig. 1 as a function of  $V$ . It is found that multiplying the

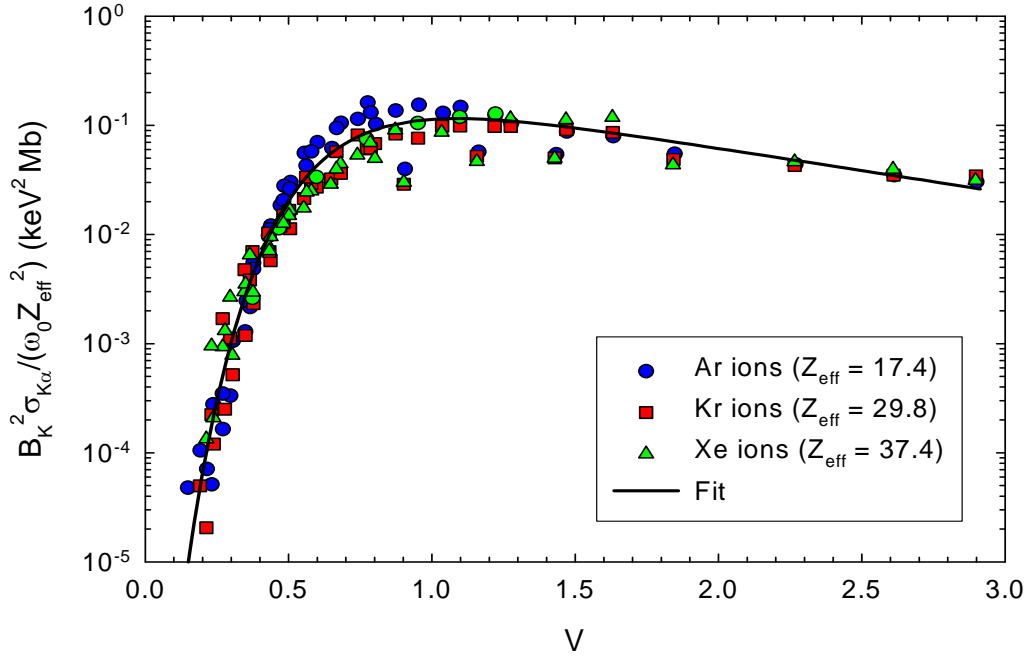


**Figure 1.** The fully scaled  $K\alpha$  x-ray production cross sections as a function of speed ratio. A semiempirical “universal” curve has been fit to the data points.

measured K x-ray production cross sections by  $B_K^2/(\omega_0 Z_{\text{eff}}^2)$  has the remarkable effect of grouping most of the data points for all three projectiles along a “universal” curve. A fit to the data points (which excluded the Al points for the measurements at 2.5, 4, and 6 MeV/amu) using an extreme value four parameter tailed function [3] is shown by the solid curve in Fig. 1. The equation of this curve is

$$F(V) = a_0 \exp(B) \quad (2)$$

where  $B = (1/a_2 a_3) \{-V + a_1 + a_2 - a_2 a_3 \exp[-(V + a_2 \ln a_3 - a_1)/a_2]\}$

with  $a_0 = 0.113262$ ,  $a_1 = 1.069489$ ,  $a_2 = 0.233611$ , and  $a_3 = 4.485867$ . The average absolute deviation of the  $K\alpha$  x-ray production cross sections calculated using Eq. (2) from the experimental cross sections is  $(26 \pm 9)\%$ .

A graph of  $Z_{\text{eff}}$  versus  $Z_1$  is shown in Fig. 2. The error bars on the data points for Ar, Kr, and Xe represent the standard deviations from the average values of  $Z_{\text{eff}}$  determined using the four Al cross sections. The other data points in Fig. 2 were calculated using Al cross sections from a previous study [4]

at 10 MeV/amu that were re-evaluated to include the double K-vacancy production contributions. The equation of the fitted solid curve in this figure is

$$Z_{\text{eff}} = 46.29[1 - \exp(-0.0256Z_1)]. \quad (3)$$

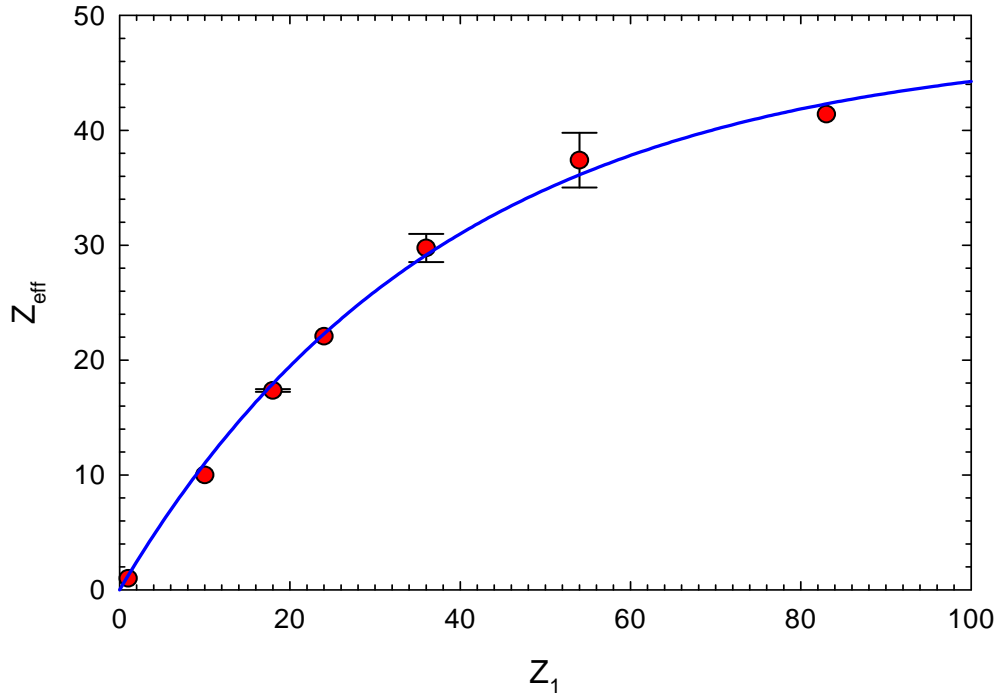


**Figure 2.** A graph showing the dependence of the projectile effective charge on the projectile atomic number. The solid curve has been fit to the data points.

- [1] P. Richard, *Atomic Inner-shell processes* (edited by B. Crasemann), Academic Press, New York, Vol. I, p. 73 (1975).
- [2] R. L. Watson, Y. Peng, V. Horvat, and A. N. Perumal, *Phys. Rev. A* **74**, 062709 (2006).
- [3] R. L. Watson, V. Horvat, J. M. Blackadar, and K. E. Zaharakis, *Phys. Rev. A* **62**, 052709 (2000).
- [4] *Peakfit peak separation and analysis software*, version 4.0, AISN Software Inc., Jandel Scientific, 2591 Kerner Blvd., San Rafael, CA 94901 (1995).

## Systematics of $L$ x-ray satellite spectra

V. Horvat, R. L. Watson, Y. Peng, J. M. Blackadar

Systematic analysis of the spectra of  $K\alpha$  x rays emitted from thick solid targets under bombardment by fast heavy ions [1] has established that the apparent average fraction of  $L$  vacancies at the time of  $K$  x-ray emission can be described by a semiempirical function of the “universal variable” [2]. Presented here is an extension of this analysis to the spectra of  $L$  x rays. The targets used in the study contained elements with atomic numbers ranging from 49 (In) to 67 (Ho).

Texas A&M’s K-500 cyclotron was used to produce the beams of Ne, Ar, Kr, and Xe ions, at 6, 10, and 15 MeV/amu. Target  $L$  x rays were measured in high resolution using a Johansson-type curved crystal spectrometer employing a LiF crystal. The spectra were measured in the first order of reflection.

The dependence of the spectral features on the target atomic number is illustrated in Figure 1. To facilitate comparison of the spectra, the horizontal axis has been scaled such that the  $L\alpha_1$  and  $L\beta_2$  energies correspond to the values of 1 and 2, respectively.

Centroids of the peaks due to  $L\alpha_1$  and  $L\beta_2$  diagram transitions are indicated by the vertical dashed lines. The prominent narrow peak between the two corresponds to the  $L\beta_1$  diagram transitions. Peaks due to the other diagram transitions, such as  $L\beta_3$  and  $L\beta_4$ , are hardly noticeable. The diagram transitions are a consequence of  $L$ -shell ionization by secondary processes [1].

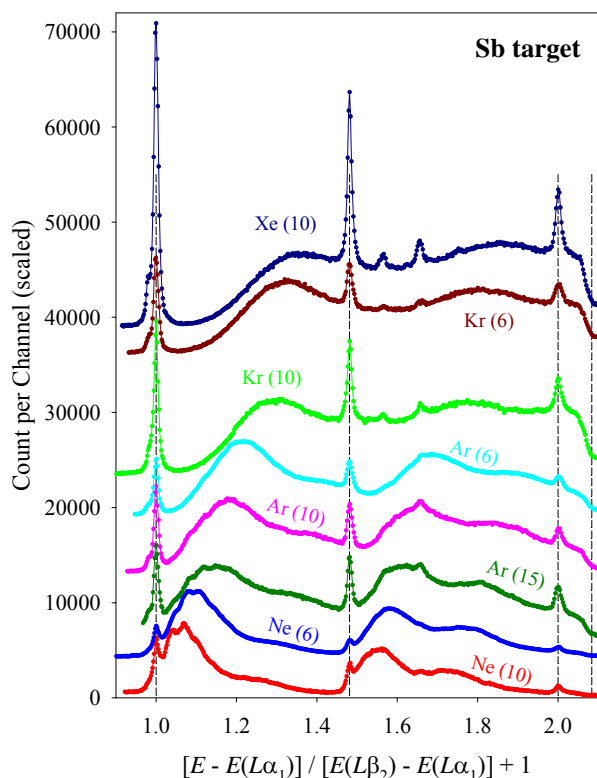


**Figure 2.** Spectra of  $L$  x rays emitted from thick solid target of Sb under bombardment by fast heavy ions. The projectile species is indicated along with its energy in MeV/amu enclosed in parenthesis. The vertical dashed lines indicate, respectively, the positions of the  $L\alpha_1$ ,  $L\beta_1$ , and  $L\beta_2$  diagram transitions as well as the  $L_3$  absorption edge (at the high-energy end).

The broad distributions on the high-energy sides of the diagram peaks, known as satellite peaks, are due to multiple  $M$ -shell ionization caused by the projectiles. The centroid energies of these distributions increase with the degree of  $M$ -shell ionization, while their widths depend mostly on the energy spread of the underlying unresolved peaks.

The degree of  $M$ -shell ionization at the time of  $L$  x-ray emission can be described in terms of the apparent average fraction of  $M$  vacancies ( $p_M$ ). From Figure 1 it can be concluded that this parameter increases as the target atomic number decreases. Figure 2, on the other hand, shows the

dependence of the spectral features on the projectile atomic number. It is apparent that  $p_M$  increases with the projectile atomic number, but decreases as the projectile energy increases. The value of  $p_M$  was determined from the measured spectra in a least squares curve-fitting procedure similar to that described in ref.[3].

The dependence of the measured  $p_M$  values on the universal variable [2] is given in Figure 3. The solid line in Figure 3 is a logistic curve that has been fit to the data points. It is given by

$$p_M^x = a/[1 + (b/X_n)^c], \quad (1)$$

where  $a = 0.530 \pm 0.012$ ,  $b = 1.507 \pm 0.044$ , and  $c = 2.15 \pm 0.12$ . The standard deviation of the residuals was found to be 0.013. Chemical effects are believed to be the main cause for the deviations of the data points from the fitted curve. This assertion was supported by the results of measurements involving the same target element in different chemical states. Specifically, Sn targets were prepared in the form of a thick metallic foil, SnO<sub>2</sub>, and SnCl<sub>2</sub>. It was found that the variations in the values of  $p_M$  determined from the spectra of Sn *L* x rays emitted from these targets under bombardment by 6 MeV/amu Kr projectiles were comparable to the residuals shown in the insert of Figure 3.

The curve given by eq.(1) lies slightly above the one established previously [1] for the apparent average fraction of *L* vacancies at the time of *K* x-ray emission ( $p_L$ ).

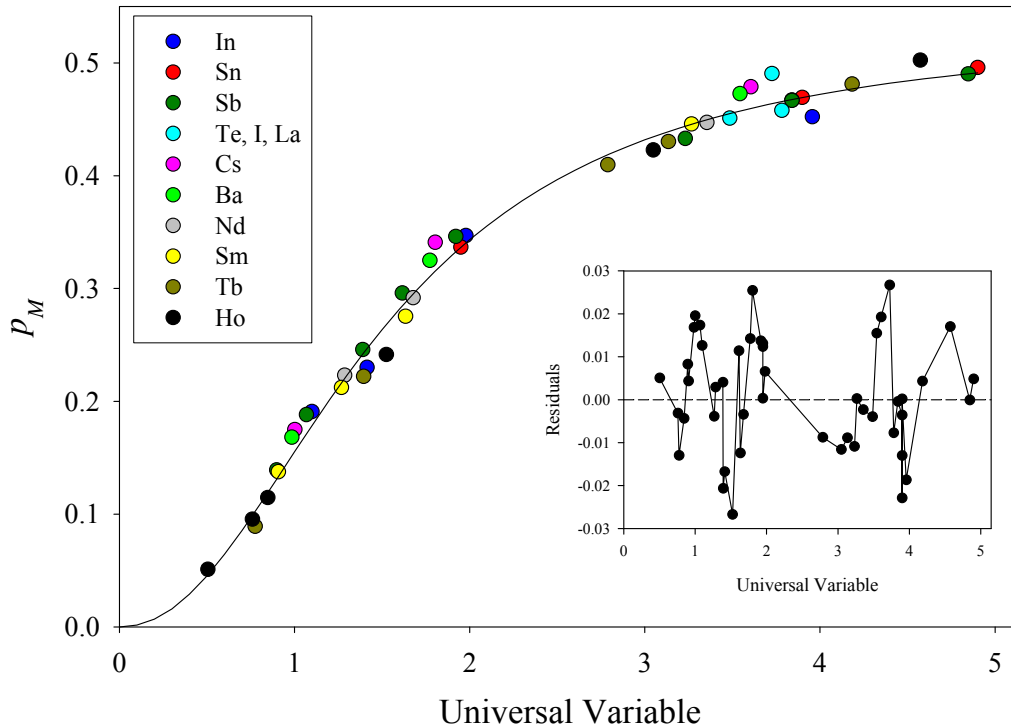


**Figure 3.** Apparent average fraction of  $M$ -shell vacancies at the time of L x-ray emission ( $p_M$ ) as a function of the universal variable [2] for various targets employed in the measurements. The solid curve represents the best fit of a logistic curve to the data points. The insert shows the residuals, i.e. the deviations of the data points from the fitted curve.

- [1] V. Horvat, R. L. Watson, J. M. Blackadar, A. N. Perumal, and Yong Peng, Phys. Rev. A **74**, 022718 (2006).
- [2] B. Sulik, I. Kadar, S. Ricz, D. Varga, J. Vegh, G. Hock, and D. Berenyi, Nucl. Instrum. Methods Phys. Res. **B28**, 509 (1987).
- [3] V. Horvat, R. L. Watson, J. M. Blackadar, A. N. Perumal, and Yong Peng, Phys. Rev. A **71**, 062709 (2005).

## Single and multiple $L$ -shell ionization by fast heavy ions

V. Horvat, R. L. Watson, Y. Peng, J. M. Blackadar

Spectra of  $L$  x rays emitted from a variety of solid targets (atomic number  $Z_2 = 49-67$ ) under bombardment by fast heavy ions (atomic number  $Z_1 = 10-54$ ) at 6-15 MeV/amu were measured in high resolution using a curved crystal spectrometer equipped with a LiF crystal. The spectra were measured in the first order of reflection and then analyzed in order to examine the systematics of  $L$  x-ray satellite structure [1]. In this report the focus is on multiple  $L$ -shell ionization.

The measured spectra were described in terms of a background function (a straight line) and peaks having Voigt profiles. The method of analysis was similar to the one used previously for spectra of Ho  $L$  x rays measured in the second order of reflection [2]. The procedure was somewhat simplified due to the fact that the distributions of  $L$  x-ray satellite peaks for a given transition type showed no evidence of underlying structure in all but a few of the measured spectra. On the other hand, the fitting function was amended in order to take into account the effects of the absorption edges.

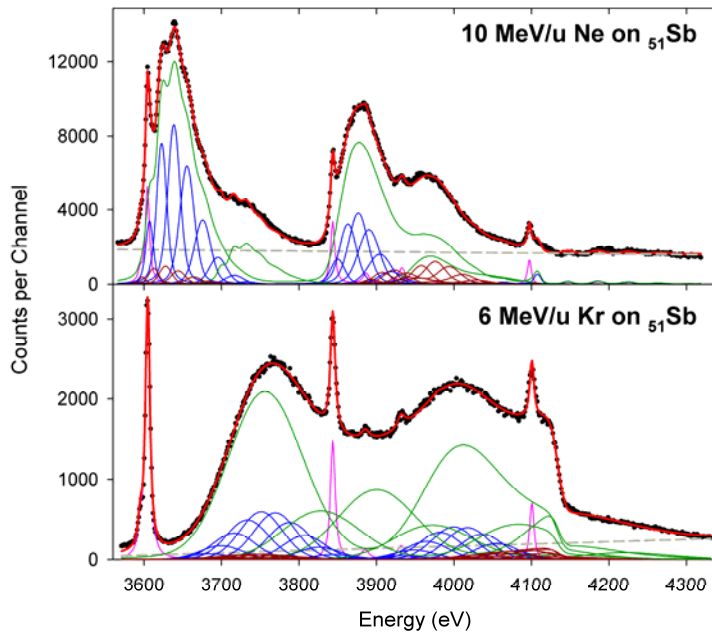


**Figure 1.** Solid circles: Measured spectra of Sb  $L$  x rays obtained under bombardment of a thick solid Sb target by 10 MeV/amu Ne (top) and 6 MeV/amu Kr ions (bottom). Lines: Overall fitting function (red) and its components (blue, brown, green, and gray).

Two examples of the fitted spectra (those obtained with 10 MeV/amu Ne on Sb and 6 MeV/amu Kr on Sb) are shown in Figure 1. Measured numbers of counts are shown as solid black circles, while the red line represents the overall fit. The background is shown as a dashed gray line, while the pink lines outline the combined contributions from the diagram x rays.  $L\alpha_1$ ,  $L\beta_1$ ,  $L\beta_6$ , and  $L\beta_2$  x-ray satellites are shown in blue,  $L\alpha_2$ ,  $L\beta_{15}$ ,  $L\eta$ ,  $L\beta_3$  and  $L\beta_4$  x-ray satellites are shown in and brown, while the green lines represent the combined contributions from all the  $L$  x-ray transitions involving  $n$   $L$  vacancies in the initial state

(i.e., the  $L^n$  components, where  $n = 1, 2, 3, \dots$ ).

The spectrum of Sb  $L$  x rays induced by 10 MeV/amu Ne projectiles shows  $L^n$  components for  $n = 1$  and 2, but there is no evidence of contributions from components having  $n > 2$ . In contrast, the

spectrum obtained with 6 MeV/amu Kr projectiles clearly exhibits  $L^n$  components with  $n$  ranging from 1 to 4.

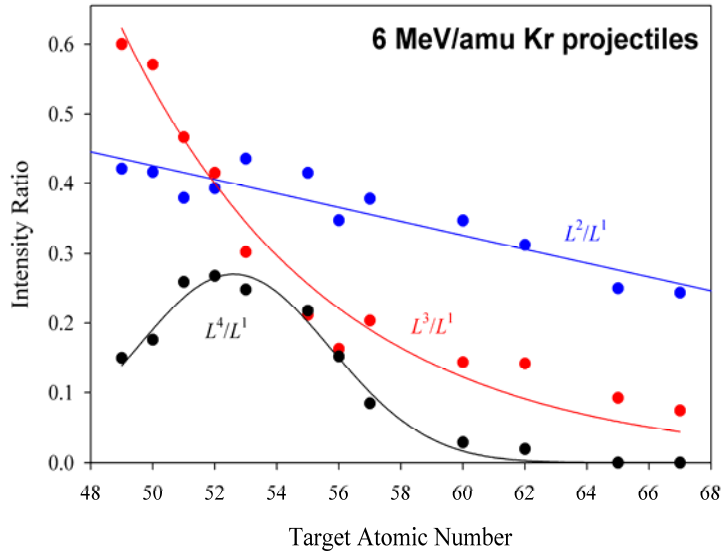


**Figure 2.** Relative intensities of  $L^n$  x-ray components as a function of target atomic number for 6 MeV/amu Kr projectiles.

For 6 MeV/amu Kr projectiles, the dependence of  $L^n$  component relative intensities on the target atomic number is shown in Figure 2. Relative to the  $L^1$  component, the  $L^2$  component decreases in intensity as the target atomic number increases. This dependence appears to be linear. In contrast, the intensity ratio of  $L^3$  to  $L^1$  component decreases much faster as a function of  $Z_2$  and exceeds the intensity

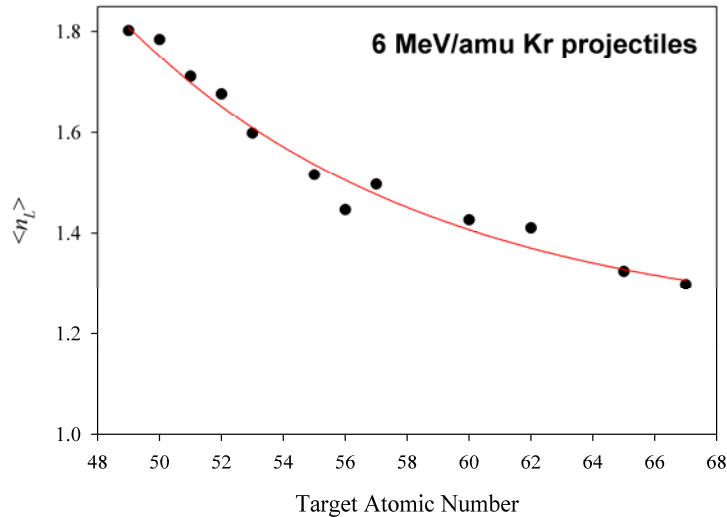


**Figure 3.** Apparent average number of  $L$  vacancies at the time of  $L$  x-ray emission as a function of target atomic number for 6 MeV/amu Kr projectiles.

In the spectrum shown at the bottom of Figure 1, the  $L^3$  component is more intense than the  $L^2$  component. This is somewhat surprising, since it is expected that the cross section for  $n$ -fold  $L$ -shell ionization monotonically decreases as  $n$  increases. A tentative explanation for the observed effect might involve the effects of vacancy rearrangement between the time of  $L$ -shell ionization and  $L$  x-ray emission, combined with the  $n$ -dependence of the  $L$  x-ray fluorescence yield.

ratio of  $L^2$  to  $L^1$  at  $Z_2 < 52$ . The intensity ratio of the  $L^4$  to  $L^1$  component, on the other hand, seems to peak around the value of  $Z_2 = 52$ , where the intensity ratios  $L^3 / L^1$  and  $L^2 / L^1$  are equal.

The dependence on target atomic number of the apparent average number of  $L$  vacancies at the time of  $L$  x-ray emission ( $\langle n_L \rangle$ ) for 6 MeV/amu Kr projectiles is shown in Figure 3. This average value was calculated from the raw intensities of the  $L^n$  components. The red line in

Figure 3 represents the best-fit exponential decay curve.

The dependence on projectile atomic number of the apparent average number of *spectator L* vacancies at the time of *L* x-ray emission ( $\langle n_L \rangle - 1$ ) for Sb target is shown in Figure 4. The blue and red circles represent the results of measurements with 10 MeV/amu and 6 MeV/amu beams, respectively. The lines represent best fits of logistic curves. More measurements are needed to establish whether logistic curves adequately represent the data points over a wider range of projectile atomic numbers and energies.

[1] V. Horvat *et al.*, *Progress in Research*, Cyclotron Institute, Texas A&M University (2006-2007), p.

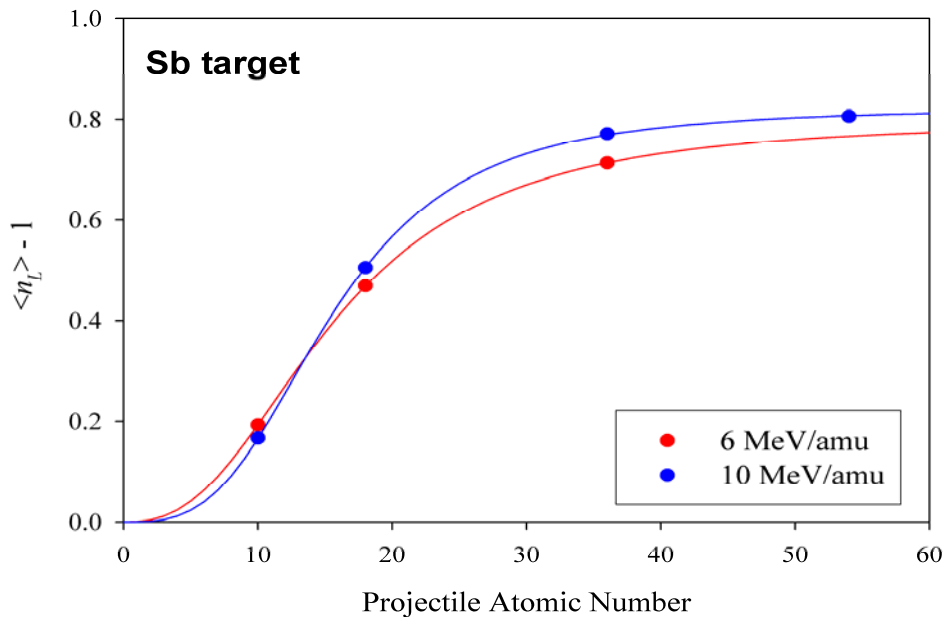


**Figure 4.** Projectile atomic number dependence of the apparent number of spectator *L* vacancies at the time of *L* x-ray emission.

IV – 4.

[2] V. Horvat, R. L. Watson, J. M. Blackadar, A. N. Perumal, and Yong Peng, *Phys. Rev. A* **71**, 062709 (2005).

## **SECTION V**

# **SUPERCONDUCTING CYCLOTRON AND INSTRUMENTATION**

## **K500 operations and development**

D. P. May, G. J. Kim, H. L. Clark, and F. P. Abegglen

### **Introduction**

During the 2006-2007 reporting period a total of 37 different beams, including 7 newly developed beams, were used for experiments. There were a total of 69 beam tunings not counting multiple tunes of beams for the SEE program. The SEE program will be treated separately.

### **Ion Sources**

An attempt to sputter titanium resulted in 4  $\mu\text{A}$  of  $^{48}\text{Ti}^{14+}$  and 5.5  $\mu\text{A}$  of  $^{48}\text{Ti}^{13+}$ . A high sputter voltage of 4.5 kV was required. The titanium was introduced into the plasma chamber as a target on the 8-finger sputter fixture, so its position could not be adjusted to enable optimizing this beam.

ECR2 was used occasionally to provide beams for the K500, notably high-charge-state gold. Progress on the ECR2 ion source will be described in a separate contribution.

### **Cyclotron Beams**

New beams of  $^{10}\text{B}$  at 15 AMeV,  $^{14}\text{N}$  at 14 and 45 AMeV,  $^{18}\text{O}$  at 15 AMeV,  $^{39}\text{K}$  at 10 AMeV and  $^{165}\text{Ho}$  at 15 AMeV were developed. The  $^{165}\text{Ho}$  beam was developed for the SEE program with charge state 31+ since a previous beam solution using charge state 30+ resulted in confusion with the 4+ charge state of  $^{22}\text{Ne}$  in the cyclotron. Sometimes residual neon in the ion source from previous SEE beams does not clear out quickly enough to avoid this confusion.

### **Operations**

For the period April 1, 2006 through March 31, 2007, the operational time is summarized in Table I, while Table II lists how the scheduled time was divided. There were three major repairs that caused significant loss of time. In September a water leak in a cyclotron dee shell caused a loss of almost eight days of beam time, followed in October by a breakdown in the expansion engine of the helium refrigerator that resulted in six and one half days of lost beam time. Finally, the repair of a water leak in the inner copper rf liner cost six days of beam time in February. The unscheduled maintenance for this year represents a much higher percentage of time than for previous years.

**Table I.** 2006-2007 operational time.

<b>Time</b>	<b>Hrs.</b>	<b>%Time</b>
Beam on target	5948.25	<b>73.3</b>
Tuning, optics, set-up	410.25	<b>5.1</b>
Beam development	423.75	<b>5.2</b>
Scheduled maint.	594.50	<b>7.3</b>
Unscheduled maint.	633.25	<b>7.8</b>
Idle time	102.00	<b>1.3</b>
<b>Total</b>	<b>8112.00</b>	<b>100.0</b>

**Table II.** 2006-2007 scheduled beam time.

<b>Time</b>	<b>Hrs.</b>	<b>%Time</b>
Nuclear physics	2196.25	<b>30.9</b>
Nuclear chemistry	1146.25	<b>16.2</b>
Atomic physics	143.50	<b>2.0</b>
Outside collaboration	36.00	<b>0.5</b>
Outside users	3150.25	<b>44.4</b>
Beam development	423.75	<b>6.0</b>
<b>Total</b>	<b>7096.00</b>	<b>100.0</b>

## Progress on ECR2

D. P. May

### I. INTRODUCTION

Since the progress report of last year, the performance of the ECR2 ion source has continued to improve due in large part to vacuum improvements. At this time last year, the vacuum pressure, as measured with an ion gauge on a port external to the plasma chamber, had not declined to the low values common in other ECR ion sources. This was the case even though the source had been operated at high power for extended periods. With no gas flow and no microwave injection, it was common to see this pressure in the mid  $10^{-7}$  torr range. Since the oxygen ions predominated the beam coming from the ion source with no gas flow, it was assumed that the background arose mainly from water vapor. A residual-gas analyzer confirmed this. The vacuum also was sensitive to the temperature of the low-conductivity water used to cool the plasma chamber. This water temperature varies slowly between 22 °C and 27 °C between seasons, and by about 1 °C through the day. The plasma chamber of ECR2 has a surface area of 0.2 m<sup>2</sup>, much larger than typical sources, and it was supposed that the pumping speed to the vacuum pumps and to the extracted beam is insufficient to handle the outgassing load. Several approaches were explored to solve this problem.

### II. SLOTTED EXTRACTION PLATE

In order to achieve more pumping speed on the plasma chamber, a slotted extraction plate was substituted for the original solid one. The three slots are 13 mm wide, at an outer radius and angled so that there is no direct line of sight from the interior of the plasma chamber to the puller (Fig. 1). Initially this plate seemed to be more prone to a PIG discharge in the extraction region, but after a short conditioning period

source



**Figure 1.** Slotted extraction plate, plasma side up, showing slots.

performance improved to the point where a source record beam of  $^{16}\text{O}^{7+}$  was achieved.

### III. PLASMA CHAMBER WATER-COOLING

Since the vacuum as well as the performance of the source was observed to be sensitive to the temperature of the plasma-chamber cooling water, an effort was made to lower this temperature. The low-conductivity water supply for the plasma chamber was plumbed through a heat exchanger with a supply of chilled water. This system immediately lowered the temperature of the plasma-chamber water from 27 °C to 22 °C. The background pressure was observed to drop from  $4.0 \times 10^{-7}$  torr to  $3.0 \times 10^{-7}$  torr. Figure 2 shows a comparison of charge-state spectra of argon taken with the chilled water on and off.

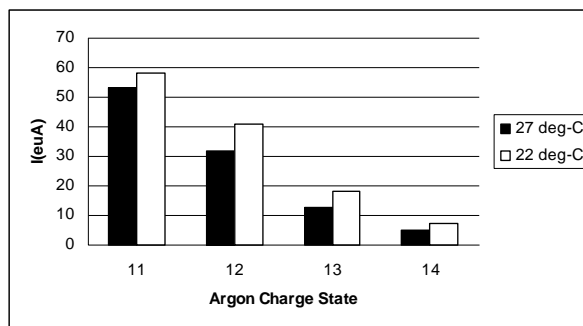


**Figure 2.** Argon charge states acquired with chilled water off (27 °C) and on (22 °C).

### IV. PERFORMANCE

ECR2 has produced 258 eμA of  $^{16}\text{O}^{6+}$  and 168 eμA of  $^{16}\text{O}^{7+}$  through a 13 mm collimator. This compares with 239 eμA of  $^{16}\text{O}^{6+}$  and 131 eμA of  $^{16}\text{O}^{7+}$  reported last year. The microwave power level was 1.3 to 1.4 kW. New results for argon are 69 eμA of  $^{40}\text{Ar}^{12+}$ , 48 eμA of  $^{40}\text{Ar}^{13+}$ , and 27 eμA of  $^{40}\text{Ar}^{14+}$ . At 1.5 kW of microwave power ECR2 has produced 5.0 eμA of  $^{197}\text{Au}^{35+}$ . The gold was introduced via a fixed sputtering device inserted into the plasma chamber through a radial slot. For all these results, the extraction voltage was 10 kV and currents were measured after analysis on a faraday cup immediately downstream of collimation in the plane of analysis. This collimator is biased at -120 volts for suppression of back-scattered electrons.

After these results were obtained, the manifold for the turbomolecular pump was replaced. The original stainless steel manifold had been used on both older versions of the ECR1 and ECR2 ion sources and has an unnecessarily large surface area. The new stainless steel manifold has about one half this surface area and also increased pumping conductance. However, there was no opportunity to obtain new beam results before ECR2 was disassembled and moved into position above the K150 cyclotron.

## Radiation effects facility

H. L. Clark, J. Brinkley, G. Chubarian, V. Horvat, B. Hyman, G. Souliotis and G. Tabacaru

The activity of the Radiation Effects Facility (REF) increased over the previous reporting year. In this reporting period, the facility was used for 2,498 hours, which is a ~8% increase over the 2,314 hours used in the 2005-2006 reporting period. Users of the facility (and hours used) over the past year were: Boeing Satellite Systems (528), NASA GSFC (374), NASA JPL (273), Xilinx (165), Stapor Research (162), Aeroflex (117), Ball Aerospace (103), NAVSEA (96), BAE Systems (91), Raytheon (89), General Dynamics (86), International Rectifier (86), Sandia National Lab (76), SEAKR (47), Northrop Grumman (45), NASA JSC (39), Lockheed Martin (32), Johns Hopkins (24), Actel (17), Maxwell Technologies (17), Boeing Seattle (13), Harris (8), Prairie View A&M University (8) and Radiation Assured Devices (6).

Table I compares the facility usage by commercial and government customers. The ratio from this reporting year (64% to 36%) is similar to the trend seen in previous reporting periods and commercial hours still dominate. Commercial hours increased by 22% and government hours decreased by 11% over hours from 2005-2006. Much of the testing conducted at the facility continues to be for defense systems by both government and commercial agencies. It is expected that the facility will continue to be as active in future years.

**Table I.** Radiation Effects Facility usage by commercial and government customers for this and previous reporting years.

Reporting Year	Total Hours	Commercial Hours (%)	Government Hours (%)
2006-2007	2,498	1,608 (64%)	890 (36%)
2005-2006	2,314	1,314 (57%)	1,000 (43%)
2004-2005	2,012	1,421 (71%)	591 (29%)
2003-2004	1,474	785 (53%)	689 (47%)
2002-2003	1,851	1,242 (67%)	609 (33%)
2001-2002	1,327	757 (57%)	570 (43%)
2000-2001	1,500	941 (63%)	559 (37%)
1999-2000	548	418 (76%)	131 (24%)
1998-1999	389	171 (44%)	218 (56%)
1997-1998	434	210 (48%)	224 (52%)
1996-1997	560	276 (49%)	284 (51%)
1995-1996	141	58 (41%)	83 (59%)

Table II lists the beams used this year and the number of times each was requested. In total, 552 beams were run this year which is 10% more than the previous year. 15 and 25 MeV/u Kr and Xe were most utilized as well as 15 MeV/u Au. No new beams were added to SEELine users list.

**Table II.** Beams used and the number of times requested for this reporting year and previous years. 511 beams were run this year.

Particle Type	A MeV	Requests 2000-01	Requests 2001-02	Requests 2002-03	Requests 2003-04	Requests 2004-05	Requests 2005-06	Requests 2005-06
<sup>20</sup> Ne	15	1	13	19	15	23	36	39
<sup>40</sup> Ar	“	4	24	43	46	51	56	60
<sup>63</sup> Cu	“	N/A	N/A	5	14	22	23	25
<sup>84</sup> Kr	“	6	26	55	47	49	75	81
<sup>109</sup> Ag	“	N/A	N/A	6	18	15	26	28
<sup>129</sup> Xe	“	5	18	43	51	50	78	84
<sup>141</sup> Pr	“	N/A	N/A	2	2	1	4	4
<sup>165</sup> Ho	“	3	11	17	7	8	22	24
<sup>181</sup> Ta	“	4	5	4	3	5	3	3
<sup>197</sup> Au	“	12	9	23	34	34	46	50
<sup>22</sup> Ne	25	27	13	19	6	15	21	23
<sup>40</sup> Ar	“	31	20	32	16	25	31	33
<sup>84</sup> Kr	“	32	20	35	26	33	40	43
<sup>129</sup> Xe	“	25	18	24	15	25	34	37
H-D	40	1	8	10	4	7	4	4
<sup>20</sup> Ne	“	5	3	5	6	11	2	2
<sup>40</sup> Ar	“	12	8	10	7	13	7	8
<sup>78</sup> Kr	“	13	9	6	5	10	3	3
<b>Total</b>		<b>192</b>	<b>207</b>	<b>360</b>	<b>324</b>	<b>399</b>	<b>511</b>	<b>552</b>

## Cyclotron computing

R. Burch, and K. Hagel

This past year we completed the migration of all lab computational servers and all but three administrative servers to SL 4.4 (Scientific Linux<sup>1</sup> v 4.4). SL has shown to be very a stable and capable operating system which uniquely fits the needs and mission of our lab.

We also finished our evaluation<sup>2</sup> of SATA drives as a cheap alternative to SCSI drives which we use to add storage to the file-server and found them acceptable. Since then we increased the file-server's available disk capacity by replacing a four port SATA card that we used for the evaluation with an eight port SATA card and two 4-disk enclosures. This gives us eight SATA disk bays, four which are populated with 500GB drives and four free for future expansion. The file-server is now also being utilized as a centralized print server for the lab's general computational servers, offering single point computational print que maintenances.

Three new servers were brought on-line this year with SL 4.4. The aging data acquisition server, ACQ, was replaced with a Dell PowerEdge 2950 with two Xeon 3.7GHz dual core processors and 4GB RAM. A new computational server (Dell PowerEdge 1950 with two Xeon 3.0GHz processors and 4GB RAM) was added to the lab's general computing facility. We also replaced the aging backup sever, a Dell PowerEdge 850 with a Pentium 4 2.8GHz and 1GB RAM. This server also supports USB2 which enables us to utilize external USB2 disks which we are currently using to make snapshots of HOME and critical directories with RSnapshot, internal and two external USB2 disks. The external disks are rotated off-site monthly.

The lab's firewall was migrated to SL 4.4, first on old hardware then on newer hardware. This leaves us with a backup firewall should the production firewall develop problems. In addition we added intrusion detection and network monitoring software to the firewall to aid in detecting lab wide security issues.

The aging DNS server was migrated to newer hardware this past year, and we are adding DHCP to the server. We also rewrote the NetReg WebApp (network registration web application) in Ruby on Rails and added it to the DNS/DHCP server. The new NetReg WebApp automates some of the network registration process making it less man power intensive while being more flexible. Also the web server was migrated to SL 4.4. This enable the installation of Cern's Indigo<sup>3</sup>, a WebApp for meeting agenda, which is available for general lab use.

[1] <https://www.scientificlinux.org/>

[2] R. Burch, K. Hagel, Progress in Research, Cyclotron Institute, Texas A&M University (2005-2006), p.V-12

[3] <http://indico.cern.ch/>

## Cyclotron institute upgrade project

H. L. Clark

On January 3, 2005 the Cyclotron Institute Upgrade Project (CIUP) began with the approval of the CIUP management plan by the Department of Energy Nuclear Physics Office. The project will extend to the first quarter of calendar year 2011. When completed, the upgraded facility will provide high-quality re-accelerated secondary beams in a unique energy range in the world. Funding for the upgrade comes from several sources: the Department of Energy, matching support from TAMU, the Robert A. Welch Foundation and beam time sales for testing electronics components at the Cyclotron Institute.

The CIUP is divided into three major tasks: (1) Re-commission of the existing K150 (88") cyclotron and refurbish beam lines; (2) Construct light-ion and heavy-ion guides and produce 1+ radioactive ions; (3) Transport and charge boost radioactive ions and accelerate these in the K500 cyclotron.

Most of the effort during this reporting period focused on Task 1, restoring the K150 cyclotron major equipment. This included commissioning the K150 cyclotron initial vacuum system, coil power supplies and sub-systems. Each component of the K150 RF system has been tested and full commissioning should take place in early summer 2007. Installation of K150 ECR & injection line and assembly of K150 beam line equipment has begun. The ECR & injection line should be completed by mid summer 2007, and the beam line should be functional by spring 2008. Progress was also made on Tasks 2 and 3. This included testing of the light ion guide chambers vacuum equipment and development of the SPIG ion transport device. The beam dump and radiation shielding has been designed by utilizing complex radiation transmission computer codes. The design was approved by a panel of experts that visited in March 2007. Development of heavy ion guide gas cell system with collaboration with ANL and GSI still continues. The CBECR ion source constructed through a DOE SBIR project is nearly complete. The CBECR is scheduled to arrive in September 2007. Below is a description of the progress made. Figure 1 illustrates the revised project schedule and major milestones.

### **TASK 1:**

- 1) **K150 Cyclotron Vacuum System:** The design calls for vacuum equipment to be installed on the two main sections of the vacuum space (resonator tank and dee tank) as follows: The resonator tank will be equipped with one new 35" diffusion pump with a modern cryogenic baffle system and one new roots blower package (initial system). The initial system will provide a vacuum pressure of  $5 \times 10^{-6}$  torr for testing the RF System, identifying any major leaks and producing first beams. The dee tank will be equipped with one internal liquid nitrogen cryogenic panel and four external cryopumps (high vacuum system). The high vacuum system will provide a vacuum pressure of low  $10^{-7}$  torr for beams later in the project.

All components of the initial system (35" diffusion pump, cryobaffle and roots blower) have been procured and installed on the cyclotron including electrical power, interlock/control system, cooling water and pneumatic control. For the high vacuum system, the external cryopump system (four pumps, two compressors and helium transfer lines) and VAT isolation valves have been procured.

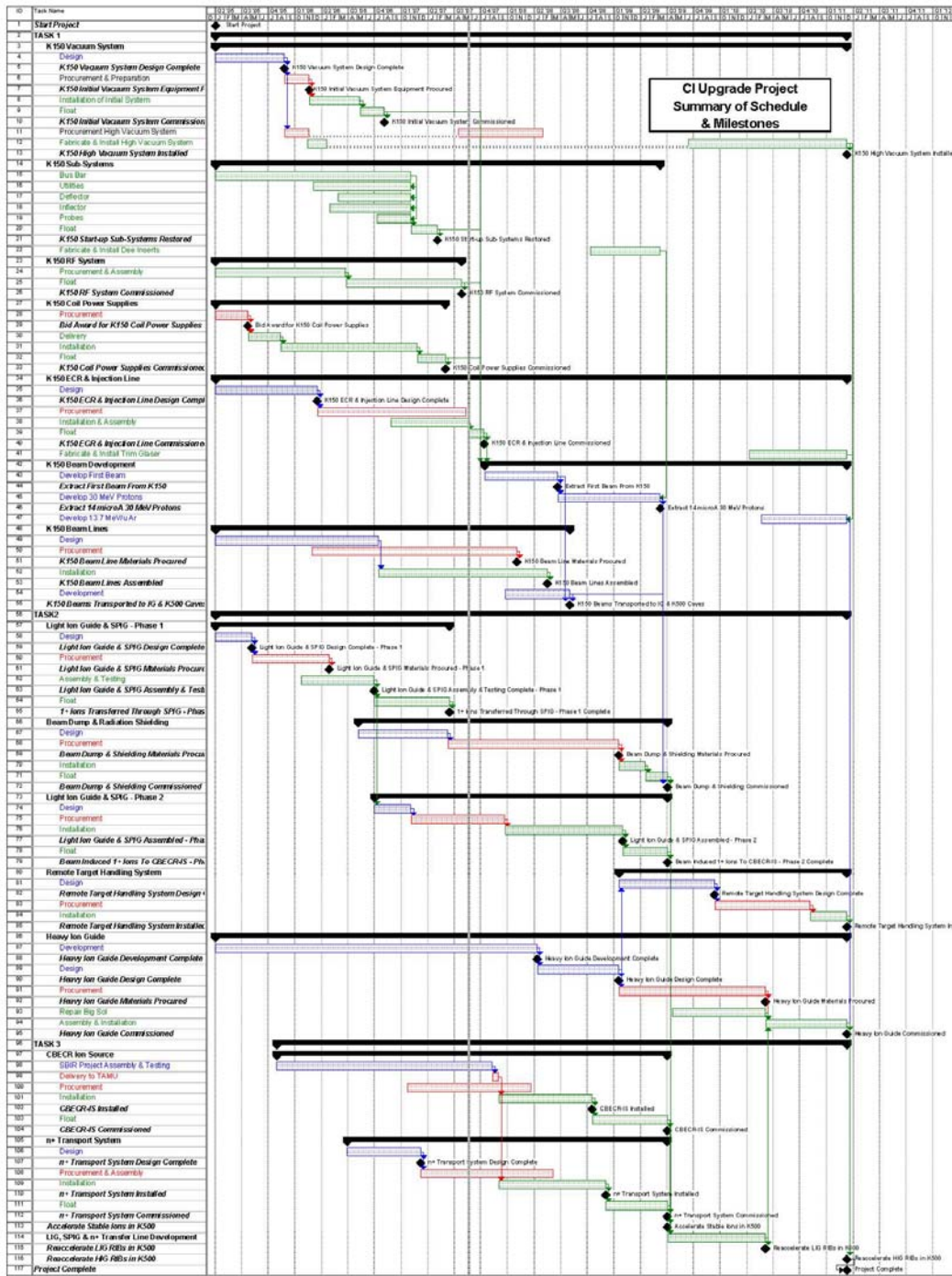


Figure 1. The project schedule and major milestones.

The VAT valves for the external cryogenic system have also been installed. A quote for the LN2 transfer and dewar system has been received from Technifab Inc. This system will be used to feed LN2 to both the internal cryopanel of the cyclotron and to the cryopanel system in the vertical injection line. Materials for the cryogenic panels are being procured.

In late September 2006, the initial system was turned on, and all large external vacuum leaks were identified and repaired. After ~20 hours of pumping, vacuum was measured to be  $2 \times 10^{-6}$  torr at the bottom of the resonator tank (closest to the diffusion pump) and  $2 \times 10^{-5}$  torr at the top of the resonator tank (furthest from the diffusion pump). Initial start-up showed that the initial system was functioning properly and according to design.

In March 2007, several leaks were identified at various locations outside and inside the cyclotron and were repaired. After repairs were made, noticeable improvement was observed. Vacuum of  $2 \times 10^{-6}$  torr was measured at the extraction region of the dee tank and also at the top of the resonator tank (locations furthest from the 35" diffusion pump). Vacuum was also measured to be  $2 \times 10^{-7}$  torr at the bottom of the resonator tank, which is closest to the 35" diffusion pump. Pump down time from atmosphere to these values was recorded to be several hours which was also a significant improvement.

- 2) **K150 Cyclotron Buss Bar Work:** Buss bar installation is complete for all twenty three coil power supplies, including the final connections to the main coil power supply. The main coil power supply arrived in late June 2006 and has been installed.
- 3) **Upgrade Project Utilities:** The building power improvement (to add electrical power capacity for the K150 cyclotron, K150 coil power supplies, K150 RF system, K150 beam lines, ion guides, etc.) is complete. All Upgrade Project equipment is now utilizing the new building power improvement including the K150 vacuum system, K150 RF system and the Light Ion Guide vacuum system.

Construction of the new LCW loop (to add cooling water capacity for the K150 cyclotron, K150 coil power supplies, K150 RF system, K150 beam lines, ion guides, etc.) is complete. All pipes, connectors, valves, pumps and control gear have been installed including the surge tank, demineralizer, heat exchanger and cooling tower pumps. The start-up occurred during annual maintenance (January 2007). This new LCW system will provide water to the K500 experimental beam lines. Since the inception of the K500 cyclotron, the 88" LCW system provided this water, however now the 88" LCW system has been restored to the K150 cyclotron.

- 4) **K150 Cyclotron Deflector:** Two new Spellman deflector power supplies were purchased. Installation of the supplies and control equipment is complete. The deflector assembly was removed from the cyclotron with the original trolley system. The deflector assembly was cleaned and the LCW cooling lines were checked for leaks and some were replaced with new lines. The controls for positioning the deflectors have been restored and the system appears to be functioning properly.
- 5) **K150 Cyclotron Inflector:** The existing mirror inflector has been removed, cleaned and tested with high voltage and appears to be working properly (off-line). Spare screens and other components are being constructed. During initial startup, the mirror inflector will be used to make the first beams. Once the operation of the central region of the K150 cyclotron is well understood, then a spiral inflector may be introduced.

- 6) **K150 Cyclotron RF System:** The construction of the RF system was completed in the fall of 2006. It consists of the RF power supplies, control system, RF driver amps, and RF final amplifier.

The control system consists of low voltage power supplies, the modules needed for the RF signal processing, RF driver amplifiers needed to drive the main RF amp, and controls for driving the various machine components relative to the RF system. All the components were built in house and have been tested individually. Spares were built at the same time.

The anode power supply has been built in house. This power supply cabinet provides all the power requirements for the 4CW150,000 power tube used in the final amplifier, as well as the interlock system involved in protecting the power supply, final amplifier, and cyclotron components. The final amplifier tube requires grid, screen, and anode power supplies. The grid and screen power supply chassis are contained inside the main power supply cabinet, and have both been fully tested. In addition, two spares of each have been built. In the summer of 2006, the anode supply was turned on and tested at 150 kilowatts, using the final amplifier as a load. The final amplifier tube was biased on and run at 7.5 amps at 20 kilovolts for 1 hour. The expected temperature rise was seen in the tube cooling water to verify actual power consumption measured at the power supply.

The final amplifier cabinet has been rebuilt with new components and installed on the back of the cyclotron. A filament power supply provides the 15 volts at 200 amps d.c. for the 4CW150,000 tube filament, and was built for us by an outside vendor. A spare supply was also built, and both are compatible with the units used on the K500 cyclotron.

The various machine components pertaining to the running/tuning of the RF system have been repaired as needed and tested for proper operation. Water leaks have been repaired in the resonator panels, as well as associated components involving the movement of the panels. The trimmer drive system has been rebuilt and tested. Now that the cyclotron vacuum system and the new LCW system are functional, the testing of the RF system has begun.

- 7) **K150 Cyclotron Coil Power Supplies:** All twenty-three coil power supplies have been installed on the cyclotron including the 3000 amp - 180 volt main coil power supply. This supply was placed on the footprint of the original (Ling) main coil power supply which was removed.
- 8) **K150 ECR & Injection Line:** The design for the injection line was determined by closely following the Berkeley design for their AEER and incorporating the existing elements from our ECR2 injection line. To obtain the highest transmission efficiency possible, two additional focusing elements (Glaser lenses) and one additional set of steering magnets will need to be procured. Power supplies and control equipment for these additional elements will be procured as well. The shape of the hole through the upper center plug has also been redesigned. The original upper center plug cannot be modified since it has retained activity from its years of use. Enough iron has been purchased for both the upper and lower center plugs if rebuilding the lower center plug becomes necessary. Machine work on the new center plug has is nearly complete. All beam line components have been constructed and leak checked. The center plug Glaser lens has been wound including the x-y steering magnets.

Vacuum pressure in the low  $10^{-7}$  torr will be obtained along the entire injection line and into the inflector region with two new external cryopumps and an internal liquid nitrogen cryopanel. The components of the beam line will be joined together using copper conflat seals rather than rubber o-

rings. All valves, flanges and cryogenics systems have been received. The internal liquid nitrogen cryopanel is also complete.

ECR2 and its associated equipment have been dismantled from the K500 cyclotron and moved over to the top of the K150 cyclotron. Installation of ECR2 has begun. It is anticipated that the commissioning milestone for the ECR and injection line will be met in early summer 2007 as described in the management plan.

- 9) **First Beams from K150:** Over the last year, progress has been made on understanding the CYDE program which calculates the cyclotron parameters for a given beam. The original TAMU version of CYDE was lost, but we were able to obtain the code that is currently used at Berkeley for their 88" cyclotron. For  ${}^7\text{Li}^{2+}$  accelerated to 62 MeV, it is found that the values from this program, which uses the Berkeley field map, agree with the old values from our 88" cyclotron runs from 20 years ago. A set of parameters has been developed for 25 MeV/nucleon alphas and 7.5 MeV/nucleon Argon.
- 10) **K150 Beam Line:** All magnets, support structures and beam boxes will be built by the cyclotron personnel. All materials needed to fabricate 25 quadrupole magnets, 14 x-y magnets and their support structures have been procured, including insulated copper wire for the magnet coils. All pole and yoke pieces have been machined. The winding and potting of all quadrupole magnet coils has been completed. Early on, two quadrupole magnets made entirely from surplus materials at the lab were completed. Thirteen quadrupole magnets have been completely assembled and are ready for installation. All pieces for x-y magnets have been machined and are ready for assembly. Stands for x-y magnets, quadrupole magnets and beam boxes have been constructed and are assembled. The bid for the beam line magnet power supplies was awarded to Alpha Scientific (same company that built the supplies for the K150 cyclotron coils).

Nine turbo molecular pumping stations will be required for the K150 beam lines. All items needed to build the pumping stations, except the roughing pumps, turbo molecular pumps and their controllers have been received. The bid for the turbo pumps and mechanical pumps was awarded to Pfeiffer Vacuum Systems. The pumps should arrive in June 2007.

- 11) **K150 Control System:** A new control system for the K150 cyclotron project has been developed. The new system was developed since the equipment of the current K500 control system is being phased out by industry. A prototype unit using a "Rabbit" brand control card was developed and thoroughly tested by incorporating it into the existing K500 control system and was found to operate the K500 equipment properly. The prototype was also configured to control the new coil power supplies of the K150 cyclotron and was found to operate this equipment properly as well. This new system is both simpler in design and much less expensive compared to the existing K500 control system.

Materials needed to build the new control system have been procured. The new system has been installed and is currently operating twenty-two of twenty-three coil power supplies and is now being developed to read-out the vacuum systems of the K150 cyclotron, beam lines and experimental areas.

## TASK 2:

- 1) **Light Ion Guide:** All materials have been procured including materials for both ion guide chambers, support structure, vacuum pipe, flanges, gas control system and SPIG. The Pfeiffer oil-free Roots1 and Roots2 vacuum systems arrived in May 2006.
- 2) Ion guide chambers 1 and 2 have been constructed, cleaned, vacuum tested and mounted on the support structure. The internal spark discharge chamber has been fabricated and installed in ion guide chamber 1 and is working properly. All flanges and piping between the Roots1 and Roots2 vacuum systems have been installed. The electrical switch gear needed to power the roots systems and ion guide equipment has been installed. The gas management system has been assembled and attached to the ion guide chamber.

The Roots1 and Roots2 vacuum systems and gas management systems were checked for proper operation and control. 1+ ions were transferred from the spark discharge chamber to a Faraday cup and the differential pumping system was optimized. Since very large flow will be used in the final design of the light ion guide system, a gas recirculation system is being developed in order to reclaim and reuse the helium gas. To determine the type and level of cleaning system needed, we measured the levels of contaminants in the exhaust of the roots blower. Different systems and pricing are currently being investigated.

In March 2007, 1+ ions were created in chamber 1 (via spark discharge), transferred into chamber 2 (via differential pumping) and then guided 20 cm through the SPIG device to a Faraday cup positioned at the end of the SPIG. After adjustments to pressure, voltage and RF were made, it was found that nearly 100% of 1+ ions were transported through the 20 cm SPIG device. The SPIG is the device that will transport the radioactive ions from the Light Ion Guide to the CB-ECR ion source.

The bids for the oil-free Roots 3 blower and turbo molecular vacuum systems have been awarded to Pfeiffer Vacuum. These systems are required for the final differential pumping system that will connect the Light Ion Guide system to the CB-ECR IS.

- 3) **Beam Dump and Radiation Shielding:** The design for the beam dump and shielding structure has been completed by using the modeling codes obtained (PHITS, MORITZ and MCNPX). A review panel made from outside experts approved the design during a visit in March 2007. The panel consisted of Reg Ronningen (NSCL), Igor Remec (ORNL) and Don Cossairt (FNAL). A materials list for the beam dump has been compiled.
- 4) **Heavy Ion Guide:** The collaboration with the ANL gas cell group is in continuation. Plans go as follows:
  - Measure main parameters (isotopic yields, energy and space distributions) of secondary species at the K150 beam energies with Big Sol at Texas A&M
  - Test the efficiency of the heavy ion gas cell at ANL at high input densities (similar to the gas cell we are planning to build at Texas A&M)
  - Reassemble the gas cell at GSI including:
    - a. Install thermo-resistant insulation and sealing ceramic rings
    - b. Install oil-free roots blower system
    - c. Test the cell off-line to prepare for an experiment on the FRS (time of the experiment at the GSI is under discussion)

### TASK 3:

- 1) **CBECR Ion Source:** SBIR Phase 2 funding was awarded to Scientific Solutions to build a CB-ECRIS. Once completed, this CB-ECRIS will be installed at the Cyclotron Institute. The SBIR project schedule has been determined to be 18 months and should be delivered in August 2007 which matches well the schedule for the Upgrade Project. It has been estimated that ~\$250k of major equipment will need to be supplied by the Cyclotron Institute to complete the CB-ECRIS. This will include turbo molecular pump systems, coil power supplies, microwave transmitters and control equipment.

The construction of the CB-ECRIS by Scientific Solutions is proceeding on schedule. The bid for the two sets of turbo molecular and mechanical pumps was awarded to Pfeiffer Vacuum. The pumps were received in March 2007 and delivered to Scientific Solutions.

- 2) **n+ Transfer System:** The design for the n+ transfer system that will connect the CB-ECRIS to the K500 cyclotron has been completed. All solenoids and x-y steering magnets will be built by in-house personnel. The 90° bending magnets will be built through a collaboration with the NSCL and the Cyclotron. Construction will follow the recent design made by the NSCL which will improve transmission efficiency over the current design. The Cyclotron will build the coils and NSCL will build the yokes and vacuum chambers. Two complete magnets are needed by each laboratory and should be completed in the summer of 2007. The list of materials and power supplies needed to complete the beam line is being compiled.

High vacuum will be maintained at low  $10^{-7}$  torr with several cryopump stations and all connections along the beamline will be made with conflate flanges and copper seals. Diagnostic stations will also be installed along the beam line.

# Compact injection line for K150 cyclotron

G. J. Kim

A compact injection line has been designed for the K150 Cyclotron, which is being refurbished to provide intense beams for the production of radioactive beams. The ions for the cyclotron will be produced from ECR2, an AECR-U class, two-frequency ion source.[1] The injection line will use a single 90 degree magnet to analyze the beam as well as to bend the beam vertically into the cyclotron, see Fig. 1. The beam focusing will be accomplished with four solenoidal magnets, the last one of which is located inside the yoke of the cyclotron. (The short Berkeley-designed solenoidal magnets are also referred to as Glaser lenses.) Other components in the injection lines are: x-y steering magnets, faraday cups and slits, beam attenuation screens, a beam buncher, and vacuum pumps and valves.

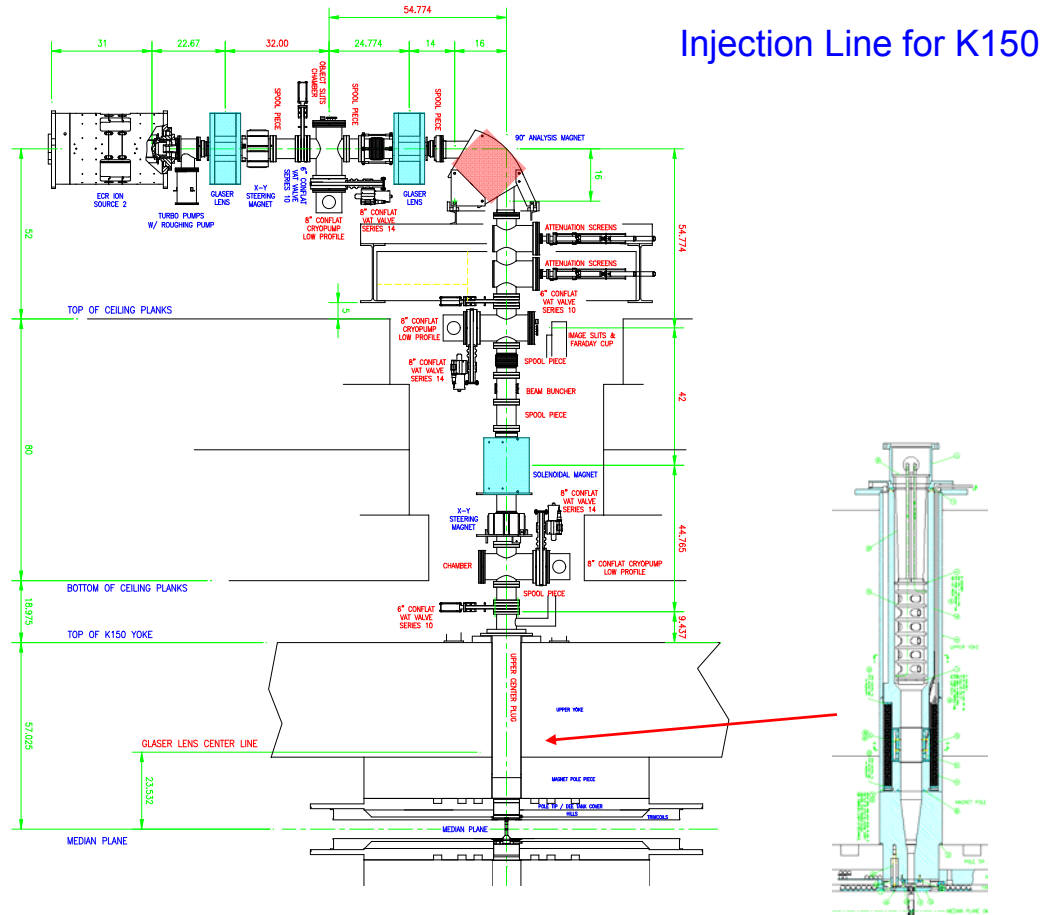


**Figure 1.** Layout of the injection line for the K150 Cyclotron.

The injection line was designed in a modular fashion using as much as possible existing equipment. The fundamental element in the injection line is the 90 degree analysis magnet. The MSU designed bending magnet has a short 16" (40.64 cm) radius of curvature and with 30 degree entrance and exit edge angles to give a double x and y focusing at about 98 cm object and image distances. The bending magnet section achieves a modest charge-to-mass resolution of 1/70 through 1/2" object and image slits. The magnet has 4.2" vertical and 6" wide opening. (The beam pipe diameter will be 6" outside of the cyclotron.) Additionally, in order to compensate for space charge effects in this section of the injection line, a Glaser lens will be added just upstream of the 90 degree magnet as shown in Fig. 1. The ECR2 ion source and a Glaser lens are located upstream of the bending magnet section. The first Glaser lens is placed close to the ion source to efficiently collect ions and to refocus them onto the object slit for the bending magnet. The nominal magnification of the Glaser lens from the exit of the ion source to the object slit is 1.4, and this helps to control the divergence of the beam through the rest of the injection line. Vertically downstream of the bending magnet section, a long, MSU designed solenoidal magnet and a short solenoidal magnet in the yoke, located just above the funnel shaped iron plug, are used to focus the beam into the cyclotron. The general scheme of this section is to focus the beam point-to-parallel from the image slit of the bending magnet to the long solenoid, and then run parallel between the two solenoidal magnets, and then focus parallel-to-point with the last solenoidal magnet onto the mirror inflector. Thus, optically the compact 8 m-long injection line naturally divides into three sections.

The injection line design and some of its parameters were initially determined with the first order TRANSPORT code. To study next the space charge effects from intense beams, two other beam transport programs, which include first order space charge effects, were used: Trace3d from Los Alamos [2] and TransOptr from Chalk River, now maintained by Rick Baartman at TRIUMF.[3] Interestingly, initially the results from the two programs did not agree, however later this was traced to the extra factor of 1.5 for the beam current in the Trace3d program. A simple transport test using a 2m drift space using, for example, 0.10 mA beam current for Trace3d and 0.15 mA for TransOptr, confirmed that to get an agreement between the two programs, the input beam current for the Trace3d must be reduced by 1.5 from that for TransOptr. Additionally, the numerical integration of the K-V equations, using 0.15 mA beam current for the present example over the 2 m drift space, also gave the same results as the two programs.

The standard beam emittance used for the transport calculations was  $4 \times 30 \pi$ -mm-mr, which is adequate for the most beams [4], however, for the light ions a larger  $6 \times 75 \pi$ -mm-mr was used to test the injection line. The Trace3d calculations with 0.15 mA beam current through the injection line for the two emittance values are shown Fig. 2.

To study the effects of the cyclotron fringe field on the injection line, first the cyclotron fringe field through the 4" hole in the yoke was determined with a Poisson calculation, see Fig. 3. The calculation is compared with a field measurement from Berkeley, reported in the 2000 LBNL Report[5]. The figure shows good agreement between the calculation and the measurement for the rapid falloff of the main field through the yoke hole, however the calculation could not reproduce the small field bumps. One interesting bump in the calculation at 60 cm from the median plane is due to the open structure of the Glaser lens in the yoke hole. Overall, the cyclotron field is well shielded in the yoke hole, away from

## Large Emittance Study with Trace3d

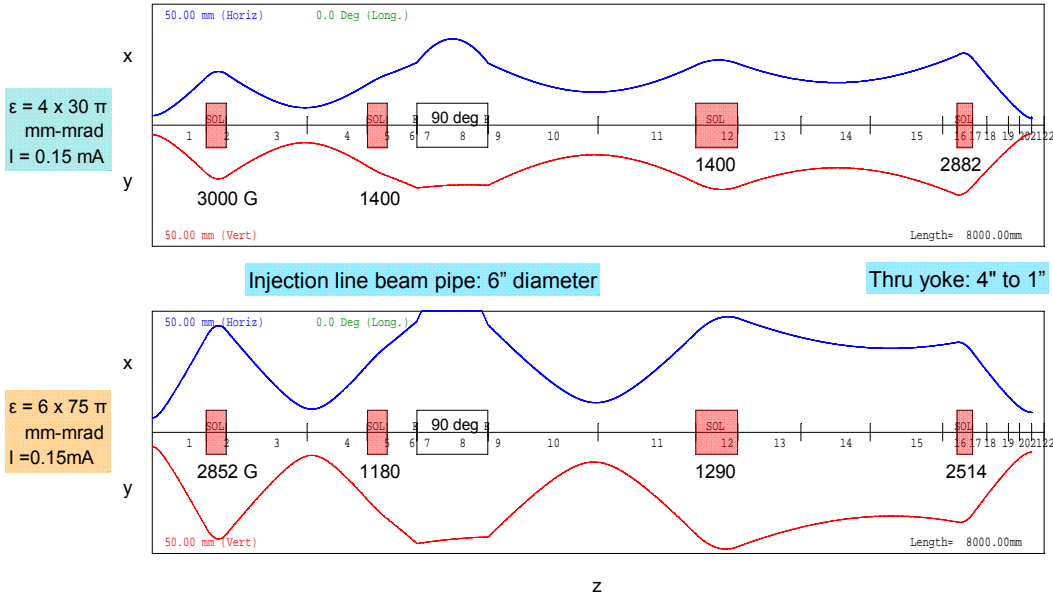


**Figure 2.** X and Y beam envelopes for transport from the exit of the ion source to the center of cyclotron. The indicated field values for the four solenoidal magnets are possible solutions to keep the beam envelopes under 50 mm half width through the injection line.

the main volume of the cyclotron. The effects of the cyclotron fringe field was studied with TransOptr, which integrates over a user specified external field. Fig. 4 shows the effects of turning on the cyclotron field at 14.4 kG. Clearly the strong cyclotron field provides an extra focusing on the beam, which makes the beam spot smaller and also shifts the waist of the beam slightly upstream as shown on the figure. While playing with the last two solenoidal magnets, it was found that the waist of the beam can be brought back to the center of the cyclotron for this particular cyclotron field (14.4 kG). The effects on the beam at two lower cyclotron field levels of 5 and 10 kG were also studied. The effects were weak at 5 kG and only a small additional focusing was seen. At 10 kG level, similar to the 14.4 kG field effects were observed but less severely. However, more work will need to solve how to properly use the last two solenoidal magnets to focus the beam at the center of the cyclotron. A new central region calculation will be useful to set the beam conditions.

We would like to express our thanks to Claude Lyneis and Daniela Wutte of LBNL for their help and providing us with drawings for the components in the cyclotron yoke.

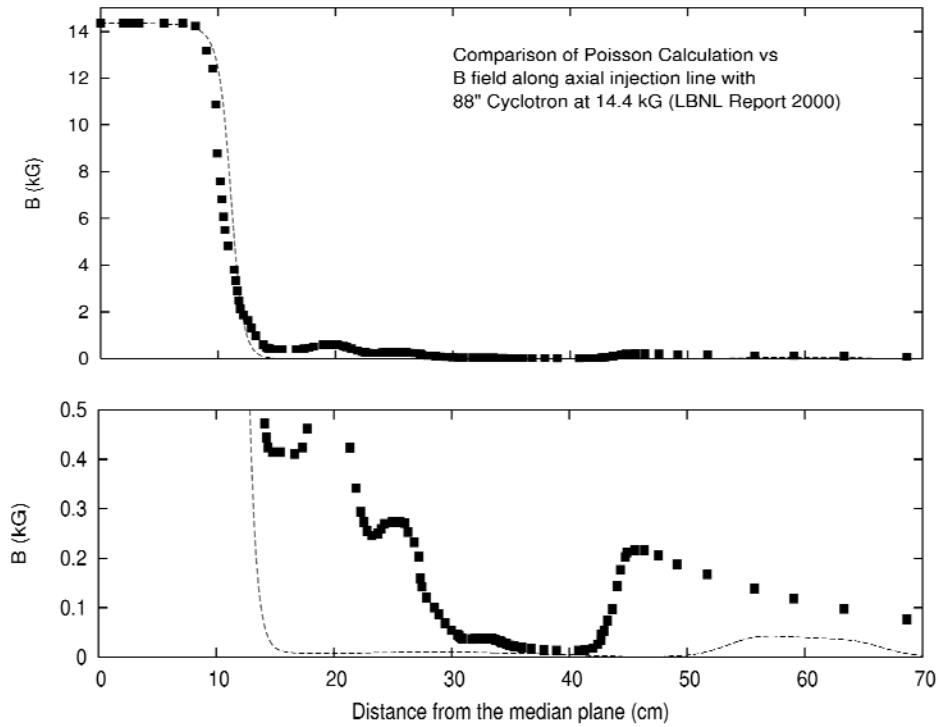


**Figure 3.** The axial field of the cyclotron through the yoke of the cyclotron.

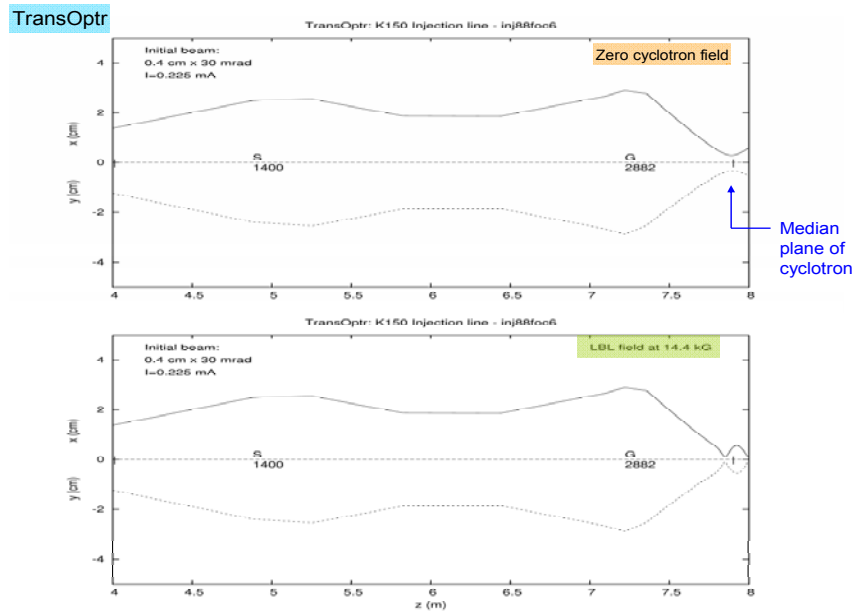


**Figure 4.** Effects on the beam due to the fringe field of the cyclotron at 14.4 kG.

- [1] Z. Q. Xie and C. M. Lyneis, Proceedings of the 13<sup>th</sup> International Workshop on ECR Ion Sources, College Station, Texas (1997) p.16.
- [2] K. R. Crandall and D. P. Rusthoi, "Trace 3-D Documentation," Los Alamos National Lab. report LA-UR-97-886 (1997).
- [3] E. A. Heighway and M. S. de Jong, "TRANSOPTR," Chalk River Nucl. Lab. Report AECL-6975 (1984).
- [4] D. Wutte *et al.*, in Proc. of the 16<sup>th</sup> International Conference on Cyclotrons and their applications in East Lansing, MI 2001 (2001), p.445.
- [5] D. Wutte, "The 88-inch Cyclotron External Injector System," LBNL Report (2000).

## Progress on the light ion guide facility

G. Tabacaru, J. Arje, and H. L. Clark

The Light Ion Guide (LIG) is part of the future development of the Cyclotron Institute. The LIG is a device that produces radioactive ions using the IGISOL technique: Ion Guide with a Separator On-Line. The principle of functioning is the following:

The beam (a proton beam around 30 MeV) interacts with a production target (e.g.  $^{27}\text{Al}$ ) that's playing also the role of a separation foil for the gas cell. In the gas cell helium gas is flowing continuously at constant pressure of 500 mbar maximum. The recoil ions (e.g.  $^{27}\text{Si}$  from  $^{27}\text{Al}(p,n)^{27}\text{Si}$ ) are trapped in the buffer gas and ejected at a  $90^\circ$  direction (with respect to the beam direction) through a small exit hole. The  $1+$  ions are collected and transported by a Sextupole Ion Guide: a non-resonant structure similar to the RFQ's from residual gas analyzers. A differential pumping system evacuates all the residual Helium gas.

In the last year, extensive tests were performed in order to find optimum conditions of functioning of the differential pumping system. We have acquired two Pfeiffer pumping stations with oil free roots blowers and competitive mechanical pumps. The first pumping station has capability to pump Helium gas at speed of  $1900\text{ m}^3/\text{h}$  and the second one at speed of  $900\text{ m}^3/\text{h}$ .

A spark chamber was built for the off-line tests and various experiments were performed. First series of experiments were done in order to tests the pumping speed for the entire system and the conclusions are that an ultimate pressure of 1.6 mbar is obtained in the first roots chamber when a maximum pressure of 500 mbar is kept in the spark chamber, 2 mm exit hole being used. These results confirm the vendor pumping speed curves for Helium.

After testing the pumping speed we have tested the production of  $1+$  ions using DC voltage in the spark chamber. Current up to  $100\ \mu\text{A}$  was observed in a Faraday Cup placed in front of the spark chamber.

The tests performed last year showed a very stable and reliable system. The challenge is to transport

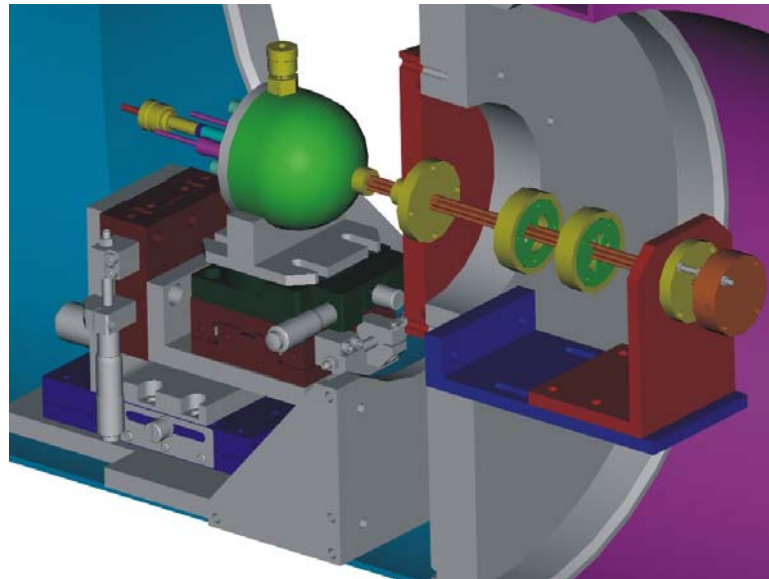


**Figure 1.** View of the spark chamber coupled with the Sextupole Ion-Guide.

with very high efficiency ions through a long Sextupole Ion-Guide, in order to be able to inject them in the future Charge Breeding ECR source.

## Progress on the shielding evaluation for the beam dump

G. Tabacaru and H. L. Clark

The facility upgrade project includes the commissioning of the Light Ion Guide, a device capable to produce radioactive beams via (p,n) reaction [1]. The primary beam (proton) should have high intensity, in order to increase the efficiency of the entire system. The primary beam will be stopped in a beam dump located at about 3 meters away from the gas cell.

We propose to build the beam dump from Aluminum (1199 alloy). Initially we have considered Carbon and Copper as material for the beam dump. Carbon has poor heat transfer and Copper will lead to higher prompt neutron flux, approx. 5 times bigger than in the case of Aluminum. The particular shape was chosen in order to increase the thermal radiation surface, an important parameter for the efficient cooling. The fairly large diameter, 19 cm, is enough to contain the entire beam. The power distribution in the beam dump was introduced from a PHITS [2] calculation. This power dumped highly exceeds the normal operation of the device. Engineering calculations done with ALGOR software show a temperature

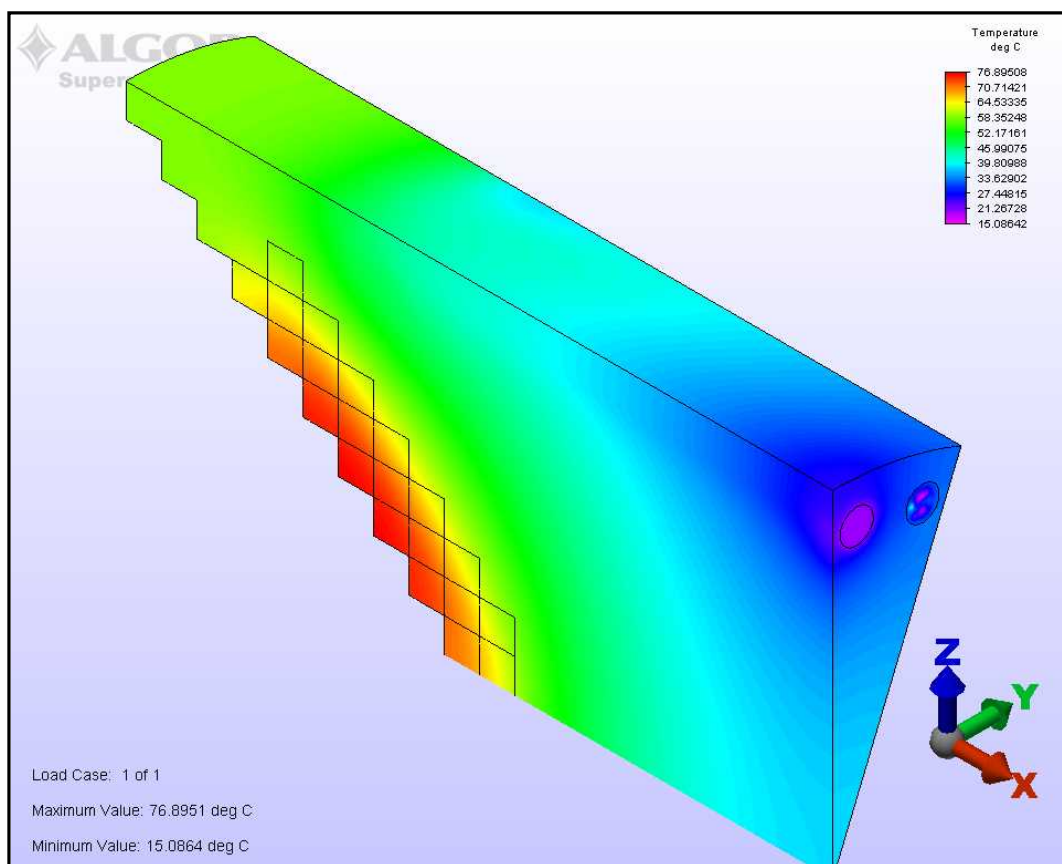


**Figure 1.** Beam dump view with the temperature profile.

of about 1000° C without cooling. A cooling tube was attached running a coolant with entrance

temperature of 15° C. It was found that the temperature will not exceed 100° C locally. Commercial chillers with closed loop cycles easily can provide the performance required.

The shielding proposed is based on concrete blocks, borated polyethylene and lead. The beam dump will be located in vacuum and the vacuum pipe will be enclosed in a concrete castle. Also a concrete block is place on top of this structure. In the Table 1 we present the equivalent dose estimations in five locations:

**Table I.** Equivalent dose [mrem/h] in 5 different locations at three different times after shutdown.

<b>Time after shutdown</b>	<b>Location 1 Outside cave [mrem/h]</b>	<b>Location 2 Behind beam dump [mrem/h]</b>	<b>Location 3 Side [mrem/h]</b>	<b>Location 4 Top [mrem/h]</b>	<b>Location 5 Upstream [mrem/h]</b>
<b>10 min</b>	$3.90 \times 10^{-6}$	2.5	6.8	7.6	62.9
<b>1 hour</b>	$1.96 \times 10^{-6}$	1.8	5.9	6.1	35.2
<b>1 day</b>	$7.02 \times 10^{-8}$	0.6	2.1	2.1	12.9

The equivalent doses estimated shows reasonable values in five different locations after a day following 10 days of intense irradiation. The Health Physics Department will enforce the rules concerning the access in the cave.

- [1] G. Tabacaru, J. Arje and H. L. Clark. *Progress in Research*, Cyclotron Institute, Texas A&M University (2006-2007), p.V-20.
- [2] H. Iwase, K. Niita and T. Makamura, *J. Nucl. Sci. Tech.*, **39**, 1142 (2002).

## The use of Geant4 simulate the response function of a plastic $\beta$ -detector to standard $\beta$ -sources of $^{133}\text{Ba}$ and $^{137}\text{Cs}$

V. V. Golovko, J. C. Hardy, and V. E. Jacob

Knowledge of the response function of our plastic  $\beta$ -detector is crucial in precision measurements of branching ratios, which is one component of our experimental program aimed at testing the Standard Model. In particular, the  $ft$  values from superallowed  $0^+ \rightarrow 0^+$  nuclear transitions yield the value of  $V_{ud}$ , the up-down quark-mixing element of the Cabibbo-Kobayashi-Maskawa (CKM) matrix. This requires that the half-lives, branching ratios and decay energies be measured to high precision. (The most recent review of this work can be found in Ref. [1]). Since branching ratios are typically determined from the intensities of  $\beta$ -delayed  $\gamma$  rays that are observed in  $\beta$ - $\gamma$  coincidence measurements, the  $\beta$ -detector response function – and thus its efficiency as a function of energy – is crucially important to our achieving high precision. Here we report studies of our  $\beta$ -detector's response function based on Monte Carlo (MC) calculations performed with the Geant4 code [2]. The Geant4 results will be compared with experimental measurements.

The  $\beta$ -detector assembly is illustrated in Fig. 1a, with a detailed description of materials given in Ref [3]. For our measurements of the detector response function, each radioactive source was placed at a distance of 13 mm from the havar window of the detector assembly and axially alligned with it. Both were placed on a lab table (in air at atmospheric pressure) as far away as possible from other objects. The three radioactive sources we used –  $^{133}\text{Ba}$ ,  $^{137}\text{Cs}$  and  $^{207}\text{Bi}$  – were 37-kBq conversion-electron sources purchased from Isotope Products Laboratories. Previous work [4] has reported the response function of  $\beta$ -particles from the  $^{207}\text{Bi}$  source. Here, we concentrate on the comparison of MC simulated data with the measurements from  $^{133}\text{Ba}$  and  $^{137}\text{Cs}$ . All three sources, being specially prepared to minimize scattering or degradation of the emitted electrons, were deposited as 5-mm-diameter spots on a thin foil – stainless steel in the case of  $^{207}\text{Bi}$ , aluminized Mylar for the other two – and covered only by a  $100\text{-}\mu\text{g}/\text{cm}^2$  acrylic film. The source-holder geometry is shown in Fig. 1b.

In defining the laboratory geometry in Geant4 we included all components of the detector assembly and source housing (see Fig. 1a and Fig. 1b), with all objects placed in air. Special care was taken to include all elements present in the various materials, and the natural abundance of isotopes for each chemical element was properly accounted for. In this work, we concentrated on comparisons between Geant4 calculations and experiment for the energy deposited by electrons in a thin plastic scintillator. We have used the simplest possible laboratory geometry so that the Monte Carlo geometry could reproduce it exactly.

The Geant4 code software used in treating the transportation of  $\beta$  and  $\gamma$  particles through matter is both modular and flexible, especially in the description of low-energy electromagnetic processes down to 250 eV. In addition, it is also possible to simulate a rather complicated 3-D geometry, select a variety of materials and decay products (including radioactive ions), and choose how to handle the physical processes governing particle interactions. Moreover, it provides output of the simulated data at different

stages in the calculation and under various selection criteria. An overview of recent developments in diverse areas of this toolkit is presented in Ref. [4].

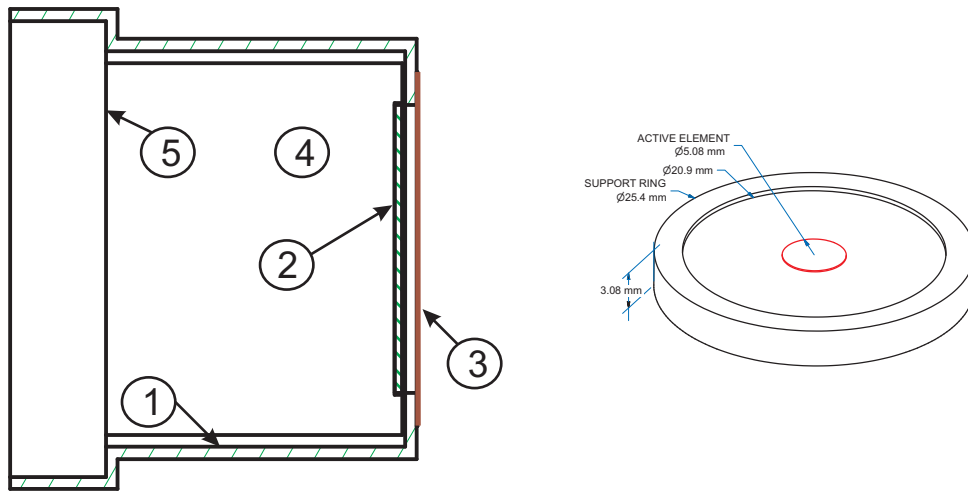


**Figure 1.** (a): Incident  $\beta$ -particles from a radioactive source pass through a thin havar-foil window (3) into the plastic-scintillator disc (2). The disc is recessed into a lucite light guide (4), which is coupled to a phototube (not shown in the figure) at surface 5. The scintillator and light guide are enclosed in a cylindrical cover (1) made from PVC. (b): Radioactive-source geometry: the support ring is made from aluminum.

All three radioactive sources emit  $\gamma$  rays as well as  $\beta$  particles and, although our thin scintillator is relatively insensitive to the former, we nonetheless took extra precautions to ensure that we were only studying the detectors' response to the latter. In addition to recording a spectrum from each source as already described, we also recorded a second spectrum with a 2-mm-thick aluminum plate inserted between the source and the detector. This plate was thick enough to remove all the  $\beta$  particles without significantly attenuating the  $\gamma$  rays. We then subtracted this second spectrum from the first, and considered the resultant spectrum to be a “pure”  $\beta$  spectrum. This method has one flaw, however: the spectrum obtained with the aluminum plate includes some contribution from the bremsstrahlung created by the  $\beta$  particles as they stop. Thus, we took the same approach with the calculated Monte Carlo spectra: we made two calculations for each source, one with an aluminum plate and one without, took the difference between them and then compared that difference spectrum with the “pure” experimental  $\beta$  spectrum.

To simulate the decay of a radioactive nuclide with Geant4, it is possible to define each  $\gamma$  transition, internal-conversion line and  $\beta$ -decay spectrum individually and require Geant4 to transport all particles through the specified materials and determine the spectrum in the scintillator. However, the code also offers a radioactive decay module, which generates all the decay components radiated from a specified source using information from the Evaluated Nuclear Structure Data File (ENSDF) [5]. We used this module to generate the emission spectra from  $^{207}\text{Bi}$  and  $^{137}\text{Cs}$ . An example – the primary electron spectrum emitted from  $^{207}\text{Bi}$  – is shown in Fig. 1 of Ref. [3].

To our surprise, in the case of  $^{133}\text{Ba}$  we found that the initial decay spectrum produced by the radioactive module of Geant4 was simply not correct, yielding relative conversion-electron intensities in significant disagreement with ENSDF data. Therefore, for this decay only, we inserted each decay mode and transition individually.

Based on a primary emission spectrum thus generated, the Monte Carlo code then determines the total energy deposited into the scintillator for each source. However, before this result can be compared with the experimental spectrum, it is necessary to add in the effects of statistical fluctuations introduced by the processes of light production and transmission, as well as photomultiplication and electronic pulse analysis. For this purpose, we looked to a published study of the response of a plastic scintillator to mono-energetic beams of positrons and electrons [6], which graphed the width of the full-energy Gaussian peak as a function of energy between 0.8 and 3.8 MeV. Since we also needed to deal with energies lower than that, we took the width to be linearly dependent on energy below 0.8 MeV.

Our procedure was to take the scintillator spectrum produced by Geant4 and process it by a randomization algorithm written in C++ in the ROOT [7] analysis framework. In essence, this process spread the number of counts in each energy bin into a Gaussian distribution centered at the original energy and with a width,  $\sigma$ , taken or extrapolated from Ref. [6]. The results could then be compared directly with the measured spectra. The comparisons for two sources,  $^{133}\text{Ba}$  and  $^{137}\text{Cs}$ , appear in Figs. 2a and 2b respectively.

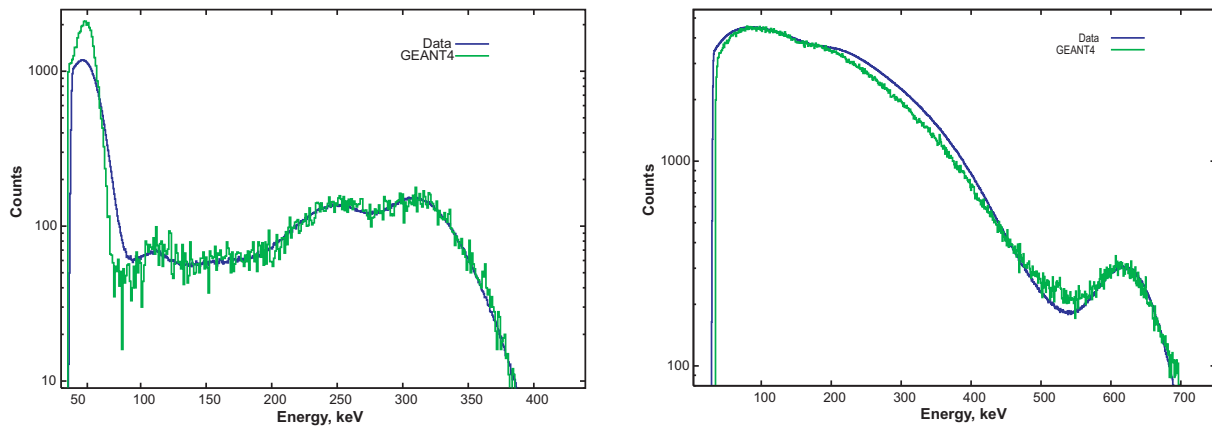


**Figure 2.** (a) Net spectrum of the decay of  $^{133}\text{Ba}$  as recorded from our plastic  $\beta$  detector. (b) Net spectrum of the decay of  $^{137}\text{Cs}$  similarly recorded. Each is compared with a Geant4-simulated result.

The results obtained in this work from Monte Carlo simulations are in quite good agreement with the data. All features that appear in the experimental spectra are also seen in the simulated ones. Additional final turning of the Monte Carlo model is required for each case however. For example, in calculating the  $\beta$  continuum from the decay of  $^{137}\text{Cs}$ , we used an “allowed” shape. Since the decay is actually of “forbidden” character with a known shape-correction factor, it is likely that the observed small difference between the simulated and measured spectra (see Fig. 2b) can be removed by our using the

correct shape-correction factor. We plan to incorporate this improvement. In addition, some adjustment of the low-energy behavior of the peak resolution is probably warranted.

- [1] J. C. Hardy, and I. S. Towner, *Phys. Rev. C* **71**, 055501 (2005).
- [2] S. Agostinelliae, J. Allisonas, K. Amakoe, *et al.*, *Nucl. Instrum. Methods Phys. Res.* **A506**, 250 (2003).
- [3] V. V. Golovko, V. E. Iacob, and J. C. Hardy, *Progress in Research*, Cyclotron Institute, Texas A&M University (2005-2006), p.I-43.
- [4] J. Allison, K. Amako, J. Apostolakis, *et al.*, *IEEE Trans. Nucl. Sci.* **53**, 270 (2006).
- [5] J. Tuli, *Evaluated nuclear structure data file - a manual*, Formal report, BNL-NCS-51655-02-Rev (2001).
- [6] E. T. H. Clifford, E. Hagberg, and V. T. Koslowsy, *et al.*, *Nucl. Instrum. Methods* **224**, 440 (1984).
- [7] R. Brun, and F. Rademakers, *Nucl. Instrum. Methods Phys. Res.* **A389**, 81 (1997).

**SECTION VI**  
**PUBLICATIONS**

**PAPERS PUBLISHED**  
**April 1, 2006 – March 31, 2007**

**Giant resonances in  $^{46,48}\text{Ti}$** , Y. Tokimoto, Y.-W. Lui, H.L. Clark, B. John, X. Chen, and D.H. Youngblood, *Phys. Rev. C* **74**, 044308 (2007).

**Precise half-life measurements for the superallowed  $\beta^+$  emitters  $^{34}\text{Ar}$  and  $^{34}\text{Cl}$** , V.E. Iacob, J.C. Hardy, J.F. Brinkley, C.A. Gagliardi, V.E. Mayes, N. Nica, M. Sanchez-Vega, G. Tabacaru, L. Trache, and R.E. Tribble, *Phys. Rev. C* **74**, 055502 (2006).

**$\beta$  decay of the proton-rich nucleus  $^{23}\text{Al}$  and astrophysical consequences**, V.E. Iacob, Y. Zhai, T. Al-Abdullah, C. Fu, J.C. Hardy, N. Nica, H.I. Park, G. Tabacaru, L. Trache, and R.E. Tribble, *Phys. Rev. C* **74**, 045810 (2006).

**Branching ratios for the beta decay of  $^{21}\text{Na}$** , V.E. Iacob, J.C. Hardy, C.A. Gagliardi, J. Goodwin, N. Nica, H.I. Park, G. Tabacaru, L. Trache, R.E. Tribble, Y.J. Zhai, and I.S. Towner, *Phys. Rev. C* **74**, 015501 (2006).

**Structure of  $^{12}\text{N}$  using  $^{11}\text{C} + \text{p}$  resonance scattering**, K. Peräjärvi, Changbo Fu, G.V. Rogachev, G. Chubarian, V.Z. Goldberg, F.Q. Guo, D. Lee, D.M. Moltz, J. Powell, B.B. Skorodumov, G. Tabacaru, X.D. Tang, R.E. Tribble, B.A. Brown, A.B. Volya, and Joseph Cerny, *Phys. Rev. C* **74**, 024306 (2006).

**An indirect method using ANCs in nuclear astrophysics**, R.E. Tribble, T. Al-Abdullah, C. Fu, C.A. Gagliardi, A.M. Mukhamedzhanov, F. Pirlepesov, G. Tabacaru, X. Tang, L. Trache, P. Bem, V. Burjan, V. Kroha, J. Novak, S. Piskor, E. Simeckova, F. Vesely, J. Vincour, and F. Carstoiu, *Proc. Carpathian Summer School, Romania, 2005*, ed. by S. Stoica, L. Trache, and R.E. Tribble (World Scientific, Singapore, 2006) pg. 307.

**Exotic Nuclei and Nuclear/Particle Astrophysics**, eds. by S. Stoica, L. Trache, and R.E. Tribble, *Proceedings of the Carpathian Summer School of Physics 2005, Mamaia-Constanta, Romania, 2005* (World Scientific, Singapore, 2006).

**Breakup of loosely bound nuclei as indirect method in nuclear astrophysics:  $^8\text{B}$ ,  $^9\text{C}$ ,  $^{23}\text{Al}$** , L. Trache, F. Carstoiu, C.A. Gagliardi, and R.E. Tribble, *Eur. Phys. J. A* **27**, 237 (2006).

**Test of internal-conversion theory with precise  $\gamma$ - and x-ray spectroscopy**, J.C. Hardy, N. Nica, V.E. Iacob, M.B. Trzhaskovskaya, and R.G. Helmer, *Appl. Radiat. Isot.* **64**, 1392 (2006).

**Precise half-life measurement of  $^{34}\text{Ar}$ , a superallowed  $\beta$  emitter**, V.E. Iacob, J.C. Hardy, C.A. Gagliardi, V.E. Mayes, N. Nica, G. Tabacaru, L. Trache, and R.E. Tribble, *Exotic Nuclei and*

*Nuclear/Particle Astrophysics*, eds S. Stoica, L. Trache and R.E. Tribble (World Scientific, Singapore, 2006) pg 387.

**The status of  $V_{ud}$** , J.C. Hardy, *Intersections of Particle and Nuclear Physics 2006: 9<sup>th</sup> Conference*, ed. T.M. Liss, AIP Conference Proceedings **870**, 309 (2006).

**Q-values of the superallowed  $\beta$ -emitters  $^{26}\text{Al}^m$ ,  $^{42}\text{Sc}$  and  $^{46}\text{V}$  and their impact on  $V_{ud}$  and the unitarity of the Cabibbo-Kobayashi-Maskawa matrix**, T. Eronen, V Elomaa, U. Hager, J. Hakala, A. Jokinen, A. Kankainen, I. Moore, H. Penttila, S. Rahaman, A. Saastamoinen, T. Sonoda, J. Aysto, J.C. Hardy and V.S. Kolhinen, *Phys. Rev. Lett.* **97**, 232501 (2006).

**Test of internal-conversion of theory with measurement in  $^{134}\text{Cs}$  and  $^{137}\text{Ba}$** , N. Nica, J.C. Hardy, V.E. Jacob, W.E. Rockwell and M.B. Trzhaskovskaya, *Phys. Rev. C* **75**, 024308 (2007).

**Probing the standard model with superallowed nuclear beta decay**, J.C. Hardy and I.S. Towner, *Nuclear Physics News International*, **16**, No. 4 (2006) pg 11.

**Mass measurements of  $^{22}\text{Mg}$  and  $^{26}\text{Si}$  via (p,t) reactions and penning traps**, J.A. Clark, A. Parikh, F. Buchinger, J.A. Caggiano, J.E. Crawford, C. Deibel, J.P. Green, S. Gulick, J.C. Hardy, A.A. Hecht, J.K.P. Lee, A.F. Levand, R. Lewis, B.F. Lundgren, P.D. Parker, G. Savard, N.D. Scielzo, K.S. Sharma, I. Tanihata, W. Trimble, J.C. Wang, Y. Wang, C. Wrede and Z. Zhou, *Proceedings of International Symposium on Nuclear Astrophysics – Nuclei in the Cosmos – IX*, Proceedings of Science PoS(NIC-IX) 081.

**Superallowed beta decay studies at TRIUMF – nuclear structure and fundamental symmetries**, E.F. Zganjar, T. Achtzehn, D. Albers, C. Andreoiu, A.N. Andreyev, R.A.E Austin, G.C. Ball, J.A. Behr, G.C. Biosvert, P. Bricault, S. Bishop, R.S. Chakrawarthy, R. Churchman, D. Cross, E. Cunningham, J.M. D’Auria, M. Dombisky, P. Finlay, P.E. Garrett, G.F. Grinyer, G. Hackman, V. Hanamaayer, J.C. Hardy, D.F. Hodgson, B. Hyland, V. Jacob, P. Klages, K.A. Koopmans, W.D. Kulp, J. Lassen, J.P. Lavoie, J.R. Leslie, T. Linder, J.A. Macdonald, H.-B. Mak, D. Melconian, A.C. Morton, W.E. Ormand, C.J. Osborne, C.J. Pearson, M.R. Pearson, A.A. Phillips, A. Piechaczek, J. Ressler, F. Sarazin, G. Savard, M.A. Schumaker, H.C. Scraggs, C.E. Svensson, J.J. Valiente-Dobon, I.S. Towner, J.C. Waddington, P.M. Walker, K. Wendt and J.L. Wood, *Acta Physica Polonica B* **38**, 1179 (2007).

**Nuclear spin-lattice relaxation of  $^{62}\text{Cu}$  at low temperatures in iron**, V.V. Golovko, I.S. Kraev, T. Phalet, N. Severijns, D. Venos, D. Zakoucky, P. Herzog, C. Tramm, U. Koester, D. Srnka, M. Honusek, B. Delaure, M. Beck, V.Yu. Kozlov, and A. Lindroth, *Phys. Rev. C* **74**, 044313 (2006).

**The WITCH experiment: completion of a set-up to investigate the structure of weak interactions with a penning trap**, V.Yu. Kozlov, N. Severijns, D. Beck, M. Beck, S. Coeck, B. Delaure, A. Lindroth,

P. Delahaye, F. Wenander, V.V. Golovko, I.S. Kraev and T. Phalet, *Int J. Mass Spectrometry* **251**, 159 (2006).

**Microchannel plate response to high-energy ion bunches**, S. Coeck, M. Beck, B. Delaure, V.V. Golovko, M. Herbane, A. Lindroth, S. Kopecky, V.Yu. Kozlov, I.S. Kraev, T. Phalet and N. Severijns, *Nucl. Instrum. Methods Phys. Res. A* **557**, 516 (2006).

**Photoneutron cross section measurements on the  $N=82$  nuclei  $^{139}\text{La}$  and  $^{141}\text{Pr}$ : implications for p-process nucleosynthesis**, H. Utsunomiya, A. Makinaga, S. Goko, T. Kaihori, H. Akimune, T. Yamagata, M. Ohta, H. Toyokawa, S. Müller, Y.-W. Lui, and S. Goriely, *Phys. Rev. C* **74**, 025806 (2006).

**Partial photoneutron Cross Sections for the Isomeric State  $^{180}\text{Tam}$** , S. Goko, H. Utsunomiya, S. Goriely, A. Makinaga, T. Kaihori, S. Hohara, H. Akimune, T. Yamagata, Y.-W. Lui, Toyokawa, A.J. Koning, and S. Hilaire, *Phys. Rev. Lett.* **96**, 192501 (2006)

**Experimental determination of the symmetry energy of a low density nuclear gas**, S. Kowalski, J.B. Natowitz, S. Shlomo, R. Wada, K. Hagel, J. Wang, T. Materna, Z. Chen, Y.G. Ma, L. Qin, A.S. Botvina, D. Fabris, M. Lunardon, S. Moretto, G. Nebbia, S. Pesente, V. Rizzi, G. Viesti, M. Cinausero, G. Prete, T. Keutgen, Y. El Masri, Z. Majka, A. Ono, *Phys. Rev. C* **75**, 014601 (2007).

**Properties of the initial participant matter interaction zone in near Fermi-energy heavy ion collisions**, J. Wang, T. Keutgen, R. Wada, K. Hagel, S. Kowalski, T. Materna, L. Qin, Z. Chen, J.B. Natowitz, Y.G. Ma, M. Murray, A. Keksis, E. Martin, A. Ruangma, D.V. Shetty, G. Souliotis, M. Veselsky, E.M. Winchester, S.J. Yennello, D. Fabris, M. Lunardon, S. Moretto, G. Nebbia, S. Pesente, V. Rizzi, G. Viesti, M. Cinausero, G. Prete, J. Cibor, Z. Majka, W. Zipper, P. Staszal, Y. El Masri, R. Alfarro, A. Martinez-Davalos, A. Menchaca-Rocha, A. Ono, *Phys. Rev. C* **75**, 014604 (2007).

**Nuclear thermometry**, A. Kelic, J.B. Natowitz, and K.H. Schmidt, *Eur. Phys. J. A* **30**, 203 (2006).

**Comment on breakup densities of hot nuclei**, V.E. Viola, K Kwiatkowski, S.J. Yennello, and J.B. Natowitz, *Phys. Lett. B* **637**, 176 (2006).

**Density dependence of the symmetry energy and the equation of state of isospin asymmetric nuclear matter**, D.V. Shetty, S.J. Yennello, and G.A. Souliotis, *Phys. Rev. C* **75**, 034602 (2007).

**Symmetry energy in the equation of state of asymmetric nuclear matter**, S.J. Yennello, D.V. Shetty, and G.A. Souliotis, *AIP Conference Proceedings*, **884**, 351 (2007).

**Tracing the evolution of the symmetry energy of hot nuclear fragments from the compound nucleus towards multifragmentation**, G.A. Souliotis, A.S. Botvina, D.V. Shetty, A. Keksis, M. Jandel, M. Veselsky, and S.J. Yennello, *Phys. Rev. C* **75**, 011601 (2007).

**Production of cold fragments in nucleus-nucleus collisions in the Fermi-energy domain**, M. Veselsky and G.A. Souliotis, Nucl. Phys. A **781**, 521 (2007).

**Neutron-to-proton ratios of quasiprojectile and midrapidity emission in the  $^{64}\text{Zn} + ^{64}\text{Zn}$  reaction at 45 MeV/nucleon**, D. Theriault, J. Gauthier, F. Grenier, F. Moisan, C. St-Pierre, R. Roy, B. Davin, S. Hudan, T. Padaszynski, R.T. deSouza, E. Bell, J. Garey, J. Iglio, A.L. Keksis, S. Parketon, C. Richers, D.V. Shetty, S.N. Soisson, G.A. Souliotis, B.C. Stein, and S.J. Yennello, Phys. Rev. C **74**, 051602 (2006).

**Signatures of critical behavior in the multifragmentation of nuclei with charge  $Z = 12 - 15$  and the  $N/Z$  dependence**, M. Jandel, S. Wuenschel, D.V. Shetty, G.A. Souliotis, M. Veselsky, A.L. Keksis, S.J. Yennello, Phys. Rev. C **74**, 054608 (2006).

**Symmetry energy and the isoscaling properties of the fragments produced in  $^{40}\text{Ar}$ ,  $^{40}\text{Ca} + ^{58}\text{Fe}$ ,  $^{58}\text{Ni}$  reactions at 25, 33, 45 and 53 MeV/nucleon**, J. Iglio, D.V. Shetty, S.J. Yennello, G.A. Souliotis, M. Jandel, A.L. Keksis, S.N. Soisson, B.C. Stein, S. Wuenschel, and A. Botvina, Phys. Rev. C **74**, 024605 (2006).

**Isospin flows**, M.D. Toro, S.J. Yennello, and B.A. Li, Eur. Phys. J. A **30**, 153 (2006).

**Challenges in nuclear dynamics and thermodynamics**, F. Gulminelli, W. Trautmann, S.J. Yennello, and Ph. Chomaz, Eur. Phys. J. A **30**, 1 (2006).

**Comment on breakup densities of hot nuclei**, V. Viola, K. Kwiatkowski, S.J. Yennello, and J.B. Natowitz, Phys. Lett. B **637**, 176 (2006).

**Light ion-induced multifragmentation: The ISiS project**, V.E. Viola, K. Kwiatkowski, L. Beaulieu, D.S. Bracken, H. Breuer, J. Brzychczyk, R.T. de Souza, D.S. Ginger, W.-C. Hsi, R.G. Korteling, T. Lefort, W.G. Lynch, K.B. Morley, R. Legrain, L. Pienkowski, E.C. Pollacco, E. Renshaw, A. Ruangma, M.B. Tsang, C. Volant, G. Wang, S.J. Yennello, N.R. Yoder, Phys. Rep. **434**, 1 (2006).

**A systematics of  $K\alpha$  X-ray satellite structure**, V. Horvat, R.L. Watson, Yong Peng, Phys. Rev. A **74**, 022718 (2006).

**A Target K vacancy production by 2.5 to 25 MeV/amu Ar, Kr, and Xe ions**, R.L. Watson, Y. Peng, V. Horvat, Jand A.N. Perumal, Phys. Rev. A **74**, 062709 (2006).

**Fission and binary fragmentation reactions in  $^{80}\text{Se} + ^{208}\text{Pb}$  and  $^{80}\text{Se} + ^{232}\text{Th}$  systems**, R.G. Thomas, ASaxena, P.K. Sahu, R.K. Choudhury, I.M. Govil, S. Kailas, S.S. Kapoor, M. Cinausero, G. Prete, V. Rizzi, D. Fabris, M. Lunardon, S. Moretto, G. Viesti, G. Nebbia, S.

Pesente, B. Dalena, G.D'Erasmus, E.M. Fiore, M. Palomba, A. Pantaleo, V. Patocchio, G.Simonetti, N. Gelli, and F. Lucarelli, Phys. Rev. C **75**, 024604 (2007).

**Fission time scale from precision neutron, proton, and  $\alpha$  particle multiplicities in  $^{28}\text{Si}+^{175}\text{Lu}$** , K. Ramachandran, A. Chatterjee, A. Navin, K. Mahata, A. Shrivastava, V. Tripathi, S. Kailas, V. Nanal, R.G. Pillay, A. Saxena, R.G. Thomas, Suresh Kumar, and P.K. Sahu, Phys. Rev. C **73**, 064609 (2006).

**Fusion barrier distribution derived from quasielastic excitation functions in  $^{11}\text{B}$ ,  $^{12}\text{C}$ ,  $^{13}\text{C}+^{209}\text{Bi}$  reactions**, P.K. Sahu, A. Saxena, B.K. Nayak, R.G. Thomas, B.V. John, and R.K. Choudhury, Phys. Rev. C **73**, 064604 (2006).

**Unified theory of scattering for arbitrary potentials**, A.S. Kadyrov, A.M. Mukhamedzhanov, I. Bray and A.T. Stelbovics, Proceedings of the 3rd Asia-Pacific Conference on Few-body problems in physics, Nakhon Ratchasima, Thailand, 2005, ed. by Yupeng Yan, C Kobdaj & P Suebka, 2007

**Are spectroscopic factors from transfer reactions consistent with asymptotic normalization coefficients?** D.Y. Pang F.M. Nunes, A.M. Mukhamedzhanov, Phys. Rev. C **75**, 024601 (2007).

**Lowest excited states of  $^{13}\text{O}$** , B.B. Skorodumov, G.V. Rogachev, P. Boutachkov, A. Aprahamian, V.Z. Goldberg, A.M. Mukhamedzhanov, S. Almaraz, H. Amro, F.D. Becchetti, S. Brown, Y. Chen, H. Jiang, J.J. Kolata, L O. Lamm, M. Quinn, and A. Woehr, Phys. Rev. C **75**, 024607 (2007).

**Astrophysical reaction rate for the neutron-generator reaction  $^{13}\text{C}(\alpha, n)^{16}\text{O}$  in asymptotic giant branch stars**, E.D. Johnson, G.V. Rogachev, A.M. Mukhamedzhanov, L.T. Baby, S. Brown, W.T. Cluff, A.M. Crisp, E. Diffenderfer, V.Z. Goldberg, B.W. Green, T. Hinners, C.R. Hoffman, K.W. Kemper, O. Momotyuk, P. Peplowski, A. Pipidis, R. Reynolds, and B.T. Roeder, Phys. Rev. Lett. **97**, 192701 (2006).

**Indirect techniques in nuclear astrophysics**, A.M. Mukhamedzhanov, G. Rogachev, L. D. Blokhintsev, S. Brown, V. Burjan, S. Cherubini, V. Z. Goldberg, B. F. Irgaziev, E. Johnson, K. kemper, V. Kroha, A. Momotyuk, R. G. Pizzone, B. Roeder, S. Romano, C. Spitaleri, R. E. Tribble and A. Tumino, AIP Proceedings, Origin of Matter and Evolution of Galaxies, **847**, 255 (2006).

**Erratum: relation between proton and neutron asymptotic normalization coefficients for light mirror nuclei and its relevance to nuclear astrophysics**, N.K. Timofeyuk, R.C. Johnson, A.M. Mukhamedzhanov, Phys. Rev. Lett. **97**, 069904 (2006).

**Probing properties of neutron stars with terrestrial nuclear reactions**, B.A. Li, L.W. Chen, C.M. Ko, A.W. Steiner, and G.C. Yong, Proceedings of Nuclear Physics Trend: 6<sup>th</sup> China-Japan Joint Nuclear

Physics Symposium, Shanghai, China, May 2006, ed. by Y.G. Ma and A. Ozawa, AIP Conf. Proc. **865**, 268 (2006).

**A dynamical quark coalescence model for  $\phi$  and  $\Omega$  production in heavy-ion collisions at RHIC**, L.W. Chen and C.M. Ko, Proceedings of Nuclear Physics Trend: 6th China-Japan Joint Nuclear Physics Symposium, Shanghai, China, May, 2006, ed by Y.G. Ma and A. Ozawa, AIP Conf. Proc. **865**, 318 (2006).

**$\phi$  and  $\Omega$  production in relativistic heavy-ion collisions in a dynamical quark coalescence model**, L. W. Chen and C. M. Ko, Phys. Rev. C **73**, 044903 (2006).

**Rapidity and system size dependence of anisotropic flows in relativistic heavy ion collisions**, C.M. Ko and L.W. Chen, Nucl. Phys. **A744**, 527 (2006).

**Charm elliptic flow in Au+Au collisions at RHIC**, B. Zhang, L.W. Chen, and C.M. Ko, Nucl. Phys. **A774**, 665 (2006).

**Nuclear symmetry potential in the relativistic impulse approximation**, Z.H. Li, L.W. Chen, C.M. Ko, B.A. Li, and H.R. Ma, Phys. Rev. C **74**, 044613 (2006).

**Parton degrees of freedom and hadronization dynamics at RHIC**, C.M. Ko, L.W. Chen, and B. Zhang, J. Phys. G **32**, S143 (2006).

**Constraining the Skyrme effective interactions and the neutron skin thickness of nuclei using isospin diffusion data from heavy ion collisions**, L.W. Chen, C.M. Ko, and B.A. Li, Int. J. Mod. Phys. E **15**, 1385 (2006).

**Constraining properties of neutron stars with heavy-ion reactions**, B.A. Li, L.W. Chen, C.M. Ko, and A.W. Steiner Rev. Mex. Fis. S **52**, 56 (2006).

**Suppression of heavy quarks in heavy ion collisions**, C.M. Ko and W. Liu, Nucl. Phys. **A783**, 233c (2007).

**Bottomonium production at RHIC and LHC**, L. Grandchamp, S. Lumpkins, D. Sun, H. van Hees, and R. Rapp, Phys. Rev. C **73**, 064906 (2006).

**Comprehensive interpretation of thermal dileptons at the SPS**, H. van Hees and R. Rapp, Phys. Rev. Lett. **97**, 102301(2006).

**Scattering of quark quasiparticles in the quark-gluon plasma**, M. Mannarelli and R. Rapp, Nucl. Phys. **A774**, 761 (2006).

**Heavy-quark spectra at RHIC and resonances in the QGP**, R. Rapp, V. Greco and H. van Hees, Nucl. Phys. **A774**, 685 (2006).

**Medium modifications of vector mesons and NA60**, H. van Hees and R. Rapp, Proc. of 22<sup>nd</sup> Winter Workshop on Nuclear Dynamics 2006, EP Systema, Budapest (Hungary), 91-98

**Heavy-quark diffusion, flow and recombination at RHIC**, R. Rapp and H. van Hees, J. Phys. G **32**, S351 (2006).

**Dileptons and medium effects in heavy-ion collisions**, R. Rapp, Nucl. Phys. **A782**, 275 (2007).

**The influence of memory effects on dispersions of kinetic energy at nuclear fission**, V.M. Kolomietz, S.V. Radionov, and S. Shlomo, Physica Scripta **73**, 458 (2006).

**Current status of the equation of state of nuclear matter**, S. Shlomo, Tapas sil, V. Kim Au, and O.G. Pochivalov, Phys. At. Nucl. **69**, 1132 (2006).

**Small damping approach in Fermi-liquid theory**, V.M. Kolomietz, S.V. Lukyanov, and S. Shlomo, Central Eur. J Phys. **4**, 393 (2006).

**Deducing the nuclear matter incompressibility coefficient from data on isoscalar compression modes**, S. Shlomo, V.M. Kolomietz, and G. Colo, in *Dynamics and Thermodynamics with Nucleonic Degree of Freedom*, ed. by P.Chomaz, F. Gulminelli, W. Trautmann, and S.J. Yennello (Springer Verlag, Berlin, 2006), Eur. Phys. J. A **30**, 23 (2006).

**New Skyrme type effective nucleon-nucleon interaction**, S. Shlomo, Proceedings of International Symposium on Structure of Exotic Nuclei and Nuclear Forces (SENUF06), Tokyo, Japan, March, 2006, J. Phys. : Conf. series **49**, 186 (2006).

**Nuclear matter properties from collective modes in nuclei**, S. Shlomo and V. Kim Au, International Conference on Nuclear Structure Physics, Int. J. Mod Phys. **E15**, 1909 (2006).

**The equation of state of symmetric and asymmetric nuclear matter**, S. Shlomo, Proceedings of the International Conference on Current Problems in Nuclear Physics and Atomic Energy, Kyiv 2006, part I, p. 22.

**Equation of state of symmetric and asymmetric nuclear matter**, S. Shlomo, VI LatinAmerican Symposium on Nuclear Physics and Application, AIP Conference Proceedings **884**, 340 (2006).

**Hadronization of dense partonic matter**, R.J. Fries, J. Phys. G **32**, s151 (2006).

**Hadron correlations and parton recombination**, R.J. Fries, Nucl. Phys. **A783**, 125 (2007).

**The energy dependence of  $p_t$  angular correlations inferred from mean- $p_t$  fluctuation scale dependence in heavy ion collisions at the SPS and RHIC**, J. Adams *et al.* (STAR Collaboration), J. Phys. G **34**, 451 (2007).

**Neutral kaon interferometry in Au+Au collisions at  $\sqrt{s_{NN}} = 200$  GeV**, B.I. Abelev *et al.* (STAR Collaboration), Phys. Rev. C **74**, 054902 (2006).

**Two-particle correlations on transverse momentum and momentum dissipation in Au-Au collisions at  $\sqrt{s_{NN}} = 130$  GeV**, J. Adams *et al.* (STAR Collaboration), J. Phys. G **34**, 799 (2007).

**Longitudinal double-spin asymmetry and cross section for inclusive jet production in polarized proton collisions at  $\sqrt{s_{NN}} = 200$  GeV**, B.I. Abelev *et al.* (STAR Collaboration), Phys. Rev. Lett. **97**, 252001 (2006).

**$\Delta\phi\Delta\eta$  correlations in central Au+Au collisions at  $\sqrt{s_{NN}} = 200$  GeV**, J. Adams *et al.* (STAR Collaboration), Phys. Rev. C **75**, 034901 (2007).

**Scaling properties of hyperon production in Au+Au collisions at  $\sqrt{s_{NN}} = 200$  GeV**, J. Adams *et al.* (STAR Collaboration), Phys. Rev. Lett. **98**, 062301 (2007).

**Identified baryon and meson distributions at large transverse momenta from Au+Au collisions at  $\sqrt{s_{NN}} = 200$  GeV**, J. Adams *et al.* (STAR Collaboration), Phys. Rev. Lett. **97**, 152301 (2006).

**Strange baryon resonance production in  $\sqrt{s_{NN}} = 200$  GeV p+p and Au+Au collisions**, J. Adams *et al.* (STAR Collaboration), Phys. Rev. Lett. **97**, 132301 (2006).

**The multiplicity dependence of inclusive  $p_t$  spectra from p-p collisions at  $\sqrt{s_{NN}} = 200$  GeV**, J. Adams *et al.* (STAR Collaboration), Phys. Rev. D **74**, 032006 (2006).

**Direct observation of dijets in central Au+Au collisions at  $\sqrt{s_{NN}} = 200$  GeV**, J. Adams *et al.* (STAR Collaboration), Phys. Rev. Lett. **97**, 162301 (2006).

**Forward neutral pion production in p + p and d + Au collisions at  $\sqrt{s_{NN}} = 200$  GeV**, J. Adams *et al.* (STAR Collaboration), Phys. Rev. Lett. **97**, 152302 (2006).

**Identified hadron spectra at large transverse momentum in p + p and d + Au collisions at  $\sqrt{s_{NN}} = 200$  GeV**, J. Adams *et al.* (STAR Collaboration), Phys. Lett. B **637**, 161 (2006).

**Directed Flow in Au + Au Collisions at  $\sqrt{s_{NN}} = 62$  GeV**, J. Adams *et al.* (STAR Collaboration), Phys. Rev. C **73**, 034903 (2006).

**Proton – lambda correlations in central Au+Au collisions at  $\sqrt{s_{NN}} = 200$  GeV**, J. Adams *et al.* (STAR Collaboration), Phys. Rev. C **74**, 064906 (2006).

**Transverse-momentum  $p_T$  correlations on  $(\eta, \phi)$  from mean- $p_T$  fluctuations in Au + Au Collisions at  $\sqrt{s_{NN}} = 200$  GeV**, J. Adams *et al.* (STAR Collaboration), J. Phys. G **32**, L37 (2006).

**Minijet deformation and charge-independent angular correlations on momentum subspace  $(\eta, \phi)$  in Au-Au collisions at  $\sqrt{s_{NN}} = 130$  GeV**, J. Adams *et al.* (STAR collaboration), Phys. Rev. C **73**, 064907 (2006).

**Some striking new STAR results**, C.A. Gagliardi (for the STAR collaboration), Nucl. Phys. **A774**, 409 (2006).

**Measurement of the absolute differential cross section for np elastic scattering at 194 MeV**, M. Sarsour *et al.*, Phys. Rev. C **74**, 044003 (2006).

**Hypernuclear spectroscopy using the  $(e, e' K^+)$  reaction**, L. Yuan and M. Sarsour *et al.* (HSNN collaboration), Phys. Rev. C **73**, 044607 (2006).

**Measurement of  $P_\mu \xi$  in polarized muon decay**, B. Jamieson, R. Bayes, Yu.I. Davydov, P. Depommier, J. Doornbos, W. Faszer, M.C. Fujiwara, C.A. Gagliardi, A. Gaponenko, D.R. Gill, P. Gumplinger, M.D. Hasinoff, R.S. Henderson, J. Hu, P. Kitching, D.D. Koetke, J.A. Macdonald, R.P. MacDonald, G.M. Marshall, E.L. Mathie, R.E. Mischke, J.R. Musser, M. Nozar, K. Olchanski, A. Olin, R. Openshaw, T.A. Porcelli, J.-M. Poutissou, R. Poutissou, M.A. Quraan, N.L. Rodning, V. Selivanov, G. Sheffer, B. Shin, T.D.S. Stanislaus, R. Tacik, V.D. Torokhov, R.E. Tribble, and M.A. Vasiliev (TWIST Collaboration), Phys. Rev. D **74**, 072007 (2006).

**d+Au Collisions at STAR**, C.A. Gagliardi (STAR Collaboration), Proc. XIV Int. Workshop Deep Inelastic Scatt. (DIS2006), Tsukuba, Japan, 2006, ed. by M. Kuze, K. Nagano, and K. Tokushuku (World Scientific, Singapore, 2007) pg. 169.

**Transverse spin studies with STAR at RHIC**, C.A. Gagliardi (STAR Collaboration), Proc. XIV Int. Workshop Deep Inelastic Scatt. (DIS2006), Tsukuba, Japan, 2006, ed. by M. Kuze, K. Nagano, and K. Tokushuku (World Scientific, Singapore, 2007) pg. 699.

**High transverse momentum eta meson production in p+p, d+Au and Au+Au collisions at  $\sqrt{s_{NN}} = 200$  GeV**, S.S. Adler *et al.* (PHENIX Collaboration), Phys. Rev. C **75**, 024909 (2007).

**Measurement of direct photon production in p+p collisions at  $\sqrt{s_{NN}} = 200$  GeV**, S.S. Adler *et al.* (PHENIX Collaboration), Phys. Rev. Lett. **98**, 012002 (2007).

**Evidence for a long-range component in the pion emission source in Au+Au collisions at  $\sqrt{s_{NN}} = 200$  GeV**, S.S. Adler *et al.* (PHENIX Collaboration), Phys. Rev. Lett. **98**, 132301 (2007).

**Measurement of high-p(T) single electrons from heavy-flavor decays in p+p collisions at  $\sqrt{s_{NN}} = 200$  GeV**, A. Adare *et al.* (PHENIX Collaboration), Phys. Rev. Lett. **97**, 252002 (2006).

**Jet properties from dihadron correlations in p+p collisions at  $\sqrt{s_{NN}} = 200$  GeV**, S.S. Adler *et al.* (PHENIX Collaboration), Phys. Rev. D **74**, 072002 (2006).

**Nuclear effects on hadron production in d+Au and p+p collisions at  $\sqrt{s_{NN}} = 200$  GeV**, S.S. Adler *et al.* (PHENIX Collaboration), Phys. Rev. C **74**, 024904 (2006).

**Azimuthal angle correlations for rapidity separated hadron pairs in d + Au Collisions at  $\sqrt{s_{NN}} = 200$  GeV**, S.S. Adler *et al.* (PHENIX Collaboration), Phys. Rev. Lett. **96**, 222301 (2006).

**Improved measurement of double helicity asymmetry in inclusive midrapidity  $\pi^0$  production for polarized p+p collisions at  $\sqrt{s_{NN}} = 200$  GeV**, S.S. Adler *et al.* (PHENIX Collaboration), Phys. Rev. D **73**, 091102 (2006).

**Common suppression pattern of  $\eta$  and  $\pi^0$  mesons at high transverse momentum in Au+Au collisions at  $\sqrt{s_{NN}} = 200$  GeV**, S.S. Adler *et al.* (PHENIX Collaboration), Phys. Rev. Lett. **96**, 202301 (2006).

**Jet structure from dihadron correlations in d+Au collisions at  $\sqrt{s_{NN}} = 200$  GeV**, S.S. Adler *et al.* (PHENIX Collaboration), Phys. Rev. C **73**, 054903 (2006).

**Dense-Medium Modifications to Jet-Induced Hadron Pair Distributions in Au+Au Collisions at  $\sqrt{s_{NN}} = 200$  GeV**, S.S. Adler *et al.* (PHENIX Collaboration), Phys. Rev. Lett. **97**, 052301 (2006).

**Strangeness enhancement in p-A collisions: Consequences for the interpretation of Strangeness production in A-A collisions**, B.A. Cole, X.H. Yang, V. Cianciolo, A. Frawley, E.P. Hartouni, H. Hiejima, A. Lebedev, N. Maeda, S. Mioduszewski, K. Read, M. Rosati, R.A. Soltz, S. Sorensen, J.H. Thomas, Y. Torun, D. Winter, and W.A. Zajc, Phys. Lett. B **639**, 210 (2006).

# **SECTION VII**

## **APPENDIX**

## TALKS PRESENTED

April 1, 2006 – March 31, 2007

*Inelastic  ${}^6\text{Li}$  Scattering Studies of the ISGMR – Prospects with Radioactive Beams*, **D.H. Youngblood**, **Invited Talk**, NSCL User Workshop on, East Lansing, Michigan, (May 2006).

*Systematic of Giant Monopole Resonance and its Isotopic Dependence*, **Y.-W. Lui**, D.H. Youngblood, H.L. Clark, Y. Tokimoto and X. Chen, **Invited Talk**, Workshop on In Heaven and On Earth 2006 – The Equation of State in Astrophysics, Montreal, Canada, (July 2006).

*Report to NuPECC (Nuclear Physics European Collaboration Committee) on Nuclear Science Advisory Committee Activities*, **R.E. Tribble**, **Invited Talk**, Nuclear Physics European Collaboration Committee, Cracow, Poland, (July, 2006).

*Report to International Union of Pure and Applied Physics Working Group 9 on Nuclear Science Advisory Committee Activities*, **R.E. Tribble**, **Invited Talk**, International Union of Pure and Applied Physics Working Group 9, Vancouver, British Columbia, Canada, (July, 2006).

*Indirect Techniques (I): Asymptotic Normalization Coefficients and the Trojan Horse Method*, **R.E. Tribble**, **Invited Talk**, Nuclei in the Cosmos IX, CERN, Geneva, Switzerland, (June, 2006).

*Facility Upgrade at Texas A&M University for Accelerated Beams*, **R.E. Tribble**, **Invited Talk**, RNB7 (Radioactive Nuclear Beams), Cortina d'Ampezzo, Italy, (July, 2006).

*Asymptotic Normalization Coefficients as an Indirect Technique for Nuclear Astrophysics – Past, Present and Future Prospects*, **R.E. Tribble**, **Invited Talk**, International Summer School on Subatomic Physics, Beijing, China, (August, 2006).

*Towards the 2007 Long Range Plan*, **R.E. Tribble**, **Invited Talk**, APS Division of Nuclear Physics, Nashville, Tennessee, (October, 2006).

*Radioactive Ion Beams at TAMU*, **R.E. Tribble**, **Invited Talk**, presentation to Nuclear Science Advisory Committee Task Force on Rare Ion Beams, Chicago, Illinois, (December 2006).

*How Does Nuclear Physics Apply To Astrophysics?*, **R.E. Tribble**, **Invited Talk**, North Houston Astronomy Club, Houston, Texas, (April, 2006).

*New Approaches to Old Problems with Asymptotic Normalization Coefficients*, **R.E. Tribble**, **Invited Talk**, Shanghai Institute of Applied Physics, Shanghai, China, (August, 2006).

*Understanding the Evolution of the Universe: A Nuclear Physics Perspective*, **R.E. Tribble**, University of Missouri – Columbia, Columbia, Missouri, (September, 2006).

*Stellar Evolution: A Nuclear Physics Perspective*, **R.E. Tribble**, Argonne National Laboratory, Argonne, Illinois, (December, 2006).

*QCD at High Energy/Small-x*, **C.A. Gagliardi**, **Invited Talk**, Workshop on Future Opportunities in QCD, Washington, DC, (December 2006).

*Exploring Muon Decay with TWIST*, **C.A. Gagliardi (for the TWIST Collaboration)**, **Invited Talk**, Joint Meet. Pacific Region Part. Phys. Communities (APS DPF2006+JPS2006), Honolulu, Hawaii, (October 2006).

*Recent Results from STAR*, **C.A. Gagliardi (for the STAR Collaboration)**, **Invited Talk**, IX Int. Conf. Nucl.-Nucl. Coll. (Nucleus-Nucleus 2006), Rio de Janeiro, Brazil, (August 2006).

*Transverse Spin Studies with STAR at RHIC*, **C.A. Gagliardi (for the STAR Collaboration)**, **Invited Talk**, XIV Int. Workshop Deep Inelastic Scatt. (DIS2006), Tsukuba, Japan, (April 2006).

*d+Au Collisions at STAR*, **C.A. Gagliardi (for the STAR Collaboration)**, XIV Int. Workshop Deep Inelastic Scatt. (DIS2006), Tsukuba, Japan, (April 2006).

*Nuclear Physics for Astrophysics with Radioactive Beams: Indirect Methods*, **L. Trache**, **Invited Talk**, Predeal International Summer school in Nuclear Physics, Predeal, Romania, (August 2006).

*Nuclear Physics for Astrophysics with Radioactive Beams: Indirect Methods*, **L. Trache**, **Invited Talk**, The 5<sup>th</sup> International Balkan School in Nuclear Physics, Brasov, Romania, (September 2006).

*Breakup and Transfer Reactions with Radioactive Beams for Nuclear Astrophysics*, **L. Trache**, HRIBF Workshop – Nuclear Measurements for Astrophysics, Oak Ridge, Tennessee, (October 2006).

*Cross Sections for Reactions in Explosive H-Burning from Indirect Methods*, **L. Trache**, T. Al-Abdullah, A. Banu, C. Fu, C.A. Gagliardi, J.C. Hardy, V.E. Iacob, M. McClesky, A.M. Mukhamedzhanov, G. Tabacaru, R.E. Tribble, and Y. Zhai, Minisymposium on Questions and Techniques in Low energy Nuclear Astrophysics Measurements, Nashville, Tennessee, (October 2006).

*Development of New Techniques to Determine Neutron and Charged-Particle Induced Reaction Rates*, **L. Trache**, R.E. Tribble, C.A. Gagliardi, A.M. Mukhamedzhanov, M. McClesky, SSAA Grants Symposium, Washington, DC, (February 2007).

*Determination of the Reaction Rate for  $^{17}\text{F}(p,\gamma)^{18}\text{Ne}$  using the Neutron Transfer reaction  $^{13}\text{C}(^{17}\text{O},^{18}\text{O})^{12}\text{C}$* , **T. Al-Abdullah**, X. Chen, C.A. Gagliardi, Y.-W. Lui, G. Tabacaru, Y. Tokimoto, L. Trache, R.E. Tribble, Y. Zhai, and C. Carstoiu, 2006 APS Division of Nuclear Physics Annual Meeting, Nashville, Tennessee, (October 2006).

*Beta-decay of Proton-Rich Nucleus  $^{23}\text{Al}$  and Astrophysical Consequences*, **Y.J. Zhai**, V.E. Iacob, T. Al-Abdullah, C. Fu, J.C. Hardy, N. Nica, H.-I. Park, G. Tabacaru, L. Trache, and R.E. Tribble, APS April Meeting, Dallas, Texas, (April 2006).

*Longitudinal Double-spin Asymmetry for Inclusive Jet Production in Polarized p+p Collisions at  $\sqrt{s} = 200$  Gev*, **M. Sarsour**, 2006 APS Division of Nuclear Physics Annual Meeting, Nashville, Tennessee, (October 2006).

*Recent Results from STAR Spin program at RHIC*, **M. Sarsour**, **Invited Talk**, APS Topic Group on Hadronic Physics, Nashville, Tennessee, (October 2006).

*Elliptic Flow Measurements of Inclusive Photons and Neutral Pion Reconstructions*, **Ahmed Hamed**, Wayne State University, Detroit, Michigan, (July 2006).

*Inclusive Photons-Charged Hardrons Azimuthal Correlations*, **Ahmed Hamed**, Star Analysis Meeting, Brookhaven National Laboratory, Upton, New York, (March 2007).

*Superallowed Nuclear Beta Decay: A Window on the Weak Interaction*, **J.C. Hardy, Invited Talk**, Bonner Prize Lecture, The American Physical Society April Meeting, Dallas, Texas, (April 2006).

*The Status of  $V_{ud}$* , **J.C. Hardy, Invited Talk**, Conference on the Intersections of Particle and Nuclear Physics, CIPANP 2006, Puerto Rico, (May 2006).

*Precision Measurements (two talks)*, **J.C. Hardy, Invited Lectures**, The RIA Summer School, Oak Ridge National Laboratory, Oak Ridge, Tennessee, (July 2006).

*The Value of  $V_{ud}$  from Nuclear Decays and summary of  $V_{ud}$* , **J.C. Hardy, Invited Talk**, The 4<sup>th</sup> International Workshop on the CKM Triangle (CKM2006), Nagoya, Japan, (December 2006).

*Superallowed Nuclear Beta Decay: A Window on the Weak Interaction*, **J.C. Hardy**, Colloquium at Texas A&M University, College Station, Texas, (March 2006).

*Precise Branching Ratio Measurements for the  $\beta$  Decay of  $^{21}\text{Na}$* , **V.E. Jacob**, J.C. Hardy, C.A. Gagliardi, J. Goodwin, N. Nica, H.-I. Park, G. Tabacaru, L. Trache, R.E. Tribble, Y.J. Zhai and I.S. Towner, APS Meeting, Dallas, Texas, (April 2006).

*Further Tests of Internal-Conversion Theory with Precise  $\gamma$  – and X – Ray Spectroscopy*, **N. Nica**, W.E. Rockwell, J.C. Hardy, V.E. Jacob, H.-I. Park, J. Goodwin and M.B. Trzhaskovskaya, APS Meeting, Dallas, Texas, (April 2006).

*Further Tests of Internal-Conversion Theory with Precise  $\gamma$  – and X – Ray Spectroscopy: Texas A&M Program to Measure  $^{134}\text{Cs}^m$  and  $^{137}\text{Ba}$* , **N. Nica**, National Nuclear Data Center, Brookhaven National Laboratory, Upton, New York, (June 2006).

*Mass-Chain Evaluation for ENSDF*, **N. Nica**, seminar at National Nuclear Data Center, Brookhaven National Laboratory, Upton, New York, (June 2006).

*Cross Section for reactions in Explosive H Burning from Indirect Methods*, **L. Trache**, T. Al-Abdullah, A. Banu, C. Fu, C.A. Gagliardi, J.C. Hardy, V.E. Jacob, M. McCleskey, A.M. Mukhamedzhanov, G. Tabacaru, R.E. Tribble, and Y.J. Zhai, 2006 APS Division of Nuclear Physics Annual Meeting, Nashville, Tennessee (October 2006).

*Measurement of the  $\gamma$  Branches in the  $\beta^+$  Decay of  $^{32}\text{Cl}$* , **D. Melconian**, C. Bordeanu, A. Garcia, J.C. Hardy, V.E. Jacob, N. Nica, H.-I. Park, G. Tabacaru, L. Trache, S. Triambak, R.E. Tribble and Y.J. Zhai, 2006 APS Division of Nuclear Physics Annual Meeting, Nashville, Tennessee (October 2006).

*Precise Half Life Measurement of  $^{10}\text{C}$* , **V.E. Jacob**, V. Golovko, J. Goodwin, J.C. Hardy, N. Nica, H.-I. Park, L. Trache and R.E. Tribble, 2006 APS Division of Nuclear Physics Annual Meeting, Nashville, Tennessee (October 2006).

*Validation of the GEANT4 Code for Simulations of a Plastic  $\beta$  Detector and Its Application to Efficiency Calibration*, **V. Golovko**, V.E. Jacob, and J.C. Hardy, 2006 APS Division of Nuclear Physics Annual Meeting, Nashville, Tennessee (October 2006).

*Further Tests of Internal-Conversion Theory with Precise  $\gamma$ - and x-Ray Spectroscopy: Texas A&M Program to Measure  $^{134}\text{Cs}^m$  and  $^{137}\text{Ba}$* , **N. Nica**, Predeal International School on Collective Motion and Phase Transitions in Nuclei, Predeal, Romania (August 2006).

*Evaluated Nuclear Data File*, **N. Nica**, Predeal International School on Collective Motion and Phase Transitions in Nuclei, Predeal, Romania (August 2006).

*Testing the Standard Model via Precise Measurements: the Cases of  $^{34}\text{Ar}$  and  $^{21}\text{Na}$* , **V.E. Jacob**, Predeal International School on Collective Motion and Phase Transitions in Nuclei, Predeal, Romania (August 2006).

*Further Tests of Internal-Conversion Theory with Precise  $\gamma$ - and x-Ray Spectroscopy: Texas A&M Program to Measure  $^{134}\text{Cs}^m$  and  $^{137}\text{Ba}$* , **N. Nica**, Meeting of the U.S. Nuclear Data Program, Upton, New York (November 2006).

*Results from RHIC and a Look to the Future*, **S. Mioduszewski**, **Invited Talk**, CAARI, Fort worth, Texas, (February 2006).

*Experimental Overview of High- $p_T$  Results from RHIC*, **S. Mioduszewski**, **Invited Talk**, Workshop on High- $p_T$  physics at LHC, Jyväskylä, Finland, (March 2007).

*Progress in Studies of Resonance Reactions Induced by r/a Beams*, **V.Z. Goldberg**, **Invited Talk**, The 56<sup>th</sup> International CONFERENCE – NUCLEUS 2006, Sarov, Russia (2006).

*The Lightest Drip-Line Nuclei and Hydrogen-7*, **V.Z. Goldberg**, Joint Institute of Nuclear Research, Dubna, Russia, (August 2006).

*Physicists, Governments, People and Weapon of Mass Destruction*, **V.Z. Goldberg**, University of Jyvaskyla, Finland, (September 2006).

*Study of  $^{18}\text{Ne}$  Structure by  $^{14}\text{O}+\text{Alpha}$  Elastic Resonance Reaction*, **Changbo Fu**, V.Z. Goldberg, G.V. Rogachev, G.G. Chubarian, G. Tabacaru, M. McCleskey, Y. Zhai, T. Al-Abdullah, L. Trache, A. Banu, R.E. Tribble, 2006 APS Division of Nuclear Physics Annual Meeting, Nashville, Tennessee, (October 2006).

*Single and Double Protons from the  $^{14}\text{O}+\text{alpha}$  Interaction*, **Changbo Fu**, V.Z. Goldberg, G.V. Rogachev, G.G. Chubarian, M. McCleskey, Y. Zhai, T. Al-Abdullah, L. Trache, A. Banu, R.E. Tribble, 2006 APS Division of Nuclear Physics Annual Meeting, Nashville, Tennessee, (October 2006).

*From Nuclear Collisions to the Equation of State of Nuclear Matter*, **J.B. Natowitz**, **Invited Talk**, Department of Chemistry, Washington University, St Louis, Missouri, (March 2006).

*Experimental Determination of the Symmetry Energy in a Low Density Nuclear Gas*, **J.B. Natowitz**, **Invited Talk**, Workshop on In Heaven and On Earth 2006 – The Equation of State in Astrophysics, Montreal, Canada, (July 2006).

*Expansion, Clustering and Symmetry Energies in Low Density Nuclear Gases*, **J.B. Natowitz**, **Invited Talk**, Gordon Research conference on Nuclear chemistry, New London, New Hampshire, (June 2006).

Experimental Determination of The Symmetry Energy of Low Density nuclear Matter, **J.B. Natowitz**, **Invited Talk**, NN2006 Conference, Rio de Janeiro, Brazil, (August, 2006).

*Nuclear Symmetry Energies at Low Density*, **J.B. Natowitz**, **Invited Talk**, Department of Physics, University of Padova, Italy, (March 2006).

*Nuclear Symmetry Energies at Low Density*, **J. B. Natowitz**, **Invited Talk**, Laboratory Nazionale di Sud, Catania, Italy, (March 2006).

*A Large Acceptance Spectrometer for Re-accelerated Radioactive Beams of  $E/A=6-25$  MeV at the US Advanced Exotic Beam Facility*, **G.A. Souliotis**, DNP/NSAC Town Meeting, Chicago, Illinois, (January 2007).

*Neutron-rich Rare Isotope Production at Fermi Energies and Application to the Texas A&M Radioactive Beam Upgrade Project*, **G.A. Souliotis**, **Invited Talk**, LNS, INFN, Catania, Italy, (December 2006).

*Properties of Hot Neutron-rich Nuclei Formed in Multifragmentation and Their Importance to Supernova Nucleosynthesis*, **G.A. Souliotis**, **Invited Talk**, Institute of Nuclear Physics of NCSR 'Demokritos', Athens, Greece, (November 2006).

*Symmetry Energy of Hot Heavy Fragments Produced in the Multifragmentation of Neutron-rich Systems at Fermi Energies*, **G.A. Souliotis**, 2006 APS Division of Nuclear Physics Annual Meeting, Nashville, Tennessee, (October 2006).

*Symmetry Energy, Temperature, Density, and Isoscaling Parameter as a Function of Excitation Energy in  $A \sim 100$  Mass Region*, **D.V. Shetty**, 2006 APS Division of Nuclear Physics Annual Meeting, Nashville, Tennessee, (October 2006).

*Multifragmentation Reactions, Phase Transitions and the Nuclear EOS*, **S.J. Yennello**, **Invited Talk**, International Summer School in Nuclear Physics Collective Motion and Phase Transitions in Nuclear Systems, Predeal, Romania, (September 2006).

*Extracting Information about the Symmetry Energy Using Heavy-ion Collisions*, **S.J. Yennello**, **Invited Talk**, International Summer School in Nuclear Physics Collective Motion and Phase Transitions in Nuclear Systems, Predeal, Romania, (September 2006).

*Rare Isotope Production around and below the Fermi Energy and its Application to the Texas A&M Radioactive Beam Upgrade*, **G.A. Souliotis**, **Invited talk**, 232<sup>nd</sup> National Meeting of the American Chemical Society, San Francisco, California, (September 2006).

*Properties of Hot Nuclear Fragments Formed in Multifragmentation and Their Astrophysical Implications*, **G.A. Souliotis**, 19<sup>th</sup> International Conference on the Application of Accelerators in Research and Industry (CAARI), Fort Worth, Texas, (August 2006).

*Rare Isotope Production in the Fermi Energy Regime and Application to the Texas A&M RIB Upgrade*, **G.A. Souliotis**, **Invited Talk**, 19<sup>th</sup> International Conference on the Application of Accelerators in Research and Industry (CAARI), Fort Worth, Texas, (August 2006).

*Constraining the Density Dependence of Symmetry Energy in the Nuclear Equation of State Using Heavy Ion Beams*, **D.V. Shetty**, **Invited Talk**, 19<sup>th</sup> International Conference on the Application of Accelerators in Research and Industry (CAARI), Fort Worth, Texas, (August 2006).

*Neutron-rich Rare Isotope Production below the Fermi Energy and Its Application to the Texas A&M RIB Upgrade*, **G.A. Souliotis**, **Invited Talk**, Institute of Physics of the Slovak Academy of Science, Bratislava, Slovakia, (July 2006).

*Neutron-rich Rare Isotope Production below the Fermi Energy and Its Application to the Texas A&M RIB Upgrade*, **G.A. Souliotis**, 7<sup>th</sup> International Conference on radioactive nuclear beams (RNB7), Cortina d'Ampezzo, Italy, (July 2006).

*Extracting Information about the Symmetry Energy Using Heavy-ion Collisions*, **S.J. Yennello**, **Invited Talk**, Nuclear Chemistry Gordon Conference, New Hampshire, (June 2006).

*Density Dependence of the Symmetry Energy in the Equation of State of Asymmetric Nuclear Matter*, **D.V. Shetty**, APS Meeting, Dallas, Texas, (April 2006).

*Exploring the Evolution of the Symmetry Energy of Hot Fragments from the Compound Nucleus towards Bulk Multifragmentation*, **S.J. Yennello**, APS meeting, Dallas, Texas, (April 2006).

*Properties of Hot Neutron-drip-line Nuclei Formed in the Multifragmentation of Neutron-rich Systems. Importance to Supernova Nucleosynthesis*, **G.A. Souliotis**, **Invited Talk**, Department of Physics, Notre Dame University, south Bend, Indiana, (April 2006).

*Quasielastic and Deep-inelastic Collisions with Stable and Re-accelerated Beams at  $E/A=10-20$  MeV/nucleon*, **G.A. Souliotis**, ATLAS User Group Meeting, Physics Division, Argonne National Laboratory, Argonne Illinois, (April 2006).

*Properties of Hot Neutron-rich Nuclei Formed in Multifragmentation and Their Importance to Supernova Nucleosynthesis*, **G.A. Souliotis**, **Invited Talk**, Department of Physics, Western Michigan University, Kalamazoo, Michigan, (April 2006).

*Studying the Symmetry Energy of Excited Projectile-like Sources*, **A.L. Keksis**, APS meeting, Dallas, Texas, (April 2006).

*Collective Dynamics in Heavy Ion Collisions at FAIR*, **C.M. Ko**, **Invited Talk**, International Workshop on the Physics of High Density Matter, Trento, Italy, (May 2006).

*Quark Coalescence in Relativistic Heavy Ion Collisions*, **C.M. Ko**, **Invited Talk**, Gordon Research Conference in Nuclear Chemistry, New London, New Hampshire, (June 2006).

*Viscous Effects on Flow at RHIC*, **C.M. Ko**, **Invited Talk**, AGS/RHIC Users' Meeting Workshop, Brookhaven National Laboratory, Upton, New York, (June 2006).

*Suppression of heavy quarks in Heavy-Ion Collisions*, **C.M. Ko**, **Invited Talk**, 2<sup>nd</sup> International Conference on Hard and Electromagnetic Probes of High-Energy Nuclear Collisions, Pacific Grove, California, (June 2006).

*Searching for the Quark-Gluon Plasma in Relativistic Heavy Ion Collisions*, **C.M. Ko**, **Invited Talk**, Summer School on Nuclear Collective Dynamics III, Istanbul, Turkey, (June 2006).

*Jet Conversions in the Quark-Gluon Plasma*, **C.M. Ko**, **Invited Talk**, International Symposium on Multiparticle Dynamics, Paraty, Brazil, (September 2006).

*Heavy Ion Collisions at LHC in a Multiphase Transport Mode*, **C.M. Ko**, **Invited Talk**, International Workshop on Particle Correlations and Femtoscopy, Sao Paulo, Brazil, (September 2006).

*Partonic Transport Description of Heavy Ion Collisions*, **C.M. Ko**, **Invited Talk**, The 19<sup>th</sup> International Conference on Ultra-Relativistic Nucleus-Nucleus Collisions, Shanghai, China, (November 2006).

*Heavy Quark Three-Body Scattering in QGP*, **C.M. Ko**, **Invited Talk**, International Workshop on Selected Topics in Heavy Flavor Production in High-Energy Collisions, Beijing, China, (November 2006).

*Indirect Techniques in Nuclear Astrophysics*, **A.M. Mukhamedzhanov**, **Invited Talk**, IX International Conference on Nucleus Nucleus Collisions 2006 - NN2006, Rio-de Janeiro, Brazil, (August 2006).

*Theory of the Trojan Horse*, **A.M. Mukhamedzhanov**, **Invited Talk**, University of Notre Dame, South Bend, Indiana, (October, 2006).

*Trojan Horse as Indirect Technique in Nuclear Astrophysics*, **A.M. Mukhamedzhanov**, 2006 APS Division of Nuclear Physics Annual Meeting, Nashville, Tennessee, (October 2006).

*Nuclear Reactions and Nuclear Astrophysics*, **A.M. Mukhamedzhanov**, Town meeting, Chicago, Illinois, (January 2007).

*Overlap Functions and Nuclear Reactions Future*, **A.M. Mukhamedzhanov**, Town meeting, Chicago, Illinois, (January 2007).

*Indirect Techniques in Nuclear Astrophysics: Asymptotic Normalization Coefficient and Trojan Horse*, **A.M. Mukhamedzhanov**, Town meeting, Chicago, Illinois, (January 2007).

*Indirect Techniques in Nuclear Astrophysics: Asymptotic Normalization Coefficients and Trojan Horse*, **A.M. Mukhamedzhanov**, **Invited Talk**, Joint Japanese-American Meeting, Oak Ridge National Laboratory, Oak Ridge, Tennessee, (March 2007).

*Indirect Techniques in Nuclear Astrophysics*, **A.M. Mukhamedzhanov**, Nuclear Physics in Nuclear Astrophysics III, Dresden, Germany, (March 2007).

*Charm and Charmonium in the Quark-Gluon Plasma*, **R. Rapp**, **Invited Talk**, International Workshop on Continuous Advances in QCD, University of Minnesota, Minneapolis, Minnesota, (May 2006).

*Dileptons and Medium Effects in Heavy-Ion Collisions*, **R. Rapp**, **Invited Talk**, The 5<sup>th</sup> International Conference on Perspectives in Hadronic Physics, Trieste, Italy, (May 2006).

*Phenomenology of Dilepton Production in Heavy-Ion Collisions*, **R. Rapp**, **Invited Talk**, The International Workshop on “The Physics of Compressed Baryonic Matter”, ECT\* Trento, Italy, (May 2006).

*Kinetics of Charm in Medium*, **H. van Hees**, **Invited Talk**, The International Workshop on “The Physics of Compressed Baryonic Matter”, ECT\* Trento, Italy, (May 2006).

*Q-Qbar Modes in the Quark-Gluon Plasma*, **D. Cabrera**, IV<sup>th</sup> International Conference on Quarks and Nuclear Physics, Madrid, Spain, (June 2006).

*The Kaon Optical Potential modified by Theta<sup>+</sup> Pentaquark Excitation*, **D. Cabrera**, IV<sup>th</sup> International Conference on Quarks and Nuclear Physics, Madrid, Spain, (June 2006).

*Electromagnetic and Heavy-Quark Probes of the Quark-Gluon Plasma*, **R. Rapp**, **Invited Talk**, The International Symposium on “Hadrons, Nuclei and Stars” on the Occasion of G.E. Brown’s 80<sup>th</sup>, P. Braun-Munzinger’s and W. Weise’s 60<sup>th</sup> Birthday, Darmstadt, Germany, (June 2006).

*Medium Modifications of Hadrons and the NA60 Dimuon Data*, **H. van Hees**, Frankfurt University, Frankfurt, Germany, (June 2006).

*Quarkonia in Medium and their Fate at Future RHIC*, **R. Rapp**, **Invited Talk**, The International Workshop on “Future Prospects in QCD at High Energy”, Brookhaven National Laboratory, Upton, New York, (July 2006).

*Sonden des Quark-Gluon Plasmas: Schwere Quarks und Thermische Strahlung*, **R. Rapp**, Tübingen University, Tübingen, Germany, (July 2006).

*Kinetics of Charm in Medium*, **H. van Hees**, Los Alamos National Laboratory, Los Alamos, New Mexico, (July 2006).

*Hot and Dense QCD Matter and Heavy-Ion Collisions*, **R. Rapp**, **Invited Talk**, 19<sup>th</sup> International Conference on the Application of Accelerators in Research and Industry (CAARI 2006), Fort Worth, Texas, (August 2006).

*Melting Rho Meson and Thermal Dileptons*, **R. Rapp**, XXXVI International Symposium on Multiparticle Dynamics, Paraty, Rio de Janeiro, Brazil, (September 2006).

*Heavy-Quark Energy Loss in the QGP and non-photon Single-Electron Observables*, **H. van Hees**, **Invited Talk**, Pre-conference workshop on “Properties and Signatures of sQGP”, 2006 APS Division of Nuclear Physics Annual Meeting, Nashville, Tennessee, (October 2006).

*In-Medium Modifications of Hadrons and the NA60 Dimuon Measurements*, **H. van Hees**, 2006 APS Division of Nuclear Physics Annual Meeting, Nashville, Tennessee, (October 2006).

*T-Matrix Approach to Quarkonium Correlation Functions in the QGP*, **D. Cabrera**, 2006 APS Division of Nuclear Physics Annual Meeting, Nashville, Tennessee, (October 2006).

*Properties of Vector Mesons in Matter – Theory and Phenomenology*, **R. Rapp**, **Invited Talk**, The 19<sup>th</sup> International Conference on Ultrarelativistic Nucleus-Nucleus Collisions (Quark Matter 2006), Shanghai, China, (November 2006).

*Theoretical Interpretation of Recent SPS Dilepton Data*, **H. van Hees**, The 19<sup>th</sup> International Conference on Ultrarelativistic Nucleus-Nucleus Collisions (Quark Matter 2006), Shanghai, China, (November 2006).

*Heavy Quarks and Quark-Gluon Plasma*, **R. Rapp**, State University of New York at Stony Brook, Stony Brook, New York, (January 2007).

*Heisse und Dichte Materie und Ultrarelativistische Schwerionenkollisionen*, **R. Rapp**, **Invited Talk**, XXXVIII. Arbeitstreffen Kernphysik, Schleching, Germany, (February 2007).

*Quark and Gluon Jet Conversion in the Quark-Gluon Plasma*, **Wei Liu**, **Invited Talk**, Brookhaven National Laboratory, Upton, New York, (October 2006).

*Heavy Quark Energy Loss due to Three-Body Scattering in a Quark-Gluon Plasma*, **Wei Liu**, **Invited Talk**, Quark Matter 2006, Shanghai, China, (November 2006).

*Hard Probes in quark Gluon Plasma*, **Wei Liu**, **Invited Talk**, Shanghai University, Shanghai, China (November 2006).

*Jet Quenching and Conversions in a Quark Gluon Plasma*, **Wei Liu**, **Invited Talk**, Fudan University, Shanghai, China, (November 2006).

*Fully Self Consistent Description of Collective Modes in Nuclei*, **S. Shlomo**, **Invited Talk**, Ben-Gurion University, Beer Sheva, Israel, (May 2006).

*The Equation of Symmetric and Asymmetric Nuclear Matter*, **S. Shlomo**, **Invited Talk**, International Conference on Actual Problems of Nuclear Physics and Atomic energy (NPAAE006), Kiev, Ukraine, (May 2006).

*Nuclear Matter Properties from Collective Modes in Nuclei*, **S. Shlomo**, **Invited Talk**, International Conference on Nuclear Structure Physics, Shanghai, China, (June 2006).

*Some Thoughts on BRAHMS Physics*, **R.J. Fries**, **Invited Talk**, BRAHMS Collaboration Meeting, College Station, Texas, (October 2006).

*Early Time Evolution of High Energy Ion Collisions*, **R.J. Fries**, XIX International Conference on Ultrarelativistic Nucleus-Nucleus Collisions (Quark Matter 2006), Shanghai, China, (November 2006).

*Precision Probes for Hot QCD Matter*, **R.J. Fries**, **Invited Talk**, QCD Workshop in Preparation of the Town Meeting in January, Washington DC, (December 2006).

*Early Time Evolution of Heavy Ion Collisions*, **R.J. Fries**, **Invited Talk**, Strongly Coupled Quark-Gluon Plasma: SPS, RHIC and LHC, Nagoya, Japan, (February 2007).

## RESEARCH PERSONNEL AND ENGINEERING STAFF

April 1, 2006 - March 31, 2007

### Faculty and Research Group Leaders

Rainer Fries, Assist. Prof. of Physics – From 9/1/06  
Carl A. Gagliardi, Professor of Physics  
John C. Hardy, Professor of Physics  
Che Ming Ko, Professor of Physics  
Saskia Mioduszewski, Assist. Prof. of Physics  
J. B. Natowitz, Professor of Chemistry, Bright Chair  
Ralf Rapp Associate Prof. of Physics – From 9/1/06  
Shalom Shlomo, Senior Scientist  
Robert E. Tribble, Professor of Physics, Director  
Rand L. Watson, Professor of Chemistry  
Sherry J. Yennello, Professor of Chemistry  
Dave H. Youngblood, Professor of Physics  
Akram M. Zhanov, Senior Scientist

### Research Staff

Henry Clark, Accelerator Physicist (50%)  
Grigor Chubaryan, Research Scientist  
John C. Hagel, Research Scientist (50%)  
Vladimir Horvat, Research Scientist (50%)  
Victor Iacob, Associate Research Scientist  
Yiu-Wing Lui, Research Scientist  
Ninel Nica, Assist. Research Scientist  
George Souliotis, Associate Research Scientist- From  
9/1/06  
Livius Trache, Research Scientist  
Ryoichi Wada, Research Scientist

### Visiting Scientists

Daniel Cabrera-Urban  
Vladilen Goldberg  
Ian Towner – From 6/22/06 To 8/22/06

### Accelerator Physics and Radiation Line Staff

Juha Arje, Research Scientist – From 3/23/07  
Joseph Brinkley, Research Associate – From  
2/12/07  
Henry Clark, Accelerator Physicist (50%)  
Vladimir Horvat, Research Scientist (50%)  
Bruce Hyman, Research Associate

George Kim, Accelerator Physicist  
Don May, Accelerator Physicist  
Gabriel Tabacaru, Accelerator Physicist

### Computer Systems Staff

Robert Burch, Jr., Systems Analyst/Sr.  
Microcomputer/LAN Administrator  
John C. Hagel, Assoc. Research Scientist (50%)

### Engineering Staff

Greg Derrig, Senior Mechanical Engineer  
Robert Olsen, Senior Mechanical Engineer

### Postdoctoral Research Associates

Adriana Banu  
Zhiqiang Chen  
Rory Clarke – From 7/19/06  
Stratos Galanopoulos – From 10/30/07  
Victor Golovko  
Ahmed Hamed – From 8/1/06  
Wei Liu  
Thomas Materna – To 8/18/06  
Yong S. Oh – From 2/1/07  
Yong Peng – From 1/2/07  
Lorenzo Ravagli – From 9/1/06  
Prakash Sahu  
Murad G. Sarsour  
Dinesh Shetty  
Tapas Sils – To 1/31/07  
Yoshiaki Tokimoto – To 1/30/07  
Hendrik van Hees  
Au Kim Vuong – From 3/16/07  
Benwei Zhang – From 5/15/06

## STUDENTS

April 1, 2006 - March 31, 2007

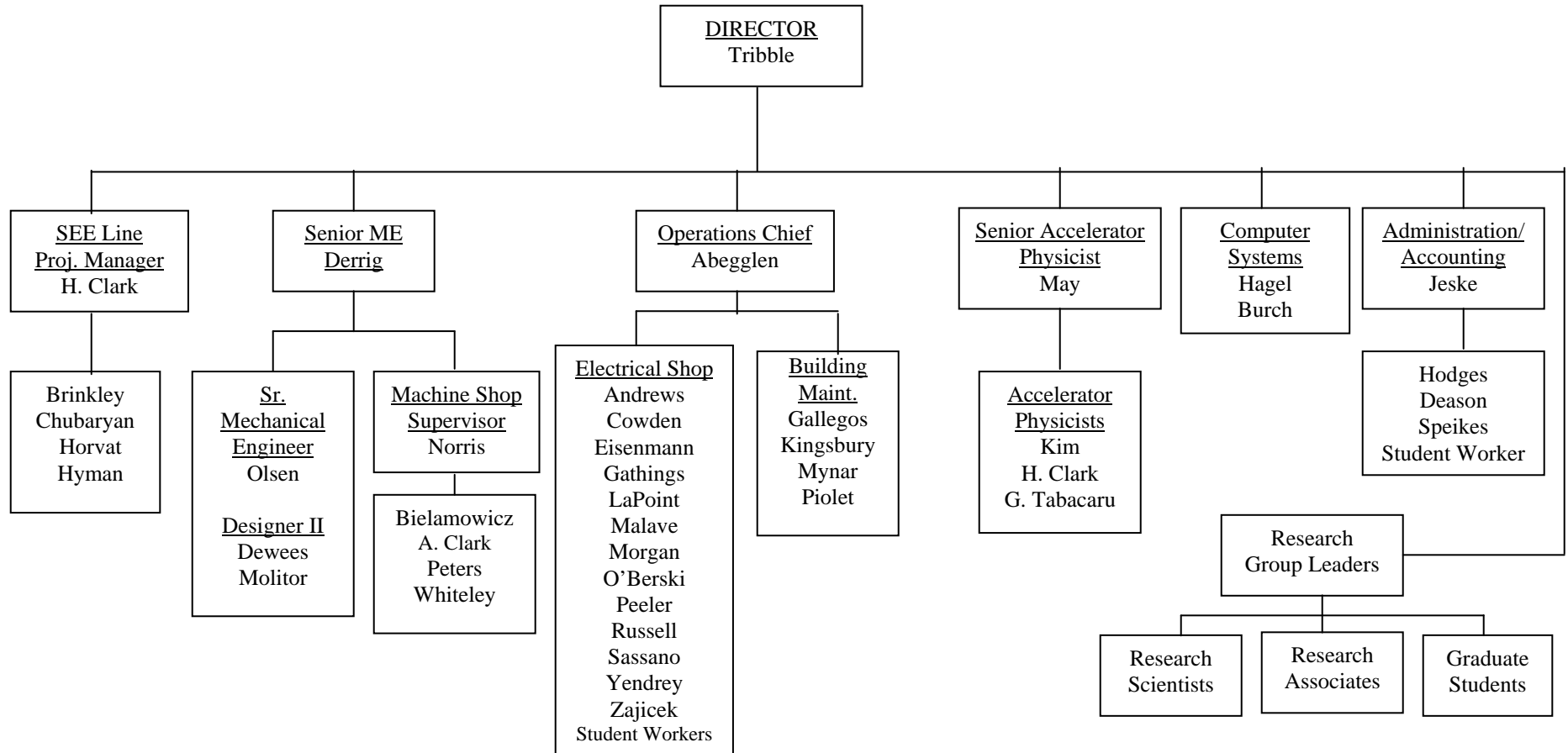
### Graduate Students

Tariq Al-Abdullah  
Matthew Cervantes – From 6/1/06  
Xinfeng Chen  
Martin Codrington  
James Drachenberg  
Changbo Fu  
John Goodwin  
Thomas Henry – To 1/15/07  
August Keksis  
Zach Kohley – From 1/16/07  
Yun Li  
Matthew McCleskey – From 9/1/06  
Hyo-In Park  
Yong Peng – To 1/1/07  
Oleksiy Pochivalov – To 8/31/06  
Li Jun Qin  
Sarah Soisson  
Brian Stein  
Deqiang Sun – To 8/15/06  
Au Kim Vuong – To 3/15/07  
Sara Wuenschel  
Yongjun Zhai  
Xingbo Zhao

### Undergraduates and Student Technicians

Alfredo J. Echeverria  
Joshua Garey – To 5/15/06  
Jonathan Hunt – To 4/13/06  
Katie Huseman – From 9/1/06  
Joshua Kammer – From 3/19/07  
Jennifer Jeffress  
Meagan Makarenko – To 5/31/06  
Toby Martin – From 1/5/07  
Larry May  
Matthew McCleskey – 8/31/06  
Robert Polis – From 2/13/07  
Casseday Richers – To 5/15/06  
Derek Wilson  
Shauna Yow

## ORGANIZATIONAL CHART - CYCLOTRON INSTITUTE



**STUDENTS WHO RECEIVED GRADUATE DEGREES  
FROM THESIS WORK CONDUCTED  
AT  
THE CYCLOTRON INSTITUTE**

**April 1, 2006 – March 31, 2007**

Name	Year	Thesis Title	Advisor	First Position	Present Position
Oleksiy Grigorievich Pochivalov	2006	<i>Description of isoscalar giant dipole resonance in nuclei</i>	S. Shlomo	Graduate Research Assistant	Graduate student at Department of Geology and Geophysics, Texas A&M University
Yong Peng	2006	<i>Systematics of Cross Sections for Target K-Vacancy Production in Heavy Ion Collisions</i>	R. L. Watson	Graduate Research Assistant	Postdoctoral Research Associate, Cyclotron Institute, Texas A&M University

## INSTITUTE COLLOQUIA AND SEMINARS

April 1, 2006-March 31, 2007

### 2006

- |              |  |   |
|--------------|--|---|
| April 6      | Dr. Jamal Jalilian-Marian, Institute for Nuclear Theory, University of Washington, Seattle, Washington   | <i>An Introduction to Particle Production in High Energy Nuclear Collisions</i>   |
| April 7      | Professor Taka Kajino, National Astronomical Observatory, University of Tokyo, Tokyo, Japan  | <i>A Frontier of Nuclear Astrophysics: Big-Bang Cosmology and Supernova Nucleosynthesis</i>                               |
| April 19     | Dr. Anna Stasto, Brookhaven National Laboratory, Upton, New York   | <i>High Energy Limit and Parton Saturation in QCD</i>   |
| April 21     | Dr. Stefan Bathe, University of California, Riverside, California  | <i>Direct Photon Production at RHIC</i>   |
| April 28     | Dr. Ahmed Hamed, Wayne State University, Detroit, Michigan   | <i>Toward the Elliptic Flow of Direct Photons</i>   |
| June 6       | Dr. Reg Ronningen, NSCL, Michigan State University, East Lansing, Michigan   | <i>Radiation Transport Simulations and Pre-Conceptual Designs of High-Power Target Stations in Support of RIA R&amp;D</i> |
| June 12      | Dr. Michal Mocko, NSCL and Department of Physics& Astronomy, Michigan State University, East Lansing, Michigan   | <i>Fragmentation of Ca and Ni Isotopes</i>  |
| June 23      | Mr. Matthew Cervantes, Cyclotron Institute, Texas A&M University, College Station, Texas   | <i>Journal Summary of J/psi in a Quark Gluon Plasma</i>   |
| July 25      | Dr. Robert Charity, Washington University at St. Louis, St. Louis, Missouri  | <i>Asymmetry Dependence of Proton Correlations</i>  |
| August 28    | Dr. Stratos Galanopoulos, Department of Physics, National Technical University of Athens and Institute of Nuclear Physics, NCSR "Demokritos", Athens, Greece | <i>Experimental and Theoretical Studies of Neutron Activation Reactions on Ge and Hf Isotopes</i>                         |
| September 14 | Dr. Chandana Sumithrarachchi, Department of Chemistry and NSCL, Michigan State University, East Lansing, Michigan  | <i>The Study of Beta-Delayed Neutron Decay Near Neutron Dripline</i>  |

October 17	Professor W. Bauer, NSCL, Michigan State University, East Lansing, Michigan	<i>The Origin of Elements</i>
October 19	Professor S. Oryu, University of Science, Tokyo, Japan	<i>Few-Body Coulomb Scattering in Momentum Space</i>
October 23	Professor H. A. Schuessler, Department of Physics, Texas A&M University, College Station, Texas Station, Texas	<i>Laser Spectroscopy of Neutron Deficient La Isotops: Results and Plans</i>
November 7	Professor Juha Aysto, Physics Department, University of Jyväskylä, Finland	<i>Trap-Assisted (Nuclear) Spectroscopy</i>
December 5	Professor G. Vesti, INFN and Dipartimento di Fisica – Università di Padova, Padova, Italy	<i>The EURITRACK Project : Status of a Tagged Neutron Inspection System for Cargo Containers</i>
December 5	Dr. Ahmed Hamed, Cyclotron Institute, Texas A&M University, College Station, Texas	<i>Forward Neutral Pions Production in p+p and d+Au Collisions at <math>\sqrt{s_{NN}}=200</math> GeV</i>

## 2007

January 23	Professor Raj K. Gupta, Physics Department, Panjab University, India	<i>Compactness of Hot Fusion Reactions for Super-Heavy Elements</i>
January 30	Professor Su Houn Lee, Yonsei University, Korea	<i>Perturbative QCD Approach to Quarkonium Dissociation</i>
January 31	Mr. Kevin I. Hahn, Ewha Womans University, Seoul, Korea	<i>Measurements of the <math>^{14}\text{O}(\alpha,p)^{17}\text{F}</math> Cross Section</i>
February 21	Dr. Sean Liddick, Oak Ridge National Laboratory, Oak Ridge, Tennessee	<i>Nuclear Structure through Decay Spectroscopy</i>
February 28	Dr. Andreas Schiller, NSCL, Michigan State University, East Lansing, Michigan	<i>Proposed Research at the Texas A&amp;M Cyclotron laboratory and Elsewhere</i>
March 6	Dr. Steven C. Pieper, Physics Division, Argonne National Laboratory, Argonne, Illinois	<i>Ab-initio Calculations of Light Nuclei</i>
March 7	Dr. Dan Melconian, University of Washington, Seattle, Washington	<i>Outline of a Research Program to complement and Diversify Fundamental-symmetry Research at TAMU</i>

March 13	Dr. Hanan Amro, Physics Department, University of Notre Dame, south Bend, Indiana	<i>Nuclear Structure and Reactions with Exotic Beams</i>
March 20	Dr. Jason Clark, Department of Physics, Yale University, New Haven, Connecticut	<i>Laboratory Measurements for Explosive Astrophysics</i>